Université des sciences et technologies de Lille
Laboratoire de Mécanique de Lille
Ecole Doctorale Sciences Pour l'Ingénieur

THÈSE

Pour obtenir le grade de

Docteur de l'Université Lille1 Sciences et Technologies

Discipline : Mécanique, Energétique, Matériaux

Présentée par

Abdelhakim DORBANE

Caractérisation Mécanique et Microstructurale d'un Soudage Hétérogène Par Friction Malaxage de Tôles en Alliage d'Aluminium et de Magnésium

Mechanical and Microstructural Characterization of a Dissimilar Friction Stirred Welded Aluminum-to-Magnesium Alloy Sheets

Soutenue publiquement le 25 Mars 2016 devant le jury composé de :

Aude SIMAR, Professeur	UCL, Louvain, Belgique	Rapporteure
Véronique FAVIER, Professeur	Arts et Métiers ParisTech	Rapporteure
Jean-Michel BERGHEAU, Professeur	ENI Saint-Etienne	Examinateur
Laurent DUBAR, Professeur	Université de Valenciennes	Examinateur
Georges AYOUB, Assistant Professor	Texas A&M University at Qatar	Co-encadrant de thèse
Abdellatif IMAD, Professeur	Université Lille1	Directeur de thèse
Rajashekhara SHABADI, Maître de Conférences	Université Lille1	Invité
Bilal MANSOOR, Assistant Professor	Texas A&M University at Qatar	Invité

Dedication

This Ph.D. research thesis is dedicated to my loving parents, brothers and sisters.

I also dedicate this dissertation to my all friends and university colleagues, who helped me to achieve this work, who believed and helped me to achieve this work.

Acknowledgment

I would like to thank my advisor, Pr. **Abdellatif IMAD**, who granted me the opportunity to prepare a Ph.D. from Lille1 University. I would like to thank him for his time and availability and assistance through out these three exciting years of research.

I would like to thank my co-supervisor, Dr. **Georges AYOUB**, for granting me a financial support over three years and welcoming me into his research team. I would like to thank Dr. **Georges Ayoub** for his advices, his patience, his word of encouragements and the knowledge that he never hesitate to share which had a big and positive impact on the progress of this Ph.D. research work. I will also not forget to extend my gratitude to Dr. **Bilal MANSOOR** for his financial assistance, his word of encouragements and advices.

I am also grateful to Pr. **Aude SIMAR**, Pr. **Véronique FAVIER**, Pr. **Jean-Michel BERGHEA**, Pr. **Laurent DUBAR** and Dr. **Rajashekhara SHABADI**, for accepting to participate to my PhD defense committee, and the time they spent evaluating my Ph.D. thesis manuscript.

Finally, but not the least, I would like to thank my family, my friends, and all who cheered me up to achieve this work. Especially my younger brother Zinou who did not hesitate to cheer me up and encourage me during the hard times that I faced during these past years. Also, my elder brother Zouaoui who was of great support that helped to achieve this work.

Thesis context

This work was done in collaboration with Lille University of Science and Technology (Lille1 University) and Texas A&M University at Qatar (TAMUQ), and was made possible through the NPRP Grant # 4-1063- 2-397 from Qatar National Research Fund (A member of Qatar Foundation)

Contexte de la thèse

Ce travail a été fait en collaboration entre l'Université de Lille1 et Texas A&M University at Qatar (TAMUQ), et a été possible avec les subventions NPRP # 4-1063- 2-397 de la Qatar National Research Fund (un membre de Qatar Foundation)

Abbreviations

AA	- Aluminum Alloy
Al	- Aluminum
AS	- Advancing side
ASTM	- American Society for Testing and Materials
EDS	- Energy Dispersive Spectroscopy
FSW	- Friction Stir Welding
FS Weld	- Friction stir weld
HAZ	- Heat Affected Zone
Mg	- Magnesium
MPa	- Mega Pascal
mm/min	- Millimeter per minute
OP	- Optical Microscope
rpm	- Revolution per minute
RS	- Retreating Side
SEM	- Scanning Electron Microscope
SiC	- Silicon Carbide
TMAZ	- Thermo-Mechanical Affected Zone
TWI	- The Welding Institute
UTS	- Ultimate Tensile Strength
XRD	- X-Ray Diffraction
RD	- Rolling Direction
ND	- Normal Direction
TD	- Transverse Direction

Glossary of Terms

A

Advancing side – the advancing side is the side of the weld where the local direction of the rotating tool is in the same direction of traverse.

Alloy – A substance having metallic properties and being composed of two or more chemical elements, of which at least one is a metal.

Alloying element – An element added to and remaining in metal, which changes its structure and properties.

B

Backing plate – A layer of material that is placed below the joint interfaces of the materials to be welded. It provides a surface to oppose the vertical downward force on the material, and protects the machine bed.

Base material – this is the sheet-metal plate in its as-manufactured form, as supplied.

Butt weld – A welded joint formed between the squared ends of the two joining pieces, which come together but do not overlap.

C

Clamping System – the device used to hold, locate and prevent the workpiece from moving during the large forces involved in the FSW process.

Coalescence –the merging of two or more materials (metals) into one.

D

Defect - A discontinuity or discontinuities that accumulate to render a weld or part unable to meet minimum acceptance standards or criteria of the design specifications.

Deformation – is a change in the form of a body due to stress, thermal, or other causes.

Diffraction – the scattering of electrons by any crystalline material, through discrete angles depending only on the lattice spacing of the material and the velocity of the electrons.

Ductility – the ability of a material to deform plastically before fracture.

Dwell time – the period of time after the rotating tool has been plunged into the work and for which it remains stationary. Generating frictional heat and plasticizing the materials, before commencing the traverse along the joint (seconds).

E

Elastic deformation – is the deformation of the material that is recovered when force is applied.

Elastic limit – the greatest stress which a material is capable of sustaining without any permanent strain remaining upon complete release of the stress.

Elongation – the increase in gauge length of a body subjected to a tension force, referenced to a gauge length of a body. Usually expressed as a percentage of the original gauge length.

% Elongation – the total percent increase in the gauge length of a specimen after a tensile test.

Engineering strain – this is a dimensionless value that is the change in length (ΔL) per unit length of the original linear dimension (Lo) along the loading axis of the specimen; that is $e=\Delta L/Lo$ the amount that a material deforms per unit length in a tensile test.

Engineering stress – it is the normal stress, expressed in units of applied force, F, per unit of original cross-sectional area, A_0; that is, $S=F/A_0$.

Etchant – a chemical solution used to etch a metal to reveal structural details.

Etching – subjecting the surface of a metal to preferential chemical or electrolytic attack to reveal structural details for metallographic examination.

Exit hole – a hole left at the end of the weld when the FSW tool is withdrawn, resulting from displacement of material during the plunge. Some special techniques are in-use to fill or prevent the occurrence of this hole.

F

Face Centered Cube- this is a crystal system where atoms are arranged at the corners and center of each cube face of the cell.

Force control – a mode in the friction stir welding process in which a known force from previous welds is added to other input process parameters to produce a weld.

Friction – the force required to cause one body in contact with another to begin to move.

Friction Stir Welding – Is a process developed at The Welding Institute (TWI) that utilizes local friction heating to produce continuous solid-state seams. It allows butt and lap joints to be

made without the use of filler metals. The solid-state low distortion welds produced are achieved with relatively low costs, using simple and energy-efficient mechanical equipment.

G

Grain – an individual crystallite in metals.

Grain growth – this is a phenomenon that occurs when the temperature of a metal is raised, the grains begin to grow, and their size may eventually exceed the original grain size.

Grain size – a measure of the areas or volumes of grains in a polycrystalline metal or alloy, usually expressed as an average when the individual sizes are fairly uniform. Grain size is reported in terms of some grains per unit area or volume, average diameter, or as a number derived from area measurements.

Grain boundary –an interface separating two grains, where the orientation of the lattice changes from that of one grain to that of the other. When the orientation change is minuscule, the boundary is sometimes referred to as a sub-boundary structure.

Grinding – removing material from the surface of a workpiece by using a grinding wheel or abrasive grinding papers.

H

Hardness –a term used for describing the resistance of a material to plastic deformation.

Hardness test – measures the resistance of a material to penetration by a sharp object.

Hardening – increasing hardness by suitable treatment.

Heat-Affected Zone - The portion of the base metal which has not been melted, but whose mechanical properties have been altered by the heat of welding or cutting.

Homogeneous – a chemical composition and physical state of any physical small portion, and that is the same as that of any other portion.

Hot working – deformation under conditions that result in recrystallization.

I

Interfacial region –weld joint boundary of the workpieces indicating the positions of the pin and shoulder diameters during the welding process.

Intermetallic compounds –this are any solid materials, composed of two or more metal atoms in a definite proportion, which have a definite structure that differs from those of its constituent metals.

J

Joint efficiency – The ratio of the strength of a joint to the strength of the base metal, expressed as a percentage.

M

Macrograph –a graphic reproduction of a prepared surface of a specimen at a magnification not exceeding 25x.

Macrostructure – the structure of metals as revealed by macroscopic examination of the etched surface of a polished specimen.

Magnification – the ratio of the length of a line in the image plane to the length of a line on the imaged material.

Mechanical properties – the properties of a material that reveal its elastic or inelastic behavior when force is applied, indicating the suitable mechanical applications.

Mechanical testing – the determination of mechanical properties.

Metallurgy – The science and technology of metals and their alloys including methods of extraction and use.

Microstructure – The structure of a prepared surface of a metal, as revealed by a microscope at a particular magnification.

O

Oxidation – The addition of oxygen to a compound.

P

Parameter – The minimum and maximum parameters that will describe the operating range of a variable.

Plastic deformation –this is the distortion of material continuously and permanently in any direction. The deformation that remains or will remain permanent after the release of the stress that caused it.

Plasticity – capacity of a metal to deform non-elastically without rupturing.

Polished surface – a surface that reflects a large proportion of the incident light in a peculiar manner.

Position control – a mode in FSW in which the machine automatically adjusts the forces acting during the welding process.

Plunge depth – the plunge depth is the maximum depth that the tool shoulder penetrates into the weld plates.

Plunge force – during the plunging stage of the tool pin in FSW, the vertical force in the direction of the Z-axis movement is normally referred to as the plunging force.

Porosity - A rounded or elongated cavity formed by gas entrapment during cooldown or solidification.

R

Recrystallization – a change from one crystal structure to another, such as that occurring upon heating and/or cooling through a critical temperature.

Residual stress – stress in a body which is at rest, in equilibrium, and at a uniform temperature in the absence of any external force.

Retreating side – the retreating side of the tool is where the local direction of the weld surface due to tool rotation and the direction of the traverse are in the opposite direction.

Rolling direction – refers to the direction in which the plate was rolled during the manufacturing.

Rotational speed – the tool rotation speed is the rate of angular rotation (usually specified in rpm) of the tool about its rotational axis.

S

Scanning Electron Microscope – an electron microscope in which the image is formed by a beam operating simultaneously with an electron probe scanning the object.

Solid-phase – A physically homogeneous and distinct portion of a material system the solid state.

Spindle speed – also referred to as the rotational speed, is the speed of the work holding device (chuck), measured in revolutions per minute.

Spindle torque – the spindle torque required to rotate the FSW tool when plunging into and traversing through the workpiece along the joint (Nm).

T

Tensile strength – the maximum tensile stress that a material is capable of sustaining. Tensile strength is calculated from the maximum load during a tension test carried out to rupture, and the original cross-sectional area of the specimen.

Tensile test – measures the response of a material to a slowly applied axial force. The yield strength, tensile strength, modulus of elasticity and ductility are obtained.

Tool displacement – to offset the tool at a certain distance from the weld centerline.

Tool shoulder – part of the welding tool that rotates and is normally disk-shaped.

Tool pin – the part of the tool that rotates in contact with the surface of the workpiece.

Tool plunge – the process of forcing the tool into the material at the start of the weld.

Tool tilt angle – the angle at which the FSW tool is positioned on the workpiece surface; that is, zero tilt tools are positioned perpendicular to the workpiece surface (degrees).

Travel speed – also referred to as feed rate; it is the rate at which the rotating FSW tool is translated along the joint line (mm/min).

V

Void – the space that exist between particles or grains. Normally in welding, voids are associated with defects.

U

Unaffected material – the bulk of material that is not affected by either heat or deformation during the welding process.

W

Welding – the process of joining, in which materials are enabled to form metallurgical bonds under the combined action of heat and pressure.

Weld nugget or stir zone – the recrystallized central area of the joint interface.

Weld root – the part of the joint profile opposite the shoulder is designated the root of the weld.

Welding speed – also known as the traverse speed; this is the speed (usually specified in mm/min) of the tool traversing along the workpiece per specified time.

Workpiece – the component to be welded.

Wormholes – a defect in an FS weld, usually on the advancing side of the rotating tool, due to lack of mixing and re-bonding of the plasticized material.

X

X-axis – relating to a particular axis (horizontal) or a fixed line determining the direction of movement or placement in a 2-Dimensional or 3-Dimensional coordinate system.

Y

Y-axis – relating to a particular axis (perpendicular to the x-axis) or a fixed line determining the direction of movement or placement in a 2-D or 3-D coordinate system.

Z

Z-axis – relating to a specific axis (vertical) or a fixed line determining the direction of movement or placement in a 3-D coordinate system.

Table of Contents

List of Figures

List of tables

General Introduction

➢ **Work context**

Friction stir welding (FSW) is a solid-state material joining process that was recently developed by Thomas Wayne in early 1991 at the Welding Institute (TWI), Cambridge, UK (Thomas et al., 1991). This technique mainly contributed to the welding of materials that are difficult to assemble with conventional fusion welding methods. FSW process consists of a rotating tool at ω (rpm) that penetrates between two plates to be welded with an applied force F (N), the weld will be achieved by moving the tool along the weld line with a transverse speed V (mm/min). In practice, the quality of the FSW is highly dependent on these three essential parameters. From a mechanical point view, the coupling between the heat generated by the friction between the tool and the plates and the plastic deformations resulting from the stirring, results in the creation of the weld. It is worth pointing out that the maximum induced heat is always below the melting point of the base material (T_{max}= 70 to 75% T_f). The severe deformation encountered by the material at high temperatures below the melting point during the FSW process results into very interesting mechanical microstructural properties. Therefore, FSW was attractive for many applications in the automotive, aerospace industries.

The possibility of carrying out heterogeneous welds made FSW a great alternative in the optimization of materials joining. In this regard, several works have already been achieved for heterogeneous friction stir welding, among others, we mention different sets of aluminum, aluminum / steel, aluminum / copper, aluminum / titanium, etc. are mentioned. many studies (Alvarez et al., 2010; Aonuma and Nakata, 2012; Chen and Lin, 2010; Chi et al., 2007; Fu et al., 2015; Kwon et al., 2008; Liu et al., 2007b; Mohammadi et al., 2015; Somasekharan and Murr, 2004b; T. Akinlabi and A. Akinlabi, 2012; Yan et al., 2010) have been investigated recently on the heterogeneous friction stir welding.

> ➢ **Purpose of the thesis**

This study is part of a research project initiated by Texas A&M University in Qatar and the American University of Beirut on characterizing the mechanical and microstructural properties of friction sit welded bimetallic joints. Lille 1 University joined the adventure later through a jointly co-advised PhD work with Texas A&M University in Qatar. The current researched work focused on two of the materials proposed in the initial project, namely, the 6061-T6 aluminum alloy (Al) and an AZ31B magnesium alloy (Mg). Therefore, the purpose of this investigation is to optimize the friction stir welding parameters of similar and dissimilar materials in the aim to improve the mechanical properties of welded structures. The preliminary work focused on the investigation of the microstructural and mechanical properties of the two studied base materials. In what followed, the properties of the welded parts were studied by analyzing the influence of the temperature and the strain rate via monotonous tensile tests and by analyzing the microstructural and textural properties.

> ➢ **Structuring report**

This report is organized into four main sections:

In Chapter I, a bibliographic review presents the state of the art of research work on the friction stir welding (FSW) process. In this context, we highlight the importance of the main welding parameters that help to define the optimal weldability field of FSW. Similarly, the influence of the tool morphology (size, shape) on the FSW process has been discussed. In this part, the main defects that are often encountered are presented. We have also reported on the research studies conducted to investigate several FSW processing aspects namely: the welding parameters, metallurgical aspects of welded joints and mechanical properties. Similarly, we have discussed and reported the problematic related of the homogeneous and heterogeneous welding of aluminum and magnesium alloys.

Chapter II is devoted to the characterization of the 6061-T6 aluminum and AZ31B magnesium alloys. The microstructure of the base materials have been analyzed by measuring the mean grain size of the as received and heat-treated samples. Uniaxial tensile tests were conducted at different temperatures (25, 100, 200 and 300 ° C) and under different strain rates (10^{-4}, 10^{-3}, 10^{-2} et 10^{-1} s^{-1}). By performing interrupted uniaxial tensile tests, the mechanisms of damage under different temperatures and different strain rates have been analyzed. The fractography surfaces were observed and analyzed using a scanning electron microscope (SEM).

Chapter III includes homogeneous friction stir welding (FSW) of 6061-T6 aluminum (Al) and AZ31B magnesium (Mg) sheets, with a thickness of 3 mm. A parametric study has been conducted in order to optimize the welding parameters using a specific FSW machine. The cross-sections of the welds were analyzed in terms of changes in grain size and microhardness mapping. The final damage zones have been investigated by tensile testing at different temperatures (25, 100, 200 and 300°C) under a constant strain rate of $10^{-3}s^{-1}$. Overall, the microstructural and the mechanical properties of welded joints, at different temperatures, have been studied. Particular attention was given to the analysis of the texture of the joint via EBSD observations. These different observations allowed to identify the different zones of the welded joint in the various studied configurations. The damage mechanisms occurring in welded specimens during uniaxial tensile testing were identified.

Finally, Chapter IV presents a valuable contribution to the Al/Mg dissimilar welding. Welded joints were obtained at different tool rotational and translational speeds. An analysis of the morphology of heterogeneous joint was conducted to better understand the material flow occurred during the heterogeneous FSW process of Al/Mg. Thereby, the presence of the intermetallic has been clearly demonstrated. The mechanical behavior of welded joints was evaluated from the uniaxial tensile tests at different temperatures of 25°C and 200°C. The mechanical properties of welded joints were compared to those of the base metal (BM).

Introduction Générale

> **Contexte du travail**

Le soudage par friction malaxage (FSW- Friction Stir Welding) est une technique récente d'assemblage de matériaux à l'état solide, inventé par Thomas Wayne en 1991 par l'institut de soudure (TWI), Cambridge, UK, (Thomas et al., 1991). Cette technique a contribué fortement au soudage de matériaux difficilement assemblables par les méthodes classiques basées sur la fusion. Elle repose sur des principes simples : pénétration d'un outil animé en rotation ω (tr/min) entre deux plaques à souder avec une certaine force appliquée F (en N) et une vitesse d'avance Va (mm/min). Dans la pratique, la qualité du soudage FSW repose sur l'optimisation de ces trois paramètres essentiels. Il faut alors noter que la chaleur est générée par le phénomène de friction entre les surfaces de l'outil et les tôles ainsi que des déformations plastiques résultants du malaxage, la température maximale induite est toujours inférieure à celle de fusion du matériau de base (T_{max} = 70 à 75% T_f environ). Du fait des températures raisonnables obtenues, Le soudage FSW présente plusieurs avantages à la fois à l'échelle microstructurale et mécanique. En plus, on note une diversité d'applications industrielles de cette méthode d'assemblage dans le domaine automobile, aéronautique, etc. La plupart de ces applications a été centrée sur le soudage FSW des alliages d'aluminium en soudage homogène ou hétérogène.

C'est la possibilité de réaliser des soudages hétérogènes qui fait du soudage FSW une alternative plausible dans l'optique d'optimisation d'utilisation des matériaux. A ce stade, on dénombre plusieurs travaux déjà réalisés en vue de soudage hétérogène, entre autres, nous citons : séries différentes d'Aluminium, Aluminium/Acier, Aluminium/Cuivre, Aluminium/Titane, etc. On peut citer plusieurs travaux récents dans la littérature qui ont mis ont porté sur le soudage hétérogène par friction malaxage : (Alvarez et al., 2010; Aonuma and Nakata, 2012; Chen and Lin, 2010; Chi et al., 2007; Fu et al., 2015; Kwon et al., 2008; Liu et al., 2007b; Mohammadi et al., 2015; Somasekharan and Murr, 2004a; T. Akinlabi and A. Akinlabi, 2012; Yan et al., 2010).

➢ **Objet de la thèse**

La présente étude s'inscrit dans le cadre d'un projet de recherche portant sur la soudabilité par la technique FSW d'une configuration bimétallique d'un alliage d'alliage d'Aluminium 6061-T6 (Al) et d'un alliage de Magnésium AZ31B (Mg). Le but de cette investigation est d'optimiser les paramètres de soudage FSW pour l'amélioration des propriétés mécaniques des structures soudées. Le travail préliminaire a ciblé la connaissance des propriétés microstructurales et mécaniques des deux matériaux de base utilisés. L'influence de la température et de la vitesse de déformation a été analysée via des essais de traction monotone et des observations fines microstructurales. La morphologie des joints soudés a été mise en évidence en vue de mieux comprendre le flux de matière lors du procédé FSW homogène et hétérogène.

➢ **Structuration du rapport**

Le présent rapport est organisé en 4 principaux chapitres :

Dans le chapitre I, une revue bibliographique présente l'état de l'art des travaux portant sur le soudage par friction malaxage (FSW). Dans ce cadre, il est souligné l'intérêt de maîtriser les principaux paramètres de soudage qui contribuent à définir d'une façon optimale le Domaine de Soudabilité Opératoire. De même, l'importance de la morphologie de l'outil (dimensions, forme) sur le procédé soudage FSW a été abordée. Dans cette partie, nous avons fait le bilan sur les principaux défauts souvent rencontrés. Aussi, nous avons fait état de plusieurs travaux relatifs à plusieurs aspects liés au procédé FSW à savoir : les paramètres de soudage, les aspects métallurgiques des joints soudés, les propriétés mécaniques. De même, nous avons évoqué la question sur le soudage homogène des alliages d'aluminium, de magnésium et aussi leur soudage hétérogène.

Le chapitre II est consacré à la caractérisation de l'alliage d'aluminium 6061-T6. La microstructure du matériau de base est alors analysée par la mesure des tailles des grains sur des échantillons traités thermiquement. Des essais de traction monotone ont été conduits à différentes températures (25, 100, 200 et 300 °C) et avec différentes vitesses de déformations

$(10^{-4}, 10^{-3}, 10^{-2}$ et 10^{-1} s^{-1}). En procédant à des essais interrompus, nous avons pu analyser les mécanismes d'endommagement à différentes températures et à différentes vitesses de déformation. Les faciès de rupture ont été observés et analysés à l'aide d'un microscope électronique à balayage (MEB).

Le chapitre III porte sur le soudage homogène par friction malaxage (FSW) de tôles en aluminium 6061-T6 (Al) et en magnésium AZ31B (Mg), d'épaisseur 3 mm. Une étude paramétrique préalable a été réalisée en vue d'optimiser les paramètres de soudage en utilisant une machine spécifique FSW. Les sections transversales des soudures ont été analysées en termes d'évolution des tailles des grains et de relevés de la cartographie de micro dureté. Les zones d'endommagements finaux ont été investies par des essais de tractions à différentes températures (25, 100, 200 et 300 °C) sous une vitesse de déformation constante de 10^{-3}s^{-1}.

Globalement, la microstructure et les propriétés mécaniques des joints soudés, à différentes températures, ont été étudiées. Une attention particulière a été portée à l'analyse de la texture du joint via des observations en EBSD. Ces différentes observations ont permis de mettre en évidence les différentes zones du joint soudé dans les différentes configurations étudiées. De même, une analyse des mécanismes d'endommagement au cours des tests de traction monotone a été réalisée sur les éprouvettes soudées.

Enfin, le chapitre IV présente une contribution intéressante en abordant la problématique du soudage hétérogène Al/Mg. Des joints soudés ont été obtenus à différentes vitesses de rotation et d'avance de l'outil. Une analyse de la morphologie du joint hétérogène a été réalisée en vue de mieux comprendre le flux de matière survenu au cours du procédé FSW hétérogène Al/Mg. La présence des intermétalliques a été clairement mise en évidence.

Le comportement mécanique des joints soudés a été évalué à partir des essais de traction monotone à des températures de 25°C et de 200°C. Les propriétés mécaniques des joints soudés ont été comparées à celles du métal de bases (MB).

Chapter I. **Bibliographic study**

In this chapter, a detailed description of friction stir welding process (FSW) is presented. Moreover, the various parameters that influence the mechanical and metallurgical properties of the friction stir welded joint will be listed. A complete review of studies on the heterogeneous friction stir welding process is provided.

Summary

I.1 Overview

The big challenges encountered while producing welds with high mechanical properties has long hindered the large use of welding for joining automotive and aerospace assemblies mainly made of aluminum alloys, such as highly alloyed 6XXX series. These aluminum alloys are usually categorized as non-weldable because of the poor solidification microstructure and porosity in the fusion zone. Furthermore, the loss in the mechanical properties as compared to the base material is very significant. Such constraints make the joining of these alloys by traditional welding processes not attractive. Few aluminum alloys can be resistance welded, but the surface preparation is expensive, as surface oxide is a major problem. (Mishra and Ma, 2005)

Friction stir welding (FSW) was developed at The Welding Institute (TWI) of UK in 1991 as a solid-state joining technique, and it was originally applied to join aluminum alloys (Thomas et al., 1991), and since recently it is employed to weld dissimilar materials (Kostka et al., 2009; Kwon et al., 2008; McLean et al., 2003; Mofid et al., 2012b; Sato et al., 2004; Yan et al., 2005). The basic concept of FSW is simple: a non-consumable rotating tool with a particularly designed pin and shoulder is inserted into the abutting sheets edges to be joined and traversed along the line of the joint (Figure I.1). The tool serves two principal functions: Heating of the workpiece, and stirring of material to produce the joint. The friction between the tool and the workpiece, and the plastic deformation of the plates to be welded generates the heating. The localized heating softens the material around the pin and the combination between the tool rotation and translation leads to the movement of the material from the front of the pin to the back of the pin. As a result of this process a joint is produced from 'solid state'. Because of various geometrical features of the tool, the material movement around the pin can be quite complex. During FSW process, the material experiences intense plastic deformation at elevated temperature, resulting in some cases into fine and equiaxed recrystallized grains (Benavides et al., 1999; Jata and Semiatin, 2000; Liu et al., 1997; Rhodes et al., 1997). The fine microstructure in friction stir welds leads to producing good mechanical properties (Mishra and Ma, 2005).
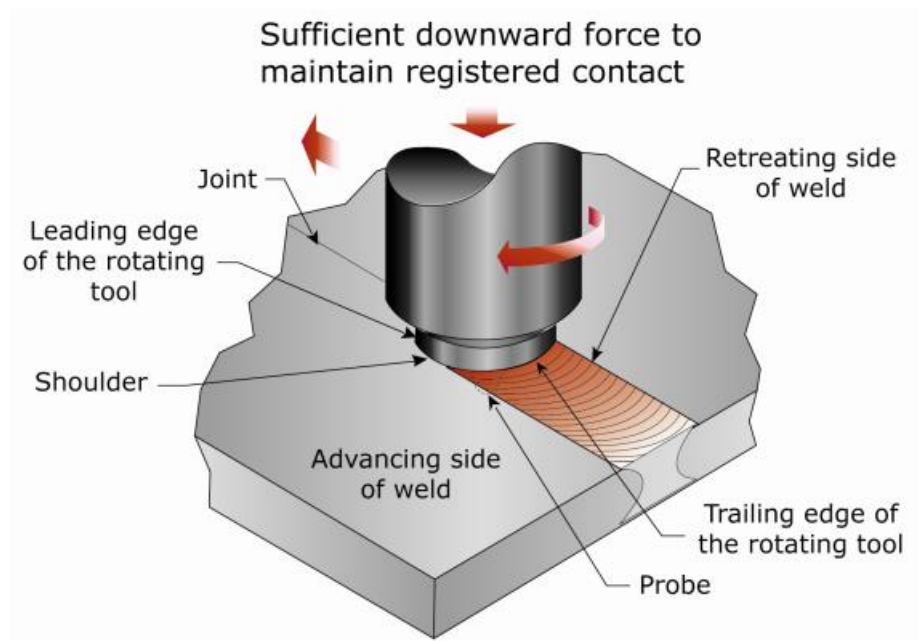
Figure I.1. Schematic drawing of friction stir welding. (Mishra and Mahoney, 2007)

Friction stir welding (FSW) is reported to be the most noteworthy enhancement in metal joining in a decade. FSW is considered as a green technology due to its energy effectiveness, environment friendliness, and flexibility. As compared to the conventional welding methods, FSW consumes significantly less energy. No cover gas or flux is needed; thereby the FSW process is environmentally friendly. The welding technique does not require any use of filler metal and therefore any aluminum alloy can be joined without concern of composition compatibility, which is a serious problem in fusion welding. When necessary, dissimilar aluminum alloys and composites can be welded with equivalent ease (Lee et al., 1999; Li et al., 2000). Conventional friction stir welding is commonly performed on small axisymmetric parts that can be rotated and pushed against each other to form a joint (Cary), friction stir welding can be also used to weld various types of joints like butt joints, lap joints, T butt joints, and fillet joints (Dawes and Thomas, 1996). The key benefits of FSW are summarized in Table I.1. (Mishra and Ma, 2005)

Metallurgical benefits	Energy benefits	Environmental benefits
• Excellent metallurgical properties in the joint area. • Low distortion in the workpiece. • Solid phase process. • Absence of cracking • Fine microstructure. • Replace multiple parts joined by fasteners. • No loss of alloying elements.	• Decreased fuel consumption in light-weight aircraft, automotive and ship applications. • Improved materials use allows a reduction in weight. • Only 2.5% of the energy needed for a laser weld.	• No surface cleaning required. • No shielding gas required. • Eliminates grinding wastes. • Consumable material saving, such as rugs, wire of any other gases. • Eliminates solvents required in degreasing.

Table I.1. Friction stir welding benefits. (Mishra and Ma, 2005)

I.2   Experimental section

I.2.1   Friction stir welding process

Ordinarily, FSW has a very simple concept, while a brief consideration of the process reveals many subtleties. The main features are demonstrated in Figure I.2. A rotating tool is inserted between two plates to be welded with a certain downward force. The side of the weld for which the rotating tool moves in the same direction as the traversing direction, is commonly known as the *'advancing side'*; the other side, where tool rotation is the opposite of the traversing direction, is recognized as the *'retreating side'*. A major feature of the tool is a probe (pin) which protrudes from the shoulder, and is of a length only slightly less than the thickness of the plate. Frictional heat is generated, mainly due to the great normal pressure and shearing action of the shoulder. Friction stir welding can be understood as a process of constrained extrusion under the action of the tool. The frictional heating makes a softened zone of material to form around the probe. This softened material cannot escape as it is constrained and kept under the tool shoulder. As the tool is traversed along the joint line, material is swept around the tool probe between the retreating side of the tool (where the local motion due to rotation opposes the forward motion) and the surrounding material that has not been deformed. The extruded material is put down to form a solid phase joint near the tool. The process is by definition asymmetrical, as most of the

deformed material is pushed out past the retreating side of the tool. The process creates very high strains and strain rates, both of which are substantially greater than found in other solid state metalworking processes (extrusion, rolling, forging, *etc*.) (Tiwari et al., 2013).
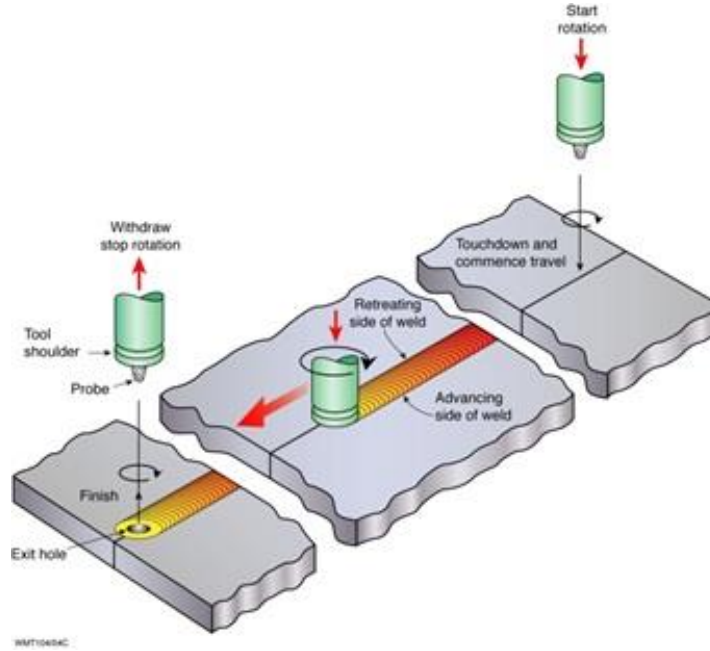
Figure I.2. Schematic representation of Friction Stir Welding phases.

I.2.2 Joint configuration

The most convenient joint configurations for FSW are butt and lap joints. A simple square butt joint is shown in Figure I.3 as a full and partial penetration butt joint. Two plates or sheets with same thickness are placed on a backing plate and clamped firmly to prevent the abutting joint faces from being forced apart. During the initial plunge of the tool, the forces are fairly large and extra care is required to ensure that plates in butt configuration do not separate. A rotating tool is plunged into the joint line and traversed along this line when the shoulder of the tool is in intimate contact with the surface of the plates, producing a weld along abutting line. On the other hand, for a simple lap joint, two lapped plates or sheets are clamped on a backing plate. A rotating tool is vertically plunged through the upper plate and into the lower plate and traversed along desired direction, joining the two plates. Many other configurations can be produced by combination of butt and lap joints. Apart from butt and lap joint configurations, other types of joint designs, such as edge butt, T-lap joint and lap fillet joint, are also possible as

needed for some engineering applications. It is important to note that no special preparation is needed for FSW of butt and lap joints. Two clean metal plates can be easily joined together in the form of butt or lap joints without any major concern about the surface conditions of the plates.
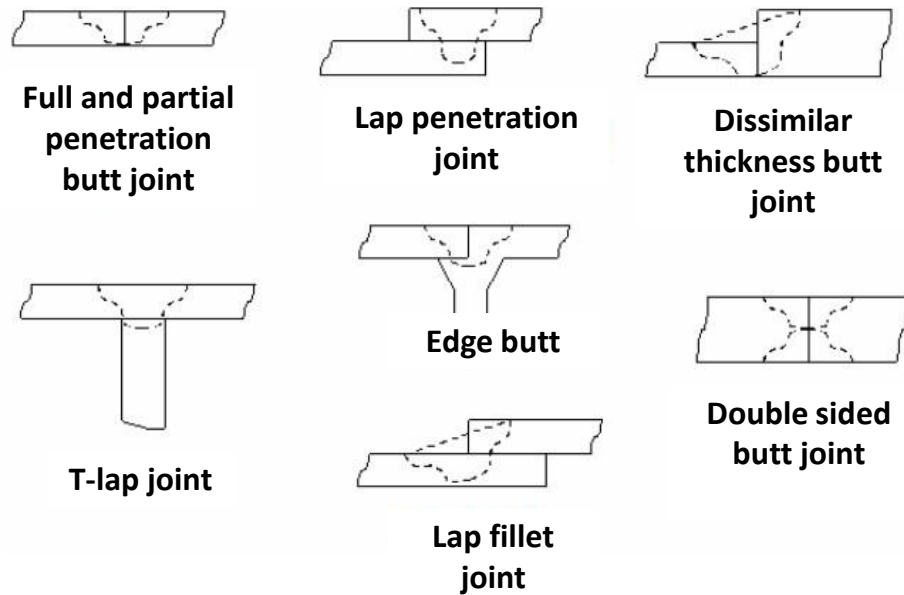
Figure I.3. Joint configurations for friction stir welding.

I.3   Metallurgical aspects of FSW joint

The effect of sever plastic deformation and high-temperature exposure on the stirred zone during FSW results in complete recrystallization, the development of texture, precipitate dissolution and coarsening (Benavides et al., 1999; Kwon et al., 2009; Li et al., 1999; Mahoney et al., 1998; Mishra and Mahoney, 2001; Tang et al., 1998). Based on microstructural characterization of grains and precipitates, three distinctive zones can be identified as shown in Figure I.4, stirred (nugget) zone (SZ), thermo-mechanically affected zone (TMAZ), and heat-affected zone (HAZ). The microstructural changes in various zones have significant effect on postweld mechanical properties. Therefore, the microstructural evolution during FSW/FSP has been studied by a number of investigators.
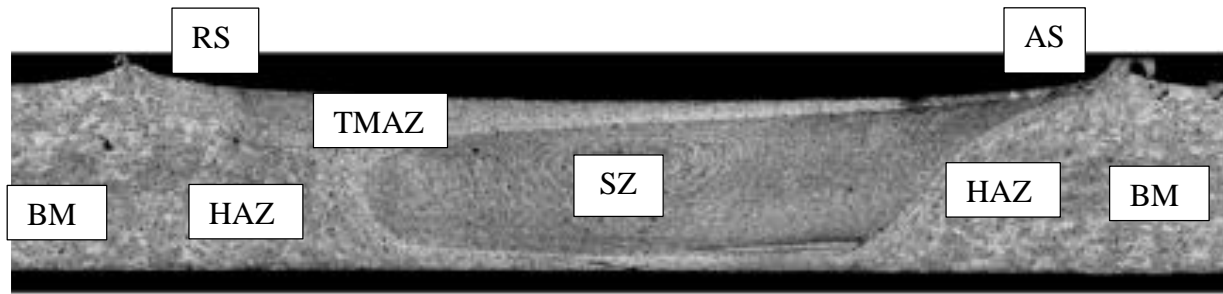
Figure I.4. Micrograph illustrating different zones in an FS welded of 5052-O Al alloy. (Kwon et al., 2009)

• **Stir zone**: Sever plastic deformation and frictional heating during FSW/FSP result in a recrystallized microstructure within stirred zone. This region is usually referred to as nugget zone (or weld nugget) or dynamically recrystallized zone (DXZ). Under some FSW/FSP conditions, onion ring structure was observed in the nugget zone (Figure I.4). In the interior of the recrystallized grains, usually there is low dislocation density (Liu et al., 1997; Rhodes et al., 1997). However, some investigators reported that the small recrystallized grains of the nugget zone contain high density of sub-boundaries (Sato et al., 1999), subgrains (Heinz and Skrotzki, 2002), and dislocations (Jata et al., 2000). The interface between the recrystallized nugget zone and the parent metal is relatively diffuse on the retreating side of the tool, but quite sharp on the advancing side of the tool (Mishra and Mahoney, 2007).

Depending on processing parameter, tool geometry, temperature of workpiece, and thermal conductivity of the material, various shapes of nugget zone have been observed. Basically, nugget zone can be classified into two types, basin-shaped nugget that widens near the upper surface and elliptical nugget. (Sato et al., 1999) reported the formation of basin-shaped nugget on friction stir welding of 6063Al-T5 plate. They suggested that the upper surface experiences extreme deformation and frictional heating by contact with a cylindrical-tool shoulder during FSW, thereby resulting in generation of basin-shaped nugget zone. On the other hand, (Rhodes et al., 1997) reported elliptical nugget zone in the weld of 7075Al-T651.

• **Thermo-mechanically affected zone**: Unique to the FSW/FSP process is the creation of a transition zone—thermo-mechanically affected zone (TMAZ) between the parent material and the nugget zone (Mahoney et al., 1998; Rhodes et al., 1997), as shown in Figure I.4. The TMAZ experiences both temperature and deformation during FSW/FSP. A typical micrograph of

TMAZ is shown in Figure I.5. The TMAZ is characterized by a highly deformed structure. The parent metal elongated grains were deformed in an upward flowing pattern around the nugget zone. Although the TMAZ underwent plastic deformation, recrystallization did not occur in this zone due to insufficient deformation strain. However, dissolution of some precipitates was observed in the TMAZ, as shown in Figure I.6 (c) and (d), due to high-temperature exposure during FSW. The extent of dissolution, of course, depends on the thermal cycle experienced by TMAZ. Furthermore, it was revealed that the grains in the TMAZ usually contain a high density of sub-boundaries (Sato et al., 1999).
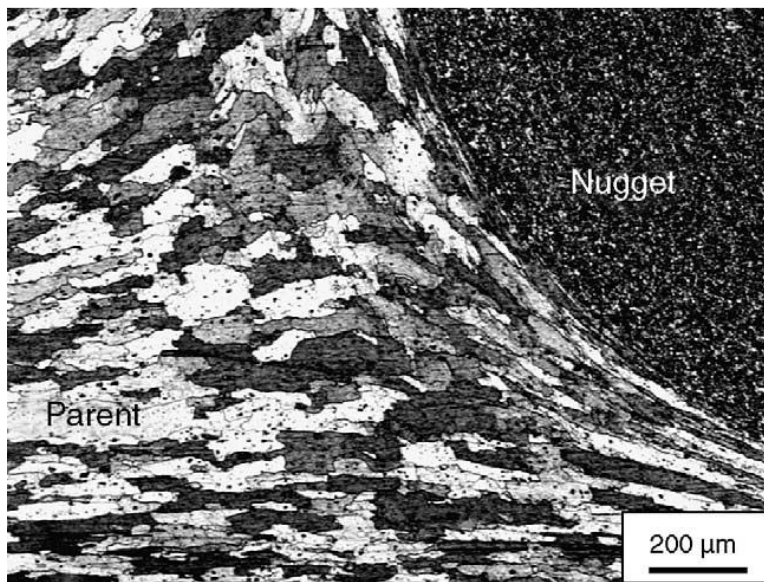
Figure I.5. Microstructure of thermo-mechanically affected zone in FSP 7075Al (Ma et al., 2002).

• **Heat affected zone**: Beyond the TMAZ there is a heat-affected zone (HAZ). This zone experiences a thermal cycle, but does not undergo any plastic deformation (Figure I.4). (Mahoney et al., 1998) defined the HAZ as a zone experiencing a temperature rise above 250 °C for a heat-treatable aluminum alloy. The HAZ retains the same grain structure as the parent material. However, the thermal exposure above 250 °C exerts a significant effect on the precipitate structure.

Recently, (Jata et al., 2000) investigated the effect of friction stir welding on microstructure of 7050Al-T7451 aluminum alloy. They reported that while FSW process has relatively little effect on the size of the subgrains in the HAZ, it results in coarsening of the precipitates and the precipitate-free zone (PFZ) increases by a factor of 5. Similar observation was also made by (Su

et al., 2003) in a detailed TEM examination on FSW 7050Al-T651 (Figure I.6 (b)). The coarsening of precipitates and widening of PFZs is evident. Similarly, (Heinz and Skrotzki, 2002) also observed significant coarsening of the precipitates in the HAZ of FSW 6013Al. (Mishra and Ma, 2005)
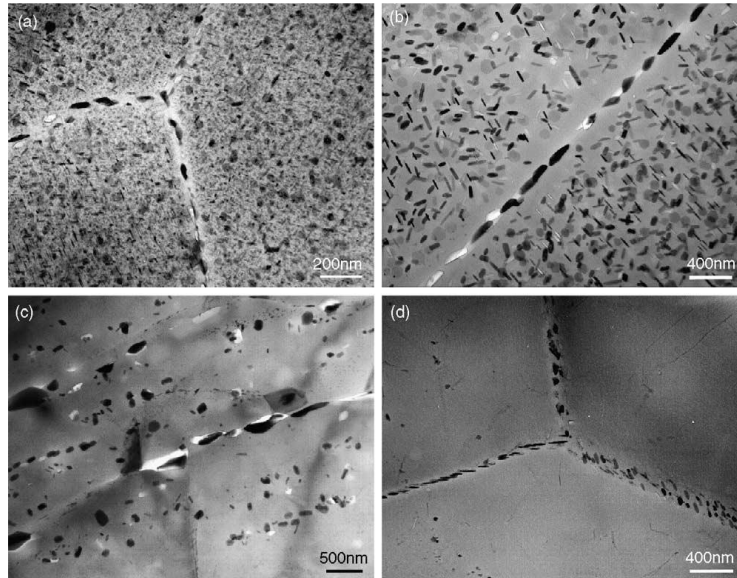
Figure I.6. Precipitate microstructures in the grain interior and along grain boundaries in: (a) base metal, (b) HAZ, (c) TMAZ near HAZ, and (d) TMAZ near nugget zone (FSW 7050Al-T651, tool rotation rate: 350 rpm, traverse speed: 15 mm/min) ((Su et al., 2003)).

I.4 FSW parameters

I.4.1 Tool rotation speed and advance speed

Two parameters are very important for friction stir welding process: tool rotation speed ω (rpm) in clockwise or counterclockwise direction and tool traverse speed V_a (mm/min) along the line of joint. The tool in rotation results in stirring and mixing of the material around the rotating pin (probe) and the tool in translation transfers the stirred material from the front to the back of the probe and finishes welding process. Higher tool rotation speeds generate higher temperature because of higher friction heating and result in more intensive stirring and mixing of material. However, it should be noted that frictional coupling of tool surface with the workpiece is going to govern the heating. (Mishra and Ma, 2005)

I.4.2   The tilt angle

In addition to the tool rotation rate and traverse speed, another important process parameter is the tool tilt or angle of spindle with respect to the workpiece surface. A suitable tilt of the spindle towards trailing direction certifies that the shoulder of the tool holds the stirred metal by threaded pin and move material efficiently from the front to the back of the pin. Furthermore, the penetration depth of the pin into the workpieces (also called target depth) is essential for creating defect-free welds with smooth tool shoulders. The penetration depth of the probe is associated with the probe length. When the penetration depth is too low, the tool shoulder does not interact with the workpiece surface. Thus, rotating shoulder cannot move the stirred material efficiently from the front to the back of the pin, resulting in generation of welds with surface groove or inner channel. When the insertion depth is too deep, the tool shoulder plunges into the workpiece creating excessive flash. In this case, a considerably concave weld is produced, leading to local thinning of the welded plates. (Mishra and Ma, 2005)
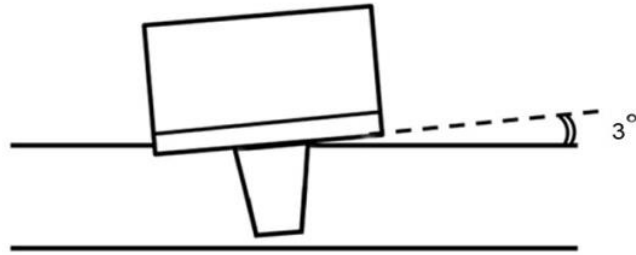
Figure I.7. Tilt angle between the surface of the weld and the FSW tool.(Pourahmad et al., 2013)

Another important matter for some specific FSW processes is preheating or cooling. The heat produced by friction and stirring may be not sufficient to soften and plasticize the material around the rotating tool for materials with high melting point such as steel and titanium or high conductivity such as copper. Therefore, it is difficult to produce continuous defect-free weld. In these cases, preheating or additional external heating source can enhance the material flow and increase the process window. On the other hand, for materials with lower melting point such as aluminum and magnesium, cooling can be used to reduce excessive growth of recrystallized grains and dissolution of strengthening precipitates in and around the stirred zone. (Mishra and Ma, 2005)

I.5   Effects of FSW process parameters on the joint quality

The tool design influences heat generation, plastic flow, the power required to perform FSW, and the uniformity of the welded joint. Two tool surfaces are needed to carry out the heating and joining processes in FSW. The shoulder surface is the area from which the majority of the heat by friction is generated. Although, it is valid for relatively thin plates; the probe surface is the area from which the majority of the heat is generated (Neto and Neto, 2013).

(Fujii et al., 2006) utilized FSW process to butt-weld 1050-H24 aluminum alloy plates with dimensions of 70×300×5 mm using three different tool shapes with smooth shoulder and a 10° concavity and diameter of 15 mm, pin length of 4.7 mm and diameter of 6 mm (Figure I.8). Regarding the welding parameters used to join the plates: the tool rotational speed was constant with a value of 1500 rpm and three tool transverse speed of 100 mm/min, 400 mm/min and 700 mm/min.
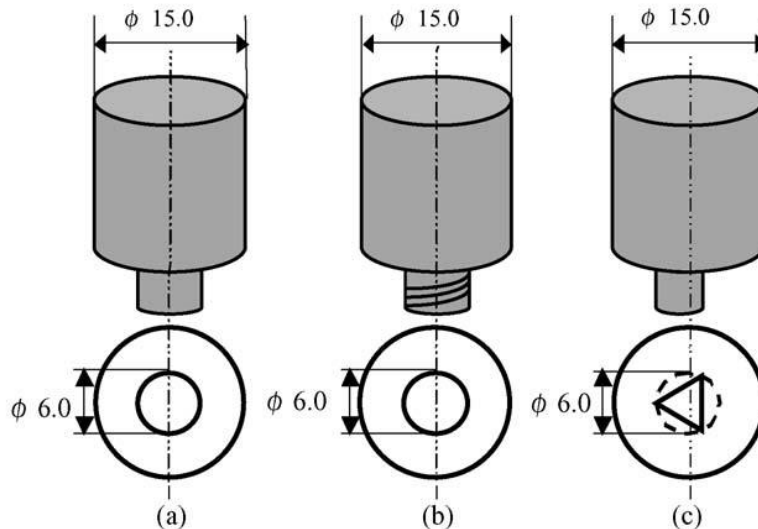
Figure I.8. FSW Tool shape: (a) non-threaded pin, (b) threaded pin, (c) triangular prism.(Fujii et al., 2006)

The welded joints were tensile tested and the tensile properties of an FS welded 1050-H24 aluminum alloy are shown in Figure I.9. The authors observed that the highest ultimate tensile strength of the joint was obtained using the tool with no threads. The welding parameters have similar effects on the tensile properties of the two columnar tools (with or without threads).

On the other hand, for the triangular prism tool, the best weld joint was obtained at 400 rpm (revolutionary pitch of 0.27 mm/r) with the formation of defects after increasing the weld pitch.
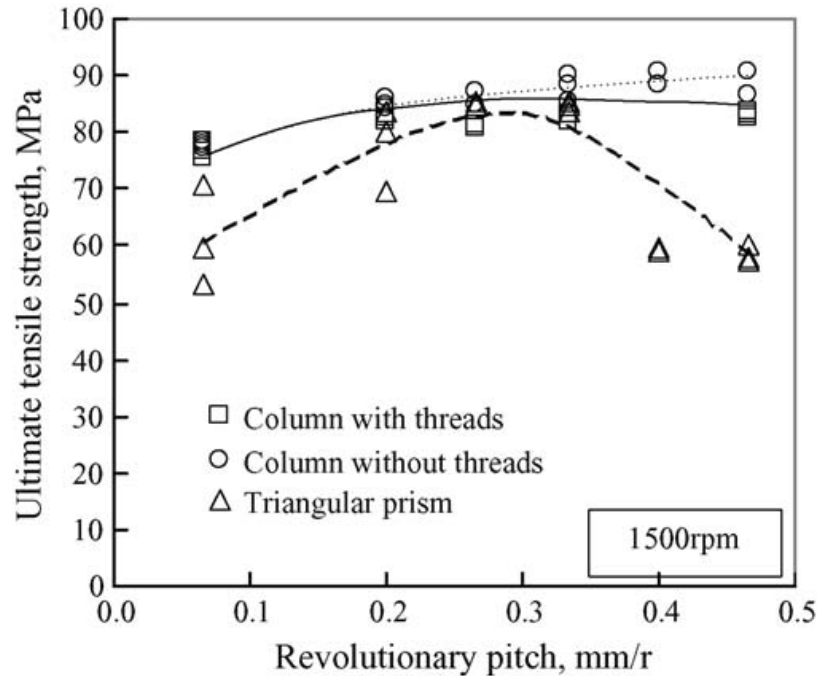
Figure I.9. Tensile strength of AA1050-H24FSW joints. (Fujii et al., 2006)

Figure I.10 shows the macrostructures in the cross section of the friction stir welded joints of the 1050-H24 aluminum alloy. When the welding speed is equal to or below 300 mm/min (the revolutionary pitch is equal to or smaller than 0.2 mm/r), the quality of the weld zone using the tool without threads is similar to that using the tool with threads. However, when the welding speed is greater than 300 mm/min (the revolutionary pitch is greater than 0.2 mm/r), a crack-like defect is more easily formed in the joints formed using the tool with threads compared to the joints formed using the tool without threads. For the triangular prism tool, the crack-like defects can be found in almost all the joints, but the welding speed is from 300 mm/min to 500 mm/min (the revolutionary pitch is from 0.2 mm/r to 0.33 mm/r), and the crack-like defects become very small.
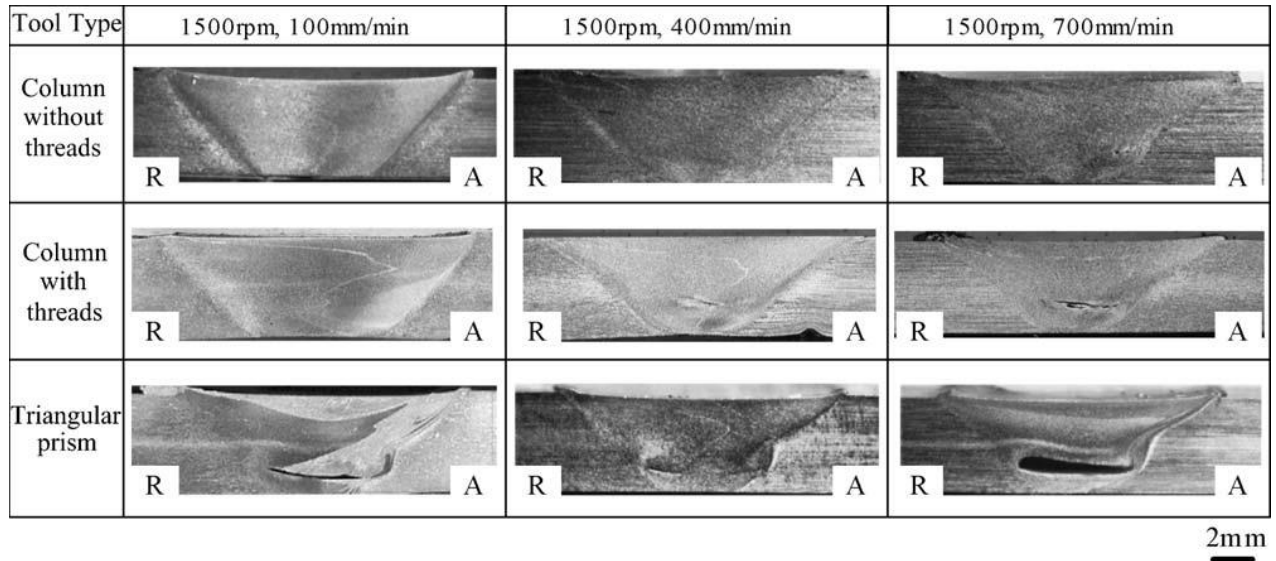
Figure I.10. Macrostructure of a cross section of AA1050-H24 FSW joints. (Fujii et al., 2006)

(Ren et al., 2007) investigated the hardness distribution, tensile properties and fracture characteristics of 6 mm thick 6061-T6 aluminum alloy FS welded at different rotation speeds and traverse speeds using a tool with a shoulder of 24 mm in diameter and a threaded cylindrical pin of 6 mm in diameter (Figure I.11). The authors observed a significant difference between the five FS welded joints, they reported that no defects were observed in the welded joints, but the shape of the joints were not the same, they changed with changing the process parameters.
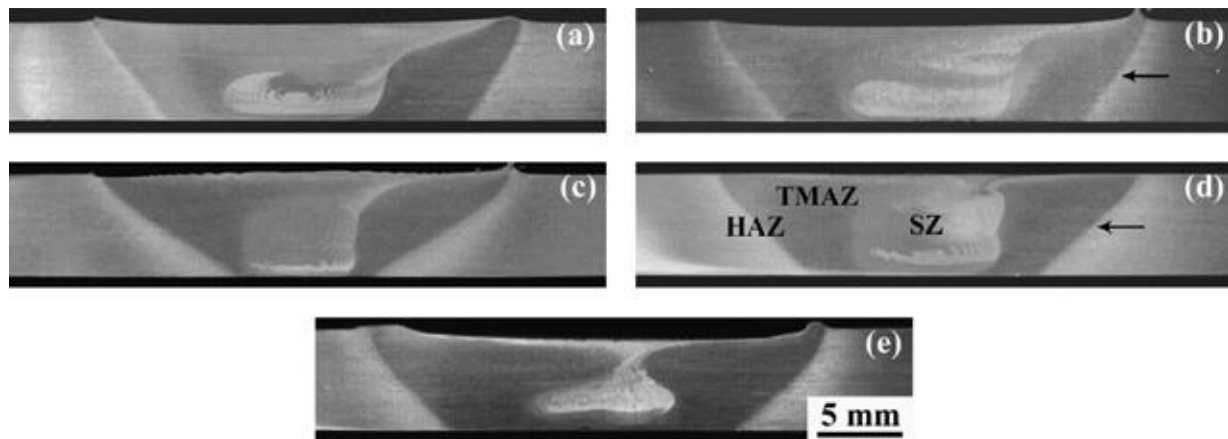
Figure I.11. Cross-sectional macrostructures of FSW 6061Al–T651, (a) 400 rpm, 100 mm/min, (b) 600 rpm, 100 mm/min, (c) 800 rpm, 400 mm/min, (d) 1200 rpm, 400 mm/min, and (e) 1600 rpm, 400 mm/min. The advancing side of the weld is on the right in all the macrographs. (Ren et al., 2007)

Furthermore, (Xunhong and Kuaishe, 2006) FS welded AZ31 magnesium alloy; the authors reported that excellent joints were obtained at optimum parameters. Tensile testing has been done for different welding parameters and the obtained mechanical properties are shown in Figure I.12. When the travel speed was 90 mm/min, the joint strength was close to the base material (about 93% of the base material at a rotation speed of 1500 rpm and 90 mm/min with a welding pressure of 150 N). However, with decreasing or increasing these parameters, some defects can occur in the welded joint.
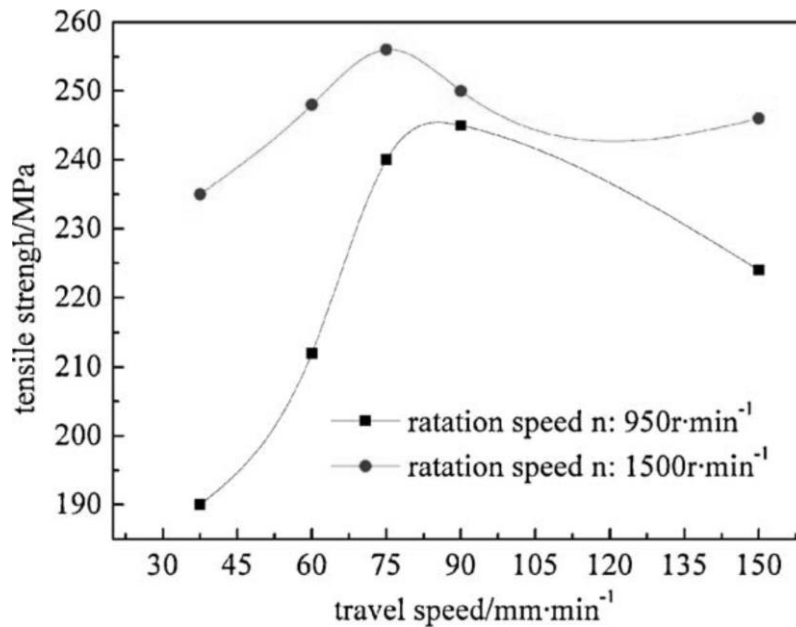
Figure I.12. Tensile strength of friction stirred welded AZ31 magnesium alloy. (Xunhong and Kuaishe, 2006)

In addition, (Kwon et al., 2009) studied the FSW of 5052-O aluminum alloy. They reported that free defect welds were obtained at rotation speeds of 1000 and 2000 rpm with a constant transverse speed of 100 mm/min. The influence of welding parameters on tensile strength and elongation are showed in Figure I.13, at rotation speeds of 500, 1000 and 2000 rpm. The tensile strength was approximately similar to that of the base metal, the elongation was lower than the base metal and the best maximum elongation was obtained at 1000 rpm.
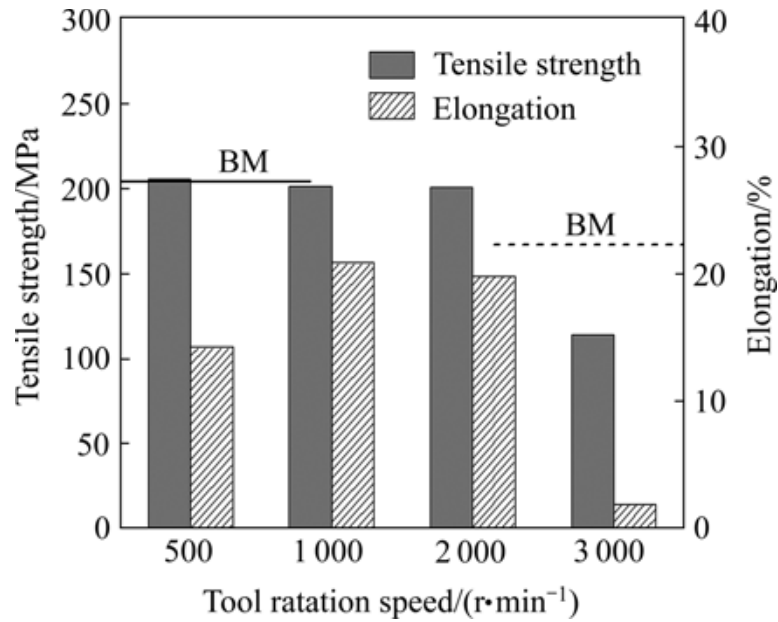
Figure I.13. Influence of tool rotation speed on ultimate tensile strength and total elongation of FS welded aluminum alloy plates (Solid and broken lines represent average ultimate tensile strength and total elongation of base metal plate). (Kwon et al., 2009)

I.6 Measurements in friction stir welding

I.6.1 Force measurements

It is necessary to measure the forces during the FSW process to evaluate the applied forces in different directions, having a feedback force signal permits certain controls schemes to be implemented that may improve the FSW process. (Vukčević et al., 2011) measured the force using precise analog digital measuring equipment, related to information measuring system. The force sensor was strain gages and the signal was converted to digital and saved on the PC with a specified installed software package for data acquisition. Figure I.14 presents an overview of their research sites.

Figure I.14. Research site: 1- The base plate, 2 - Support plate, 3 - Work piece clamp, 4 - Work piece of Al alloys, 5 - Tool for FSW, 6 - Clamp part of the milling machines, 7 - Special carrier with glued measuring tapes, 8 - Measuring bridge, 9 - BAS, 10 - PC with A/D card and software GLOBAL LAB, 11 - Work table of milling machine. (Vukčević et al., 2011)

Downward force Fz is the largest value when the rotating tool with its pin is embedded into the material. According to that, the work piece increases its temperature due to the friction of the tool pin to the work piece. Then, force Fz declines up to the moment of contact of the larger part of tool shoulder with the work piece, at that point the force Fz reaches its maximum value, because a large area of tool shoulder starts embedding in the work piece. Work piece increases its temperature even more because of friction coming from shoulder and pin simultaneously. When the milling machine is provided with crosswise movement of the work table or with selected welding speed, forces Fx, Fy and Fz are retaining constant values, to the moment when the tool is out of the work piece. Diagram of down force Fz, and diagram of forces Fx and Fy are given in the Figure I.15.
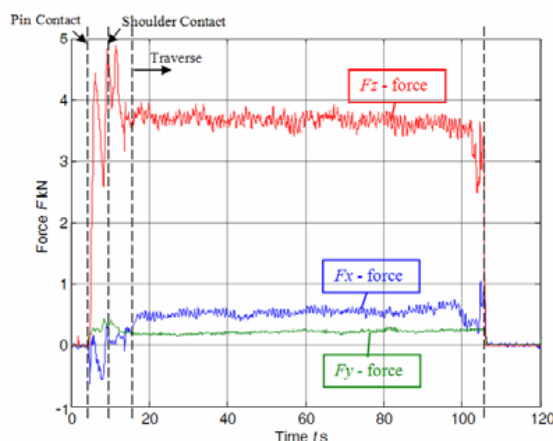
Figure I.15. Diagram of forces obtained using the sensor (strain gage). (Vukčević et al., 2011)

I.6.2 Temperature measurement

During the friction stir welding, the tool in contact with the workpieces creates heat below the melting temperature by friction allowing a plasticity deformation of the plates to be welded. Measurement of this temperature in both homogeneous and heterogeneous material joining is performed with precise analog-to-digital measuring equipment. This equipment is connected with information measurement and system consisted of sensors such as thermocouple and such as a PC equipped with software allowing the data acquisition and obtaining, at last, a graphical and data form. However, the temperature values are very helpful to quantify and correlate the three levels of energy input for all different aluminum alloys. The thermocouples are placed in specific points to measure the temperature in different zones. Figure I.16 presents a scheme of measuring points of temperature in the workpiece.
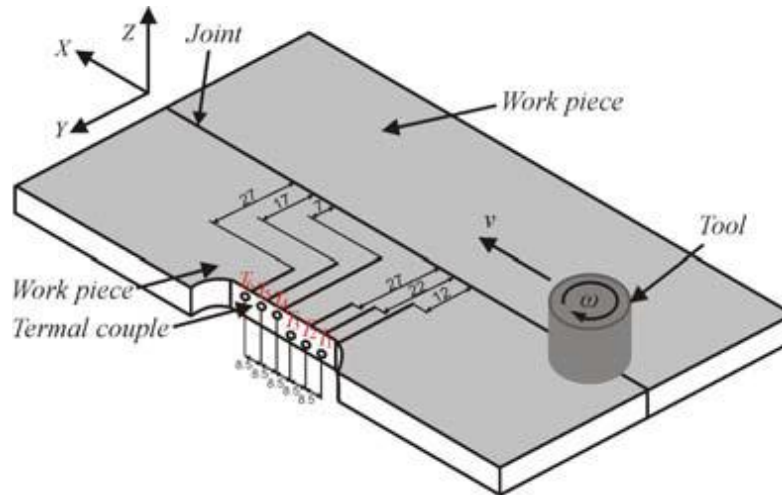
Figure I.16. Schematic drawing of temperature measuring points during FSW. (Vukčević et al., 2011)

It is well noticed that the parameters of FSW such as tool rotation speed, traverse speed influence the temperature distribution in the weld zones, the highest generated temperature during FSW is located below the shoulder. It starts to decrease from the top surface to the bottom, and from the centerline of the weld to the base metal (Mahoney et al., 1998; Tang et al., 1998).

I.7 Friction stir welding tools

I.7.1 Tool design

Tool geometry is the most influential aspect of process development. The tool geometry plays a critical role in material flow and in turn governs the traverse rate at which FSW can be conducted. An FSW tool consists of a shoulder and a pin as shown schematically in Figure I.17. As mentioned earlier, the tool has two primary functions: (a) localized heating, and (b) material flow. In the initial stage of tool plunge, the heating results primarily from the friction between pin and workpiece. Some additional heating results from deformation of material. The tool is plunged till the shoulder touches the workpiece. The friction between the shoulder and workpiece results in the biggest component of heating. From the heating aspect, the relative size of pin and shoulder is important, and the other design features are not critical. The shoulder also provides confinement for the heated volume of material. The second function of the tool is to 'stir' and 'move' the material. The uniformity of microstructure and properties as well as process loads are governed by the tool design. Generally a concave shoulder and threaded cylindrical pins are used. (Mishra and Ma, 2005)
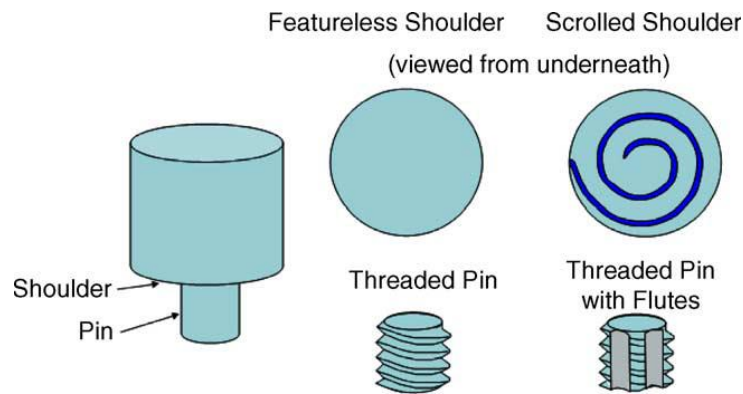
Figure I.17. Schematic drawing of the FSW tool. (Mishra and Ma, 2005)

Regarding the conventional tool geometry presented previously, other tool designs are presented including two examples in Figure I.18. MX Triflute having a three flutes is presented in Figure I.18 (a), this tool was developed by the welding institute (TWI) and made so that the pin is not parallel sided but frustum shaped. The MX Triflute pin moves considerably less material during the process (70% less) than the normal cylindrical normal pin. It allows also a

more effective flow path and less stress concentration in the cross-section of the welded joint due to the tapered pin and the radiused shape between the tool shoulder and pin. And thereby, resulting in a more homogeneous weld with superior mechanical properties. Figure I.18 (b) presents another tool geometry developed by the TWI, an MX Trivex tool, this tool consists of three convex sides that serve to present the entrapment of the material, this tool geometry was compared to the MX Triflute tool design by the TWI, and it was reported that the measured downward force using MX Trivex tool was reduced considerably compared to the MX Triflute tool, and the tensile strength of the welds produced using MX Trivex tool matched the one of the joint using MX Triflute tool.
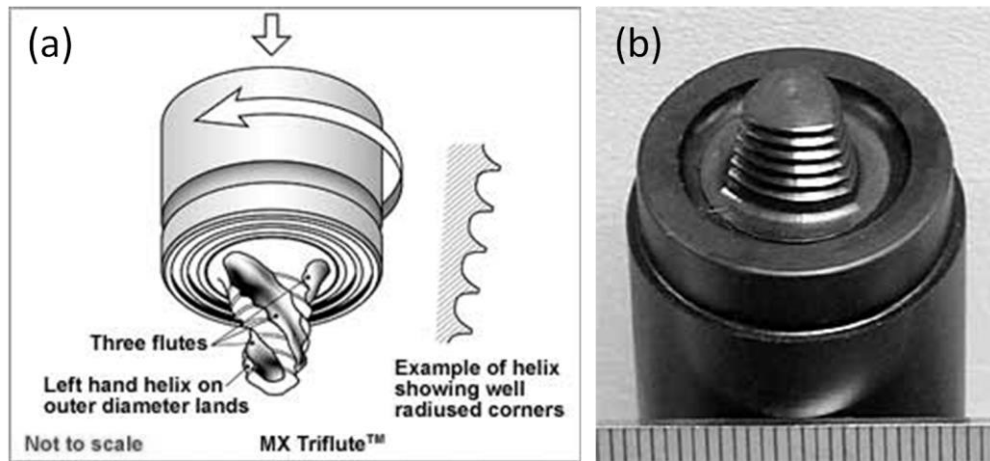
Figure I.18. Schematic drawing of (a) MX Triflute and (b) MX Trivex. (Mishra and Ma, 2005)

I.7.2   Tool pin

Friction stirring pins produce deformational and frictional heating to the joint surfaces. The pin is designed to penetrate between the two plates, the shear material in front of the tool, and move material behind the tool. Figure I.19 summarizes the different probe shapes used for FSW tools. It can be noted that the cylindrical end shape can be composed of a flat or domed shape. However, the cylindrical outer surface can be divided into several types, including circle shape, fluted cylinder, a cylinder with flats, threaded cylinder, threaded and fluted cylinder, threaded and flat cylinder. On the other hand, the tapered outer shape is also divided into six categories: smooth, fluted, tapered with flats, threaded, threaded and fluted and finally threaded and flat. Each outer surface or outer shape can have circle, triangle, hexagonal, three-sided or even four-sided, these shapes can be used or tested on welding different metal alloys, because the

tool shape can enhance the weld quality especially when welding thick plates where more heat input is needed, the metal flow can also be enhanced while using such geometries because it modifies its path while the tool is rotation. The selection of the right tool geometries can considerably enhance the weld quality in a metallurgical and mechanical point of view.
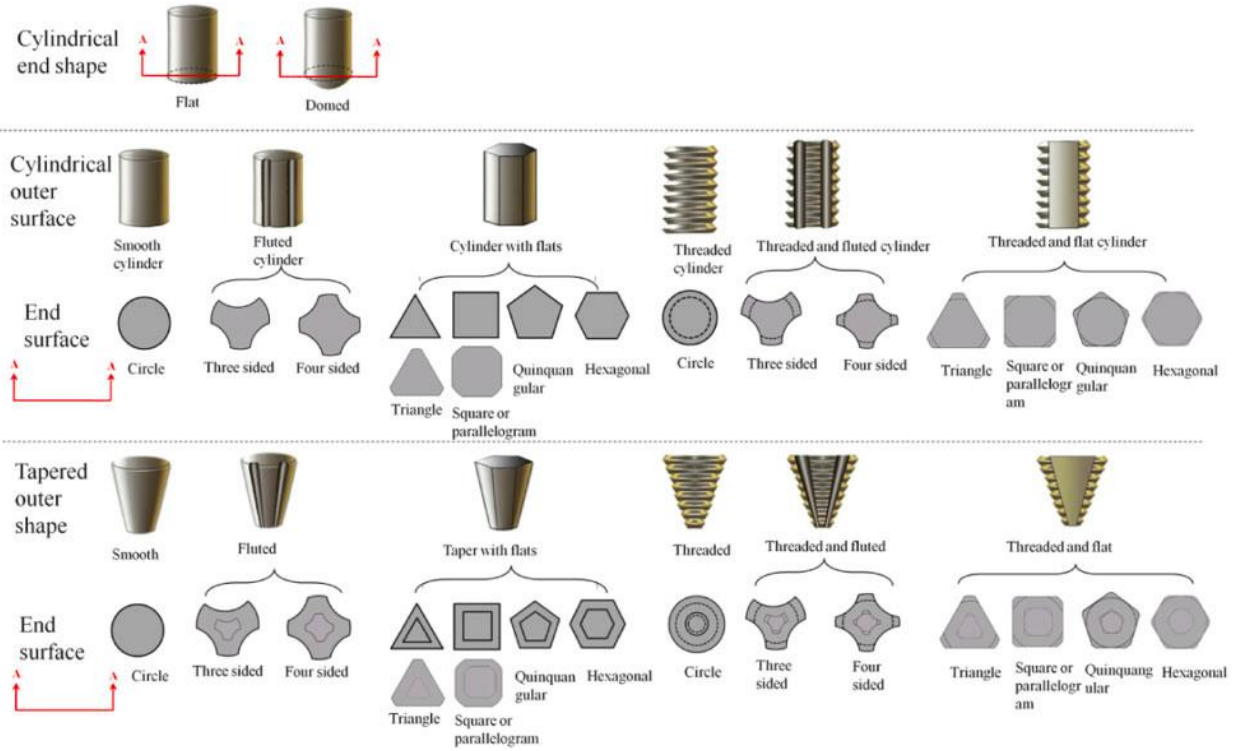
Figure I.19. Different probe shapes for friction stir welding. (Zhang et al., 2012)

I.7.3   Tool shoulder

Tool shoulders are designed to produce heat (through the friction with the workpiece and plastic deformation) to the surface and subsurface regions of the workpiece. The tool shoulder produces the majority of the deformational and frictional heating in a thin sheet while the pin produces the majority of the heating in thick workpieces. Also, the shoulder produces the necessary downward forging action for weld consolidation (Mishra and Ma, 2005).

As demonstrated in Figure I.20, three types of shoulder end surfaces are typically used (Mishra and Mahoney, 2007). Of these, the flat shoulder end surface is the simplest design. The main disadvantage of this design is that the flat shoulder end surface is not effective for trapping the flowing metal material under the bottom shoulder, leading to the production of excessive

material flash. To this end, a concave shoulder end surface was designed and has now become popular for restricting material extrusion from the sides of the shoulder. This simple shape is easy to machine and can produce sound welds. The concave shoulder inclines only a small angle (6–10°) from the flat shoulder end surface. During tool plunging, the material displaced by the probe is fed into tool shoulder cavity. Hence the concave surface profile of the tool shoulder serves as an escape volume or reservoir for the displaced material from the probe. By exerting a downward applied pressure on the tool, the displaced material held in the concave shoulder profile renders a forging action on the material behind the tool. Then the forward movement of the tool forces new material into the cavity under the shoulder and pushes the existing material behind the probe. The proper operation of this shoulder requires the tilting of the tool 1–3° from the normal of the workpiece against the direction of travel. This is necessary to maintain the material reservoir and to enable the trailing edge of the shoulder tool to produce a compressive forging force on the weld (Sutton et al., 2003). It can also lead to higher forging and hydrostatic pressures, which may promote material stirring and improve nugget integrity. Another possible end shape of the shoulder is a convex profile. Early attempts at TWI for the convex end surface were unsuccessful because the convex profile was determined to push the material away from the probe (Zhang et al., 2012).
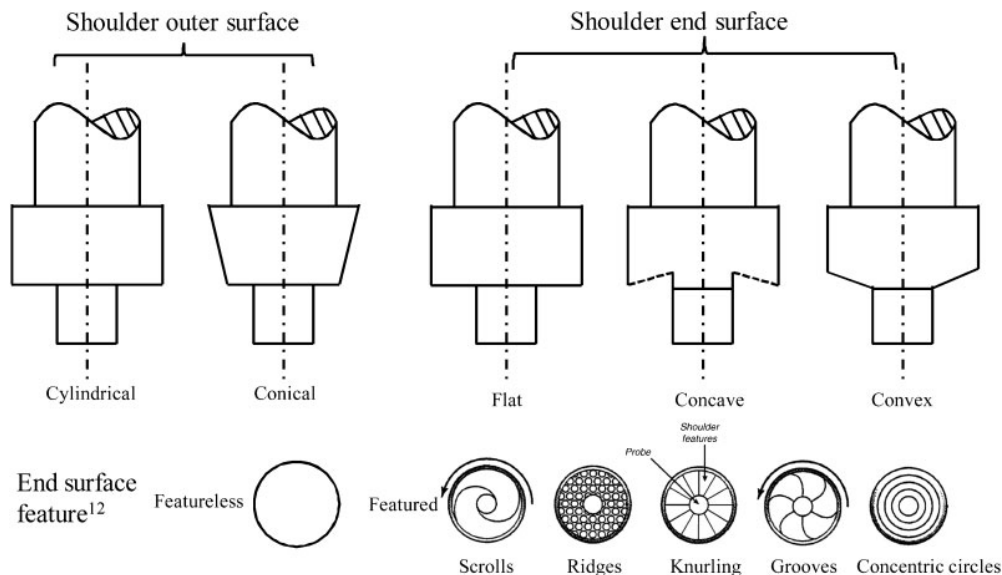
Figure I.20. Different shoulder shapes and features used to improve material flow. (Zhang et al., 2012)

I.7.4   Tool material selection

Weld quality and tool wear are two important considerations in the selection of tool material, the properties of which may affect the weld quality by influencing heat generation and dissipation. The weld microstructure may also be affected as a result of interaction with eroded tool material. Apart from the potentially undesirable effects on the weld microstructure, significant tool wear increases the processing cost of FSW. Owing to the severe heating of the tool during FSW, significant wear may result if the tool material has low yield strength at high temperatures. Stresses experienced by the tool are dependent on the strength of the workpiece at high temperatures common under the FSW conditions. Temperatures in the workpiece depend on the material properties of tool, such as thermal conductivity, for a given workpiece and processing parameters. The coefficient of thermal expansion may affect the thermal stresses in the tool. Other factors that may influence tool material selection are hardness, ductility and reactivity with the workpiece material. The tool hardness is important in mitigating surface erosion due to interaction with particulate matter in the workpiece. The brittle nature of ceramics such as pcBN may be undesirable if there is a significant probability of breakage due to vibrations or accidental spikes in loads. Tool degradation may be exaggerated if the tool material and workpiece react to form undesirable phases. The properties of some of the commonly used tool materials are given in Table I.2 along with remarks regarding their suitability for welding specific materials. Because of their high temperature strength, PCBN and W based alloys are commonly used tool materials for FSW of harder alloys. Good quality welds have been obtained for welding of steels for both tool materials. W–25 wt-%Re alloy tool, the most common W based tool material, undergoes significant wear compared with the PCBN tool which has superior wear resistance and abrasive properties. The thermal conductivity of the tool material determines the rate of heat removal and affects the temperature fields, flow stresses and weld microstructure. High thermal conductivity of PCBN avoids the formation of hot spots on tools and helps in the design of liquid cooled tools (Collier et al., 2003). However, a high thermal conductivity may be undesirable if excessive removal of heat from the tool/workpiece interface requires very high tool rotational speeds to adequately soften the workpiece and to reduce tool stresses. The appropriate value of thermal conductivity depends on the process variables, workpiece material and other tool material properties.

	Coefficient of thermal expansion (10^{-6} K^{-1})	Thermal conductivity (W m-1K-1)	Yield Strength (MPa)	Hardness (HV)	Remarks
pcBN	4.6-4.9 (Meran et al., 2007)	100-250 (Meran et al., 2007)		2600-3500	Pros: high hardness; high-temperature strength. Cons: susceptible to crack; wear may be enhanced by chemical reactions with Ti; high cost.
cp-W	~4.6 at 20-1000°C (Brandes and Brook, 1992)	167 at 20°C (Brandes and Brook, 1992) 111 at 1000°C	~100 at 1000°C (Gan et al., 2007)	360-500 (Brandes and Brook, 1992)	Pros high-temperature strength Cons: low toughness at room temperature; less strong than W alloys, WC, or pcBN
W-25 wt-%Re		55-65 (Jasthi et al., 2008)	~500-800 at 1000•c (Gan et al., 2007)		Pros: higher strength than W; tougher and easier to machine than ceramics.
WC	4.9-5.1 (Meran et al., 2007)	95 (Meran et al., 2007)		1300-1600 (Meran et al., 2007)	Pros: high-temperature strength; high hardness. Cons: wear due to oxidation at high temperatures: addition of Cr_3C_2 prevents oxidation
4340 Steel	11.2-14·3 (Meran et al., 2007)	48 (Meran et al., 2007)		280 (Meran et al., 2007)	Pros: low thermal conductivity Cons: High-temperature strength is not very high; possible alloying with Ti
TiC	8.31 (Shackelford and Alexander, 2001)	5-31 (Shackelford and Alexander, 2001)	20 000 (Shackelford and Alexander, 2001)	2800-3400 (Shackelford and Alexander, 2001)	Pros: high hardness: High-temperature strength Cons: susceptible to crack
Si_3N_4	3.9 at 20°C 6·7 at 1000°C (Jiang et al., 2002)	20-70 (De Pablos et al., 2002)		1580	Pros: high hardness: High-temperature strength Cons: susceptible to crack; decomposes at high temperatures

Table I.2. Common tool material properties. (Rai et al., 2011)

I.7.5 Tool wear

Excessive tool wear dramatically changes the tool shape, thereby increasing the probability of defect creation, and possibly degrading the weld quality. The exact wear mechanism depends on the interaction between the workpiece and the tool materials, the selected tool geometry and the welding parameters. For example, in the case of PCBN tools, the wear at low tool rotation rate is mainly caused by adhesive wear, while the wear at high tool rotation rate is due to abrasive wear (Collier et al., 2003; Mishra and Mahoney, 2007). (Shindo et al., 2002) and (Prado et al., 2003) reported on the tool wear for Al–20SiC (Ref. 58) and Al–20Al2O3 (Ref. 59) particle reinforced composites. The tool used consisted of an AISI oil hardened tool steel initially with screw nib right hand threads. Owing to the abrasive particles in the Al-MMCs, the threads of the probe wore away, leading to a slightly curve shaped probe, as shown in Figure

I.21. Remarkably, the self-optimized shape (worn tool) with no threads could result in homogenous and integral welds without further visible tool wear. These observations suggest that tool consumption can be greatly minimized even for MMCs when using the optimized tool shape. Hence to reduce tool wear and extend the tool life, understanding and controlling the material flow associated with the probe profile in the solid state are important. It is noteworthy that the self-optimized shape does change somewhat with increasing welding speed due to increasing tool wear (Prado et al., 2001). For FSW, severe tool wear has been reported after producing hundreds of welds. For light metals such as Al and Mg alloys, the welding tool is commonly made of tool steel and suffers from little wear. It was reported that no significant wear was found on the steel tool even after hundreds of thousands of spot welds for Al. However, the steel tools are not suitable for high melting point materials such as, Ti, Ni, steels, etc. For these high strength materials, the welding tools are usually made of hard metals, carbides and metal matrix composites with superior thermal and wear resistance at temperatures higher than 1000uC, such as WC–Co, TiC and PCBN (Hovanski et al., 2007).
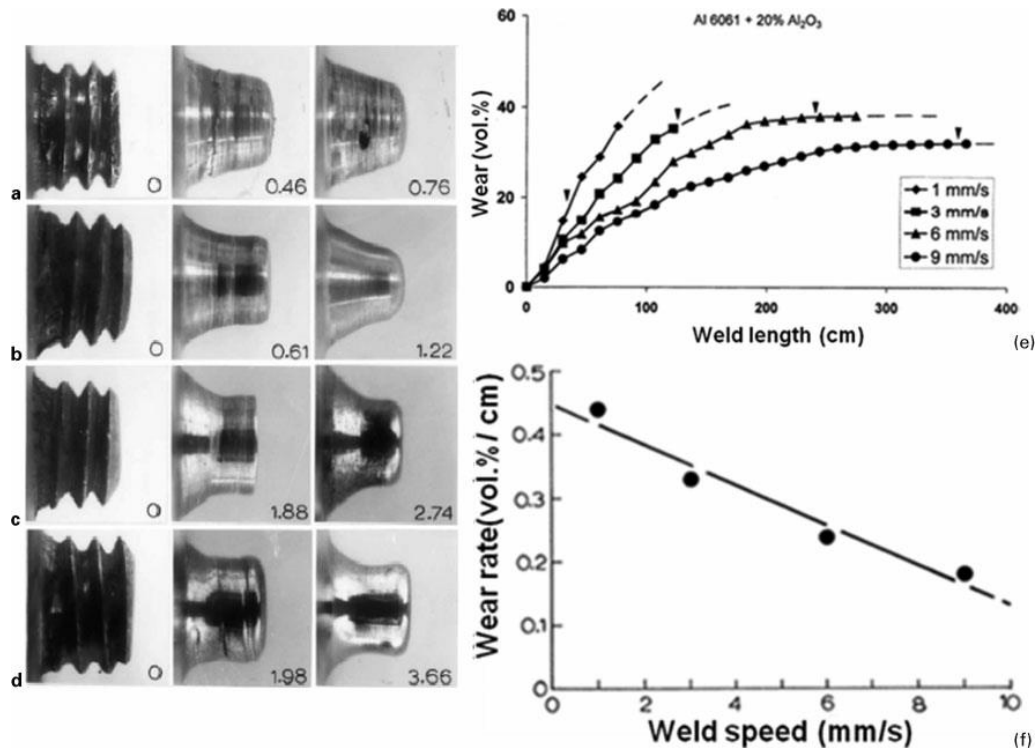
Figure I.21. Wear features of probes for Al-MMC at 1000 rev min21: welding speeds at a 1, b 3, c 6 and d 9 mm s21; e probe wear (vol.-%) versus weld length and f wear rate versus weld speed (Prado et al., 2003)

I.8   Metal flow

The material flow during friction stir welding is quite complex depending on the tool geometry, process parameters, and material to be welded. It is of practical importance to understand the material flow characteristics for optimal tool design and obtain high structural efficiency welds. This has led to numerous investigations on material flow behavior during FSW. A number of approaches, such as tracer technique by marker, welding of dissimilar alloys/metals, have been used to visualize material flow pattern in FSW. In addition, some computational methods including FEA have been also used to model the material flow (Mishra and Ma, 2005).

I.8.1   Tracer technique by marker

This technique lies on inserting a thin material that differs from the workpieces material between faying surfaces of the two workpieces. In the past decade, some investigators used different marker materials such as copper foil (Guerra et al., 2002), small steel shots (Colligan, 1999)… etc. to track the material flow during friction stir welding.

(Donath et al., 2004) investigated the material flow behavior of the weld by inserting titanium powder as a marker into 4mm thick 2024-T351 aluminum alloy sheet. They considered that the plastic material on the advancing side was partially rotated around the tool pin, while, on the retreating side, the metal was fully rotated and extruded to the near of the pin. They found that the titanium powders were less scattered on the retreating side than in the advancing side. Therefore, it was found by (Xu et al., 2011) that the softened metal adjacent to the threaded pin is transported non-symmetrically to the bottom from the top relative to the weld centerline, when copper strip was utilized as a marker to reveal the metal flow behavior. The same marker material was used by (Schmidt et al., 2006) when they utilized a copper strip in the workpiece to visualize the flow field of the material during FSW process. They presented two procedures to estimate the average velocity of a marker material through the shear layer based on the experimental study. Moreover, (Colligan, 1999) investigated the metal flow of FSW of 6061-T6 and 7075-T6 aluminum alloys using steel shot tracer. The authors observed that the material partially was stirred in the tool path and rather a large quantity of the material was extruded near

the retreating side of the FSW tool pin. However, if the material marker has different flow strength and density, it can make uncertainty about the precision of the deductions. (Mishra and Ma, 2005)

In a recent study, (Li et al., 2013) investigated the metal flow during FSW of 7075-T651 aluminum alloy by inserting 0.1 mm bronze foil between the faying surfaces of the two workpieces (Figure I.22).
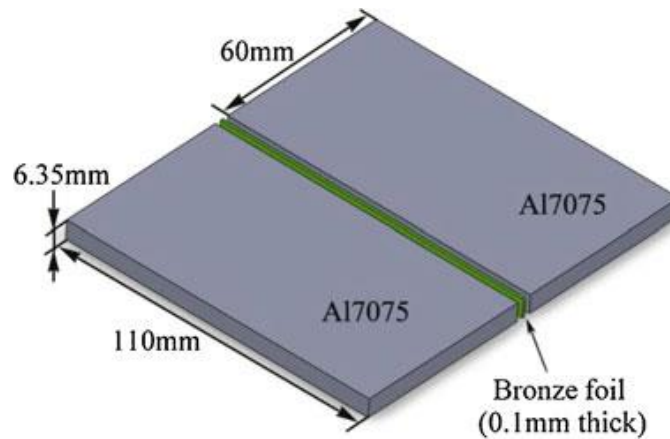
Figure I.22. Schematic diagram showing the inserting a bronze foil between the workpieces. (Li et al., 2013)

In order to reveal the flow behavior of the weld metal, the authors traced the bronze foil fragment in the welded zone after the welding process. The authors perceived that the flow behavior of the weld metal is different alongside the thickness path. Figure I.23 presents an X-ray photograph of the joint showing the equidistant bronze foil (bright fragments) and indicating the presence of periodic variation of the metal flow. Figure I.24 present the flow process of bronze foil fragments in the horizontal section. (Li et al., 2013). It can be observed from these figures that in the region I (plunge phase), the foil in the pin insert position (PIP) is not broken and presented a fan-shaped structure (FSS) by the rotation and extrusion force of the shoulder. While in region II, the bronze foil was frequently and periodically distributed. The authors observed that the bronze foil was extruded and stirred into of the weld both sides and showed a "bud" shape, the diameter of that bud shape corresponded to the diameter of the pin, suggesting that the metal flow occurs mostly around the pin in the welding phase. While in Region III (pull-

out phase), the bronze foil on the advancing side of the tool pull-out position (POP) is deformed but not slashed as in region I, the FSS is appeared to be on the retreating side. While it seemed to be on the advancing side in the region I, this observation can be referred to the fact that when the tool rotates, the material under the tool shoulder follows the tool rotation path. Also, a small bronze foil is observed in the keyhole due to the rotation of the material around the pin.
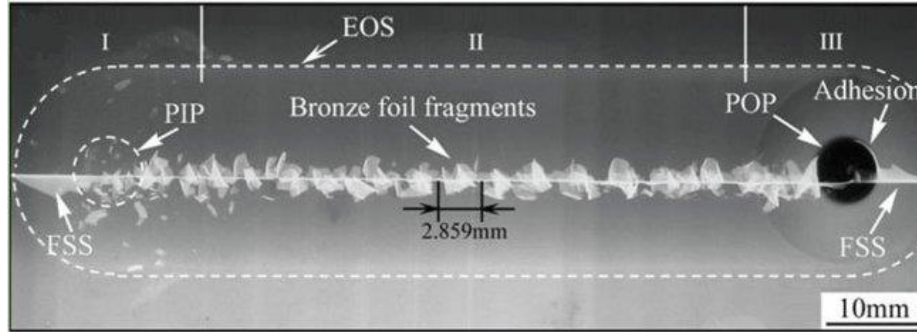
Figure I.23. X-ray photograph of the FSW joint with inserting bronze foil as a marker (I: plunging phase, II: welding phase, III: pulling-out phase, EOS: edge if the shoulder, FSS: fan-shaped structure, PIP: pin insert position, POP: pull-out position. (Li et al., 2013)
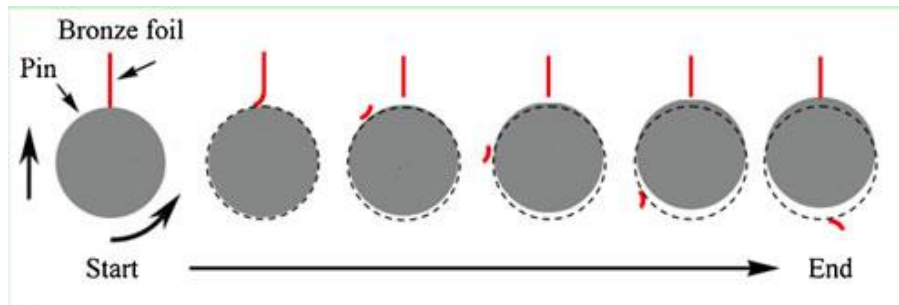
Figure I.24. Flow process of the material marker in the horizontal section. (Li et al., 2013)

I.8.2   Flow visualization by FSW of dissimilar materials

In addition to the tracer technique, several studies have used friction stir welding of dissimilar metals for visualizing the complex flow phenomenon. (Midling, 1994) investigated the influence of the welding speed on the material flow in welds of dissimilar aluminum alloys. He was the first to report on interface shapes using images of the microstructure. However, information on flow visualization was limited to the interface between dissimilar alloys.

Also, (Ouyang and Kovacevic, 2002) examined the material flow behavior in friction stir butting welding of 2024Al to 6061Al plates of 12.7 mm thick. Three different regions were revealed in the welded zone. The first was the mechanically mixed region characterized by the relatively uniformly dispersed particles of different alloy constituents. The second was the stirring-induced plastic flow region consisting of alternative vortex-like lamellae of the two aluminum alloys. The third was the unmixed region consisting of fine equiaxed grains of the 6061Al alloy. They reported that in the welds the contact between different layers is intimate, but the mixing is far from complete. However, the bonding between the two aluminum alloys was complete. Further, they attributed the vortex-like structure and alternative lamellae to the stirring action of the threaded tool, in situ extrusion, and traverse motion along the welding direction.

I.9   FSW defects

In a friction stir welding process, the joint quality depends on the combination of the welding parameters according to the specific material to be welded. If the welding parameters are not appropriate, some unwanted defects may result and present a degradation of the weld. A "Characteristic Defect" is defined as a Microstructural or Geometric Anomaly peculiar to FSW joints that adversely affects Form, Fit or Function. It may adversely affect the mechanical properties (ultimate tensile strength, yield strength, Elongation), dynamic properties (fracture and fatigue), corrosion resistance, formability and ductility of the material. Such defects make the joint not qualified to be used for industrial purposes because of the poor mechanical properties resulted in these joint. Defects in friction stir welds are related to processing temperatures, metal flow patterns, and joint geometry. FSW defects are divided into three types; cold processing defects, hot processing defects, and geometry related defects.

I.9.1   Cold Processing Defects

I.9.1.1   Wormhole

This defect is an advancing side tunnel of inadequately consolidated and forged material running in the longitudinal direction (Figure I.25). It can occur because of the insufficient metal flow into the zone interleaving area on the advancing side above the swirl zone. It can be also

created by excessive tool displacement speed [mm/min] for a given rotational speed [rpm], and also if the weld pitch is too low.
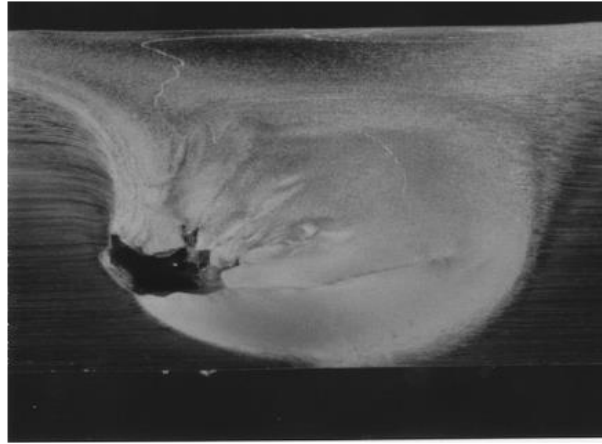
Figure I.25. Weld with a wormhole defect. (Mishra and Mahoney, 2007)

I.9.1.2 Scalloping

It is a series of small voids located on the advancing side interleaving the stir zone along the length of the weld (Figure I.26). The scalloping defect is another cold defect. It can occur when there are insufficient flow and metal forging in the forging zone, or lower limiting case of the wormhole defect, to the inadequate forging pressure. It considerably reduces the mechanical properties of the weld.
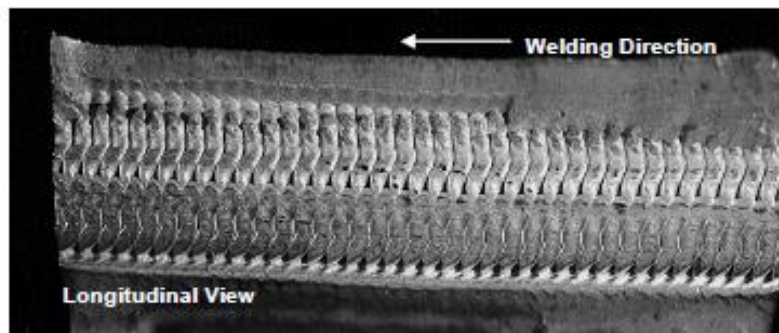
Figure I.26. Weld with a scalloping defect. (Mishra and Mahoney, 2007)

These two cold processing defects are due to the too low weld pitch and the cold weld either.

I.9.2   Hot Processing Defects

These defects are due to the excessively hot weld and the high weld pitch.

I.9.2.1   Ribbon Flash

It is an excessive expulsion of material on the top surface leaving a corrugated or ribbon-like effect on the retreating side. Figure I.27 presents a weld with a ribbon-flash defect. It can be caused by the excessive forging load or plunge depth, or of the thickness mismatch between the advancing side and retreating side, and also to the extremely hot weld.

Figure I.27. Weld with a ribbon-flash defect. (Mishra and Mahoney, 2007)

I.9.2.2   Surface lake-of-fill defect

This defect is a continuous or intermittent top surface void on the advancing side. Figure I.28 presents a weld with a surface lake-of-fill defect. It is due to the insufficient flow arm formation across the top surface, to the insufficient forging pressure and plunge depth, and the separation of the plates due to the insufficient clamping system force.
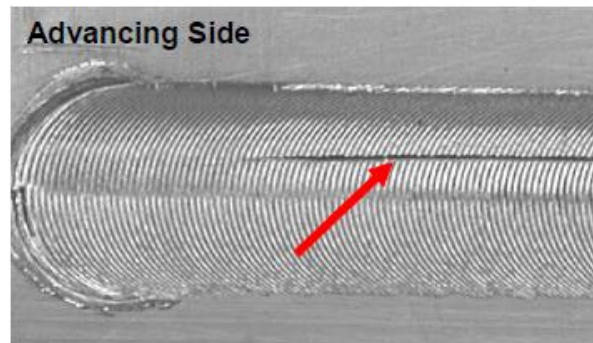
Figure I.28. Weld with a surface lake of fill defect. (Mishra and Mahoney, 2007)

I.9.2.3 Nugget Collapse

Figure I.29 presents a weld with a nugget collapse defect (highlighted by yellow arrow). It is an improper formation of nugget shape. This defect is due to the excessive flow arm formation, to the excessive material flow into the advancing zone side.
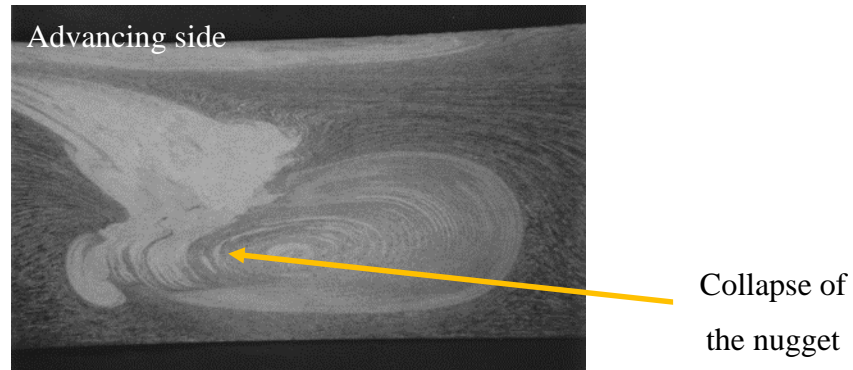
Figure I.29. Weld with a nugget collapse defect. (Mishra and Mahoney, 2007)

I.9.2.4 Surface-Galling defect

Figure I.30 shows a weld with a surface-galling defect. The galling and tearing of the metal on the top surface of the weld beneath the pin tool is due to the sticking of metal to the tool pin. Leaving an improper surface shape of the weld, which can be sites for crack initiation if not removed.
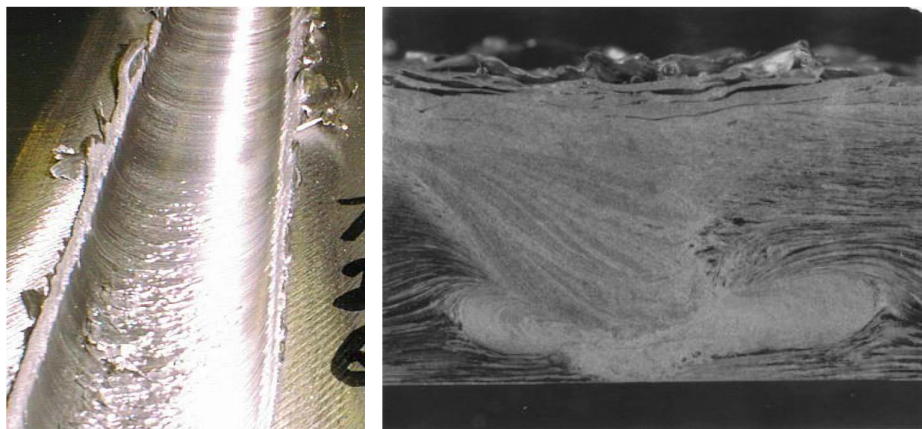
Figure I.30. Weld with a surface-galling defect. (Mishra and Mahoney, 2007)

I.9.2.5 Root Flow Defect

Figure I.31 presents a bottom view of a root flow defect. It is a chevron shaped flow patterns visible on the backside (root) surface. This defect is due to excessive metal flow within swirl zone beneath pin tip and "breakout" of flow patterns to back surface. Also, to the excessive pin length or when the pin penetrate excessively between the plates to be welded.

Root flow defect

Good root structure
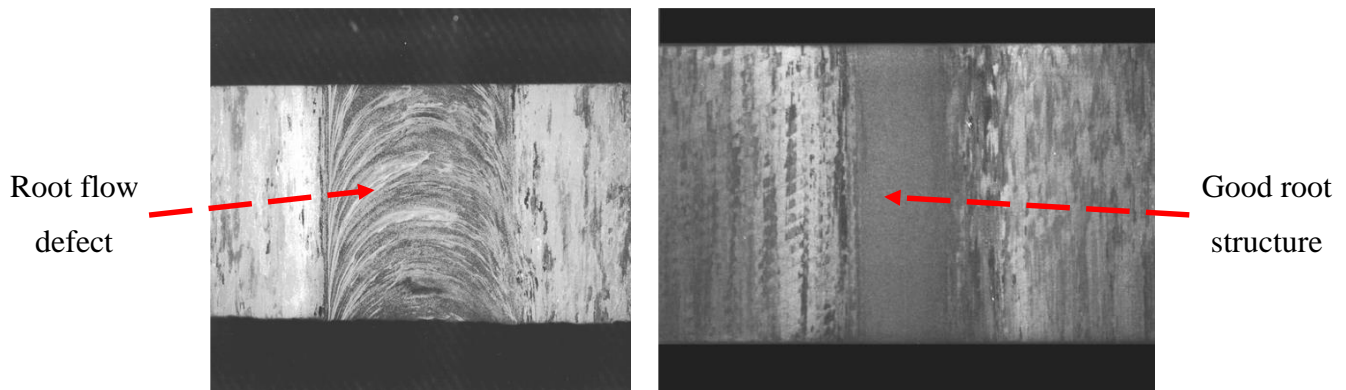
Figure I.31. Bottom view of the root flow defect. (Mishra and Mahoney, 2007)

These hot processing defects can appear because of the excessively hot weld or the high weld pitch too, and may result in a decreasing in the mechanical properties of the welded joint.

I.9.3 Geometry Related Defects

I.9.3.1 Lack of Penetration

Figure I.32 shows a welding with a lack of penetration defect. It is one of the leading causes of surface defect. This defect is due to the inadequate recrystallization and insufficient metal flow in the swirl zone on the back surface, to the insufficient pin length and improper pin tip radius or the cold weld.

Lack of penetration
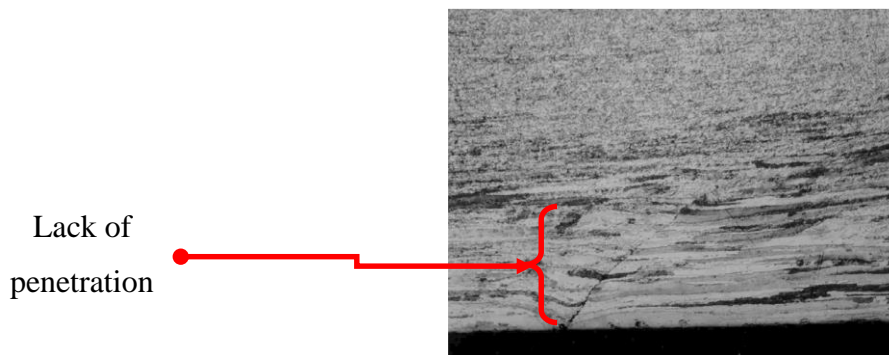
Figure I.32. Welding with a lack of penetration defect. (Mishra and Mahoney, 2007)

I.9.3.2   Lack of Fusion

Lack of fusion is the same as lack of penetration, but it appears because of the improper seam tracking. Alternatively, when the weld seam is missed, and consequently one portion of a weld joint is not fused to an adjacent portion of a weld joint. (Figure I.33)
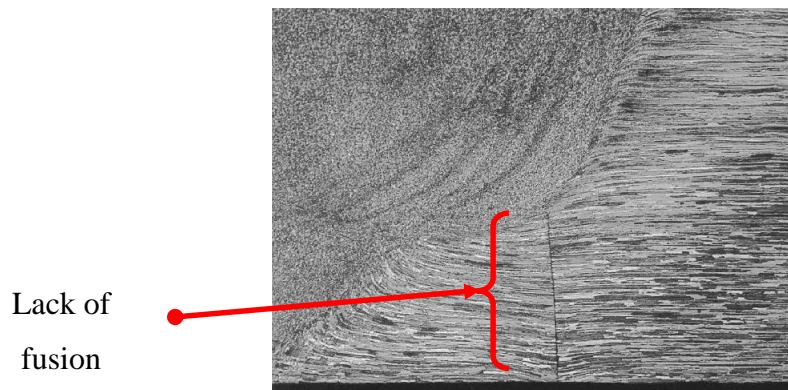
Lack of fusion

Figure I.33. Weld with a lack of fusion defect. (Mishra and Mahoney, 2007)

I.9.4   The relationship between the defects and operational parameters

In this paragraph, the relationship between FSW defects and operational parameters will be discussed. (Arbegast, 2008) studied the occurrence of defects in the function of position controlled operational parameters (advance speed and rotation speed). In Figure I.34, the process envelope to obtain defect-free joints made by FSW is highlighted in the white area. Also, the other types of defects explained previously including cold, hot and geometry related defects are illustrated in different areas on the same graph. The cold defects that occur when the rotation speed is too high or the advance speed is too small. The hot defects that occur when the rotation speed is too low or the advance speed is too high. These defects can easily be avoided by modifying the values of tool rotation speed and advance speed. However, defects in red color are the geometry related defects, including lack of penetration and lack of fusion defects.
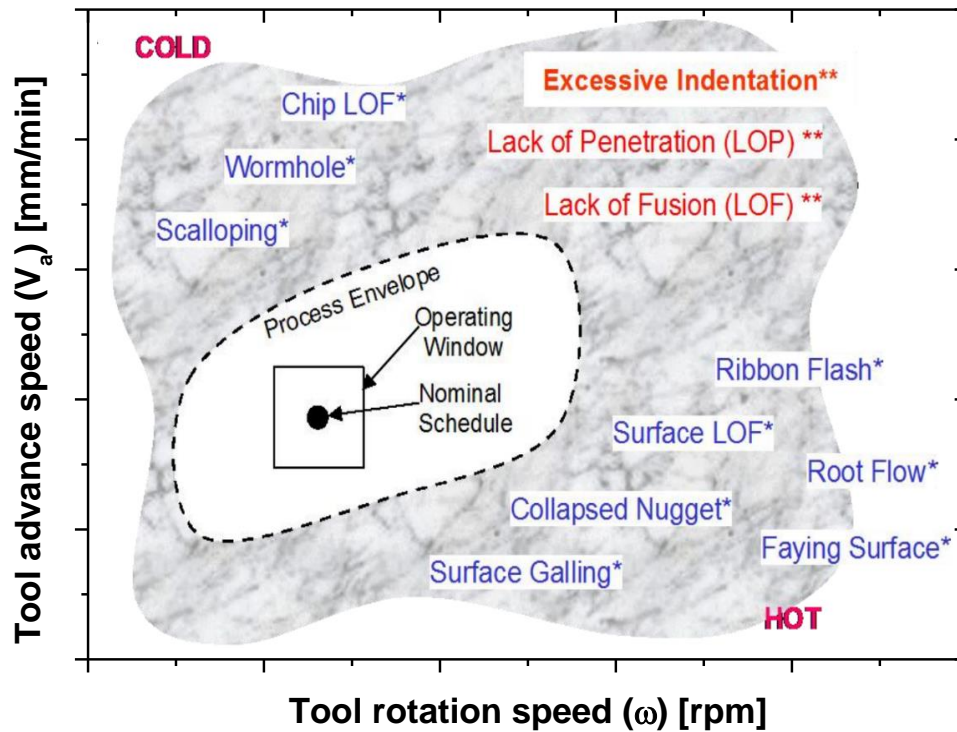
Figure I.34. Weldability field of friction stir welding. (Mishra and Mahoney, 2007)

I.10 Material Weldability

The weldability of a material is its aptitude to be welded into a specific structure that has certain properties and characteristics and will satisfactorily meet the service requirements. Weldability is often hard to define quantitatively, so most standards define it qualitatively. For instance the International Organization for Standardization (ISO) defines weldability in ISO standard 581-1980 as: "Metallic material is considered to be susceptible to welding to an established extent with given processes and for given purposes when welding provides metal integrity by a corresponding technological process for welded parts to meet technical requirements as to their own qualities as well as to their influence on a structure they form." Other welding organizations define it similarly. In what is next, the weldability of aluminum and magnesium and their alloys are hereafter discussed.

I.10.1 Aluminum Alloy

Aluminum and its alloys have several chemical and mechanical properties that need to be understood when using the various joining processes. These properties include oxide formation and solubility of hydrogen in molten aluminum. Its thermal, electrical, and non-magnetic characteristics; its lack of color change when heated and its wide range of mechanical properties and melting temperatures that result when alloying it with other metals.

The most attractive reasons for aluminum alloys assembly by FSW are the avoidance of solidification defects caused by the conventional joining processes such as fusion welds. Moreover, compared to the conventional welding methods, FSW results in low distortion and less residual stresses. Friction stir welding has been systematically developed for joining aluminum alloys, in particular for those considered to be impossible to be welded such as 2xxx and 7xxx aluminum series. (Genevois et al., 2005; Hassan et al., 2003a)

The Welding Institute (TWI) concentrated most of its efforts to optimize the process for the aluminum and its alloys joining. Subsequent studies have shown that cast to cast and cast to extruded (wrought) combinations in similar and dissimilar aluminum alloys are equally possible. The following aluminum alloys could be successfully welded to yield reproducible high integrity welds within defined parametric tolerances.

- 1000 series aluminum (pure aluminum)
- 2000 series aluminum (Al-Cu)
- 3000 series aluminum (Al-Mn)
- 4000 series aluminum (Al-Si)
- 5000 series aluminum (Al-Mg)
- 6000 series aluminum (Al-Mg-Si)
- 7000 series aluminum (Al-Zn)
- 8000 series aluminum (Al-Li)
- 9000 series aluminum (other elements)

Friction stir welding parameters, such as tool material alloy, shape and size, rotation speed and federate, can influence the joint quality, their selection according to the workpiece material is crucial to obtain defect-free joints. Some researchers investigated some metal alloys, they combined the FSW parameters and reported the mechanical properties of the obtained welded

joints. Table I.3 presents some tool materials, geometries and welding variables utilized for FSW and FSSW of several Aluminum alloys.

Workpiece material	Tool material	Tool shape and size	Operating parameters	Remarks	References
6111-T4 Al alloy, 0.9 mm thick	H13 steel	SS : flat with scroll SD : 10 mm ; Pl : 0-1.6 mm	2000 rpm ; dwell time : 2.5 s ; plunge rate : 2.5 mm/sec ; FSSW	Better quality with pinless tool	(Bakavos and Prangnell, 2009)
7075-T7351 ; 6.35 mm		PS: triflute, Trivex	394 and 457 rpm ; 300-540 mm/min	Weld UTS : 470-488 MPa	(Colegrove and Shercliff, 2004a, b)
7075-T7351 ; 6.35 mm, 16 mm	1.MP159 pin; 2.Dievar tool steel; 3.MP159 ;pin, H13 shoulder.	PS : threaded	190-457 rpm; 0.3-1.4 mm/rev	Surface scaling and voiding problems	(Colegrove and Shercliff, 2003)
Al alloys, 5 mm		SS : concave ; SD : 15 mm ; PS: SC, SCT, triangular ; PL: 4.7 mm, 6 mm	600-1500 rpm ; 25-1000 mm/min ; 3° tilt	Peak joint efficiencies : 70-100%	(Fujii et al., 2006)
7020-T6 Al alloy, 4 mm	Steel	SD: 10-20 mm, flat; PD : 3-8 mm; PL: 4.2 mm; PS : frustum and SC	1400 rpm ; 80 mm/min	Peak joint efficiency : 92%	(Kumar et al., 2008)
6082-T6 Al, 1.5 mm		SS : scroll, cavity, fillet ; PD : 1.7 mm ; PS : S, PL : 1.2 mm	1810 rev/min ; 460 mm/min ; 2° tilt	Joint efficiencies : ~76%	(Scialpi et al., 2007)
6061-T6 Al, 9.5 mm and 12.7 mm	H13 steel	SD : 25.4 mm ; PD :5.2-7.6 mm ;PL : 1.8-7.1	650 rpm ; 150 or 200 mm/min ; 3° tilt		(Sorensen and Stahl, 2007)
6061-T6 Al, 6.3 mm		SS: concave ;SD: 26 mm ;PD: 5.6 mm ;PL: 5.9 mm ;PS :SCT	86-1150 rpm ; 30-210 mm/min		(Atharifar et al., 2008)
5754 Al, 1.32 mm	H13 steel	SS: concave, convex, flat; SD: 12 mm; PD: 5 mm; PL: 1.6 mm	1500 rpm; dwell time: 2 s; plunge rate: 20 mm/min; FSSW		(Badarinarayan et al., 2009)
A319 and A413 Al alloy, 6 mm	Tool steel	PD: 6mm	1000 rpm, 120 mm/min	No property degradation in weld metal	(Rodriguez et al., 2005)
7020-T6 Al, 4 mm	High carbon steel	SS: concave; SD: 13 mm; PS: SC, TC3F; PL: 3.19 mm: PD: 5 mm	300–1620 rpm; 100–900 mm/min; 2.5° tilt		(Lorrain et al., 2010)

*SD: shoulder diameter; PL: pin length; PD: pin diameter; PS: pin shape; SS: shoulder shape; SC: straight circular; SCT: straight circular threaded; TC3F: tapered circular with three flats. UTS: ultimate tensile strength; FSSW: friction stir spot welding. Joint efficiency is the ratio of the tensile strength of the joint to that of the base metal.

Table I.3. Tool materials, geometries and welding variables used for FSW of several aluminum alloys. (Rai et al., 2011)

I.10.2 Magnesium alloy

Magnesium is the lightest structural metal available providing a combination of low density and good mechanical properties, resulting in a high strength-to-weight ratio. Magnesium components are used in applications from room temperature to about 93°C. Certain magnesium alloys can be used for short durations to about 371°C (Duffy, 1996).

In the past decade, FSW was focused to weld aluminum and its alloys, the studies on FSW focused on the effect of welding parameters on the tensile properties of aluminum and its alloys (Kang et al., 2005; Kwon et al., 2009; Liu et al., 2011; Schmidt et al., 2006). Recently, FSW started to be implemented to weld other alloys, such as copper and its alloys (Khodaverdizadeh et al., 2012), titanium and its alloys (Zhang et al., 2010b), and magnesium and its alloys (Cao and Jahazi, 2009; Commin et al., 2009; Padmanaban and Balasubramanian, 2009).

Magnesium is used today in aerospace and aircraft applications, as well as passenger cars, light weight truck components, automotive trim, automotive under-the-hood components, and camera casings. Magnesium alloys exist in different aspect such as:

a) Cast alloys: Magnesium casting proof stress is typically 75-200 MPa, its tensile strength is from 135 to 285 MPa and elongation from2 to 10%. Its average density is 1.8 g/cm^3 and Young's modulus is 42 GPa. Most common cast alloys are AZ63, AZ81, AZ91 AM50… etc.

b) Wrought alloys: Magnesium wrought alloy proof stress is typically 160-240 MPa, its tensile strength is 180-440 MPa and its elongation is between 7% and 40%. The most common wrought alloys are AZ31, AZ61, AZ80, ZK60… etc.

Wrought magnesium alloys have a special feature. Their compressive proof strength is smaller than tensile proof strength. After forming, wrought magnesium alloys have a stringy texture in the deformation direction, which increases the tensile proof strength.

I.10.2.1 Effect of processing parameters on FSW of AZ31 magnesium alloy

The FSW processing parameters have some effects on joint properties of magnesium and its alloys. In this regard, (Commin et al., 2012) investigated the effect of residual stresses

induced by friction stir welding of AZ31-O. The authors reported that the microstructural evolution of the material influences the mechanical properties of the joint compared to the base metal. Figure I.35 presents tensile properties of FSW joints produced using two different tool shoulder diameters and compared to the base material. The authors concluded that the FSW butt joints exhibit lower ultimate tensile strength and yield stresses than the base metal. The authors reported that these results are due to the softening and texture changes that occurred during the welding process.
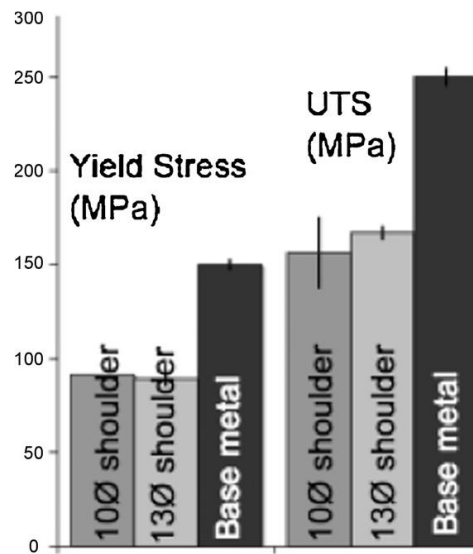
Figure I.35. Tensile properties of the FS welded AZ31-O compared to base metal. (Commin et al., 2012)

The authors also analyzed the grain size of AZ31 joints produced by FSW using two different shoulder diameters as showed in Figure I.36. The authors concluded that a larger shoulder diameter tool produces higher temperature leading to grain growth. The same phenomena were observed by (Xunhong and Kuaishe, 2006) when they studied the microstructure changes, and mechanical properties of FS welded AZ31 magnesium alloys.
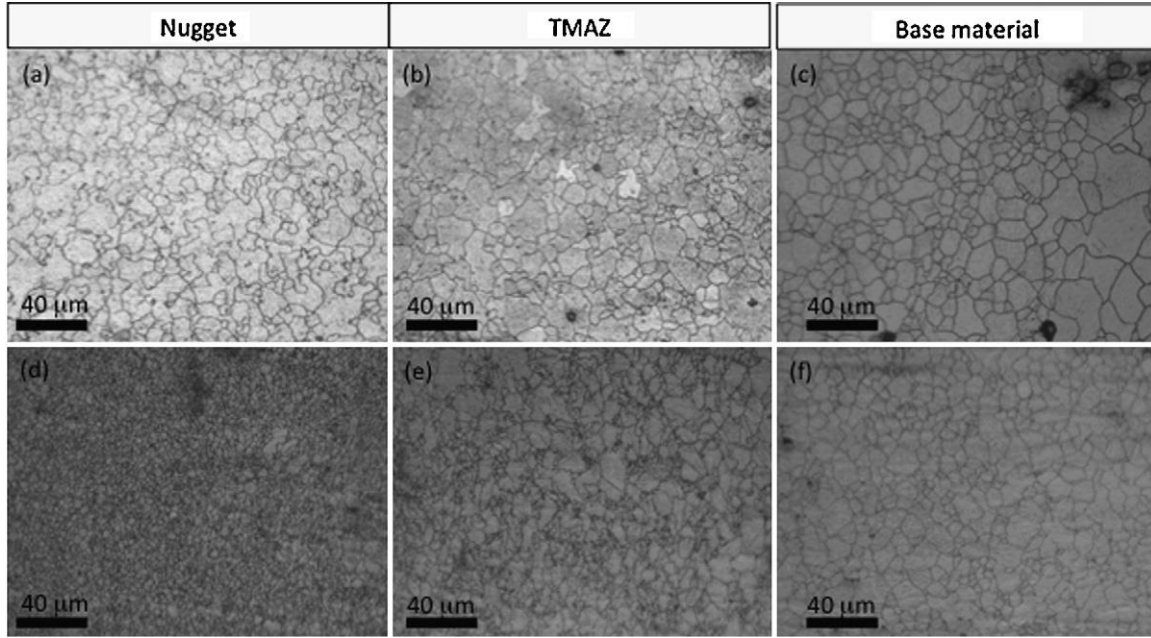
Figure I.36. Grain size evolution with shoulder diameter for 1000 rpm, 200 mm/min butt FSW (a–c) 13 mm shoulder diameter, (d–f) 10 mm shoulder diameter. (Commin et al., 2012)

I.10.2.2 Effect of tool pin geometry on the FSW joint of AZ31

To analyze the effect of the pin profile on the microstructural and mechanical properties on FS welded magnesium alloys sheets, (Padmanaban and Balasubramanian, 2009) selected some different pin profiles and kept the same geometry of the shoulder, the authors analyzed the obtained joints and reported their mechanical properties. Figure I.37 presents some tool pin profiles used in their studies, including straight cylindrical, taper cylindrical, threaded cylindrical, square and triangular shapes.
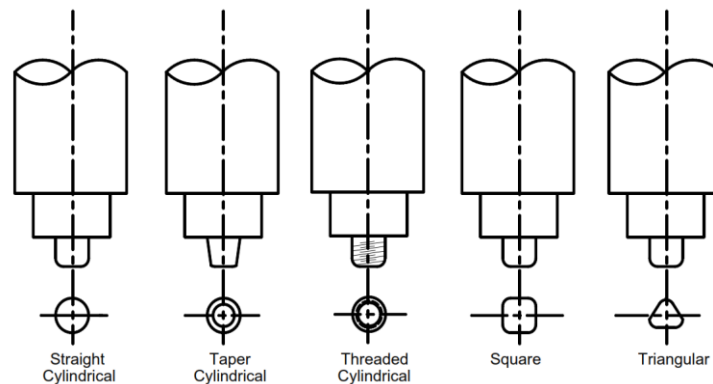
Figure I.37. Different types of tool probe profiles used in this investigation. (Padmanaban and Balasubramanian, 2009)

The authors reported the effect of FSW tool pin profiles on the joint properties in Table I.4. It can be observed that the highest join efficiency was obtained using a threaded cylindrical tool. It can be also observed in this table that the optimum weld with higher joint efficiency had the highest yield strength, ultimate tensile strength, and stir zone microhardness while it presented the lowest stir zone average grain diameter. This observation can be linked to the fact that using a threaded tool reduced the heat input during welding and enhanced the metal flow in the stir zone.

Effect of tool pin profiles on joint properties.

Tool pin profile	Yield strength (MPa)	Ultimate tensile strength (MPa)	Elongation in 50 mm gauge length (%)	Reduction in cross-sectional area (%)	Joint efficiency (%)	Stir zone hardness (Hv)	Stir zone grain diameter (µm)
SC	102	128	2.0	3.6	59.3	72	10.4
TC	84	105	2.5	4.2	48.8	71	11.1
TH	166	208	7.3	5.5	96.7	76	6.3
SQ	119	149	4.0	4.9	69.1	73	9.8
TRI	138	173	2.0	3.8	80.5	74	8.9

SC – straight cylindrical; TA – taper cylindrical; TH – threaded cylindrical; SQ – square; TRI – triangular.

Table I.4. Effect of tool pin profiles on joint properties. (Padmanaban and Balasubramanian, 2009)

The weld cross-sections for FS welded joints for several pin profiles is presented in Table I.5. The straight cylindrical and taper cylindrical joints gave joints with defects along the joint. These defects were reported to be due to the absence of vertical motion of the stirred material. While the square pin and triangular pin gave another type of defect, these defects were located to be in the bottom of the weld. The first one was reported to be due to the big amount of the metal swept from the stir zone and the second one due to the insufficient heat generation. Tensile tests have been performed and the samples were machined in the perpendicular direction to the weld. The fracture was located to be along the defect in the joints and on the advancing side of the thermomecanically affected zone for the sound weld that is obvious. The authors concluded that in their study, the threaded cylindrical pin produces a defect free joint, and the selection of the tool pin profile has a crucial effect on the joint quality.

Tools pin profile	Weld cross-section showing defect locations AS RS	Probable reasons for defect	Location of failure during tensile test
Straight cylindrical		The absence of vertical motion of the material	Along the defect
Taper cylindrical		The absence of vertical motion of the material	Along the defect
Threaded cylindrical		Defect free	In the advancing side of TMAZ
Square		A large amount of metal sweeps from the stir zone	Along the defect
Triangular		Insufficient heat generation	Along the defect

Table I.5. Effect of tool pin profiles on macrographs of stir zone. (Padmanaban and Balasubramanian, 2009)

I.10.2.3 Effect of tool shoulder diameter on FSW of AZ31

In order to investigate the impact of the tool shoulder diameter on the joint properties, some FSW welds have been established by (Padmanaban and Balasubramanian, 2009) using three tool shoulder diameters including 15, 18 and 21 mm. Table I.6 presents the mechanical and microstructural properties of 6 mm thick plates AZ31B joints produced using FSW with different tool shoulder diameters. It can be observed that the ultimate tensile strength reached its maximal value using 18 mm tool shoulder diameter. Also, higher elongation has been obtained.The authors reported that the highest joint efficiency corresponds to the 18 mm shoulder diameter is, i.e. when the ratio of shoulder diameter to pin diameter is 3 mm. Also, the optimum joint was observed to have the higher stir zone microhardness and the lowest stir zone grain diameter, due to the optimum heat input.

Effect of tool shoulder diameters on joint properties.

Shoulder diameter (mm)	D/d	Yield strength (MPa)	Ultimate tensile strength (MPa)	Elongation in 50 mm gauge length (%)	Reduction in cross-sectional area (%)	Joint efficiency (%)	Stir zone hardness (Hv)	Stir zone grain diameter (μm)
15	2.5	94	117	2.5	4.1	54.4	71	12.3
18	3.0	166	205	7.3	5.5	95.2	75	6.2
21	3.5	163	197	6.0	5.2	91.4	72	9.6

Table I.6. Effect of tool shoulder diameter on joint properties. (Padmanaban and Balasubramanian, 2009)

The microstructure of AZ31B produced by FSW with different tool shoulder diameter is presented in Table I.7. Indeed, the tool with shoulder diameter of 18 mm gave a defect free joints. While the tool with 15 mm diameter shoulder gave a defect along the stir zone, probably due to the insufficient heat generation, that explain the bigger average grain size obtained in Table I.6. On the other hand, the 21 mm tool shoulder diameter gave a defect on the advancing side along the joint, this defect was created probably due to the excessive heat generation. The tensile tested samples failed in the thermo-mechanically affected zone on the advancing side for the defect-free joints. This might be due to the changes in texture between the SZ and TMAZ, making it a stress concentration site and a failure site. On the other hand, the failure was along the defect for the two other joints, because a defect is the weakest area where a damage can occur, compared to the other regions of the weld.

Tool diameter (mm)	Weld cross-section showing defect locations AS RS	Probable reasons for defect	Location of failure during tensile test
15		Insufficient heat generation	Along the defect
18		Defect free	In the advancing side of TMAZ
21		Excessive heat generation	Along the defect

Table I.7. Effect of tool shoulder diameter on macrographs of stir zone. (Padmanaban and Balasubramanian, 2009)

The authors concluded that increasing the shoulder diameter leads to excessive heat generation and results in hot defect, while reducing the heat input leads to insufficient heat generation resulting in a cold defect.

I.10.2.4 Effect of tool material on joint properties

In order to investigate the effect of the tool material on the joint properties of AZ31B magnesium alloy, (Padmanaban and Balasubramanian, 2009) selected five different tool materials to fabricate FSW tools, and welded AZ31B magnesium sheets, the chemical composition of tool material has an influence on the joint properties, the chemical composition of the tools are presented in Table I.8.

Chemical composition and hardness of tool materials.

Tool materials	C	Si	Mn	Cr	P	S	Mo	Ni	V	W	Fe	Hardness (HRC)
MS	0.20	0.3	–	–	0.04	0.05	–	–	–	–	Bal.	30
SS	0.06	0.32	1.38	18.4	0.4	0.28	–	8.17	–	–	Bal.	40
AS	0.315	0.239	0.53	1.29	0.018	0.009	0.451	1.54	–	–	Bal.	58
HCS	0.75	0.25	0.32	–	–	–	–	–	–	–	Bal.	66
HSS	0.86	0.45	0.40	3.80	0..03	0.03	4.70	–	1.70	6.00	Bal.	73

MS – mild steel; SS – stainless steel; AS – armour steel; HCS – high carbon steel; HSS – high speed steel.

Table I.8. Chemical composition and hardness of tool materials. (Padmanaban and Balasubramanian, 2009)

The tool material has a significant effect on the mechanical properties of the weld joints, (Padmanaban and Balasubramanian, 2009) used FSW to join AZ31B magnesium alloy sheets using different tools with chemical compositions presented previously in Table I.8. The mechanical properties of the obtained welds are presented in Table I.9. Indeed, high carbon steel gave the best mechanical properties of the joint with a high joint efficiency of 96%. It was also noted that the stir zone hardness was higher than that obtained for the other welds with a value of 77 HV, and a lower stir zone average grain size diameter of 6.3 µm. Also, the elongation was higher and the reduction in the cross-sectional area was higher. These results can be referred to the fact that less heat input was induced into the joint, and thereby, lower grains size diameter resulted, and more elongation and higher reduction in the cross-sectional area was obtained due to the fact that the grain boundaries act as a barrier to prevent the deformation, so the lower grain size the more formability and elongation of the material resulted.

Effect of tool materials on joint properties.

Tool material	Yield strength (MPa)	Ultimate tensile strength (MPa)	Elongation in 50 mm gauge length (%)	Reduction in cross-sectional area (%)	Joint efficiency (%)	Stir zone hardness (Hv)	Stir zone grain diameter (µm)
MS	130	162	5.0	5.1	75.5	72	10.2
SS	128	160	3.5	4.8	74.5	73	10.7
AS	127	159	3.0	4.3	74.1	73	11.3
HCS	166	207	7.3	5.5	96.3	77	6.3
HSS	142	178	4.0	4.8	82.5	75	9.1

Table I.9. Effect of tool materials on joint properties. (Padmanaban and Balasubramanian, 2009)

To investigate the mechanical properties results listed in Table I.9, the cross-sectional area of these welds were analyzed, and the microstructure obtained for these welds are showed in Table I.10. It can be observed that the MS, SS, and AS resulted in a root defect along the cross section of the weld joints while defect free joints were obtained using HCS and HSS. The authors reported that the location of failure during tensile tests for the joints with a defect was along the defect itself while it was on the advancing side of the TMAZ, leading to conclude that the selection of the tool material has a crucial effect on the mechanical and microstructural properties of the AZ31 welded joints. And the inappropriate selection of such parameters can result in defects that reduce the joint quality.

Table I.10. Effect of tool materials on macrographs of stir zone. (Padmanaban and Balasubramanian, 2009)

Table I.11 summarize some works that have been done on FSW and FSSW of AZ31 magnesium alloy sheets with different tool parameters, including the tool material, tool shape and size, and operating parameters, followed by some observations concerning the mechanical properties of the weld. The combination of each tool parameters and operation parameters can enhance the joint properties in the mechanical, or microstructural point of view since they're related to reaching other (microstructural and mechanical properties).

Workpiece material	Tool material	Tool shape and size	Operating parameters	Remarks	references
AZ31 Mg, 1.5 mm thick	H13 steel	SD: 10 mm; PD: 4 mm; PL: 1.8 mm; PS: SCT, 3F with M4 threads	1000-3000 rpm; dwell time: 1, 4 s; plunge rate: 0-10 mm/sec; FSSW		(Sun et al., 2009)
AZ31 Mg, 1.5 mm	H13 steel, 46-48 HRC	SD: 10 mm; PD: 4 mm; PL: 1.8 mm; PS: SCT, and threaded and unthreaded 3F	1000-3000 rpm; dwell time: 1 s; plunge rate: 2.5 mm/sec; FSSW	Welds with 3F/threaded superior to those with SCT	(Yin et al., 2010)
AZ31B-H24 Mg, 2 mm		PD: 3.175 mm; PL: 1.65 mm; PS: SC:, LHT, RHT	1000-2000 rpm; 300-1800 mm/min	Joint efficiency: 74-83%	(Chowdhury et al., 2010)
AZ31B Mg, 6 mm	Mild steel, stainless steel, armor steel, high carbon steel, high-speed steel	SD: 15, 18, 21 mm; PS: SC, TC, SCT, triangular and square; PL: 5.7 mm; PD: 6 mm	1600 rpm, 40 mm/min, 0° tilt	Joint efficiency: 40.8-96.7 %	(Padmanaban and Balasubramanian, 2009)
AZ31B-H24 Mg, 2 mm	H13 steel	SD: 19 mm; PL: 2–3.5 mm; PD: 6.35 mm	500-2000 rpm; 1200 mm/min	Joint efficiency: up to 62%	(Cao and Jahazi, 2011)
AZ31-O Mg, 2 mm		SD: 10-13 mm;	1000 rpm; 200 mm/min Applied force F 6.5-6.8 kN		(Commin et al., 2012)

*SD: shoulder diameter; PD: pin diameter; PL: pin length; PS: pin shape; SC: straight circular; TC: tapered circular; SCT: straight circular threaded; LHT (RHT): left (right) handed thread; 3F: three flats; FSSW: friction stir spot welding. Joint efficiency is the ratio of the tensile strength of the joint to that of the base metal.

Table I.11. Tool materials, geometries and welding variables used for FSW and FSSW of several magnesium alloys. (Rai et al., 2011)

I.10.3 Metallurgy of Aluminum/Magnesium system

Aluminum alloys and magnesium alloys have nearly the same melting temperature, i.e. 660°C for aluminum alloy and 650°C for the magnesium alloy. If successfully welded, intermetallic compounds are observed at the joint interface.

According to the Al-Mg phase diagram shown in Figure I.38 (ASM, 1992), intermetallic compounds such Al_3Mg_2 and $Al_{12}Mg_{17}$ can form when an Al-Mg system is brought to elevated temperatures. Upon heating, the eutectic reactions $Mg + Al_{12}Mg_{17} \rightarrow L$ and $Al + Al_3Mg_2 \rightarrow L$ occur at the eutectic temperatures of 437°C and 450°C, respectively. At room temperature, Al_3Mg_2 contains about 37wt-% Mg and $Al_{12}Mg_{17}$ about 57wt-% Mg. The eutectic temperatures are below the melting point of either Al or Mg and they can be reached easily during Al-to-Mg FSW to form liquid films at the interface between Al and Mg. Upon cooling, the two eutectic reactions are reversed, and Al_3Mg_2 and $Al_{12}Mg_{17}$ are formed from the liquid (Firouzdor and Kou, 2009).
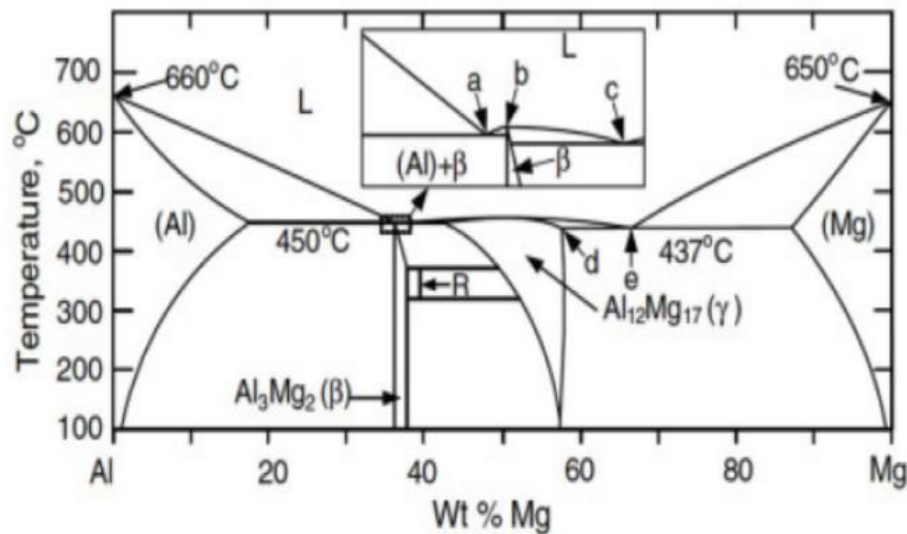
Figure I.38. Al-Mg phase diagram explaining liquid formation in Al/Mg FSW. (ASM, 1992)

I.11 Dissimilar Friction Stir Welding

Weight reduction can considerably improve fuel efficiency and reduce harmful CO_2 emissions by using lightweight metal alloys such as magnesium (Mg), aluminum (Al) and titanium (Ti) alloys in automotive vehicles. One principal objective is to improve reliable inhomogeneous metal joining technologies to endorse the production and integration of mechanical parts made from lightweight substitute metal alloys. Since recently, several studies focused on enhancing the FSW bimetallic joining process, such as Al-to-Steel (Bozzi et al., 2008; Kimapong and Watanabe, 2005; Liyanage et al., 2009; Springer et al., 2011; Tanaka et al., 2009; Watanabe et al., 2006); Mg-to-Steel (Liyanage et al., 2009); Al-to-Cu (Liu et al., 2011; Liu et al., 2008; Ouyang et al., 2006), and Al-to-Mg.

Joining lightweight metals such as Mg alloys to Al alloys presents a big challenge mainly due to the difference in the crystal lattice structure, aluminum has an FCC structure and magnesium alloy having an HCP crystal structures, and the difference in density (2.71 g/cm^3 for the aluminum alloy, and 1.74 g/cm^3 for the magnesium alloy). The resulting formation of various types of intermetallic compounds (IMC) in the weld zone undermines the weld integrity. Also, controllability of the distribution, size and type of the brittle IMCs are difficult, and their presence has a detrimental effect on the weld strength. Furthermore, the difference in mechanical, chemical and thermal properties of the materials to weld make the dissimilar friction stir welding a more challenging problems compered to the homogeneous FSW.

In dissimilar friction stir welding, the placement of the base materials in the advancing or retereating side affects the quality of the joint. Some authors (McLean et al., 2003) (Watanabe et al., 2006) reported that harder material or material with the highest melting point should be placed on the advancing side, since it helps to reduce the tool wear and provides an optimal heat input during the welding process, resulting in defect-free joints with higher mechanical properties. For example, the metallographic aspect of two welds' cross-section obtained by placing the base materials in different positions is shown in Figure I.39, it is clearly shown that material positioning has a crucial influence on the weld's metallographic aspect (Firouzdor and Kou, 2010a).
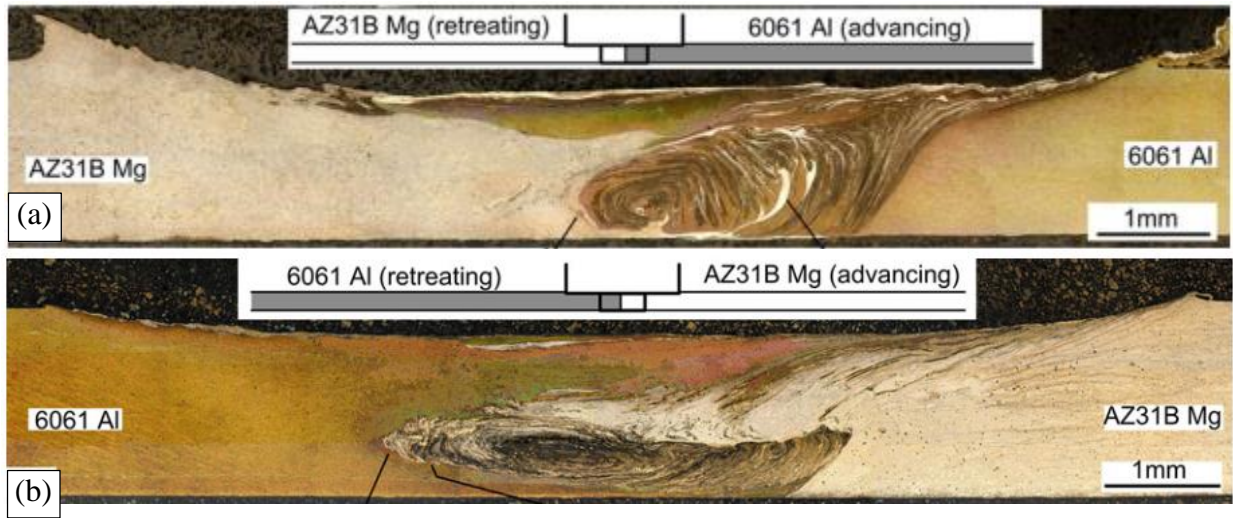
Figure I.39. Transverse cross section of a butt weld made at 38 mm/min and 1400 rpm with (a) Al 6061 on the advancing side without tool offset, (b): AZ31B on the advance side without tool offset. (Firouzdor and Kou, 2010a)

Also, Figure I.40 presents the joint strength of Al/Mg dissimilar FSW joints under various tool advance speeds by putting aluminum alloy on both the advancing and the retreating side. The figure shows that the tool advance speed has a higher effect on the joint strength with magnesium than with aluminum on the advancing side. At lower tool feed rate, putting magnesium alloy on the advancing side gives a greater joint strength, that decreases with increasing the tool advance speed. But when placing aluminum on the advancing side, the joint strength does not always increase with increasing the tool advance speed, and the optimum joint strength is obtained at a specific welding parameter (in this case at 250 mm/min) (Firouzdor and Kou, 2010a).
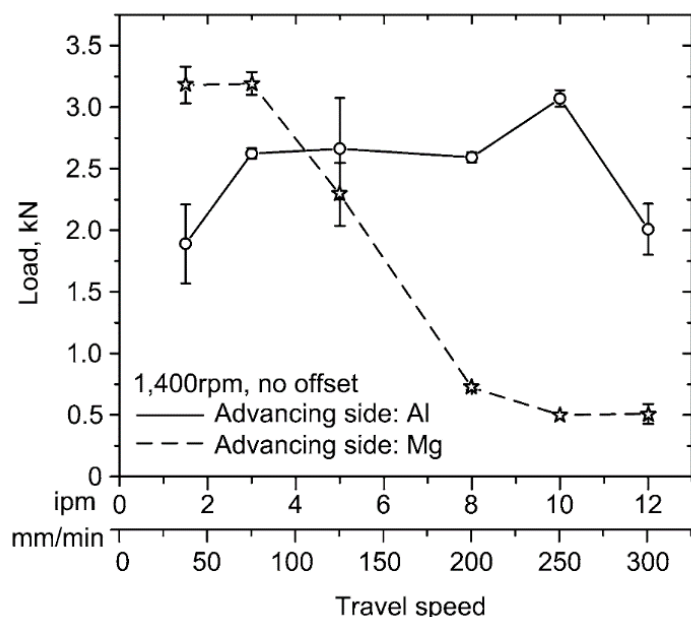
Figure I.40. Effect of travel speed and material position on join strength in FSW of Al/Mg under constant tool rotation speed of 1400 rpm. (Firouzdor and Kou, 2010a)

Other investigation were conducted on dissimilar Al/Mg FSW, (Sato et al., 2004) investigated the microstructure evolution during a heterogeneous FSW of aluminum and magnesium alloys. The authors used 6 mm thick Al 1050 and Mg AZ31 alloys as parent metals. Al 1050 alloy was placed on the retreating side at a constant tool rotation speed of 2450 rpm and a displacement speed of 90 mm/min with a 3° tilt angle. The authors analyzed the weld transverse cross-section and reported that the $Al_{12}Mg_{17}$ intermetallic phases resulted from a constitutional liquation during the heterogeneous welding causing higher hardness in the weld zone.

(McLean et al., 2003) friction stir welded 5083 aluminum alloy with AZ31 magnesium alloy by varying the tool displacement speed between 60 mm/min and 100 mm/min, and the tool rotation speed between 300 rpm and 400 rpm. The authors have reported the existence of $Mg_{17}Al_{12}$ at the interface between AZ31B and AA5083 in the dissimilar FSW butt joints. They claimed that intermetallic formation at the interface occurred by the solid-state transformation, and the formation of that thin intermetallic layer resulted in welds that exhibited virtually no ductility. Figure I.41 presents an optical micrograph of a welded joint, before and after bend test,

showing that the cracks propagated in the interface between the intermetallic compounds and the aluminum part, as it is the weakest part of the weld (McLean et al., 2003).
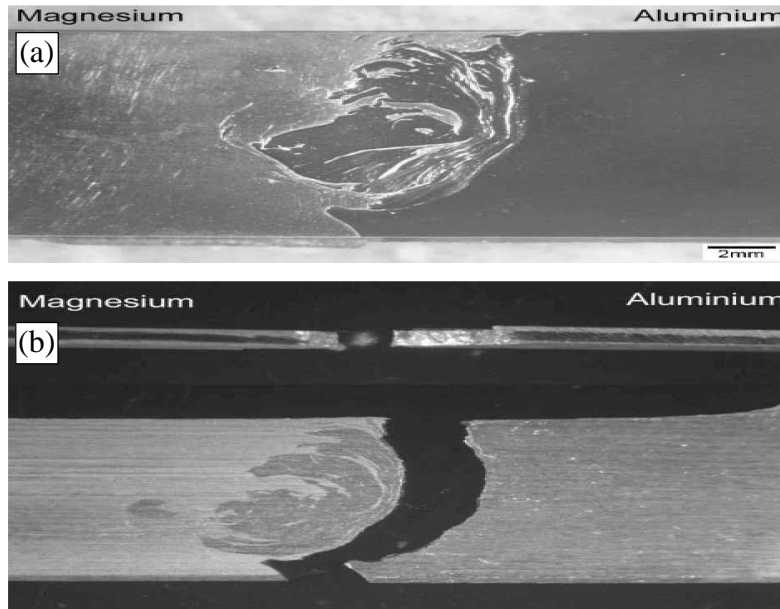
Figure I.41. Optical macrograph of welded region, (a) before fracture and (b) after bend test. (McLean et al., 2003)

(Mofid et al., 2012a) have friction stir welded, and submerged friction stir welded 3 mm thick Al 5083 alloy to AZ31C–O Mg alloy at a rotation speed of 300 rpm and travel speed of 50 mm/min. The authors measured the temperature using four K-type thermocouples that were embedded in the workpiece. The tool made of H13 steel was rotating in the counterclockwise direction with a tilt angle of 3° forward, by placing the Mg AZ31C–O alloy in the retreating side. The authors reduced the heat input by submerging the workpieces in water during the process. The authors reported that the aluminum alloy have a greater hardness and strength at elevated temperatures compared to Mg alloy, leading to a larger flow resistance. It is well evidenced from the room temperature hardness values, i.e., 105 HMV for Al 5083-T6 and 70 HMV for AZ31C–O. Figure I.42 presents Vickers microhardness map and profile measured at different cross section lines, some peaks in the hardness values are observed in the stir zone. These values are much greater than those for the recrystallized Al alloy and Mg alloy, and greater than the Al alloy base metal in some cases, due to the presence of the intermetallic compounds, as they're brittle and harder than the base materials of the weld (Mofid et al., 2012a). The same authors also

reported that in order to make good quality dissimilar joints with higher mechanical and metallurgical properties, aluminum alloy must be placed on the advancing side of the dissimilar FSW of Al and Mg alloy.
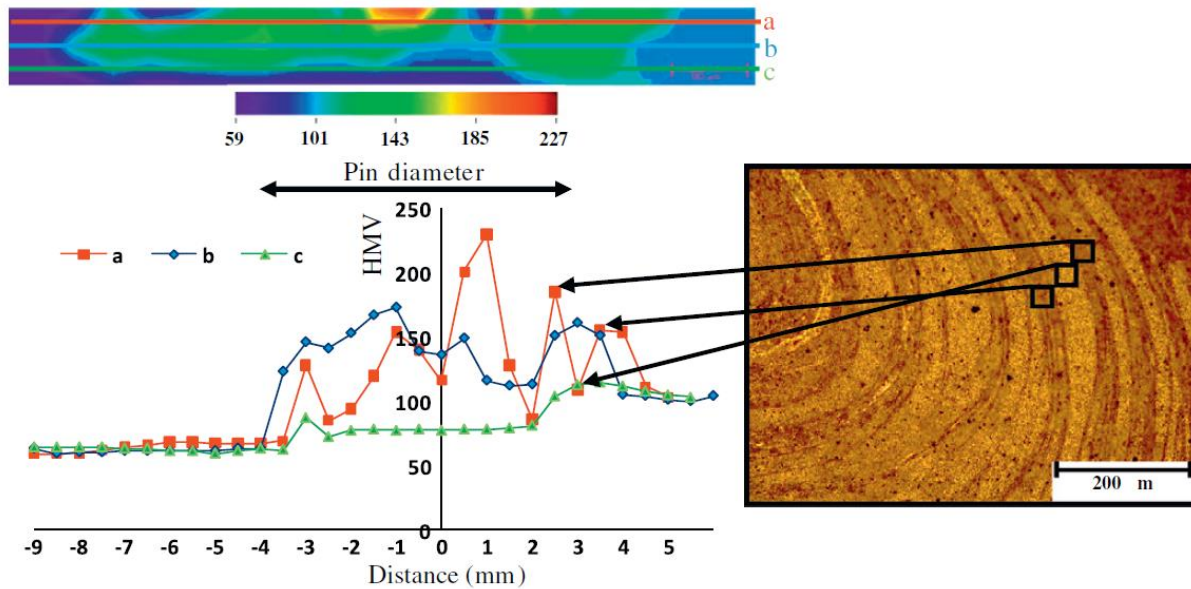
Figure I.42. Vickers microhardness (HMV) map and profile measured (a) 0.5 mm above the mid-thickness, (b) mid thickness and (c) 0.5 mm below the mid-thickness for the weld performed in air. (Mofid et al., 2012a)

Table I.12 summarizes other dissimilar friction stir welding of aluminum alloys with AZ31B magnesium alloy, with varied welding parameters, along with the weldability of the joint either by material positioning or by the tool offsetting (Firouzdor and Kou, 2009).

Ref.	Al alloy	Advancing side	Tool offset	Rotation (rpm)	Translation (mm/min)
(McLean et al., 2003)	5083	Al (better), Mg	Al, Mg (better)	300-400	60-100
(Hirano et al., 2004)	1050	Unspecified	Unspecified	1500-3000	200-800
(Okamura and Aota, 2004)	1050	Mg	None	Unspecified	Unspecified
(Somasekharan and Murr, 2004a)	6061	Al, Mg	Al, Mg (better)	800	90

(Sato et al., 2004)	1050	Al, Mg (better)	None	2450	90
(Yan et al., 2005)	1060	Al	Al, Mg (better)	200-1000	19-75
(Zettler et al., 2005)	6040	Al, Mg (better)	None	1400	200-225
(Kwon et al., 2008)	5052	Al	None	800-1600	300
(Kostka et al., 2009)	6040	Al	None	1400	225
(Liu et al., 2009a)	2024	Al	none	2500	45

Table I.12. FSW of various Al Alloys to AZ31 Mg alloy. (Firouzdor and Kou, 2009)

More specifically, some studies on dissimilar FSW of Mg AZ31 alloy with Al6061 alloy are summarized in Table I.13. The tool properties, weld parameters and the outcomes from the studies have been summarized in the table.

Study	Tool properties	Weld parameters	Outcome
(Firouzdor and Kou, 2009) Al6061 (both metals on either side)	*Shoulder dia.*: 10 mm, *Pin diameter*: 4 mm, *Pin length*: 1.3 mm (Butt joint) *Pin length*: 1.5 mm (Lap joint) H13 tool steel, concave shoulder and threaded pin	**Butt joint** *Rotation* − 800 & 1400 rpm *Tool tilt* − 3° *Travel speed* − 38 mm/min. *Tool Offset* − 1.5 mm (Al & Mg) **Lap joint** *Rotation* − 800 & 1400 rpm *Tool tilt* − 3° *Travel speed* − 38 mm/min. *Tool Offset* − 1.5 mm (Al & Mg)	1. In butt welding, higher strength was observed with mg on the advancing side. 2. Tool offset towards Mg side resulted in improved joint strength.
(Firouzdor and	*Shoulder dia.*: 10 mm,	**Butt joint**	1. The average peak temperature

Kou, 2010a) Al6061-T6 (both metals on either side)	*Pin diameter*: 4 mm, *Pin length*: 1.3 mm (Butt joint) H13 tool steel, concave shoulder and threaded pin	$Rotation - 1000 - 2200$ rpm $Tool\ tilt - 3°$ $Travel\ speed - 38 - 305$ mm/min. $Tool\ Offset - 1.5$ mm (Al & Mg)	attained decreased with increasing tool travel speed. 2. Under identical welding conditions, the average peak temperature measured is higher when Al is placed on the advancing side.
(Firouzdor and Kou, 2010b) Al6061-T6 (AS for butt weld)	*Shoulder dia.*: 10 mm, *Pin diameter*: 4 mm, *Pin length*: 1.3 mm (Butt joint) H13 tool steel, concave shoulder and threaded pin	**Butt joint** $Rotation - 1400\ \&\ 2200$ rpm $Tool\ tilt - 3°$ $Travel\ speed - 38\ \&\ 254$ mm/min. $Tool\ Offset - 1.5$ mm (Al & Mg)	1. In lap welding, the IMCs observed on the Al side of the weld was identified as Al_3Mg_2 and on the Mg side, was identified as an eutectic consisting of $Al_{12}Mg_{17}$. 2. The liquid formation during the FSW process was evidenced by the presence of $Mg_{17}Al_{12}$ and Mg in the stir zones of the butt and lap welds.
	Shoulder dia.: 10 mm, *Pin diameter*: 4 mm, *Pin length*: 1.5 & 2.3 mm H13 tool steel, concave shoulder and threaded pin	**Lap joint** $Rotation - 1400\ \&\ 2200$ rpm $Tool\ tilt - 3°$ $Travel\ speed - 38\ \&\ 254$ mm/min. $Tool\ Offset - 1.5$ mm (Al & Mg)	
(Malarvizhi and Balasubramanian, 2012) AA6061 (both metals on either side)	*Shoulder dia.*: 12 - 24 mm, *Pin diameter*: 5 - 6 mm, *Pin length*: 5.7 mm (Butt joint) HSS tool material,	**Butt joint** $Rotation - 400$ rpm $Tool\ tilt - 0°$ $Travel\ speed - 19.8$ mm/min. $Axial\ force - 12$ kN	1. Effect of tool shoulder diameter on the weld properties is studied. 2. Joint prepared with 21 mm shoulder diameter showed 192 MPa tensile strength and 89% joint efficiency in comparison to

	tapered pin		Mg alloy.
(Fu et al., 2015) 6061-T6 (both metals on either side)	*Shoulder dia.*: 10 mm, *Pin diameter*: 3.2 mm, *Pin length*: 2.8 mm (Butt joint) H13 tool steel, concave shoulder and frustum-shaped right-hand threaded pin.	**Butt joint** *Rotation* -500 - 1000 rpm *Tool tilt* $- 3°$ *Travel speed* $-$ 30 - 80 mm/min. *Tool Offset* $- 0 - 0.6$ mm *Plunge depth* $- 0.12$ mm	1. Mg on the AS resulted in higher tensile strength (140 MPa), than Al on the AS, at a tool offset of 0.3 mm. 2. The highest tensile strength (175 MPa) was observed for 700 rpm, 50 mm/min, Mg on AS and tool offsetted to 0.3 mm towards Mg.
(Masoudian et al., 2014b) Al6061 (AS)	*Shoulder dia.*: 15 mm, *Pin diameter*: 3 mm, *Pin length*: 2.9 mm (Butt joint) H13 tool steel, concave shoulder	**Butt joint** *Rotation* -600 - 1400 rpm *Tool tilt* $- 2.5°$ *Travel speed* $-$ 20 - 60 mm/min. *Tool Offset* $- 0 - 0.6$ mm	1. Defect free weld was attained for a tool rotational speed of 1000 rpm/min and translational speed of 40 mm/min, for the used tool geometry. 2. Tensile strength of the welded joint was 76% and 60% of Mg AZ31 and Al6061 alloys, respectively.
(Lee and Kwon, 2014) Al6061 – T6 (RS)	SKD61 tool steel, concave shoulder and truncated cone type pin, coated with AlTiN	**Butt joint** *Rotation* $-$ 1200 rpm *Tool tilt* $- 2°$ *Travel speed* $- 20 - 101.6$ mm/min. *Tool Offset* $-$ 0.1 mm (towards Mg)	1. Average grain size of 2.5 and 4.5 µm was observed on the Al and Mg stir zones, respectively. This is very small in comparison to 28 and 15 µm observed on the corresponding BM. 2. The interface microstructure comprised of lamellar like shear bands rich in Al or Mg.
(Somasekharan and	*Shoulder dia.*: 19 mm,	*Rotation* -800 rpm	1. Approximately three times the

Murr, 2004b)	*Pin diameter*: 5 mm,	*Travel speed* – 90 mm/min. *Tool Offset* – 75% tool towards AS. Double sided weld.	Vickers Hardness is observed in the stir zone, which is attributed to the complex vortexes and lamellar structure found in the SZ. 2. Dynamic recrystallization was observed in the weld zone and the transition zone which resulted in reduced grain size in the SZ in comparison to the BM.

Table I.13. Summary of existing literature studies on dissimilar FSW on Al6061-AZ31 alloys.

Chapter II.   Mechanical and Microstructural Characterization of Al 6061-T6 and AZ31B alloys

In chapter two, Al 6061-T6 and AZ 31B alloys have been characterized. The microstructure of the base material has been obtained, and the average grain size measurements have been calculated for the base material and the heat treated samples. Tensile testing at different temperatures (25, 100, 200 and 300 °C) under constant strain rates (10^{-4}, 10^{-3}, 10^{-2} and 10^{-1} s^{-1}) have been conducted. The damage mechanisms during deformation at different temperatures and strain rates have been investigated by means of interrupted tests and by analyzing the fracture surface of Al 6061-T6 failed specimens.

Summary

II.1 Mechanical and microstructural characterization of Al 6061-T6 alloy

Introduction

Aluminum alloys are corrosion resistant and lightweight materials, and they exhibit a medium level of strength and a modest degree of formability. Some different aluminum alloys have been developed to date for use in a wide variety of applications. These alloys are referred to as a series of numbers ranging from 1XXX to 9XXX depending on their alloying elements. Each Al alloy series has its own range of properties such as mechanical, corrosion and thermal properties.

In this chapter, we studied the commercial 6061 (or 61S) aluminum alloy. It is an age-hardened aluminum alloy that was developed in 1935 to satisfy the need in medium-strength aluminum with high toughness and weldability (Edwards et al., 1994; Sanders, 2001), that will be used in Chapter III. The aluminum 6061 exists in different tempering conditions such as O, T4, and T6. The 6061 Al alloy is commonly used in automotive industry for the production of several types of automobile parts such as wheels, panels and in the vehicle structure, aircraft & aerospace industries as part of aircraft structure like wings and fuselages; in the watercraft especially for flat bottom river and lake boats due to its light weight, high strength and corrosion resistance even when exposed to salt water (Agarwal et al., 2003).

Recently, few studies investigating the mechanical and the microstructural behavior of 6061-T6 aluminum alloy have been conducted. (Ghahremaninezhad and Ravi-Chandar, 2012) studied the ductile failure behavior of a 6061 Al alloy at room temperature by performing tensile tests, interrupted flat-notched tests and by observing the evolution of the microstructure at different stages of deformation. The authors concluded that in Al 6061-T6, nucleation of the damage appears when the plastic strain levels are about 1.0 and that the damage initiates in the form of particle fracture or decohesion at the interfaces. (Tucker et al., 2010) studied the effect of changing strain rates and stress states on the plasticity, damage, and fracture of extruded Al 6061-T6 and two other materials. The authors have observed that under tension, the damage in Al 6061- T6 initiates from two sources, (i) micron-scale particles and (ii) nano-scale precipitates inducing a strain sensitive damage that decrease with increasing strain rate. Moreover, the impact response of Al 6061-T6 at different strain rates was investigated by (Lee et al., 1999). The authors concluded that strain rates influence the work hardening rate and activation volume.

Furthermore, (Manes et al., 2011), through a combined numerical and experimental technique, studied the strain rate effect on the behavior of Al 6061-T6 and reported a significant increase in the strain rate effect under strain rates above 10^3 s^{-1}. The flow behavior of Al6061 in T6 and OA temper, under strain rates ranging from 10^{-2} to 10^5 s^{-1} was investigated by (Tang et al., 2011). They concluded that the precipitation hardened Al 6061-T6 has greater yield and flow strength than Al6061-OA. Besides, (Bahrami et al., 2013) studied the work-hardening behavior of 6061 aluminum alloy, aged at different temperatures to different duration and concluded that the dynamic recovery rates and work-hardening are lower for under-aged material than for over-aged material. They verified these results by an extended Kinetic Model Editor (KME) modeling approach through a comparison between experimental stress-strain curves and the simulation results.

A number of recent articles studied the mechanical properties and microstructural evolution of Al 6061 alloy processed by different processing techniques, namely; rolling, ECAP, forging friction stir processing and welding, and other welding technics (Ambriz et al., 2009, 2010; Chang et al., 2003; Fu et al., 2009; Kim et al., 2005; Masoudian et al., 2014a; Nageswara rao and Jayaganthan, 2012; Ozturk et al., 2010; Rao et al., 2014; Shankar et al., 2005; Tan et al., 2011; Vargas et al., 2013; Venukumar et al., 2013).

The understanding of the deformation and damage mechanisms active at elevated temperatures is important not only from a scientific viewpoint but also for the practical applications of this alloy. In this chapter, the mechanical behavior and microstructure evolution of 6061-T6 aluminum alloy that will be used in the next chapter for FSW, under various strain rates and temperature conditions have been studied. The damage mechanisms active during deformation are investigated by performing interrupted tensile tests and by analyzing resulting fracture surfaces.

II.1.1 Material, Procedure and Experimental Setup

The 6061 T6 aluminum alloy is an age-hardenable alloy. The hardening of the material, during aging, results from the dissolution, growth or coarsening of Si- and Mg-rich precipitates (Dutta and Allen, 1991; Edwards et al., 1994; Ravi and Wolverton, 2004). The mechanical properties of the 6061 Al depend on the maximum aging temperature and the heating rate that induces microstructural changes (Maisonnette et al., 2011). The T6 aging refers to the material

heat-treated at 160°C for 18 hours and then air cooled, or the materials heated at 177°C for 8 hours and then air cooled. In addition to Si and Mg alloying elements, transition metals may and certain impurities (Fe and Mn) lead to the formation of new phase components. During casting of 6xxx alloys, among the aluminum dendrites, a variety of Fe- intermetallic phases Al-Fe, Al-Fe-Si, and Al-Fe-Mn-Si are formed. It has been reported that in the absence of chromium or manganese, the iron-rich phases are β-$Fe_2Si_2Al_9$ or α-Fe_3SiAl_{12} or a mixture of both. However, in the presence of manganese and chromium which stabilize $(Fe, Mn, Cr)_3SiAl_{12}$, the iron-rich phase will be formed into α-$(Fe, Mn)_3SiAl_{12}$ or α-$(Fe, Cr)_3SiAl_{12}$ (Hatch et al., 1984; Nowotnik et al., 2007). In our investigation, commercial Al 6061-T6 rolled sheets with 3 mm thickness supplied by McMaster Inc. was studied. The nominal chemical composition of this alloy is provided in Table II.1.

Wt. %	Al	Mg	Si	Cu	Cr	Fe	Zn	Mn	Ti	Other each	Other, total
Min	95.8	0.8	0.4	0.15	0.04	-	-	-	-	-	-
Max	98.6	1.2	0.8	0.4	0.35	0.7	0.25	0.15	0.15	0.05	0.15

Table II.1. The chemical composition of Al6061. ASTM. B308/B308M–02

To investigate the microstructure, samples were prepared according to the standard metallographic preparation (as shown in Figure II.1). We first start by cutting the sample into 10 mm^2 square pieces and mounting it in a phenolic hot working resin powder, by using a "TechPress 2™" hydraulic-pneumatic automatic mounting press. The mounted specimens are then ground using silicon carbide abrasive paper. Here we used the 320, 600 and 1200 grits abrasive papers in consecutive steps while rotating the specimens of 90° between each step and water was used as a lubricant. Finally, polishing was performed using 1µm diamond polycrystalline suspension, followed by 0.04 µm colloidal suspension on Spec-Cloth by contra-rotating the sample until a clear, haze-free mirror surface was obtained while BlueLube was used as a lubricant. Excessive force was avoided during the grinding and polishing steps to prevent the polishing compound from embedding into the aluminum matrix (Ghahremaninezhad and Ravi-Chandar, 2012). Once the metallographic preparation is completed, etching is performed using Weck's reagent (4% potassium permanganate ($KMnO_4$) and 1% sodium hydroxide (NaOH) in

distilled water). The specimen is immersed in the etchant solution for roughly 20 seconds then cleaned with water, then alcohol. The etchant is innocuous from a chemical point of view as it does not attack the intermetallic phases and the precipitates (Zwieg, 2004). The microstructure is observed using a Zeiss AxioVert 40 MAT optical light microscope equipped with an ERc5s camera connected to a computer.
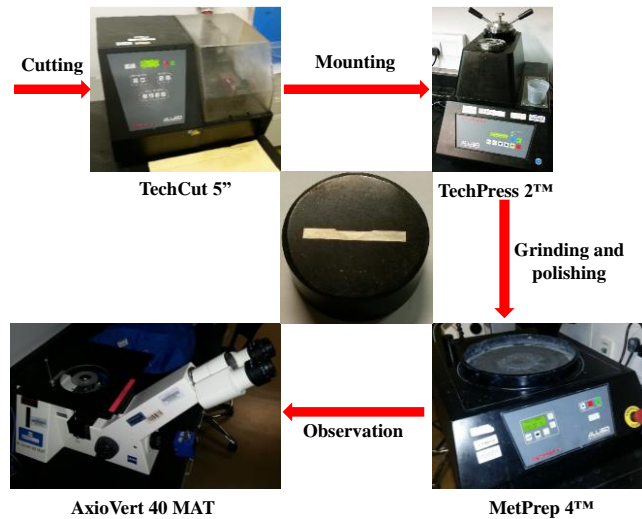
Figure II.1. Metallographic preparation equipment and procedure.

Figure II.2 presents an FEI Quanta 400 scanning electron microscope, this equipment has been used to take the SEM pictures, including microstructures and fractographs, also to measure the amount of the alloying elements present in the material alloy.

Figure II.2. SEM equipment

Tensile testing was performed using a computer controlled MTS Insight electromechanical testing machine with a 30 KN load cell equipped with an environmental chamber of type LBO-series Thermocraft LabTemp laboratory oven (see Figure II.3). The uniaxial tensile testing samples were prepared using a CNC machine, the samples were cut with their major axis parallel to the sheet rolling direction, and the geometry of the specimen is presented in Figure II.4. The geometry of the specimen is selected according to the ASTM E2448 - 11 (standard for superplastic tensile testing (Rodriguez et al., 2013)).

Figure II.3. Tensile testing material settings

The mechanical behavior of Al 6061-T6 has been studied by performing tensile tests at different temperatures ranging from room temperature to 300°C under strain rates of $10^{-4}s^{-1}$, 10^{-3} s^{-1}, 10^{-2} s^{-1}, and 10^{-1} s^{-1}. In order to perform tests at homogenized temperature, the samples were kept in the environmental chamber for 30 minutes before starting the test and when the test stopped the samples were directly water quenched to preserve the microstructure. All loading conditions were repeated at least twice to verify the reproducibility of the results.

To examine the microstructure evolution with temperature, annealing tests were conducted on the Al 6061-T6. The specimens were cut into 10 mm^2 pieces, then, placed in a Thermo-Scientific furnace for different treatment conditions.
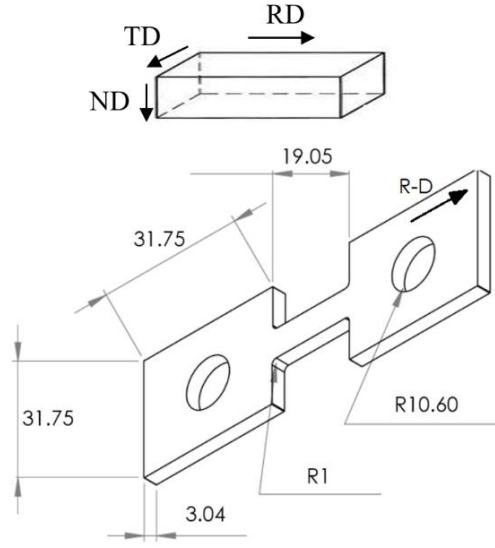
Figure II.4. Tensile test specimen geometry.

II.1.2 Mechanical testing

The 6061-T6 aluminum alloy used in this study is a polycrystalline metal, with a face cubic centered (F.C.C) crystal unit cell. The deformation of each of its crystals occurs by slipping which is defined to be the process by which a dislocation motion produces plastic deformation in crystalline materials. We assume that different slip systems are active during the deformation process of Al alloys, and slipping is the main deformation mechanism that occurs to carry out the plastic deformation (Hull and Bacon, 2011). The F.C.C unit cell has twelve $\{111\}$ <110> slip systems resulting from four $\{111\}$ planes and three <110> directions (Hull and Bacon, 2011; polmear, 2006). The texture of this rolled aluminum can be approximated by a copper type orientation of $\{112\}$<111> with Euler angles values of $\varphi_1 = 90°, \emptyset = 35°$ and $\varphi_2 = 45°$ and the so called S orientation type of $\{123\}$ <634> with Euler angles of $\varphi_1 = 59°, \emptyset = 37°$ and $\varphi_2 = 63°$ (Choi and Lee, 1997; Kashihara and Inagaki, 2009).

II.1.2.1 Effect of strain rate on tensile properties

The mechanical response of Al 6061 T6 was observed to be strain rate and temperature dependent. Figure II.5 presents the stress-strain response obtained under tensile loading for different strain rates at room temperature (Figure II.5 (a)) and 300°C (Figure II.5 (b)). At room

temperature, in the strain rate range investigated in this chapter, the material did not exhibit any significant strain rate sensitivity (Figure II.5 (a)). The mechanical properties exhibited by the material under all strain rates were otherwise a good combination of strength (UTS = 374-380 MPa) and tensile ductility (approximately 20 %). At the elevated temperature of 300°C, a significantly higher strain rate effect was observed (Figure II.5 (b)), these results are consistent with earlier reports in the literature (Blaz and Evangelista, 1996). The yield strength, ultimate tensile strength, and strain-to-failure values decrease with decreasing strain rate. The yield strength decreases from 200 MPa at a strain rate of $10^{-1}s^{-1}$, to 145 MPa at a strain rate of 10^{-4} s^{-4}. For these same testing conditions, the UTS decreases from 220 MPa ($10^{-1}s^{-1}$) to 159 MPa ($10^{-4}s^{-4}$). A 20% decrease in the elongation to fracture was obtained when decreasing the strain rate from $10^{-1}s^{-1}$ to $10^{-4}s^{-1}$. In comparison to RT response, tiny strain hardening was observed, and it consistently decreased with decreasing strain rate; at $10^{-4}s^{-1}$, no strain hardening was observed in the stress-strain curve. This is likely due to the transformation of elongated iron-rich phases β-AlFeSi to rounded α-AlFeMnSi during the homogenization temperature phase (Kuijpers et al., 2005; Lassance et al., 2007; Nowotnik et al., 2007). (Lassance et al., 2007) conducted in situ SEM uniaxial tests and reported that the α- and β- phases undergo different damage mechanisms. The authors noted that as the homogenization duration is extended, the presence of α-AlFeMnSi increased accordingly, resulting in flow strength decrease.
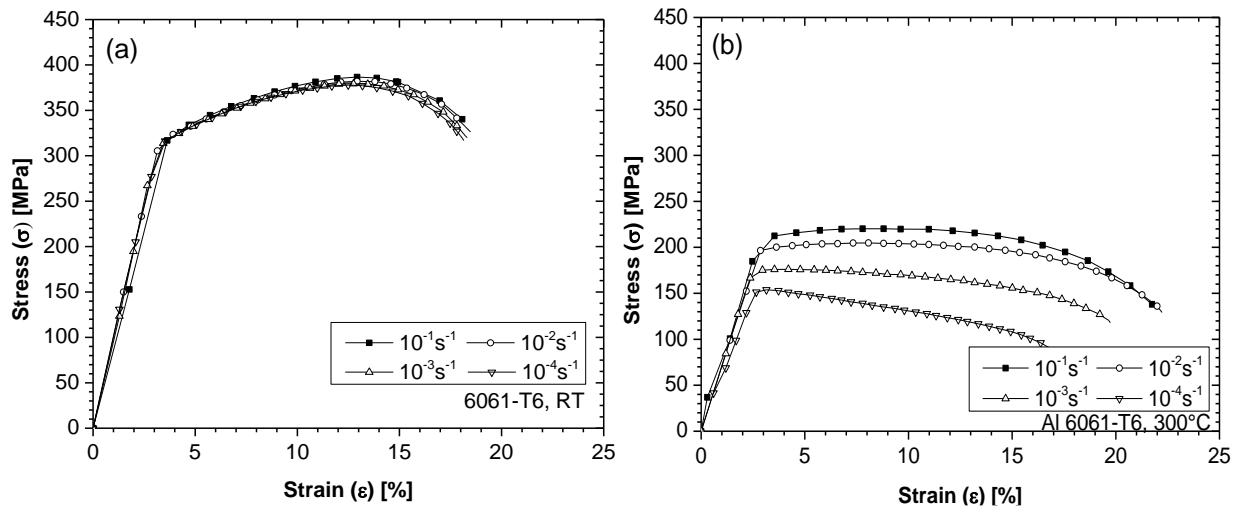
Figure II.5. Stress-Strain curves response to uniaxial loading at (a) room temperature and (b) 300°C with strain rates of 10^{-1}, 10^{-2}, 10^{-3} and 10^{-4}.

II.1.2.2 Effect of temperature on tensile properties

Figure II.6 shows the stress-strain response obtained under tensile loading for different temperatures at strain rates of (a) $10^{-1}s^{-1}$, (b) $10^{-2}s^{-1}$, (c) $10^{-3}s^{-1}$ and (d) $10^{-4}s^{-1}$. It can be clearly observed that higher temperatures lead to a decrease of the yield strength and the maximum UTS. Under a constant strain rate of $10^{-1}s^{-1}$, it can be observed that the strain to failure slightly increases with increasing the temperature; with the strain to failure reaching a value of 21% at 300°C, while at room temperature, the strain to failure value reached was 18% (Figure II.6 (a)). Furthermore, the UTS is perceived to decrease with increasing temperature, starting from a value of 386 MPa at room temperature the UTS decreases to reach a minimum value of 220 MPa at 300°C. A similar temperature sensitivity effect on the mechanical behavior was observed for tensile tests conducted at a strain rate of $10^{-2}s^{-1}$, $10^{-3}s^{-1}$ and $10^{-4}s^{-1}$ (Figure II.6 (c) and (d)); between room temperature and 200°C. However, at 300°C, it was observed that the strain to failure slightly decreases reaching a value of 20% under strain rate of $10^{-3}\,s^{-1}$ and 17% under strain rate of $10^{-4}\,s^{-1}$.
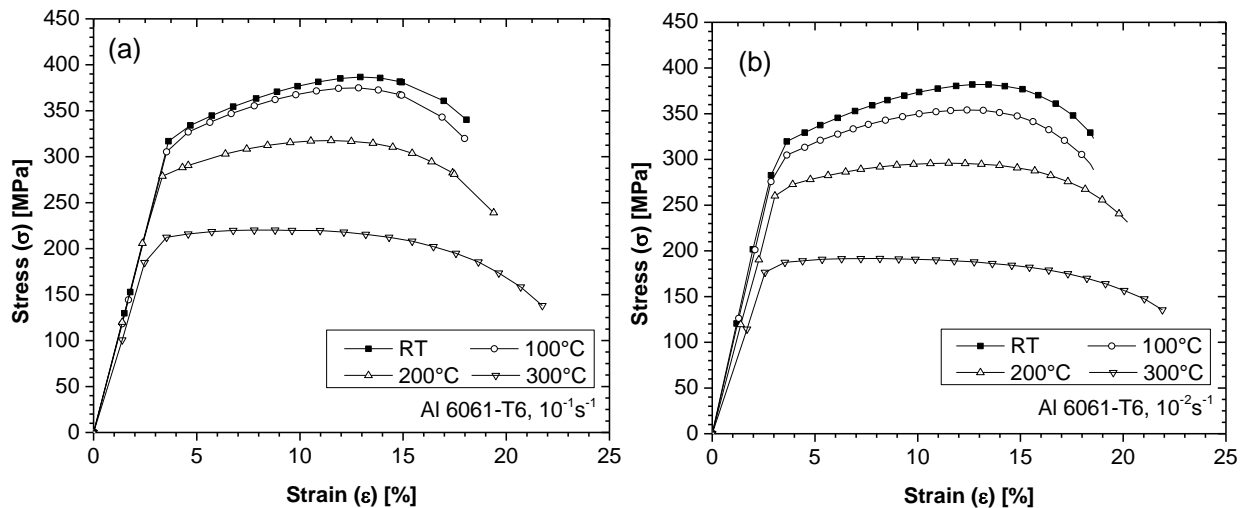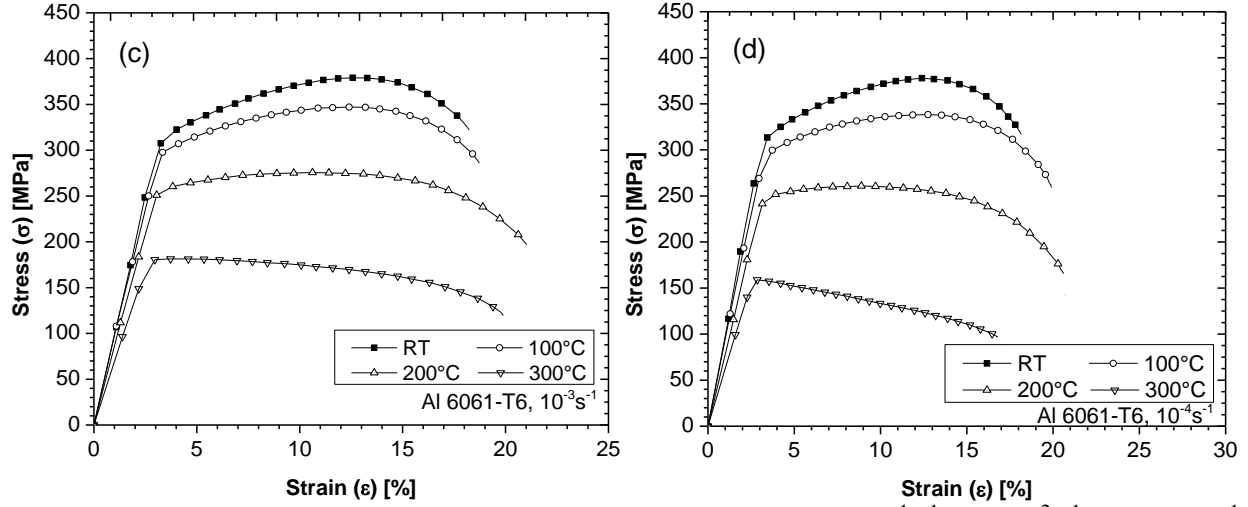
Figure II.6. Stress-strain curves response to uniaxial loading at (a) $10^{-1}s^{-1}$; (b) $10^{-2}s^{-1}$; (c): 10-3s^{-1} and (d): $10^{-4}s^{-1}$ at temperatures of 24°C, 100°C, 200°C and 300°C.

In terms of flow strength, the effect of strain rate was found to be more visible at high strain rates and much larger flow strength was observed under all temperature conditions with an increase in strain rate from 10^{-4} s^{-1} to 10^{-1} s^{-1}. The peak flow strength occurred at $10^{-1}s^{-1}$ and this is also corroborated by the strain rate sensitivity measurements discussed later in the article. On the other hand, the effect of temperature on flow strength was somewhat classical for metallic alloys and the flow strength continuously decreased with increasing temperatures. It should be noted that very high tensile elongations close to superplastic behavior have never been reported in 6061 Al alloy. Especially, under the temperature range investigated in this work, the conclusion is that although the material exhibits decrease softening in flow stress with an increase in temperature the evolution of the tensile elongations is not large.

II.1.2.3 Strain rate sensitivity

The effect of both strain rate and temperature on the yield stress of the material could be better understood by the calculation of the strain rate sensitivity parameter m given in equation II.1 (Shi and Meuleman, 1995).

$$\sigma = B\dot{\varepsilon}^m \qquad \text{II.1}$$

with σ is the stress, $\dot{\varepsilon}$ is the strain rate, $B = C^{-m}\exp(mQ/RT)$, C is a material constant, Q is the activation energy, R is the universal gas constant and T is the absolute temperature. The

strain rate sensitivity m can be calculated by plotting the natural logarithm of the yield strength in function of the natural logarithm of the strain rates (Figure II.7); m is the slope of the resultant straight line. At room temperature, the value of the strain rate sensitivity parameter is small (m =0.002) reflecting the limited strain rate effect on the mechanical behavior of the Al 6061 as shown in Figure II.5. However, the strain rate sensitivity parameter increases with increasing temperature; evolving from 0.003 at 100°C to 0.02 at 200°C and reaching 0.066 at 300°C. The strain rate sensitivity parameter points out the effect of strain rate on the strength of the materials and the ability of the material to resist plastic instability. The small value of m at room temperature indicates that the critical resolved shear stress (CRSS), indicating the resistance of the material to the plastic flow, for favorably oriented independent slip system is high and therefore, the materials mechanical response is insensitive to change in strain rate. In contrast, the higher value of m at 300°C indicates a lower resistance to plastic flow, i.e. the value of CRSS at higher temperature is lower than the CRSS value at room temperature.
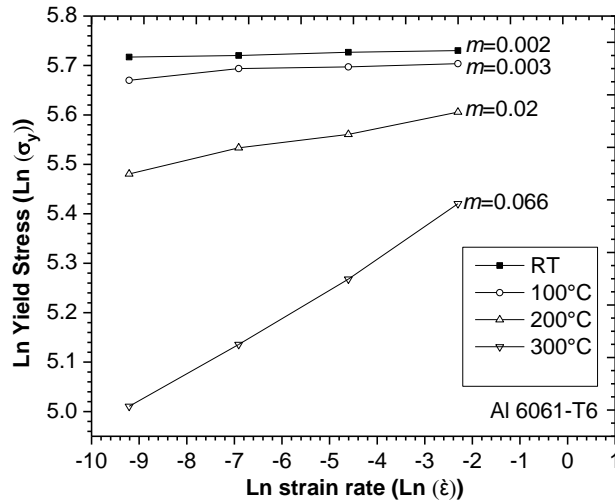
Figure II.7. Yield stress vs. strain rates at room temperature, 100°C, 200°C and 300°C.

II.1.2.4 Activation Energy

In short, the activation energy gives an insight into the deformation mechanisms occurring under given deformation conditions. The activation energy can be calculated by plotting the natural logarithm of yield strength as function of the inverse of the temperature in kelvin (K^{-1}), then multiplying the obtained average slopes by the universal gas constant R and the inverse of the average strain rate sensitivity (m^{-1}), the equation used to calculate the activation energy is the following:

$$Q_i = \frac{R}{m_i}\left(\frac{\partial \ln \sigma_y}{\partial T^{-1}}\right)$$ II.2

Two different slopes are observed in Figure II.8; it can be noticed that the activation energy increases significantly with increasing temperature. Between room temperature and 200°C, an activation energy of Q_a=52.7 kJ/mol was obtained; this value is equal to the solute diffusion energy of chrome in aluminum ($Q_{c,Cr}$=52 kJ/mol) (Chen Z., 2010) and lower than the dislocation core diffusion activation energy which is Q_c=82 kJ/mol (Balluffi, 1970).

However, between 200 and 300°C, an activation energy of Q_a= 365 kJ/mole was obtained. This value is significantly higher than that of lattice self-diffusion for pure aluminum (142 kJ/mol) (Frost and Ashby, 1982) . It seems more fitting to the activation energy for creep which is between 270 kJ/mol and 500 kJ/mol (Meyers and Chawla, 2009). It is believed that this large increase in activation energy for this alloy could partly be due to the effects of the interaction between dislocations and dispersed particles or solute atoms, and also partly a result of experimental scatter. It is, however, remarkable to note that even with such high values of activation energy which would otherwise ensure activation of grain boundary sliding leading to enhanced plastic flow did not occur in this material. The slip systems that were operative at room temperature were perhaps aided by the easy flow of dislocations but overall the precipitates present at grain boundaries and grain interior tend to be effective in suppressing dislocation motion.
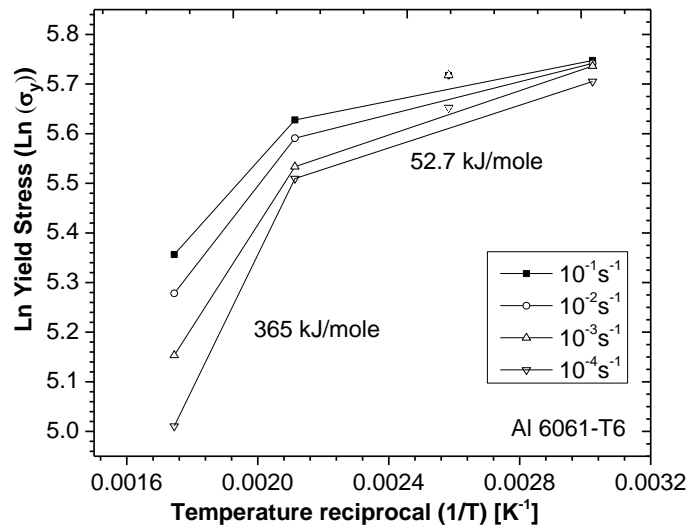
Figure II.8. Yield stress vs. temperature reciprocal for various strain rates.

II.1.3 Microstructure observation

The microstructure of the as received Al 6061-T6 is observed in two planes as showed in Figure II.9: the Rolling Direction and the Normal to the rolling Direction plane (ND-RD) and the Rolling Direction and the Transverse to the rolling Direction plane (TD-RD). Grain size analyzes are performed on microstructure taken from different zones of the specimen and then by using the grain size analysis module; AxioVision software. The grains in the ND-RD plane have elliptic shape due to rolling while they are round shaped in the TD-RD plane. The mean grain size is found to be equal to 39 μm and 25 μm in the transverse and the normal planes respectively. The iron-rich phases and the magnesium silicide particles (Mg_2Si) were clearly observed even after etching. Energy-Dispersive X-ray Spectroscopy (EDS) analysis was used to verified that the gray particles are the iron-rich phase (Fe, Mn, Cr)$_3$SiAl$_{12}$ (Figure II.9 (b)). Therefore, it can be concluded that the iron-rich phases are distributed at the grain boundaries and within the grains.
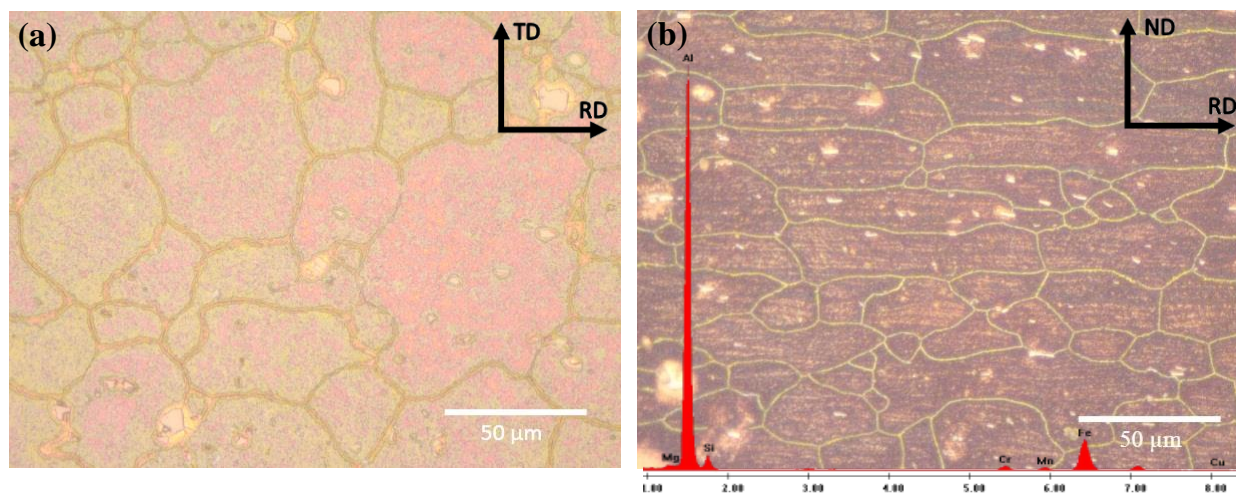
Figure II.9. OM microstructure of the as received Al 6061-T6 observed at the: (a) TD-RD direction and (b) ND-RD direction.

II.1.3.1 Microstructure observation of deformed specimens

In order to develop a better understanding of the material's behavior, the microstructure of the deformed material at different loading conditions was studied in this section. Figure II.10 presents the microstructure of the deformed Al-6061-T6 specimens with micrographs taken near the fracture zone, and the observation is conducted in two planes: TD-RD and ND-RD. Figure

II.10 (a) and Figure II.10 (b) present the microstructure of specimen tested at room temperature and strain rate of $10^{-1}s^{-1}$, it is observed that the grains are significantly elongated in the tensile loading direction i.e. RD. However, it can be observed from Figure II.10 (c) and Figure II.10 (d) that the grains are more elongated for the specimen tested at 300°C and deformed at the same strain rate. This observation can be explained by the higher strain to failure obtained in the specimen at 300°C as shown in Figure II.6 (a). Also, the grains are observed to be less elongated for specimen tested at 300°C and strain rate of $10^{-4}s^{-1}$. Furthermore, the shape of the grains is quite different from the previous cases - more rounded grains can be seen in Figure II.10 (e) and Figure II.10 (f). A grain size analysis was performed for the various testing conditions. No significant grain growth was found, as the mean grain size remained 25 µm and 39 µm in the ND-RD and TD-RD planes respectively for the different testing conditions. Moreover, it was observed that the precipitates migrated and they were more perceptible at the grain boundaries, it was concluded that these observations could explain the limited grain growth observed in the 6061-T6 aluminum alloy (Chen Z., 2010). Since there was no significant grain growth observed under the deformation range investigated in this work, it can point out that the main deformation mechanism is a slip. It goes to suggest that a better formability response, i.e. large elevated temperature tensile ductility, may be obtained at significantly higher temperatures through the activation of other deformation mechanisms. Therefore, it could possibly enable the activation of grain boundary sliding and grain fragmentation, and enhance the dislocation motion as the precipitates would grow and globalize. The evolution of the microstructure with heat treatment was checked in the following paragraph.
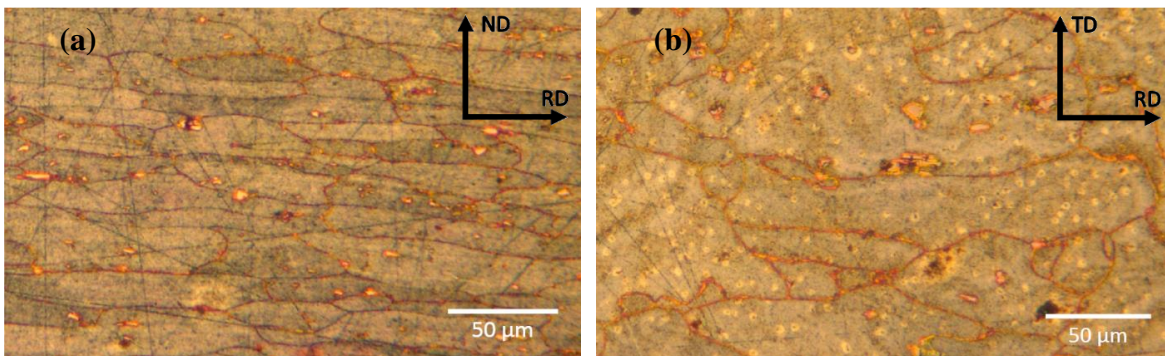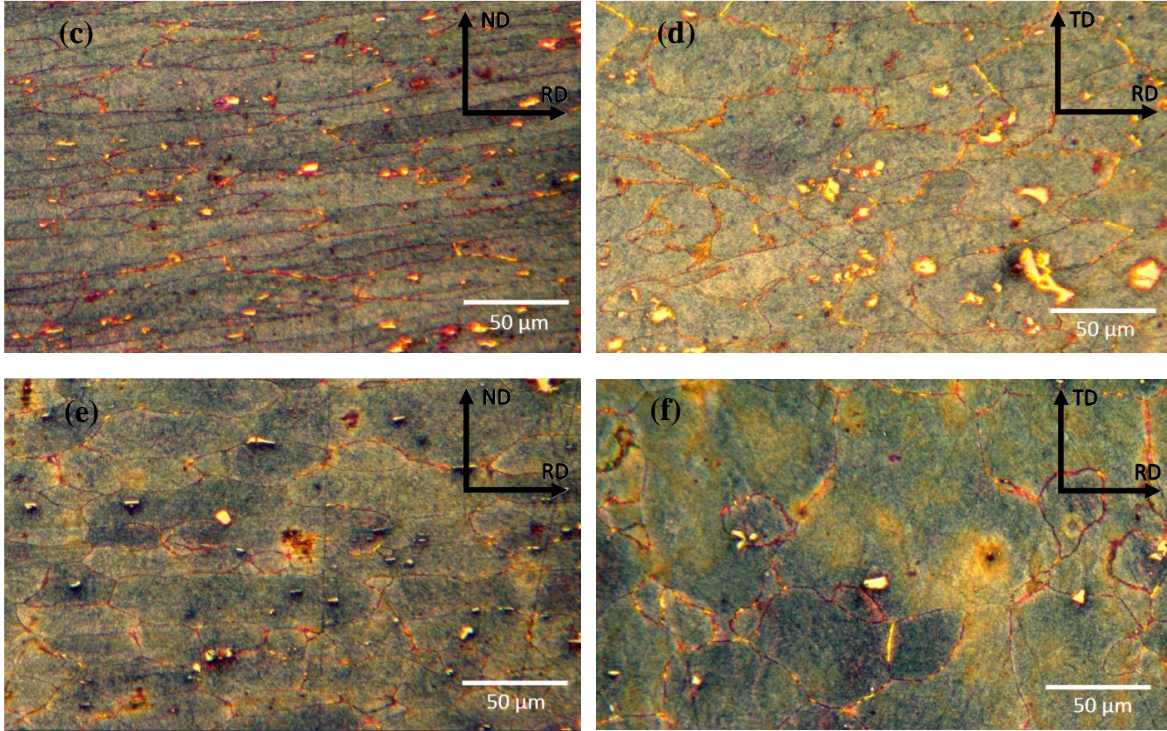
Figure II.10. OM microstructure of Al 6061-T6 samples deformed by uniaxial loading observed in the (a): ND-RD, loaded at RT, $10^{-1}s^{-1}$; (b): TD-RD, loaded at RT, $10^{-1}s^{-1}$ (c) ND-RD, loaded at 300°C, $10^{-1}s^{-1}$; (d): TD-RD, loaded at 300°C, $10^{-1}s^{-1}$;(e): ND-RD, loaded at 300°C, $10^{-4}s^{-1}$ (f): TD-RD, loaded at 300°C, $10^{-4}s^{-1}$.

II.1.3.2 Annealing tests

Figure II.11 shows the microstructure of Al6061-T6 annealed samples at 300°C±3°C for 50 minutes (Figure II.11 (a)), at 450°±3°C for 8 hours (Figure II.11 (b)) and at 580°C±3°C for 8 hours (Figure II.11 (c)). The average grain size diameter was found to be 41 μm for the Figure II.11a micrograph; this annealing condition was performed in order to confirm that no significant grain growth occurs. An average grain size of 50 μm was found for the micrographs in Figure II.11 (b) and an average grain size of 61 μm was found for the micrographs in Figure II.11 (c). Furthermore, it was observed that as the annealing temperature is increased, the diffusion and coarsening of magnesium silicide (Mg_2Si) particles in all areas of the samples was more abundant (Lee et al., 2003b).
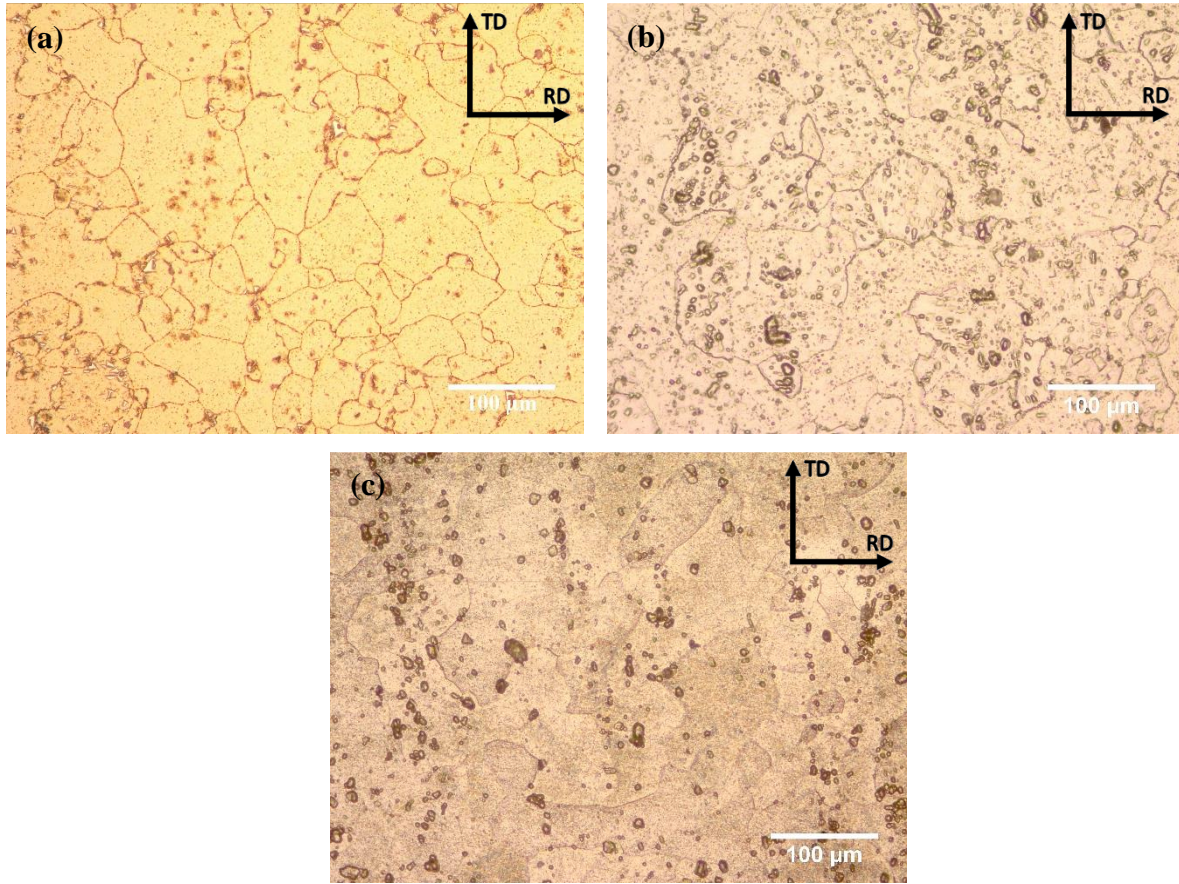
Figure II.11. Comparison between microstructure of annealed Al 6061-T6 at (a) 300°C for 8 hours (b) 450°C for 8 hours and (c) 580°C for 8 hours.

II.1.3.3 Fractography observations

Fracture surfaces were examined by Scanning Electron Microscopy (SEM). Figure II.12 presents SEM fractographs of uniaxially loaded samples at room temperature and 300°C under strain rates of $10^{-1}s^{-1}$, $10^{-3}s^{-1}$, $10^{-4}s^{-1}$. It can be observed that the fracture surface presented in Figure II.12 (e) compared to the other four conditions supported the largest strain to failure. The existence of coalesced micro-voids and microscopic dimples in all the SEM micrographs of Fig. 9, confirm that the Al 6061 T6 exhibits a ductile behavior (Tang et al., 2011). Under the strain rate of 10^{-4} s^{-1} and 300°C, the estimate mean size and the depth of these microscopic dimples are small compared to the one observed at strain rate of $10^{-1}s^{-1}$. Iron-rich phases were supposedly observed at the bottom of some micro-voids and highlighted by red circles in Figure II.12 (Ghahremaninezhad and Ravi-Chandar, 2012). These iron-rich particles were especially perceivable in the fracture surfaces of the samples deformed at room temperature (Figure II.12

(b) and Figure II.12 (d)). The microscopic dimples depth are observed to be bigger on the fracture surfaces of the samples deformed at 300°C at a strain rate of $10^{-1}s^{-1}$ (Figure II.12), which can explain the reason why intermetallic phases are less perceivable. In other words, the depth of the microscopic dimples may be used to give an approximate estimate of the ductility of a metallic alloy (Bethge and Heydenreich, 1987). Indeed, the samples with a higher strain to failure had relatively deep estimated microscopic dimples (Figure II.12 (f)) and samples with a lower strain to failure have relatively shallow estimated microscopic dimples (Figure II.12 (h)).
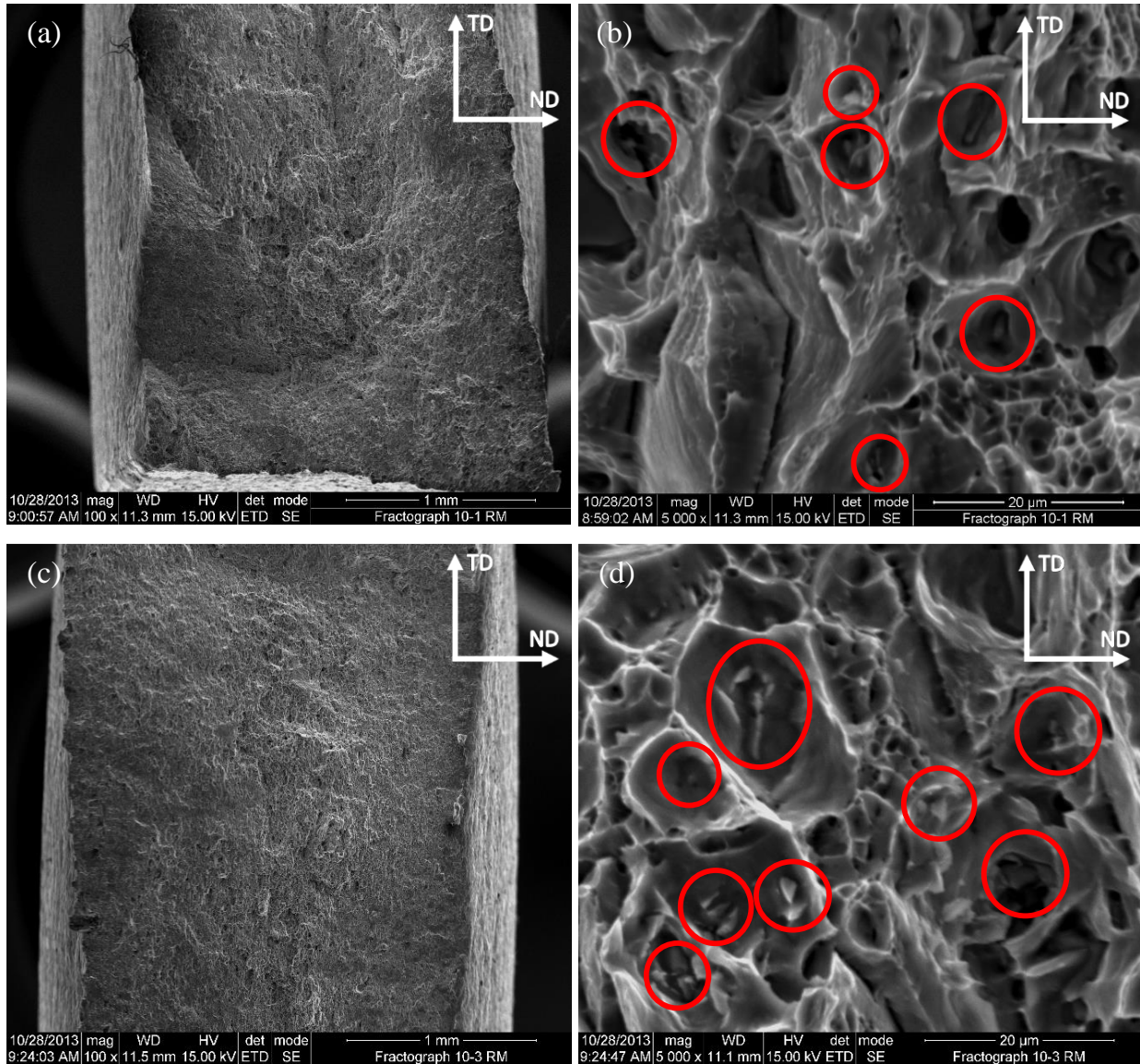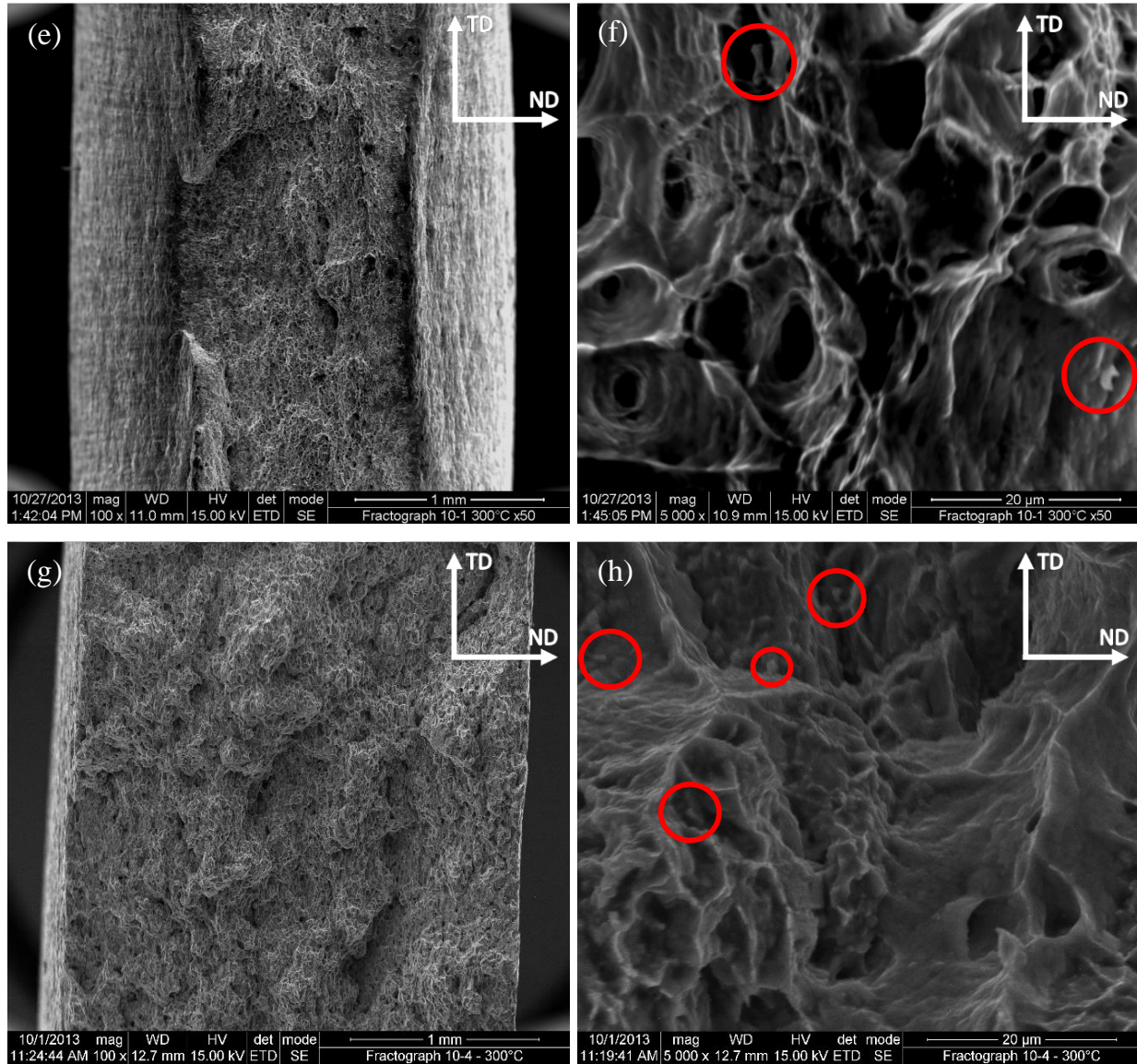
Figure II.12. SEM fractography of uniaxially loaded samples, (a) and (b) at room temperature under strain rate of $10^{-1}s^{-1}$, (c) and (d): at room temperature under strain rate of $10^{-3}s^{-1}$ (e) and (f): at 300°C under strain rate of $10^{-1}s^{-1}$, (g) and (h): at 300°C under strain rate of $10^{-4}s^{-1}$.

II.1.3.4 Work of Fracture

In order to develop a deeper insight into the evolution of the deformation and damage mechanisms under variable loading conditions, the work to fracture can be calculated. The work of fracture W_e can be estimated by calculating the area under the stress-strain curve at given loading condition. The work of fracture $W_e(T)$ of Al6061-T6 is plotted in function of the

temperature for different strain rates (Figure II.13 (a)). It is observed that the work to fracture decrease with increasing temperature and decreasing strain rate. At room temperature, the work to fracture was found to be fairly consistent i.e. 60 MPa, showed negligible strain rate sensitivity. This however began to decrease gradually with increasing temperature, and at 300°C it dropped to 42 MPa under strain rate of 10^{-1} s^{-1} and to 21 MPa under strain rate of 10^{-4}s^{-1}.

Figure II.13 (b) presents the work to fracture $W_e(\dot{\varepsilon})$ of Al 6061-T6 as a function of the natural logarithm of the strain rate for different temperatures. It is observed that at RT and 100°C the work to fracture is almost constant with evolving strain rate. However, for 200°C and 300°C, the work to fracture is observed to decrease with decreasing strain rate. The work to fracture reaches its minimal value for uniaxial test performed at 300°C at a strain rate of 10^{-4}s^{-1}.
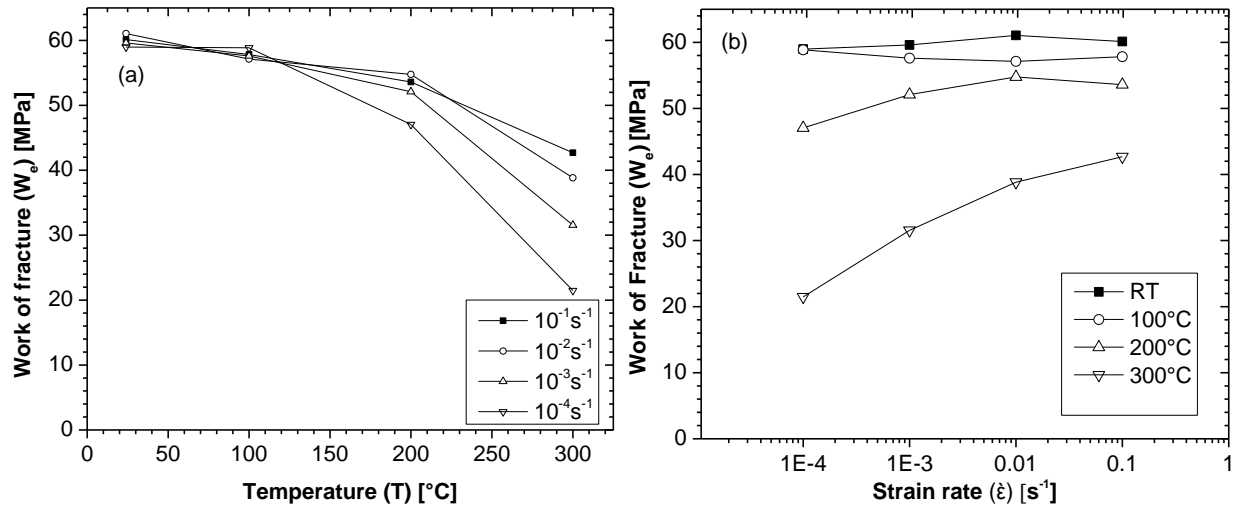
Figure II.13. (a) Work of fracture vs. temperature and (b) work of fracture vs. strain rate.

The yield stress and the strain to failure are the main parameters affected by the strain rate and the temperature evolution. We had observed that increasing strain rate results in increasing the yield stress and hence contributes to increasing in the work to fracture. However, increasing strain rate resulted in decreasing the strain to failure for tests conducted at RT and 100°C and in increasing the strain to failure for tests conducted at 200°C and 300°C. A competition between the yield stress and the strain of failure sensitivity to strain rate and temperature will determine the evolution of work to fracture. The evolutions of $W_e(T)$ and $W_e(\dot{\varepsilon})$ point out that the increases in the yield stress with increasing strain rate and decreasing

temperature is not countered by the strain to failure sensitivity. In the purpose to identify the damage mechanisms controlling the fracture behavior of the AL 6061 T6, the crack initiation, and evolution is tracked in samples loaded at 200°C and 300°C.

II.1.3.5 Damage mechanisms

In order to identify the damage mechanisms that control the fracture behavior of the Al 6061 T6, the crack initiation and evolution was tracked in samples loaded at 200°C and 300°C. The plastic deformation of ductile metals and their alloys is limited by the void nucleation and growth and associated coalescence rates (Thomson and Hancock, 1984). Figure II.14 shows SEM micrographs of a specimen take from an interrupted test at the initiation of strain to failure. The particular sample was uniaxially loaded at a strain rate of 10^{-3} s^{-1} and temperature of 200°C. Cracks were observed between broken second-phase particles or apparently iron-rich phases (white particles). These micro-voids were observed in the RD-ND and RD-TD planes but mainly in the RD-ND plan. Similar observations have been reported by (Ghahremaninezhad and Ravi-Chandar, 2012) on specimen tested at room temperature. The Iron rich phase particles are locations for stress concentration that leads to cracks initiation that was evidenced by the void growth parallel to the loading direction (Dieter, 1986; Zhu et al., 2011). These observations could give an explanation to the presence of some iron-rich phases in the bottom of the microvoids observed in the fractographic surfaces (Figure II.12).
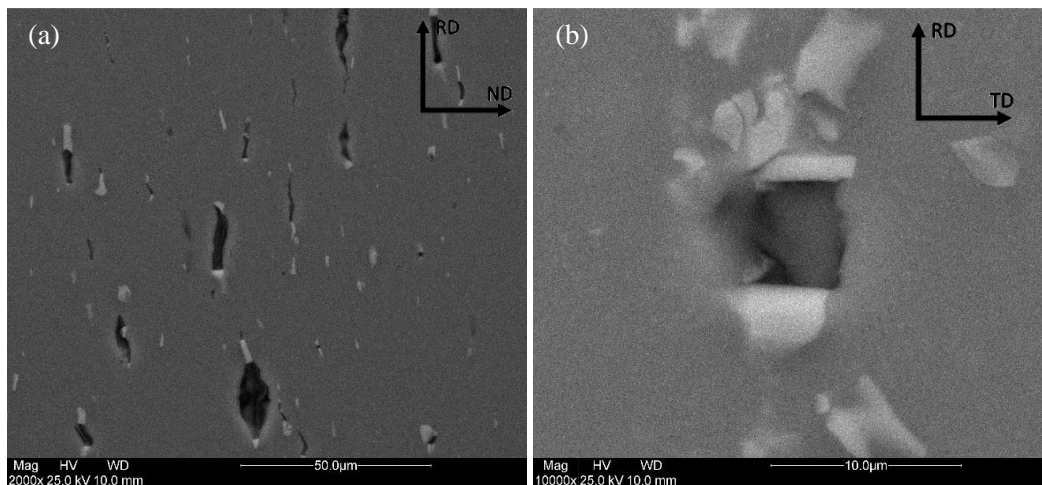
Figure II.14. SEM analysis of interrupted uniaxial tensile test of Al6061-T6 at 10^{-3}s^{-1} and 200°C, observed in the (a) RD-ND plane and (b) RD-TD plane.

Figure II.15 shows optical microscope micrographs of specimen surfaces subjected to tensile tests, conducted at 300°C, and interrupted at strains of 0.2 and 0.16 for test strain rates of

$10^{-3}s^{-1}$ and $10^{-4}s^{-1}$, respectively. These micrographs were taken in the middle of the samples; they show that the cracks leading to fracture propagate in the necked region. These cracks propagated parallel to each other and coalesce in localized shear bands formed in the thinned ligament between neighboring voids as observed in Figure II.15b. It can be noticed from Figure II.15 that in the TD-RD plan the cracks are propagating in the transverse direction (TD) (Figure II.15 a, b). However, in the RD-ND plan, a number of cracks are scattered all over the micrograph, slightly propagating along the rolling direction (RD), and coalescing in localized shear bands formed between two neighboring cracks (Figure II.15 c, d). The propagation of cracks parallel to the transverse direction (TD) and the coalescence of cracks in the RD-ND plan will lead to a macroscopic crack propagating with an α angle from the normal direction (ND) in the RD-ND plan that will result in the catastrophic failure of the sample.
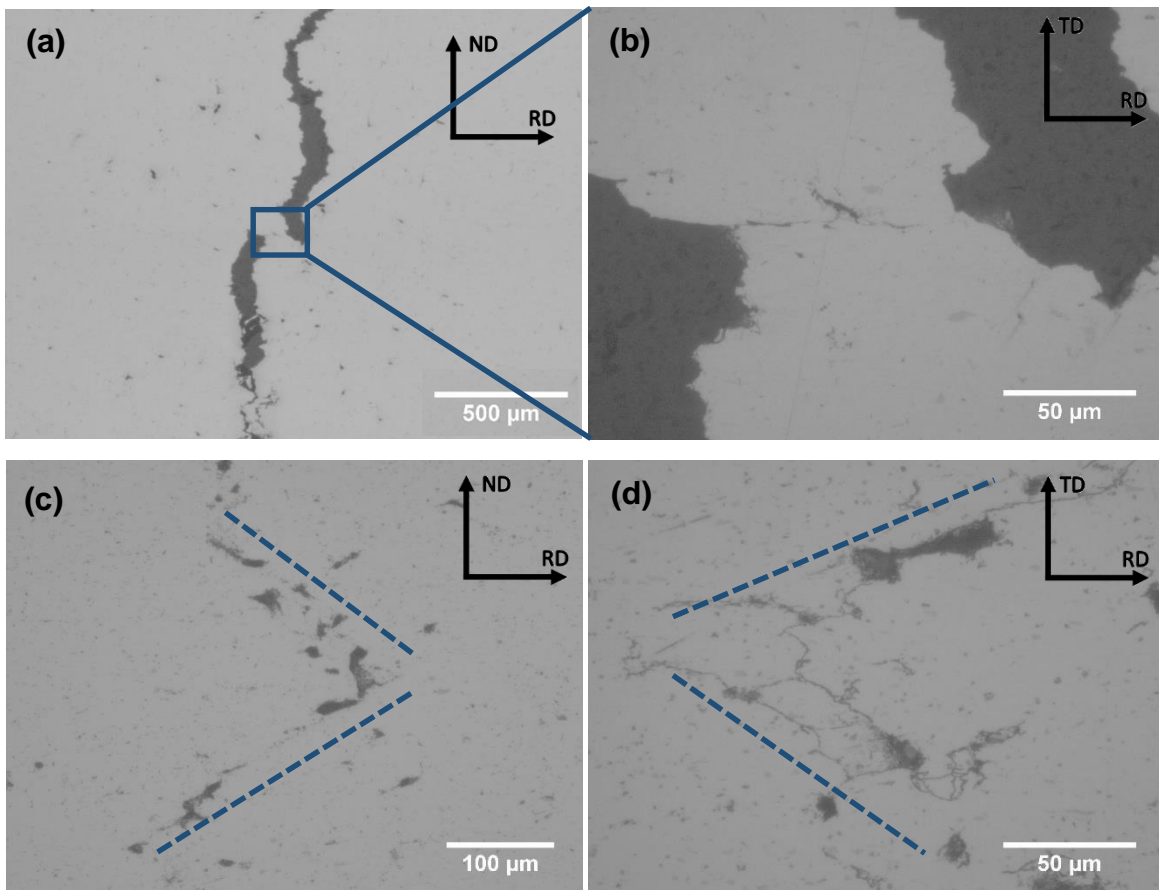
Figure II.15. OM micrographs of crack initiations of interrupted test at 300°C, (a) and (b) $10^{-3}s^{-1}$ in TD-RD plan, (c): $10^{-3}s^{-1}$ in ND-RD plan, (d) $10^{-4}s^{-1}$ in ND-RD plan.

Figure II.16 presents SEM micrographs of tensile samples tested at 300°C and $10^{-3}s^{-1}$ strain rate and interrupted at strain to failure. Similar observation as in Figure II.15 can be

noticed; cracks propagating parallel to the transverse direction (TD) and cracks coalescing in the RD-ND plan. However, it can be noticed that the intermetallic phase particles are not fractured and the cracks are developed around the particles. At 300°C, the cracks initiated at the intermetallic phase particles nevertheless in contrast with 200°C and RT the main mechanism of crack initiation is concluded to be interfacial decohesion.
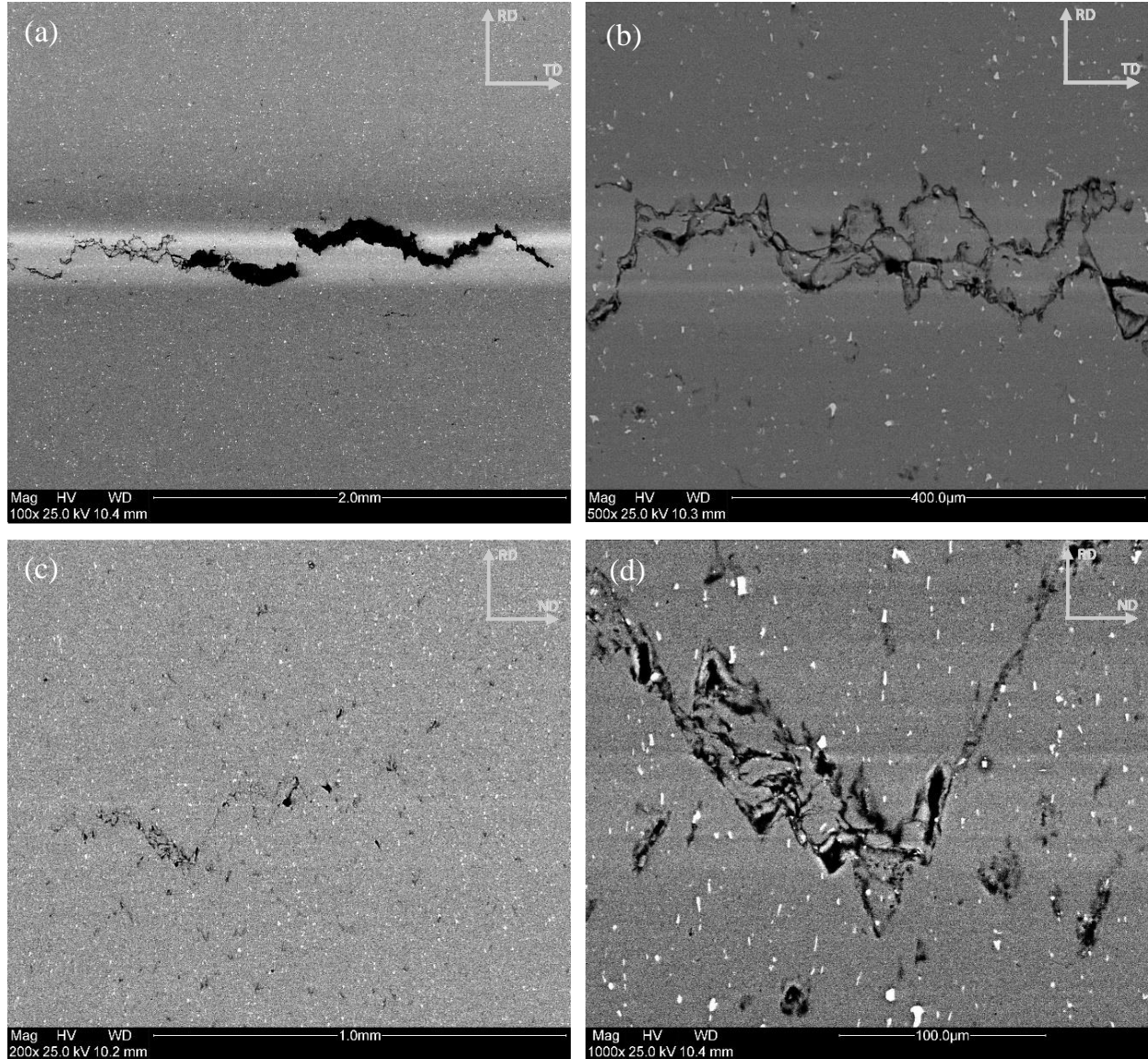
Figure II.16. SEM micrographs of interrupted test at 300°C, (a) and (b) $10^{-3}s^{-1}$ in RD-TD plan, (c) and (d): $10^{-3}s^{-1}$ in RD-ND plan.

II.1.4 Conclusion

The mechanical behavior and the microstructural evolution of Al 6061-T6 were studied uniaxial loading condition performed at different strain rate and temperature. The Yield stress and the ultimate tensile strength were observed to increase with increasing strain rate and decreasing temperature. The maximum strain to failure was found to increase with increasing temperature and decreasing strain rate for tests performed at room temperature and 100°C. By contrast, the maximum strain to failure was found to decrease with increasing temperature and decreasing strain rate for tests performed at 200°C and 300°C. The observation of the microstructure revealed that the grains were elongated in the loading direction, and the average grain size was not evolving with the different loading conditions. However, it was observed an increase of diffusion and coarsening of the precipitate with increasing temperature. This observation was confirmed by performing additional heat treatment at different conditions however the average grain size was noticed to be increased at elevated temperature and exposure time. The analysis of fracture surfaces of the tested specimen has confirmed the ductile behavior nature of the studied materials as coalesced micro-voids and microscopic dimples were observed. Insightful analysis has been conducted with the aim to track the damage mechanisms of the Al 6061 T6 by observing the microstructure of samples subjected to interrupted tests. It was noted that the intermetallic phase particles are the privileged sites of crack initiation. The initiation mechanism was evolving with temperature as between room temperature and 200°C the initiation was by particles fracture yet at 300°C the initiation was by interfacial decohesion. As the deformation progress, the crack was observed to propagate perpendicular to the rolling direction (RD) and the coalescence of cracks occurring in the RD-ND plan resulted in a macroscopic crack propagating with an α angle from the normal direction (ND) in the RD-ND plan leading to the catastrophic failure of the sample.

II.2 Mechanical and microstructural characterization of AZ31B magnesium alloy

In this chapter part, the results of an investigation of the effects of thermomechanical variables on the deformation behavior and on the microstructure of the commercially available as-rolled TRC AZ31B sheets is presented. This study aims at providing a better insight on the behavior of the material to enhance future application in the industry. The results presented in this section have been uncovered by Ana Rodriguez (Rodriguez et al., 2013) with the help of Abdelhakim Dorbane. The results are part of Ana Rodriguez master thesis prepared under the supervision of dr. Georges Ayoub, the Co-advisor on this PhD dissertation.

II.2.1 Materials

The second base material that has been investigated in order to be used for FSW in the next chapter was twin-rolled cast AZ31B magnesium sheets, rolled to a final thickness of 3 mm and supplied by POSCO. The chemical composition of the material was obtained through energy dispersive x-ray analysis. The results presented in Table II.2. The initial microstructure shown in Figure II.17 (a) had an average grain size of 8.2±0.5 μm. Tensile testing, metallographic preparation and microscopic observation methods were similar to that used to characterize the 6061-T6 aluminum alloy in the previous section. The etchant used to reveal the microstructure was a standard acetic picral solution. (Rodriguez et al., 2013)

Component	Mg	Al	Zn	Mn	Si
Amount (Wt. %)	95.43	3.32	0.80	0.30	0.15

Table II.2. The nominal chemical composition of AZ31B. (Rodriguez et al., 2013)

II.2.2 Microstructure of the base material and deformed specimens

The damaged samples at various strain rates and temperatures were analyzed by taking micrographs near the damaged surfaces of the failed samples. Figure II.17 demonstrates the microstructure of some specimens failed at 25°C under different strain rates. As an overall observation, the mean grain size of the material decreases after the deformation occurs. The

micrographs at various strain rates show bands structures that can be attributed to twinning bands with a greater density for the strain rate of $10^{-1}s^{-1}$. According to what was reported in the literature, the basal texture of the AZ31B rolled sheets (with the axis perpendicular to the load direction) promotes decreasing in the twinning occurring on the $[10\bar{1}1]$ and $[10\bar{1}3]$ twin planes (Jiang et al., 2006). On the other hand, the texture reorientation due to twinning promotes twinning at the $[10\bar{1}2]$ plane, and thus double twinning could also be taking place (Rodriguez et al., 2013).
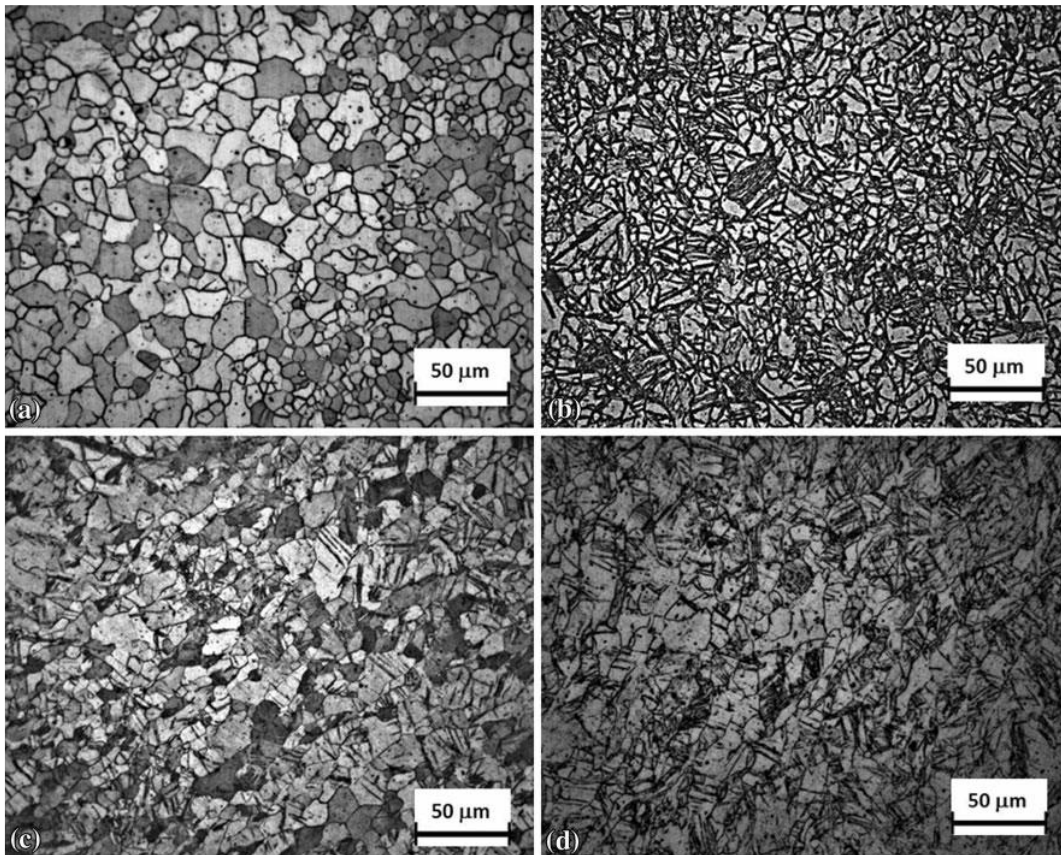
Figure II.17. Microstructure of TRC AZ31B alloy of the as-received (a) and deformed at 25°C with different strain rates at (b) at $10^{-1}s^{-1}$, (c) at 10^{-3} s^{-1}, and (d) at 10^{-4} s^{-1} (fracture zone) (Rodriguez et al., 2013)

II.2.3 Tensile testing

The mechanical behaviors of the AZ31B at 25°C and at 300°C for various strain rates are demonstrated in Figure II.18 (a) and (b), respectively. At 25°C, the strength of the AZ31B is not influenced by the strain rate; however, the strain rate seems to only influence the strain to failure.

More specifically, the yield strength and the maximum stress seem to be independent of the strain rate in the selected strain rate range, with a mean yield strength σ_y of 200 MPa and an average maximum stress equal to 310 MPa. It can be also reported that the maximum elongation to failure was gotten at the lowest examined strain rate of $10^{-4}s^{-1}$, while the minimum elongation was obtained at the highest investigated strain rate of $10^{-1}s^{-1}$. At low temperatures, the high stress and low strain exhibited by the as-rolled material are due to the limited deformation systems of magnesium. (Rodriguez et al., 2013)

The effect of the strain rate at 300°C is presented in the Figure II.18 (b). It can be observed that the comportment of AZ31B magnesium alloy is time dependent. The yield stress decreases from 104 MPa for a strain rate of $10^{-1}s^{-1}$, to 38.8 MPa for a strain rate of $10^{-4}s^{-1}$. For these testing conditions, the ultimate stress also decreased from 154.4 MPa under $10^{-1}s^{-1}$ to 48.1 MPa under $10^{-4}s^{-1}$. Figure II.18 (b) also demonstrates that the material ductility rises with rising temperature and decreasing strain rate. In fact, an increase of 78% in elongation to fracture and a decrease of 79% in the maximum stress were obtained by decreasing the strain rate from 10^{-1} to 10^{-4} s^{-1}. At lower strain rates, the strain hardening is dramatically diminished, and a more plastic deformation appears at $10^{-4}s^{-1}$. These results are in agreement with the fact that, at high temperature, both pyramidal and prismatic slips are activated. The results may also indicate the activity of other high-temperature deformation mechanisms, for instance, grain boundaries sliding (GBS) and dynamic recrystallization (DRX). (Rodriguez et al., 2013)
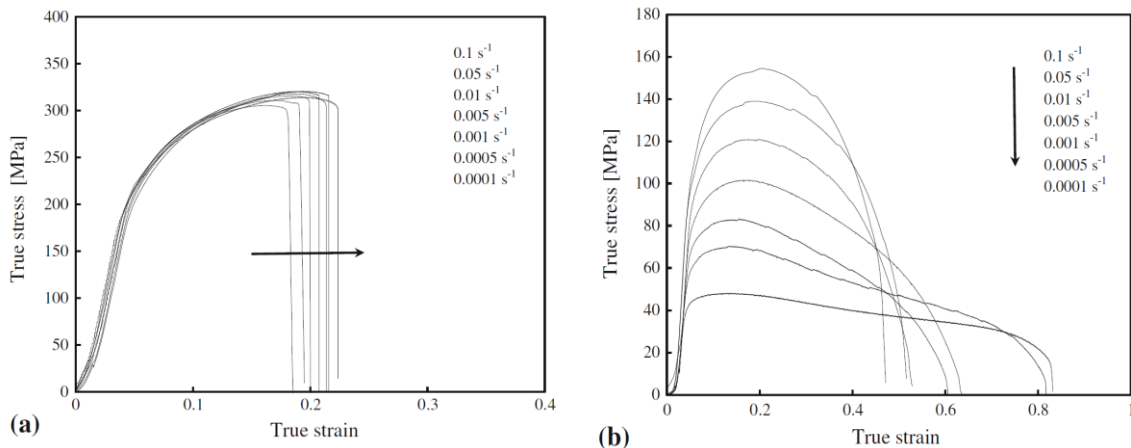
Figure II.18. Stress strain curves from tensile test of AZ31 twin-rolled cast specimens at (a) 25°C and (b) 300°C. (Rodriguez et al., 2013)

II.2.4 Heat treatment

Different as-rolled samples were heat treated at temperatures between 100 and 475°C to observe the evolution of the grain size in function of temperature. The effect of the annealing temperature after 8 h of treatment is shown in Figure II.19: While it can be observed that there is an insignificant difference in the size and configuration of the grains after treating at 100°C compared with the as-received microstructure (Figure II.17 (a)), there is an important change in the microstructure of AZ31B magnesium alloy after heat treatment above 300°C. The original grain size was reported to be increased by 385% after 8 h of heat treatment at 475°C, growing from 8.2±0.5 to 32±2 μm. (Rodriguez et al., 2013)
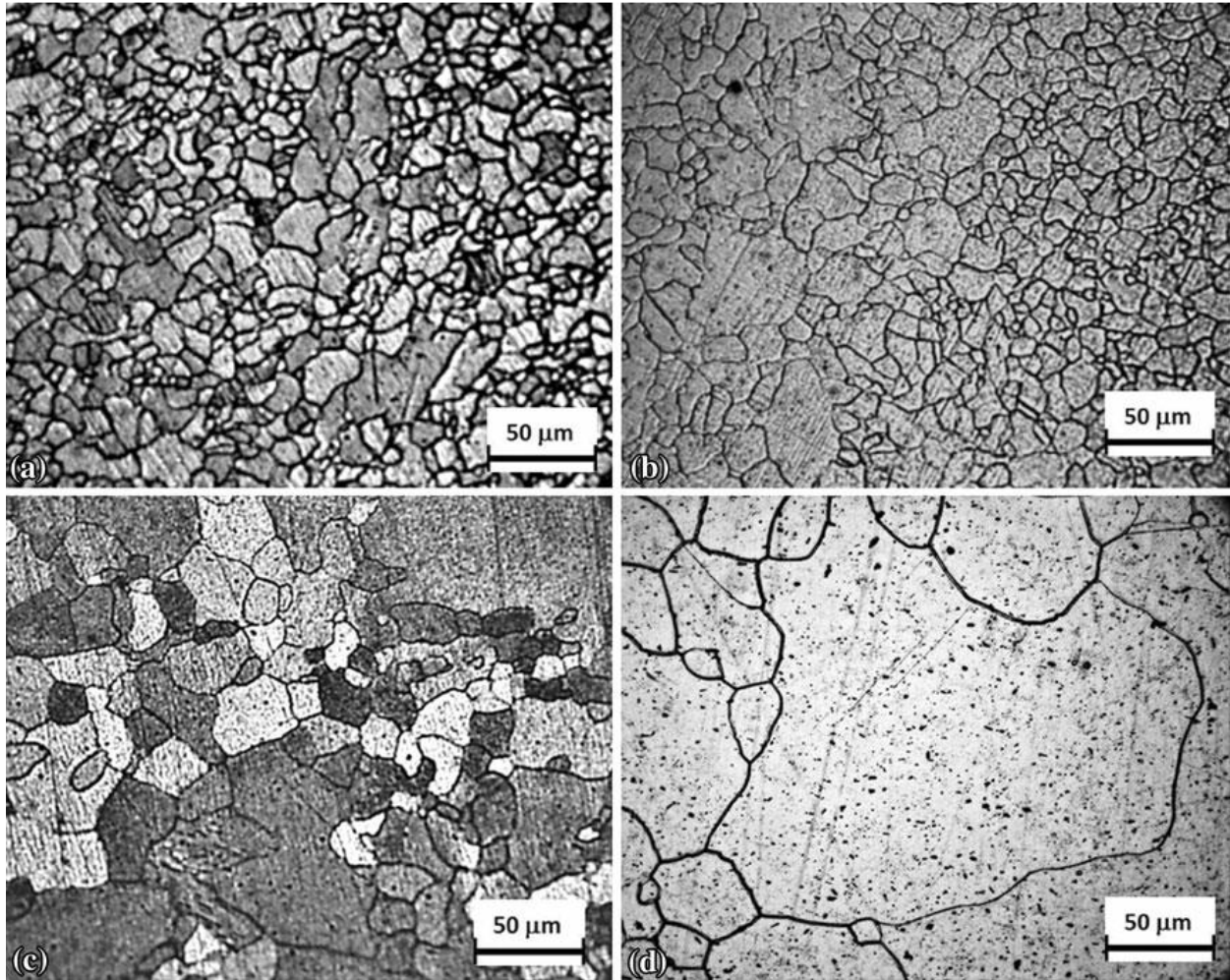
Figure II.19. Evolution of the microstructure after 8 h of annealing at different treatment temperatures (a) as-received (b) 100°C, (c) 300°C, (d) 375°C, and (e) 475°C. (Rodriguez et al., 2013)

Figure 12 displays the evolution of the grain size diameter in function of temperature after 8 hours of heat treatment. The figure shows that up to a temperature around 300°C, the grain size increases at a relatively low rate; however, significantly higher grain growth rate is observed for temperatures greater than 300°C. This involves that 300°C is approximately the critical temperature that activates the static recrystallization mechanism that occurs to the material. (Rodriguez et al., 2013)
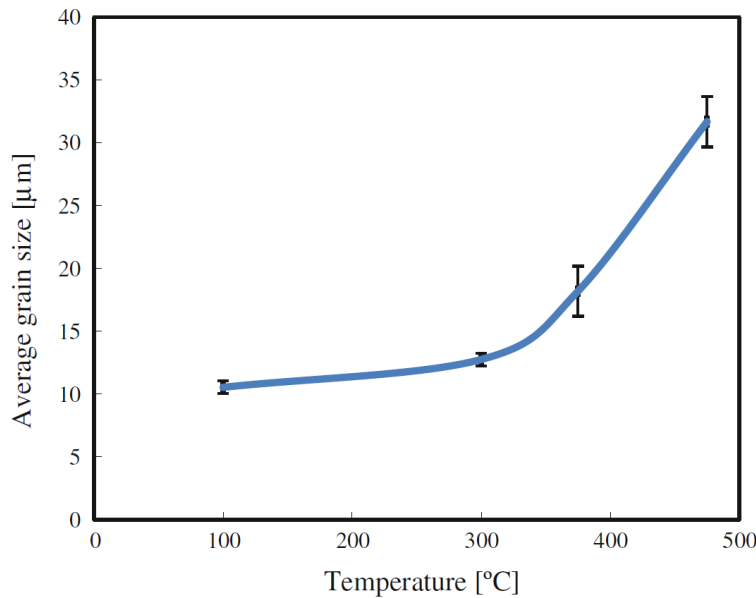
Fig. 12 Average grain size in function of temperature after 8 h of annealing. (Rodriguez et al., 2013)

II.2.5 Conclusions

Characterization of AZ31B magnesium alloy was performed using tensile testing and microstructure observations. At room temperature, AZ31B magnesium alloy is not influenced by the strain rate, but at higher temperature it shows a strong dependence of the mechanical behavior of material with the strain rate, with lowering the strain rate values, the strain to failure increases and the UTS decreases simultaneously. Slip and twinning is probably the main deformation mechanism at 25°C, moreover dynamic recrystallization is observed at 200°C, and at 300°C. Heat-treatment experiments showed that the grain growth occurs gradually when the material is exposed to high temperature, to reach its maximal values at 475°C.

Chapter III.   Homogeneous Friction Stir Welding of 6061-T6 Aluminum and AZ31B Magnesium Alloys

In chapter three, Al-to-Al joints have been produced at different welding speeds. Their cross-section microstructure have been revealed and microhardness measurements on these samples have been done and linked to their grain size. The final damage sites were investigated by conducting tensile testing at selected different temperatures (25, 100, 200 and 300 °C) and constant strain rate of $10^{-3}s^{-1}$. Also, FSW of AZ31 magnesium has been established. The microstructure, texture and mechanical response of the joints at different temperatures were studied at different temperatures. And the microstructural characteristics and propensity of crack initiation in different weld zones were studied through the tensile fracture behavior.

Summary

III.1 Microstructural observations and tensile fracture behavior of FSW Al 6061-T6 Sheets

Introduction

Aluminum is the most abundant metal, in the Earth's crust. Owing to their corrosion resistant, lightweight, formability and toughness, aluminum and its alloys are the second most important structural metal alloys (Dwight, 2002) used in the automotive, aircraft and watercraft industries, after steel and its alloys. Because of its high thermal conductivity and low melting point, welding aluminum and its alloys can present quite a challenge while using conventional welding techniques such as fusion welding, which may lead to defects due to the solidification process that occur due to the overheating of the base material. And thereby, lower mechanical properties and poor metallurgical aspects can be obtained. Friction stir welding (FSW) is a solid-state material joining technique. Introduced in 1991 (Thomas et al., 1991), FSW has been proved to be a fast and high-quality material joining. Because the total heat generated during the welding process is below the melting temperature (about 80% of the melting temperature of the base material), this welding can reduce, and sometimes eliminate the resulting defects that may occur such as high distortion when using conventional welding techniques.

Several studies contributed to enhancing FSW of aluminum and their alloys (Merzoug et al., 2010; Peel et al., 2003; Su et al., 2005; Su et al., 2003; Wadeson et al., 2006; Wan et al., 2014; Yadava et al., 2010). Regarding the different welds zones that can be observed in the cross section of a weld, fine equiaxed grains (approximately 1 μm) can be obtained in the stir zone due to the dynamic recrystallization (DRX) (Benavides et al., 1999; Jata and Semiatin, 2000; Liu et al., 1997; Mishra and Mahoney, 2001; Rhodes et al., 1997; Su et al., 2003).

Specifically, Al6061-T6, which is a high strength aluminum alloy, have been widely welded using FSW process, and investigated in various studies. (Lim et al., 2004) examined the tensile behavior of friction stir welded Al6061-T651 metal sheets joined at different welding parameters and tested at room temperature. The authors concluded that the tensile elongation increased with increasing the weld speed or decreasing the tool rotation speed, they reported that such a decrease in tensile elongation is due to the clustering of coarse magnesium silicide Mg_2si precipitates in particular locations within the nugget zone. Also, (Chao et al., 2008) investigated the experimental analyzes of thermal and mechanical phenomena during FSW of Al6061-T6

aluminum alloy thick plates. The authors reported that there is a quasi-steady state in the force-controlled FSW process during which the heat input, the temperature profiles, and the mechanical force stay the same near the tool. Yet, the measured heat input was less than the base material's melting temperature, and the total heat generated by the tool was found to be depending on the length of the pin itself. On the other hand, (Fahimpour et al., 2013) compared the FSW and gas tungsten arc welding (GTAW) of AA 6061 joints through scanning electron microscopy, hardness, tensile testing and fractography, the authors observed that the ultimate tensile strength obtained from the welds produced by FSW were superior compared to those obtained by GTAW. They also reported that post-weld aging enhanced the weld strength, but reduced its ductility. Also, (Ramulu et al., 2012) analyzed the internal defects and process parameters during FSW of Al6061-T6 metal sheets. The authors reported that higher welding speed (for about 80-120 mm/min), higher tool rotation speed (1300-1500 rpm) and higher plunge depth (1.85-2) produced defect free joint when welding 2.1 mm thick plates. Also, using all shoulder diameters (12, 15 and 18 mm) resulted in defect-free joints. The authors also confirmed that the axial force and torque were observed to increase with increasing the welding speed and tool shoulder diameter, and thereby, decreasing with increasing tool rotation speed in the defect-free joints. Furthermore, the axial force and torque were found to remain constant while forming joints without defects.

The influence of the temperature on the mechanical properties of the FS welds is missing in the literature. By the fact that the welded joints may deteriorate at elevated temperatures, especially when under constraint. In this regard, The characterization of the welded joints at different temperatures is crucial. This study attempts to observe the mechanical and microstructural properties of some welds obtained by FSW of Al 6061-T6 at various welding parameters and to evaluate the joint strength at various temperatures by doing uniaxial tensile testing, examining the hardness values of the cross section and linking it to the grain size.

III.1.1 Experimental procedure

III.1.1.1 Materials and welding

Aluminum has been used in the past decades as a lightweight material to reduce the vehicle weight, and enhance the fuel consumption. Along with using friction stir welding (FSW),

a solid-state technique that doesn't need any filler material to perform the weld. And thereby, further reduction in the total weight of the vehicle with a weight/strength quota of the joints. Also, FSW that occurs below the melting temperature of the alloy (about 70 to 80% of the melting temperature of the material) can avoid defects due to the solidification process. Therefore, due to the low heat input, the resulted weld region will be eventually composed of fine equiaxed grains, which contribute to the forming process.

The metal sheets used as base material for the welding were 3 mm thick Al6061-T6 aluminum alloy, supplied by McMaster. The same metal sheets have been studied with more details in previous studies (Dorbane et al., 2015a, b). The metal sheets were mechanically cut in the rolling direction and machined to a final size of 250*50 mm. That makes the weld path parallel to the rolling direction.

The FSW was performed using a Gantry FSW machine (FSW-LM-08, Beijing FSW Tech. Co. Ltd.) (Figure III.1 (a)). The FSW tool was made from a steel alloy with a 10 mm shoulder diameter, and a threaded pin with a major diameter of 3.2 mm and a minor diameter of 2.9 mm with a length of 2.9 mm. The workpieces were held using a conventional clamping system. (Figure III.1 (b) and (c)).

III.1.1.2 Mechanical properties

Tensile testing was performed using a screw-driven MTS insight tensile testing machine equipped with a 30 kN load cell, an LBO-series Thermocraft LabTemp laboratory oven (Environmental chamber) and controlled by a computer. The tensile test specimens were mechanically cut using a CNC machine with dimensions according to (ASTM-E8/E8M). Specimens were cut perpendicular to the weld direction, ground using 180-grit media, and followed by 1200-grit silicon carbide paper to eliminate any wrinkles or irregular surfaces along the joint. To make a systematic comparison between the welded specimens and the base material, the tensile test specimens made from base material were cut perpendicularly to the rolling direction. Moreover, the tensile testing at high temperature was according to (ASTM-E21-09).
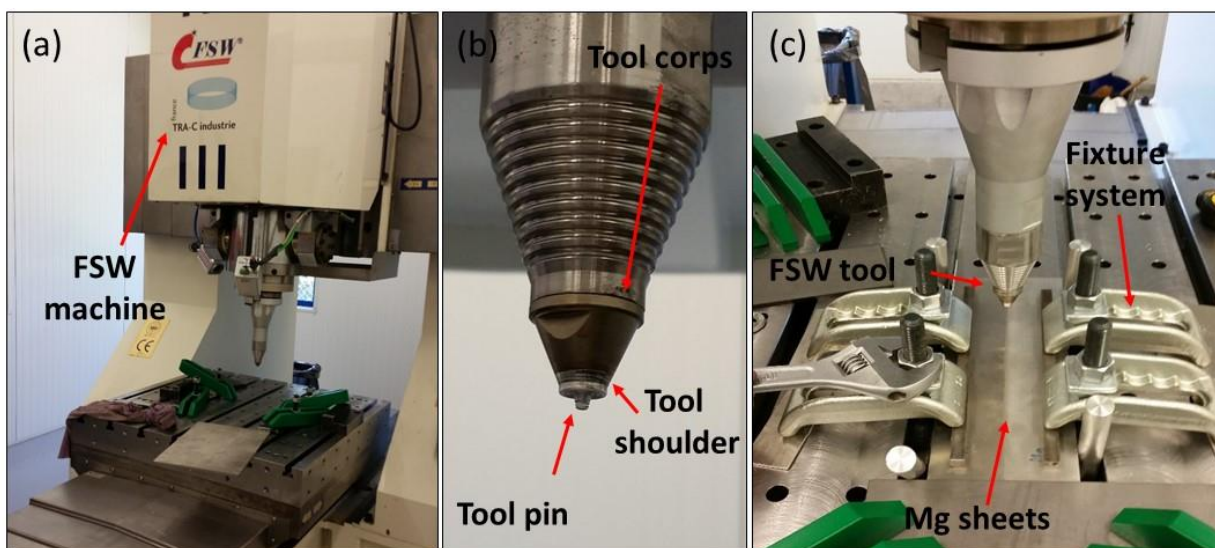
Figure III.1. Friction stir welding equipment. (a) FSW machine, (b) FSW tool and (c) the camping system.

Microhardness specimens were machined and prepared using the same procedure for microstructural characterization (further explained below). Microhardness testing was performed using a QV-1000 Series Microhardness tester. The applied force was 100 gf with a dwell time of 15 s. approximately the microhardness of 20 mm length was measured by taking indentation with a distance of 0.5 mm between each step. Five lines were analyzed for the cross-section of a welded sample using 1600 rpm and 250 mm/min. Moreover, the other specimens welded using 500, 750 and 1000 mm/min were analyzed across the mid-thickness of the cross-section. I.e., 1.5 mm from the weld top.

III.1.1.3 Microstructure

To analyze the base material and the welded joints, samples for the metallographic preparation have been produced according to the standards (ASTM-E3-11). The samples were cut in the cross-section of the weld, then mounted using a TechPress 4" using black phonelic hot mounting powder, then ground using 180, 320, 600 then 1200 silicon carbide paper grits. The specimens were then polished using 1 µm diamond polycrystalline solution on a spec-cloth and followed by 0.04 µm colloidal silica. The samples were then cleaned by water and alcohol, then air dried. The microstructure was revealed by immersing the polished sample in Weck's reagent etchant (composed of 4% potassium permanganate and 1 % sodium hydroxide, and distilled

water). The microstructure was obtained from the cross-section of the welded joints using Zeiss AxioVert 40 MAT optical microscope.

III.1.2 Microstructure observations

Figure III.2 (a) presents a schematic representative of FSW process, the three directions of the weld are indicated as follow; Transverse direction (TD), normal direction (ND) and welding direction (WD). Figure III.2 (b) reveals a cross-section mapping of an FS welded aluminum joint using 1600 rpm and 250 mm/min. The metallographic sample preparation was according to the ASTM standards (ASTM-E3-11). This macroscopy mapping was obtained by taking consecutive images and assembling them together. Four regions were distinguished in the cross-section by their morphology, BM corresponds to the base material, HAZ to the heat affected zone, TMAZ to the thermomechanically affected zone and SZ to the stir zone. Such zones have been reported by studies of different material alloys (Dorbane et al., 2016; Mansoor et al., 2015b; Mishra and Ma, 2005). The region between the dash lines refers to the area tested in the tensile testing section (further discussed in the tensile testing section).
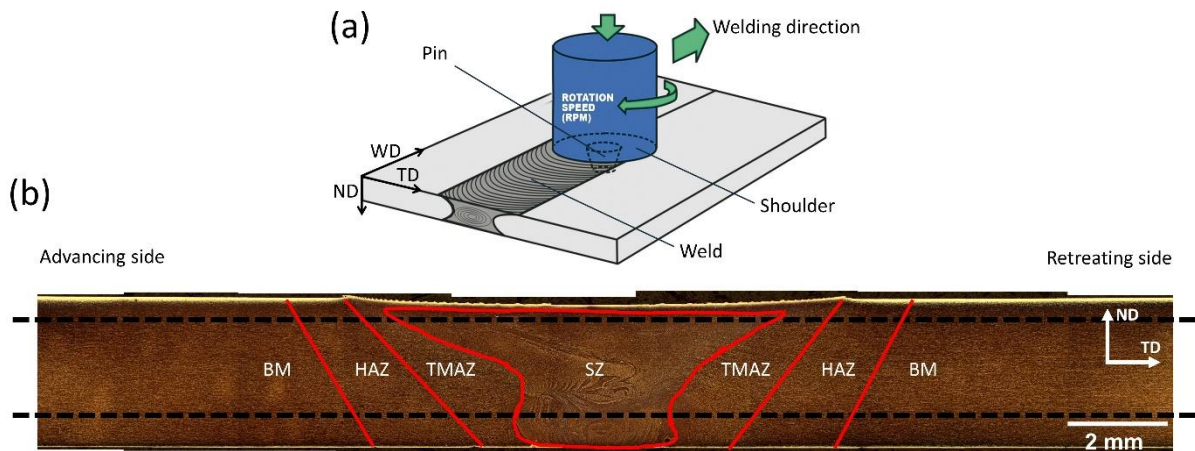
Figure III.2. (a) A schematic representative of FSW process. (b) Morphology of an FS welded Al/Al joint using 1600 rpm and 250 mm/min.

III.1.2.1 Macrograph

Figure III.3 presents macrograph of FS welded Al-Al joints cross-section using a 1600 rpm tool rotation speed and different tool advance rates. Figure III.3 (a) is a cross-section

obtained from a welded joint using 250 mm/min tool rotation speed. It can be observed from this figure that the joint has a defect in the bottom of the weld. This defect is due to an improper penetration depth, but it was removed by grinding for the tensile testing part. Figure III.3 (b) refers to a cross-section obtained from an FS welded Al/Al joint using 500 mm/min tool advance speed, it can be observed that the nugget shape is almost identical to the one obtained previously with some irregularities in the bottom nugget zone. Figure III.3 (c) and (d) present cross-sections obtained from welds performed using 750 mm/min and 1000 mm/min respectively. The nugget appeared to have a more homogeneous morphology compared to the previous welds. Moreover, a defect is perceived in the bottom of the weld; it is again due to the improper penetration depth. This defect was removed by grinding along the joint for the tensile testing specimens.
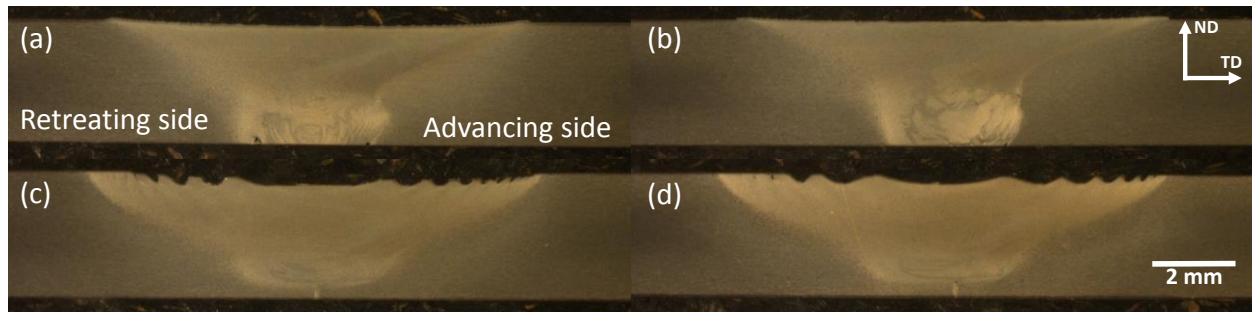
Figure III.3. Morphology of the cross-section of FS welded Al-Al joints using 1600 rpm and (a) 250 mm/min; (b) 500 mm/min; (c) 750 mm/min and (d): 1000 mm/min.

III.1.2.2 Micrograph observations

Previous studies confirmed the existence of such weld zones (Benavides et al., 1999; Jata and Semiatin, 2000; Liu et al., 1997; Mishra and Mahoney, 2001; Rhodes et al., 1997). These weld zones were reported again in this present study for grain size analyzes purpose. Grain size analysis of these zones will be studied in this work hereafter. Figure III.4 presents the microstructures of different regions obtained from a cross-section of a welded Al/Al joint using 1600 rpm tool rotation speed and 250 mm/min tool advance speed. The different zones were taken from the advancing side of the weld. Figure III.4 (a) is a microstructure of the base material obtained in the cross-section of the weld. The grain boundaries have apparently developed elongated shapes in the transverse direction; this is due to the rolling (45% reduction of the initial thickness). Also, clear intermetallic compounds or iron-rich phases (gray particles)

can be observed in the microstructure. The heat affected zone shown in Figure III.4 (b) is directly underneath the tool, was not mechanically deformed but has experienced heat input. It appears to have a slightly bigger average grain size than the base material. The thermo-mechanically affected zone (TMAZ) and the transition between TMAZ and stir zone (SZ) are presented in Figure III.4 (c) and (d) respectively. Fine grains are observed in the TMAZ with a consistent shape due to the metal flow resulted from the material stirring during welding. Figure III.4 (e) presents the stir zone, showing fine equiaxed grains with some non-dissolved iron-rich phases. Grain size measurements have been performed on the taken microstructure images. The BM exhibited a mean grain size of 21.12±9.34 µm while the HAZ exhibited a mean grain size of 24.52±10.59 µm. It is observed from Figure III.4 (a) and (b) that the heat affected zone has a slight increase in the grain size compared to the base material, which is evident due to the heat input experienced during the welding process. The stir zone exhibited fine equiaxed grains with a mean grain size of 2.99±0.83 µm obtained from the weld.
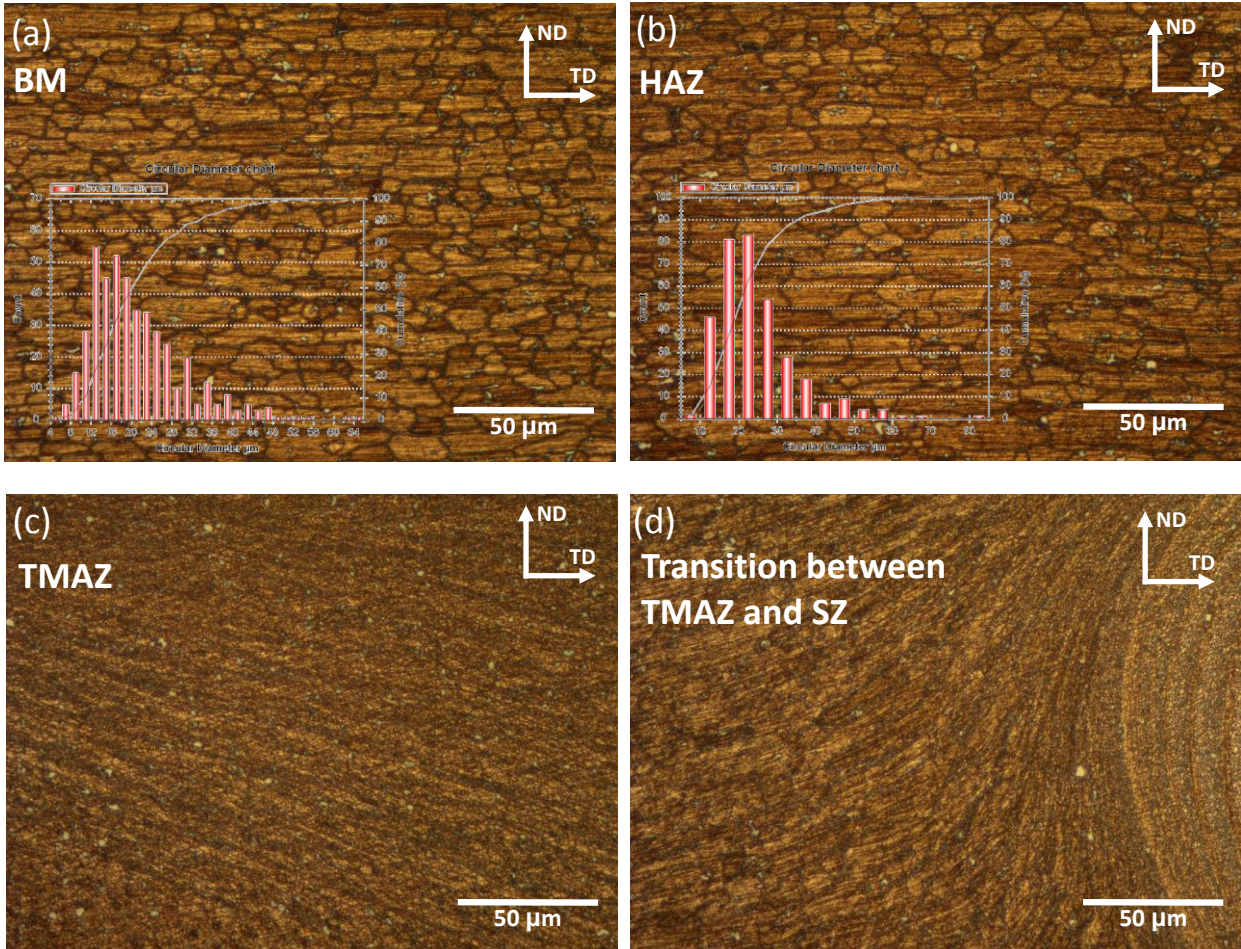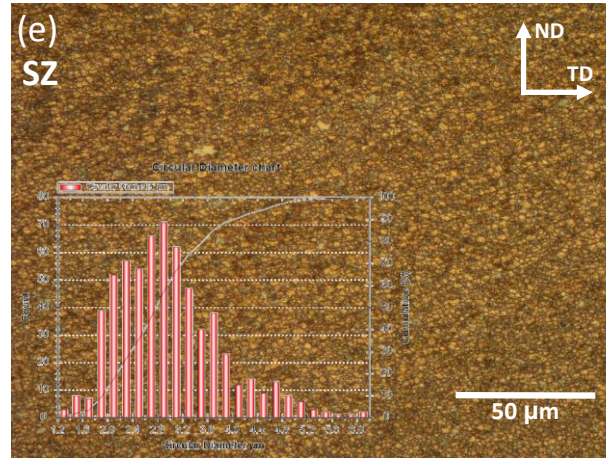
Figure III.4. Different zones of FSW zones welded using 250 mm/min_1600 rpm.

To analyze the effect of the tool travel speed on the grain size of the SZ, several micrographs were taken from the SZ and were measured using MagniSci grain size analysis software. Figure III.5 presents the nugget zone taken from FS welded Al/Al joints using 1600 rpm tool rotation speed and different tool feed rates. Figure III.5 (a) shows a microstructure of a welded joint using 250 mm/min. It can be observed that some of the precipitates are not completely dissolved during the process because the heat generated is highly inferior to the melting temperature of 6061 aluminum alloy during FS welding (Liu et al., 1997). Figure III.5 (b) represents a stir zone region taken from a sample using 500 mm/min tool advance speed. It can be observed that the grains are finer than the obtained from Figure III.5 (a). It is obvious because the induced heat is less with increasing the tool displacement speed. The same remark goes for Figure III.5 (c) and (d) where we observe that the grains are much finer with greater tool advance speed. Grain size measurements have been performed on these microstructure images; the specimen welded using 250 mm/min showed an average grain size of 2.99±0.83 µm while the microstructure of the specimen welded using 500 mm/min tool displacement speed resulted in an average grain size of 2.39±0.6 µm. A significant decrease in the average grain size is observed in Figure III.5 (c) and (d) where the obtained average grain size was 1.45±0.42 µm and 0.95±0.31 µm respectively.
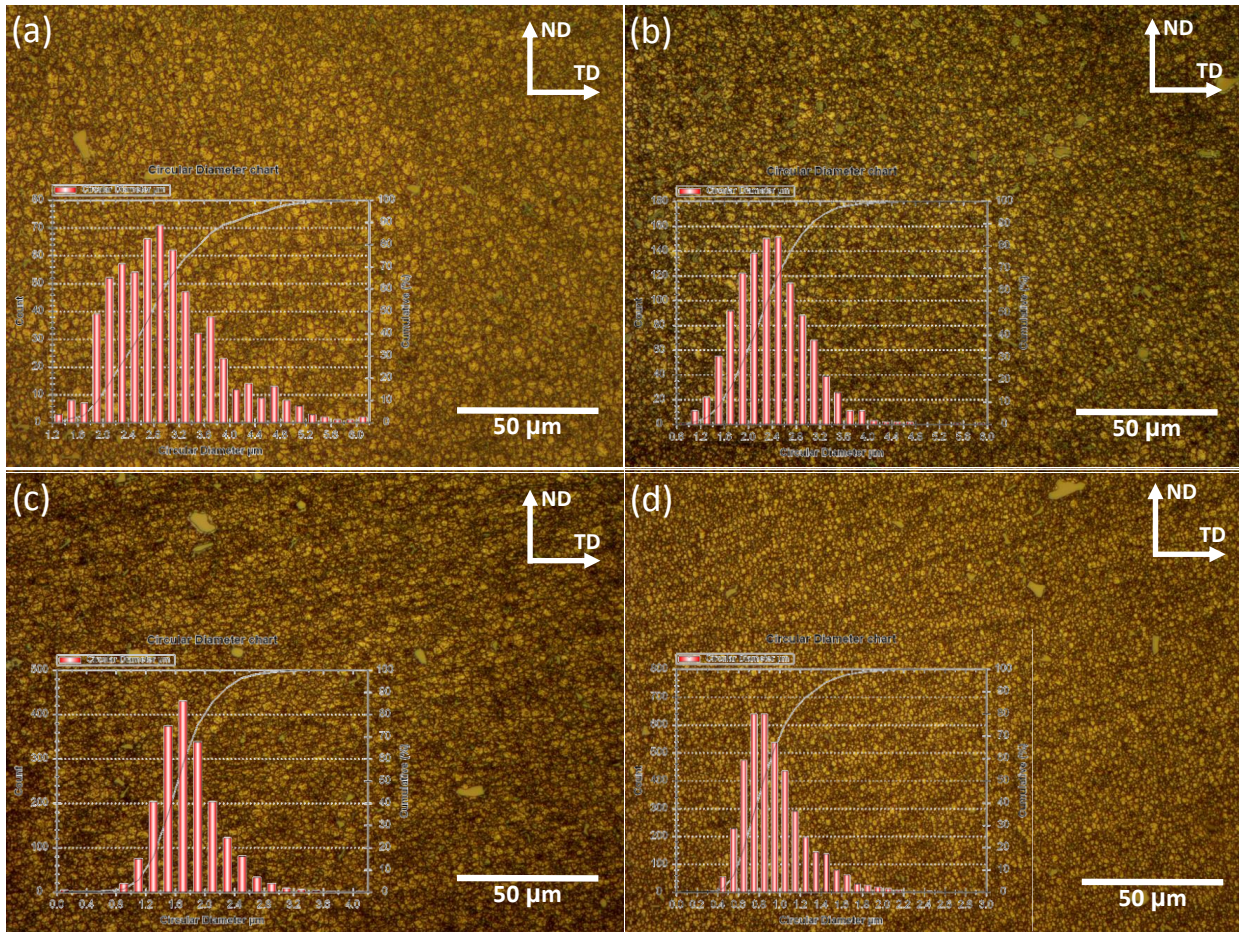
Figure III.5. Microstructure of the stir zones (SZ) obtained from FS Welded joints using 1600 rpm and: (a) 250 mm/min; (b) 500 mm/min; (c) 750 mm/min; (d) 1000 mm/min.

To investigate the relationship between the SZ grain size and the tool advance speed, the SZ average grain size diameter in function of the tool advance speed has been plotted in Figure III.6. The decrease in the grain size diameter is strongly related to the heat input as the tool advance speed increase as it decreases with increasing the tool advance speed. This trend can be explained by the fact that as the tool advance increases, the heat input decreases, resulting in finer grains.
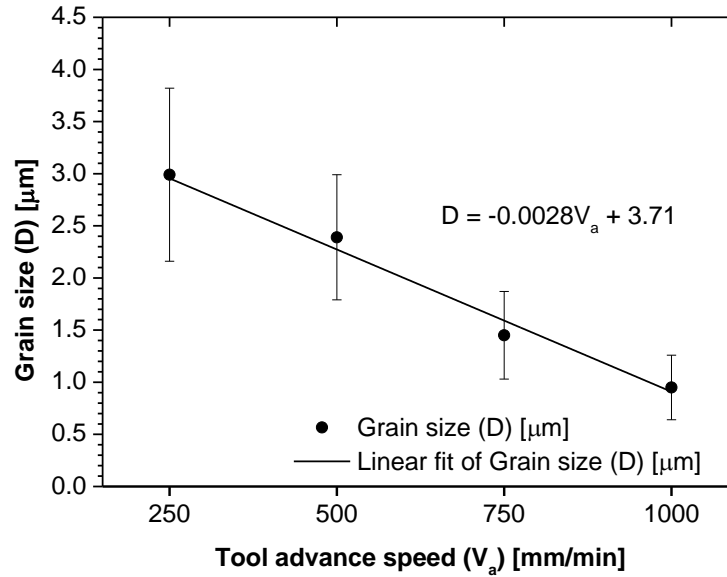
Figure III.6. Grain size of the SZ in function of tool advance speed

III.1.3 Microhardness testing

Microhardness examination can be an additional method to determine the different weld regions across the cross-section because each region will give a certain hardness which is different from the other regions. Figure III.7 shows the microhardness values in function of the distance from a welded specimen using 1600 rpm and 250 mm/min. We observe that the welded joint showed a W shape for the five measured lines. A similar trend was reported by other studies on different metal alloys (Fahimpour et al., 2013; Khodaverdizadeh et al., 2012; Kumar and Raju, 2012; Lim et al., 2004; Santos et al., 2011; Zhang et al., 2011). The mid-thickness hardness values were selected and calculated to determine the mean hardness values of the different zones distinguished on the advancing side of the cross section of the weld. The base material showed an average hardness value of 123.70±1.36 HV, the highest value in the graph. Then, the mean hardness value for the heat affected zone was found to be 105.86±7.07 HV, in this region we observe that its hardness is lower than that of the base material, it can be linked to the grain growth obtained due to the heat input during FSW. The thermomechanically affected zone mean hardness value was 86.33±6.06 HV. The stir zone mean hardness values were 87.63±2.75 HV; this value is higher than the value obtained for thermo-mechanically affected zone, because of the grain refinement in the nugget zone. Moreover, the microhardness values in the stir zone are inferior to the values obtained in the base material. This trend can be explained by the fact that

FSW induced severe plastic deformation and dynamic recrystallization, which is one of the main reasons why the iron-rich phases and precipitates could be dissolved or transformed in their shape due to the stirring resulting in a decrease in the hardness in the stir zone.
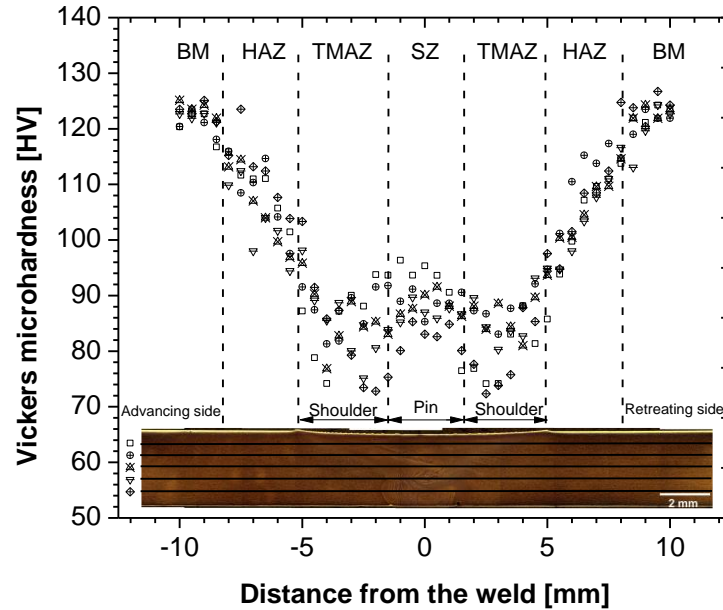
Figure III.7. Vickers microhardness of a cross-section welded using 1600 rpm and 250 mm/min

Another representation of the hardness results is plotted in Figure III.8, showing the different hardness values in 3D mapping colors, it can be observed from this figure that the region below the shoulder (TMAZ+SZ) exhibited lower hardness values compared to the other regions (HAZ+BM). Also, the lower values were identified to be in the bottom of the weld near the pin.
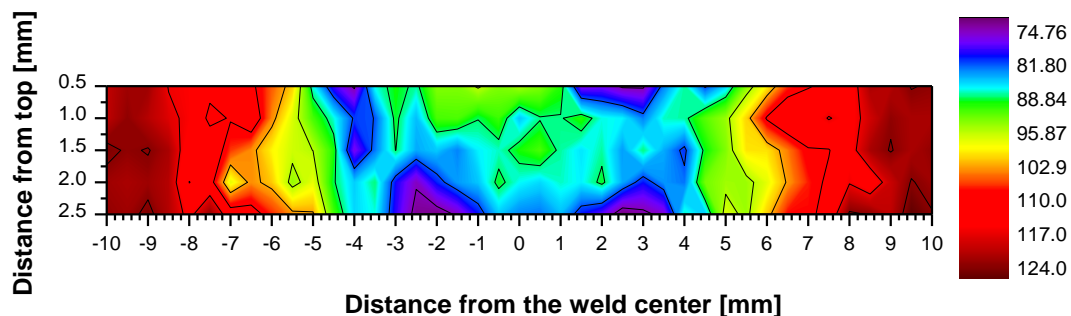
Figure III.8. Color mapping of a Vickers microhardness of a cross-section welded using 1600 rpm and 250 mm/min

Figure III.9 refers to the mid-thickness microhardness values obtained in function of the distance to the weld center for samples welded using a tool rotation speed of 1600 rpm and different tool advance speeds of 250 mm/min, 500 mm/min, 750 mm/min, and 1000mm/min. The overall microhardness values showed a W shape as observed in Figure III.9 (a). It is also observed that the microhardness values decrease with increasing the tool displacement speed for the HAZ, TMAZ, and SZ, this is referred to the decreasing in the heat generation during welding. The decreasing of the microhardness values in the stir zone compared to the base material can be explained by the fact that recrystallization has increased the softness of the material that leads to lower hardness in that zone.
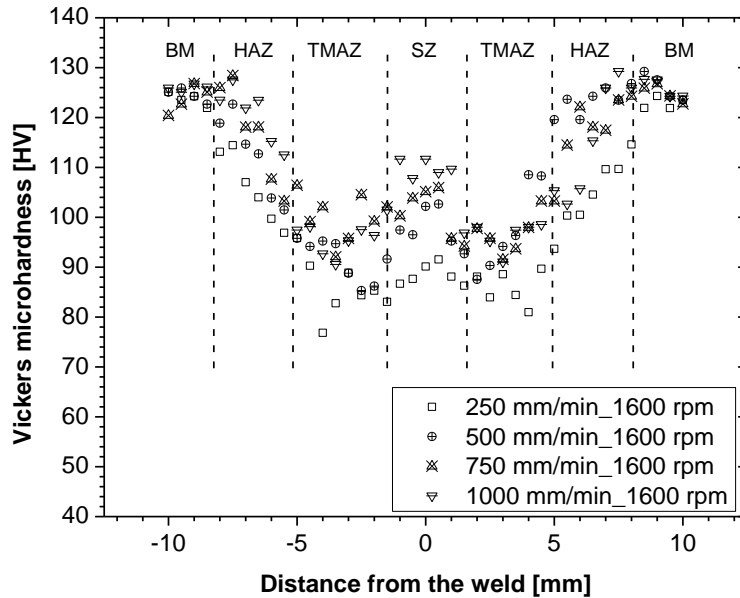
Figure III.9. Vickers microhardness of the mid-thickness values of samples welded using different welding speeds.

To emphasize the relationship between the grain size diameter and the microhardness values, the reciprocal of the square root of the average grain size ($d^{-1/2}$) in function of the average microhardness obtained along the transverse direction of the weld cross-section were plotted in Figure III.10. The average microhardness values were taken from the nugget zone welded using 1600 rpm tool rotation speed and 250 mm/min, 500 mm/min, 750 mm/min and 1000 mm/in welding speeds. It can be pointed out that a linear relationship between the microhardness and grain size was obtained in agreement with the Hall-Petch relationship. Which means that the

grain size is strongly dependent on the hardness. Such trend was reported by (Dorbane et al., 2016) and can be explained by the fact that the grains boundaries act as barriers to prevent higher deformation, and hence, smaller average grains gives greater hardness values.

$$HV = 37.784 d^{-(1/2)} + 69.007$$
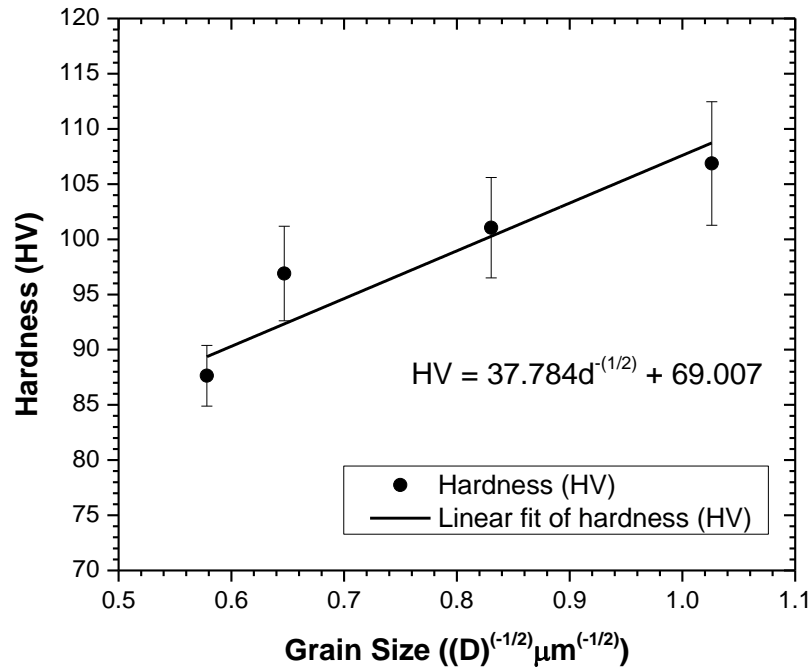
Figure III.10. Hall-Petch relationship between the grain size and microhardness.

III.1.4 Tensile testing

To analyze the deformation behavior of the welded joints, four different tool displacement speeds (250 mm/min, 500 mm/min, 750 mm/min and 1000mm/min) and a constant tool rotation speed (1600 rpm) were used to produce FSW joints, and tensile tested perpendicularly to the weld path. The tensile test specimens geometry according to the ASTM EM8 standards (ASTM-E8/E8M) are presented in Figure III.11. The tensile test samples taken from the welds were mechanically ground using 180, 600 and 1200 silicon carbide paper, their thickness was reduced to 2 mm to get rid of the bottom defects obtained in some welds, and to eliminate the wrinkles obtained in the top of the weld (Figure III.2).
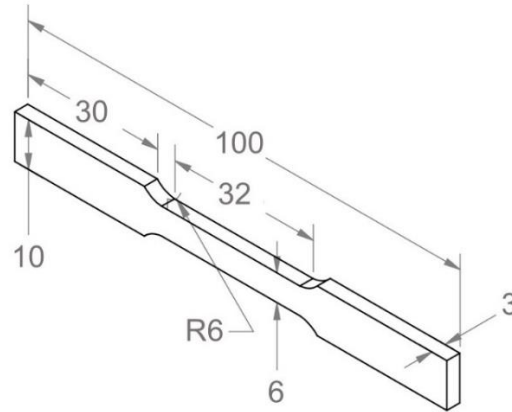
Figure III.11. Uniaxial tensile testing specimens geometry (E08/E08M) (dimensions are in mm)

Figure III.12 presents uniaxial tensile tests obtained at different temperatures under a strain rate of $10^{-3}s^{-1}$. Figure III.12 (a) shows stress-strain curves obtained from the uniaxial testing of the Al 6061-T6 base material compared with FS welded Al/Al joints using constant tool rotation speed of 1600 rpm and by displacement speeds of 250, 500, 750 and 1000 mm/min. It can be observed that the base material exhibited superior properties compared to the welded joints; the joints welded using 750 and 1000 mm/min tool displacement speed gave higher UTS compared to the joints welded using 250 and 500 mm/min. These results can be explained by the fact that inducing less heat generation enhances the joint properties. Figure III.12 (b) is obtained from tensile testing at 100°C, the strain to failure for the welded samples remain the same except for the sample welded using 250 mm/min where it failed too early compared to the other conditions. It can be also observed that a reduction in the yield strength occurred because of the temperature changes. The ultimate tensile stress started to reduce considerably at 200°C in Figure III.12 (c) with a different strain to failure values, and again, a reduction in the yield strength is observed in the stress-strain curves. A remarkable decrease in the ultimate tensile strength and strain to failure is observed in Figure III.12 (d), all the samples had approximately the same ultimate tensile strength and slightly different strain-to-failure. For all the curves obtained previously, it can be noticed that the curves exhibited work hardening and work softening before the final failure except for the base material where the work hardening was not significant at 300°C. The absence of the work hardening in the base material might be due to the transformation of the β-AlFeSi elongated iron-rich phases to α-AlFeMnSi during the homogenization temperature phase (Kuijpers et al., 2005; Nowotnik et al., 2007). Although, this

is not applicable for the welded joints were work hardening has been observed during the deformation process. But, at least, the flow strength decrease can be linked to the presence of more α-phases as explained by ([Lassance et al., 2007](#)) while conducting in situ SEM uniaxial tests and comparing with β-phases.
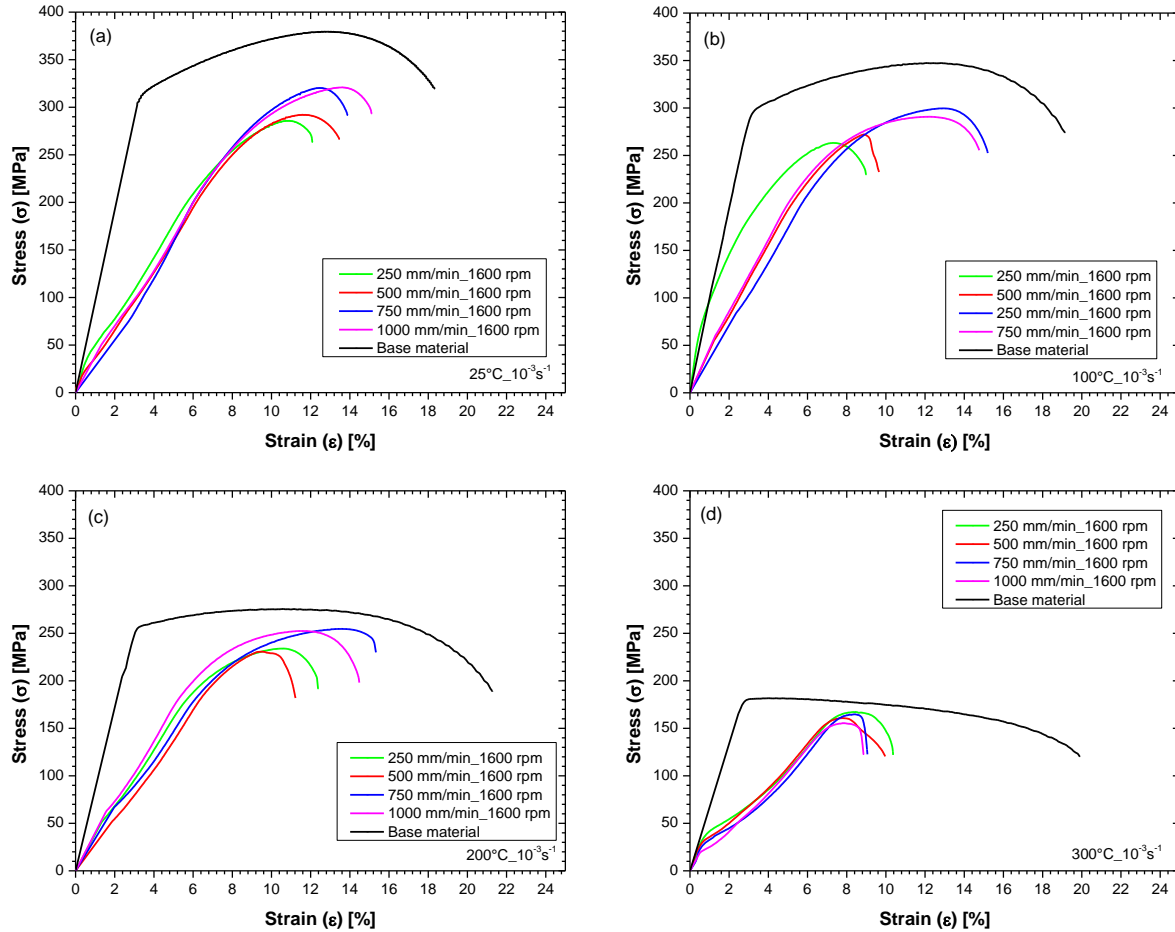
Figure III.12. Uniaxial tensile testing of FSW Al/Al joints using constant tool rotation speed of 1600 rpm and tool advance speed of 250, 500, 750 and 1000 mm/min. (a) at 25°C; (b) at 100°C; (c) at 200°C and (d) at 300°C.

To better investigate the results obtained previously, the ultimate tensile strength, strain to failure, yield strength, the strain hardening exponent and strain hardening coefficient in function of the temperature have been plotted separately to show better the material properties evolving at different temperatures. Figure III.13 (a) presents the ultimate tensile strength taken from the different tensile results in function of the temperature. It can be observed that the

ultimate tensile strength of the base material showed a superior value compared to the welded specimens. It can also be also noted that at room temperature. No significant difference was observed between the welded specimens. At ambient temperature, the joint efficiency varied between 75% and 84%, not much difference was observed between ambient temperature and 100°C. But, at 200°C, the joint efficiency started to increase to between 83% and 92%. Approximately the same maximum joint efficiency was observed at 300°C with a minimum joint efficiency of 88%.

Figure III.13 (c) presents the yield strength of the base material, compared to the welded specimens in function of temperatures, the base material showed superior values than the FS welded specimens. At 25°C, it can also be observed that the yield strength gradually decreased with increasing the temperature while testing the base material and the welded samples. The base material showed a decrease of 56% from 25°C to 300°C. While the specimen welded using 250 mm/min, 500 mm/min, 750 mm/min and 1000 mm/min showed a yield strength decrease from by 61%, 62%, 52% and 55% respectively. The welded specimens using 750 mm/min and 1000 mm/min showed higher yield strength than the samples welded using 250 mm/min and 500 mm/min, this can be explained by the fact that changing the welding speed decreases the heat input; providing better grain structure, but the joint may not be as resistant to yield as the samples welded using lower welding speed.
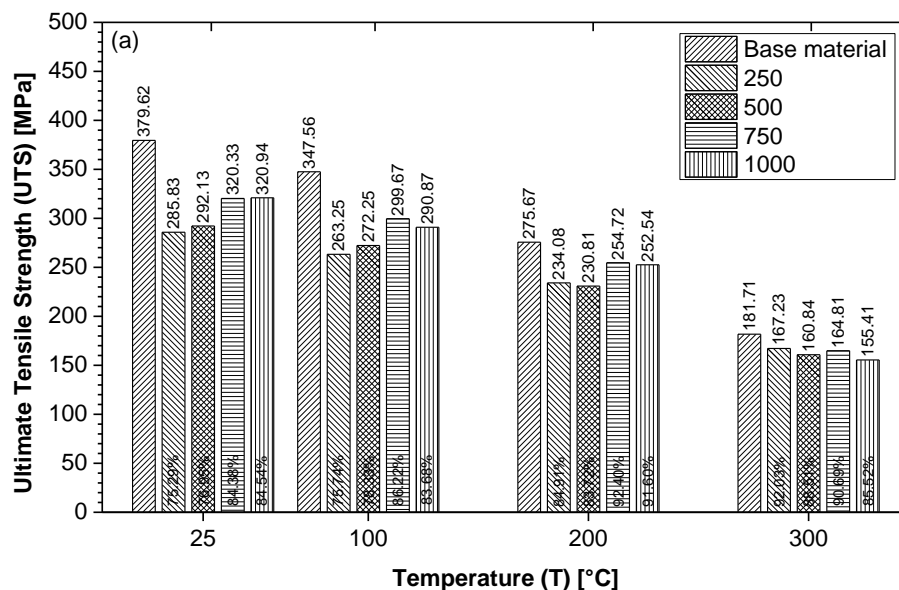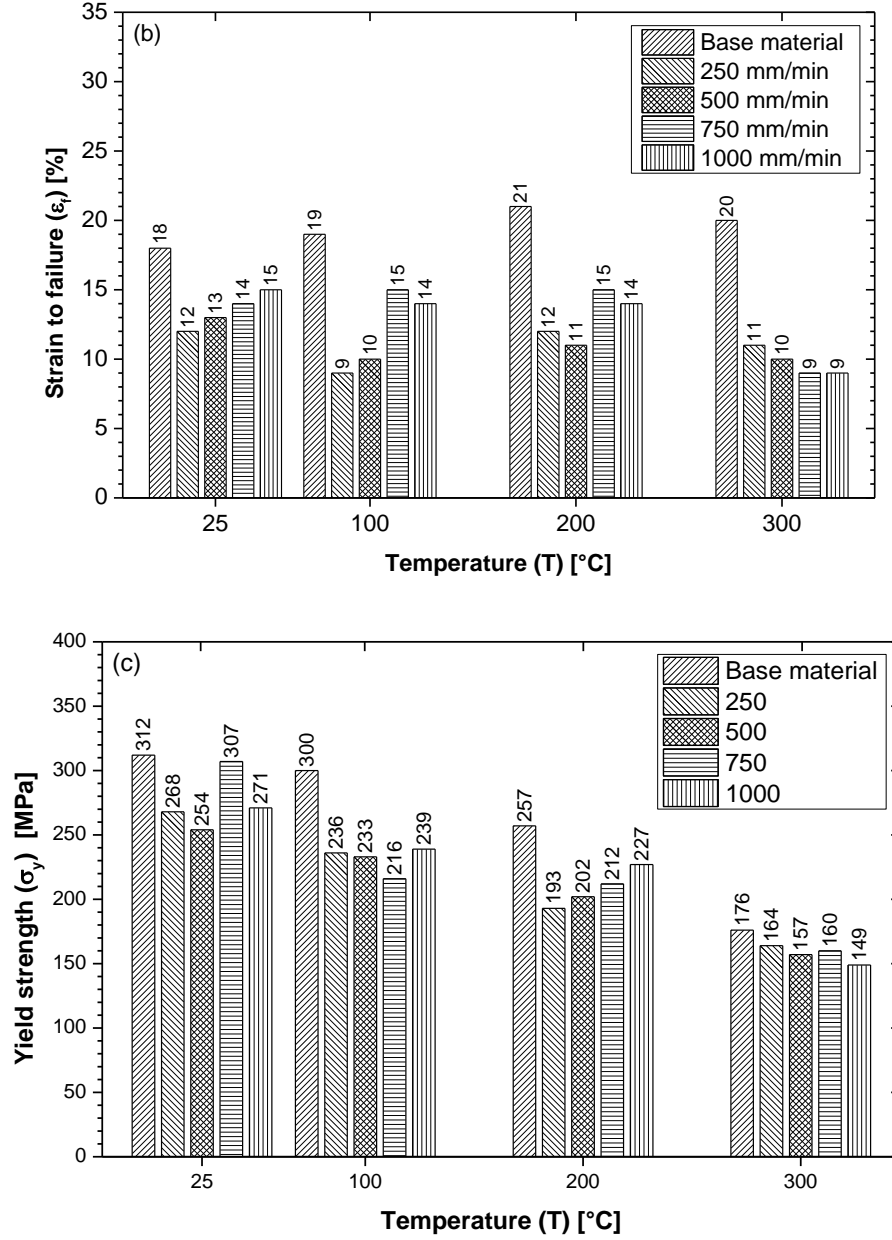
Figure III.13. (a) UTS; (b) ε_f; (c) σ_y of the base material and FS welded samples in function of different temperatures and strain rate of $10^{-3}s^{-1}$.

The characteristics of the material during the plastic deformation were analyzed using Ramberg-Osgood macroscopic model:

$$\sigma = \sigma_y + K\varepsilon_p^n \qquad\qquad \text{III.1}$$

With taking into account that σ is the stress, σ_y is the yield stress, ε^p is the plastic strain, K is the strain hardening coefficient, and n is the strain hardening exponent, K and n are acquired by linear regression, by transforming equation III.2 in a logarithmic formulation.

Figure III.14 (a) presents the strain hardening exponent variations of the base material compared to the welded samples at different welding speeds. It can be observed that the base material exhibited lower strain hardening compared to the welded samples, and decreased with increasing the temperature, while the 750 mm/min welding speed FS welded samples exhibited higher strain hardening at 25°C and 300°C. Figure III.14 (b) presents the strength coefficient. It is observed that the strength coefficient of the base material gradually decreases with increasing the temperature from 365 MPa at 25°C to 19 MPa at 300°C; it can be also noted that the base material exhibited the lowest values compared to the welded materials. For the global data, the strength coefficient values increased at 100°C, reaching maximum values of 862, 1152, 880 and 671 MPa for the samples welded using 250, 500, 750 and 1000 mm/min welding speeds respectively. Then gradually decreased to reach 123, 105, 273 and 137 MPa respectively.

It can be pointed out that the mobility of dislocations increases with increasing the temperature, leading to a decrease in the strength coefficient values; it can be also noted that the interaction between dislocations and alloying elements (such as magnesium silicide and iron-rich phases) act to increase the yield strength and reduce the ductility (Davis, 2004). These results can be linked with what we found in the microstructure section as the FSW modifies the grains size and orientation of the processed zone with recrystallization mechanisms.
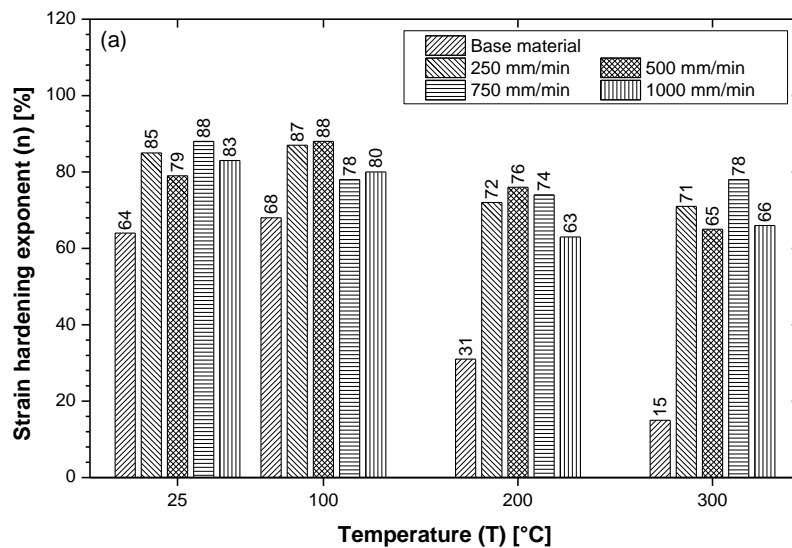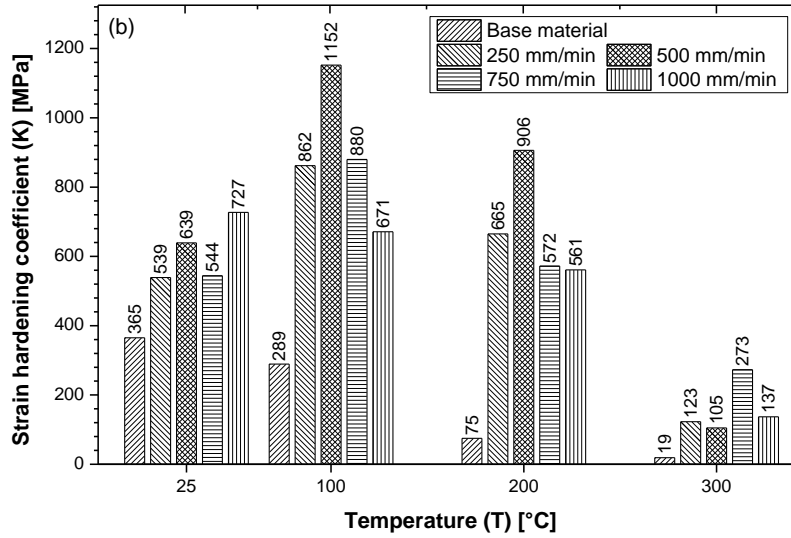
Figure III.14. (a) n and (b) K of the base material and FS welded samples in function of different temperatures and strain rate of $10^{-3}s^{-1}$.

III.1.5 Fracture analyses

To identify the damage region of the welded samples at different temperatures, the tensile tested samples were gathered based on the testing conditions and were photographed. Figure III.15 presents images of FSW tensile tested samples at various temperatures. Figure III.15 (a) and (b) show that the final fractures for the tensile tested samples at room temperature occurred between the heat affected zone (HAZ) and the thermomechanically affected zone (TMAZ) on the retreating side with different distances from the center of the weld. While, at 200°C, the final failure occurred in the center of the weld (SZ), except for the sample welded using 250 mm/min where the failure occurred between HAZ and TMAZ on the retreating side. However, at 300°C (Figure III.15 (d)), the final fracture occurred in the stir zone for all the welded samples using the four different tool displacement speeds. This phenomenon can be linked to the tensile test results obtained previously.

In a previous study, for the base material, it has been showed that the main deformation mechanism is a slip, and the crack initiation mechanism from room temperature to 200°C is the second phase particles fracture. However, at 300°C, another deformation mechanisms such as grain boundary sliding and grain fragmentation may be activated to conduct the deformation and failure at this temperature. Also, the main crack initiation mechanism is the interfacial

decohesion. These mechanisms can be applied to the welded specimens as well, with taking into account that the reduction in the strain to failure was reduced at 300°C due to the creep phenomenon that occurred at this temperature, and by the dynamic recrystallisation. The FSW made the material softer as we observed in the hardness measurements. The results obtained in Figure III.15 (d) where the final fracture can be explained by the fact that at higher temperatures, the stir zone becomes the weakest part of an FSW joint, at least for our study.
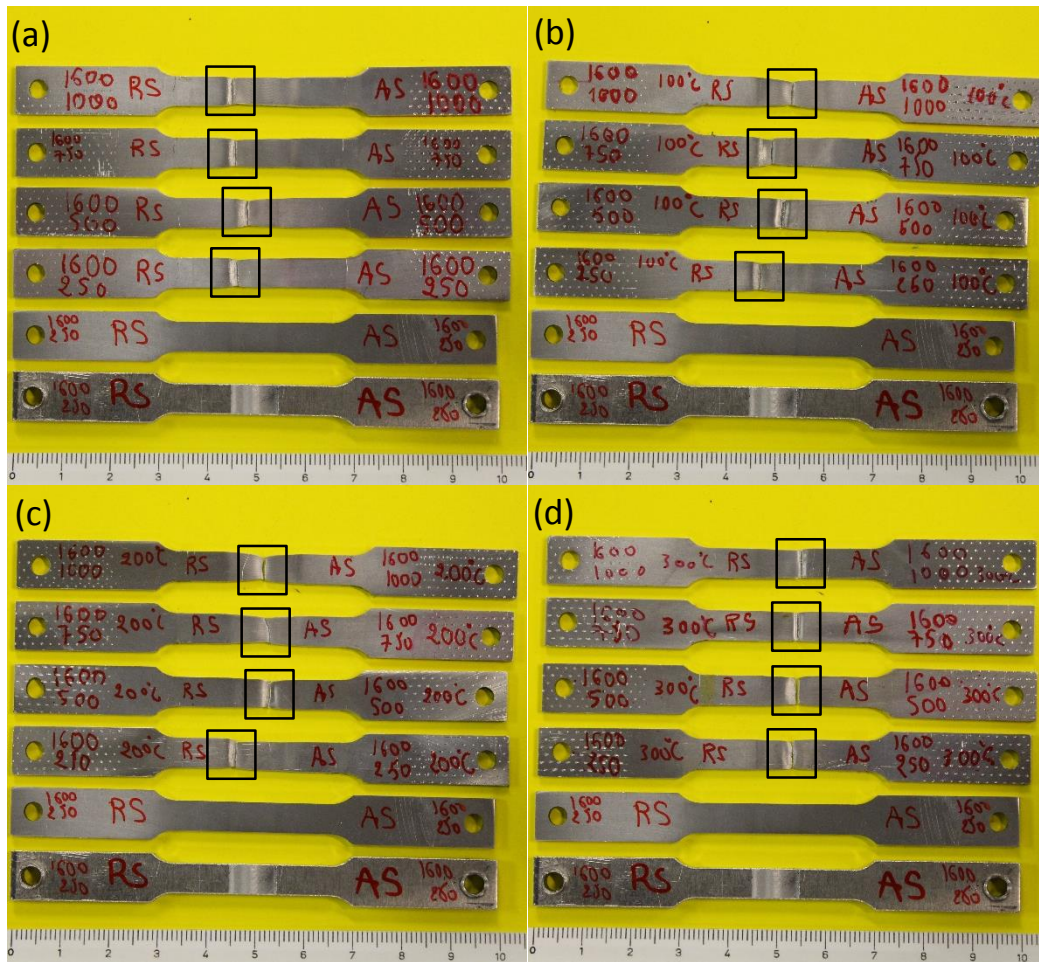
Figure III.15. FSW Al/Al after fracturing at different temperatures and welding conditions. (a) at 25°C; (b) at 100°C; (c) at 200°C and (d) at 300°C.

III.1.6 Conclusions

1. Friction stir welding of 6061-T6 aluminum alloy have been successfully processed, and internal defect-free joints were obtained.

2. Tensile testing of the obtained FSW joints was conducted at different temperatures and low strain rate of $10^{-3}s^{-1}$ and compared to the base material. The FSW joints exhibited approximately the same behavior as the base material regarding the decrease in the elongation at high temperature.

3. The hardness values showed a W-shape profile, and another representation of the hardness results showed that the region under the tool exhibited lower hardness than their counterparts.

4. The microstructure observations of cross-sections of the welds resulted in different weld aspects. Using 750 mm/min and 1000 mm/min tool rotation speed resulted in better weld morphology than their counterparts.

5. Grain size measurements of the stir zone showed that increasing the welding speed decrease the mean grain size and increase the hardness values. And a linear Hall-petch relationship between the grain size and the hardness was found.

6. The fractography observations showed that the final crack site of the welded joints is between TMAZ and HAZ between 25°C and 200°C, while at 300°C, the damage occurs in the stir zone itself.

7. The ultimate tensile strength, strain to failure and yield strength of the welded material was slightly lower than of that of the base material, due to the softening effect resulted from the welding process.

III.2 Microstructural Observations and Tensile Fracture Behavior of FSW Twin Roll Cast AZ31 Mg Sheets

Introduction

       The transportation industry has an increasing interest in replacing conventional alloys by lighter materials due to its attractive specific mechanical properties; magnesium alloys are an adequate replacement (Friedrich and Schumann, 2001; Tharumarajah and Koltun, 2007). Friction stir welding (FSW) is a promising joining method for magnesium alloys sheets. The reliability of structural parts joined by FSW is of high importance and, as such, investigating the microstructure, texture and mechanical properties of FSW joints is crucial to guide design engineers.

       Friction stir welding (FSW) is a solid-state joining process, introduced in 1991 by the welding institute. FSW is carried out by inserting a rotating tool with a shoulder and pin between two metal sheets held together and translating it along the weld line. The rubbing action of the tool shoulder on metal surface generates frictional heat that increases the temperature to reach 70 to 80% of the material's melting temperature (Hassan et al., 2003b; Lee et al., 2009). The frictional heating coupled with intense stirring and forging of the softened metal due to rotating pin creates the FSW joint (Xu et al., 2011). The microstructural and mechanical properties of welded joints are governed by the flow properties of the metal and the temperature distribution during welding. They are significantly dependent on the tool geometrical features and the choice of welding parameters e.g., rotation speed, feed rate, tilt angle and downward force (Buffa et al., 2006; Coelho et al., 2008; Cui et al., 2008; Etter et al., 2007; Leal et al., 2008; Lee et al., 2009; Pan et al., 2013; Peel et al., 2003; Su et al., 2003).

       FSW was originally developed in order to weld aluminum and its alloys, but recently it has been implemented to weld other materials such as copper and its alloys (Hwang et al., 2010; Lee and Jung, 2004; Sakthivel and Mukhopadhyay, 2007; Savolainen et al., 2012), steel and its alloys (Matsushita et al., 2011; Ofem et al., 2010; Park et al., 2003) and titanium and its alloys (Zhang et al., 2010b). Also, several studies have reported welding or processing of magnesium and its alloys using friction stir welding technique. (Afrin et al., 2008) and (Xunhong and Kuaishe, 2006) reported that, with optimized welding parameters, the maximum tensile strength of the weld reached 93% that of the base material. (Mansoor and Ghosh, 2012; Young et al.,

2015) modified the structure of the magnesium alloys using friction stir processing and studied the microstructural, mechanical and texture properties and their evolution with different processing conditions. Recently, (Ammouri et al., 2015) related the average grain size obtained during friction stir processing of twin-roll-cast AZ31B magnesium alloy to the Zener-Hollomon parameter calculated using an experimentally verified finite element model. Although, the optimization of the welding parameters such as the tool rotation speed; tool travel speed is critical to obtain high-quality welds, the optimization of the tool geometry and tool materials are also of high importance. (Padmanaban and Balasubramanian, 2009) studied the effect of tool material, pin profile and diameter and shoulder diameter on the FSW weld quality of 6 mm thick AZ31B plates.

A large body of literature exists on the fracture behavior of FSW joints in Al alloys, however in comparison, magnesium alloys have received rather less attention. Several studies have reported that in FSW of AZ31 Mg the tensile property, particularly tensile elongation, and UTS are significantly reduced which was mainly attributed to the variations in grain size, texture and nugget shape. A few studies on fracture behavior reported that when loading is applied perpendicular to the joint direction, depending on the FSW conditions, the fracture may occur in the heat affected zone (HAZ) or TMAZ either on the advancing side (AS or retreating side (RS) of the weld (Khodir et al., 2012; Li et al., 2014; Tao et al., 2014; Wan et al., 2014). The fracture behavior was mainly explained on the basis of through the thickness and length deformation and microstructural inhomogeneity in weld zones. Therefore, obtaining welds with a gradual grain size gradient between the different weld zones should be considered in the optimization schemes while selecting FSW parameters.

In this chapter, we investigate the microstructure, texture, and mechanical response of friction stir welds of twin roll cast (TRC) AZ31B Mg sheets. We study their tensile fracture behavior to reveal the interplay between microstructural characteristics and the propensity of crack initiation in different weld zones.

III.2.1 Experimental

III.2.1.1 Materials and welding

The friction stir welding setup was mounted on an HAAS VF6 vertical machining center as showed in Figure III.16 (for experimental details see (Kheireddine et al., 2013)). A backing

plate and two holders, moth made from C30 steel constituted the fixture to hold the workpiece firmly. The FSW tool was machined from SVERKER 21 (i.e., AISI-D2) tool steel supplied by Uddeholms AB (SE-683 85 Hagfors, Sweden). The tool was hardened after machining. The cylindrical tool has a shoulder diameter of 19 mm, and a pin of 6.4 mm in diameter with a pin length of 2.7 mm. Both the pin and the shoulder of the tool have smooth cylindrical shapes. All the welds, studied in this paper, were achieved using 1200 rpm tool rotation speed and 150 mm/min welding speed, and 1400 rpm tool rotation speed and 300 mm/min tool advance speed. The first process parameters (1200 rpm and 120 mm/min) yielded maximum strength (as reported by previous work of some of the authors (Ammouri et al., 2014).

Figure III.16. FSW equipment and setup.

The plates welded in this study were twin roll cast (TRC) AZ31B magnesium alloy rolled to a final thickness of 3 mm and supplied by POSCO, this material has been characterized at different temperatures and strain rates in a previous study by (Rodriguez et al., 2013). In all welds, welding was carried out parallel to the rolling direction of the AZ31B sheets.

III.2.1.2 Experimental Analyzes

To analyze the microstructure, the standard metallographic preparation method was used to prepare the samples following the ASTM standards (ASTM-E3-11). Etching was performed using an acetic picral solution composed of 4.2 g picric acid, 10 ml acetic acid, 70 ml ethanol and 10 ml water. Micrographs were taken using "Zeiss Axiovert 40 MAT" optical light microscope. The grain size analysis was performed using AxioVision software with a grain size analyzer module.

Microstructural and textural analyzes of the welds obtained by FSW of AZ31B sheets were performed using electron backscatter diffraction (EBSD). Specimens were cut from the different zones of the weld and oriented for observation in the in the TD-ND plane (refer to the section 3). The samples were prepared using a standard preparation method for EBSD. The EBSD analyzes were performed on an FEI Field Emission Scanning Microscope (FESEM). All scans were conducted using an accelerating voltage of 20 KeV and a probe current of ~10 nA. The TSL Orientation Imaging Microscopy (OIM) Analysis EBSD software was used to analyze the micrographs. A filter was used to eliminate any data with a confidence index (CI) below 0.1.

III.2.1.3 Mechanical properties

Mechanical properties of welds were characterized using Vickers hardness testing, with 100 g force for a dwell time of 15 s on the samples cut in the transverse direction to the weld. Uniaxial tensile tests were performed at 25 °C, 100 °C, 200 °C and 300 °C under constant strain rate of $10^{-3}s^{-1}$ using an MTS Insight electromechanical testing machine with a 30 kN load cell equipped with an LBO-series Thermocraft LabTemp (Environmental chamber). Tensile test samples were cut from the stir zone (SZ) to characterize purely the SZ behavior. Another set of samples was cut with the major axis being perpendicular to the welding direction, to study the influence of overall microstructural change caused by the friction stir tool movement on the mechanical properties. Samples from the SZ region and the ones taken perpendicular to the welding region are referred to in the manuscript as the FSW parallel direction and FSW perpendicular direction, respectively.

III.2.2 Microstructural observations and textural analysis

To optimize the weld, two combinations welding parameters were selected, 1400 rpm / 300 mm/min and 1200 rpm / 150 mm/min, a cross section mapping of the two welds were obtained as a first study. Figure III.17 shows cross section mapping obtained from welds with parameters as indicated previously, it can be observed that Figure III.17 (a) have a defect of type wormhole, this defect is basically due to the less heat generation induced into the material during welding. As a result, we observe that in Figure III.17 (b), a defect free-joint was obtained with a very good and clear morphology. The second weld was selected for characterization in what is next.
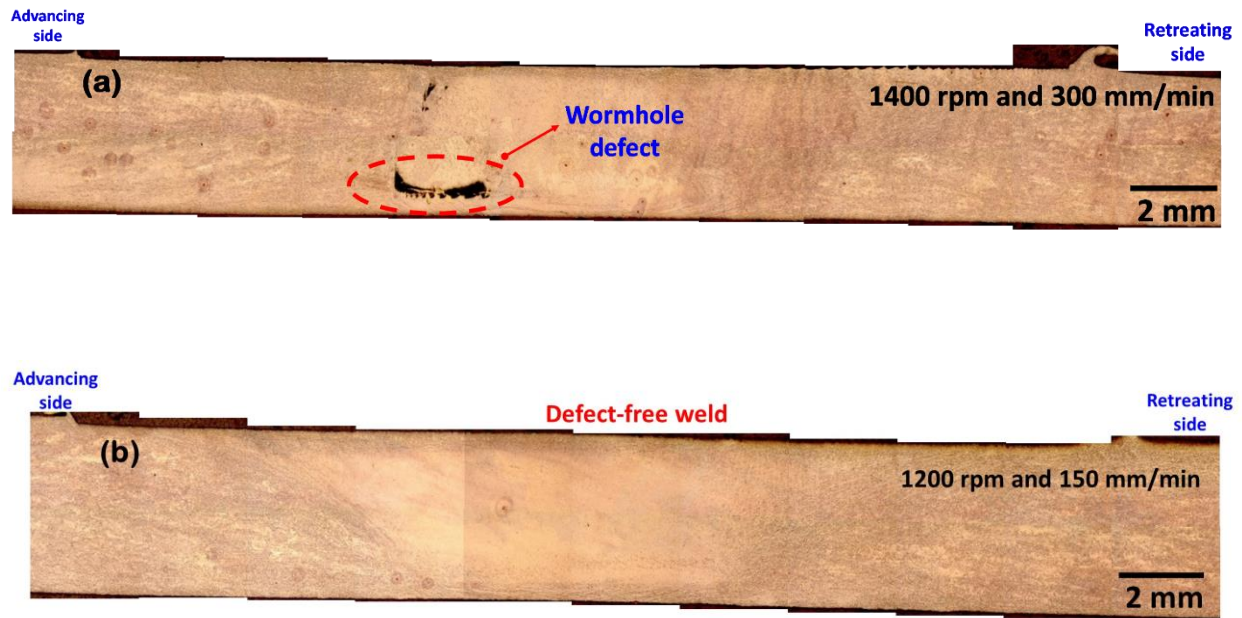
Figure III.17. Two welds performed using different welding parameters. (a) 1400 rpm and 300 mm/min; and (b) 1200 rpm and 150 mm/min.

Figure III.18 (a) shows a schematic illustration of the FSW process, the labeling of the three directions of the sheet are indicated; corresponding to the welding direction (WD), transverse direction (TD) and normal direction (ND). Figure III.18 (b) presents the overall structure of the friction stir welded joint cross-section (ND-TD plane). The contours of the different zones constituting the cross-sectional macrostructure were highlighted on Figure III.18

(b). Four distinguishable areas can be observed, such as the base metal (BM), heat affected zone (HAZ), thermo-mechanically affected zone (TMAZ) and the stir zone (SZ). Similar observations of the weld zones and shape of the nugget were reported by several studies on different alloys (Li et al., 2013; Mishra and Ma, 2005; Peel et al., 2003; Yang et al., 2012).
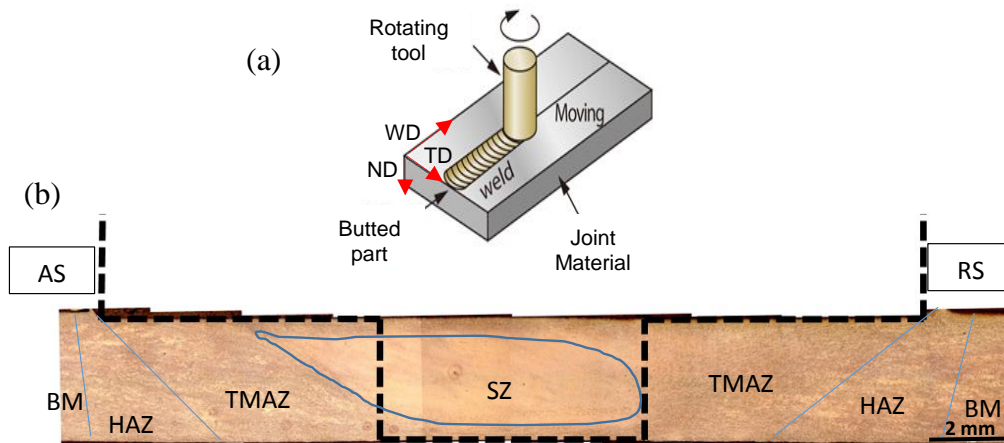
Figure III.18. (a): Schematic illustration of FSW process. (b): Microstructure of TRC AZ31B welded by FSW with parameters of 1200 rpm and 150 mm/min.

A cross section along a friction stir welded AZ31B joint is shown in Figure III.19 which shows the microstructure of the different weld zones identified in Figure III.18. The four weld zones clearly exhibit distinguishable microstructure. While the base metal contains mainly an equiaxed grain structure, the heat-affected zone may be characterized as a bimodal grain structure with a fair number of what appears to be twins present (as the AZ31B base metal was deformed by rolling). The thermo-mechanically affected zone shows elongated grains with a larger number of twins to be present. The stir zone contains mainly a homogeneous distribution of the grains. The average grain size of the different weld zones was found to be equal to 8.17 µm for the base metal, 10.45 µm for the heat affected zone, 11.47 µm for the thermo-mechanically affected zone and 12.13 µm for the stir zone. These observations are in line with observations of the microstructure of friction stir welded AZ31B reported by (Afrin et al., 2008; Albakri et al., 2013; Mansoor and Ghosh, 2012).
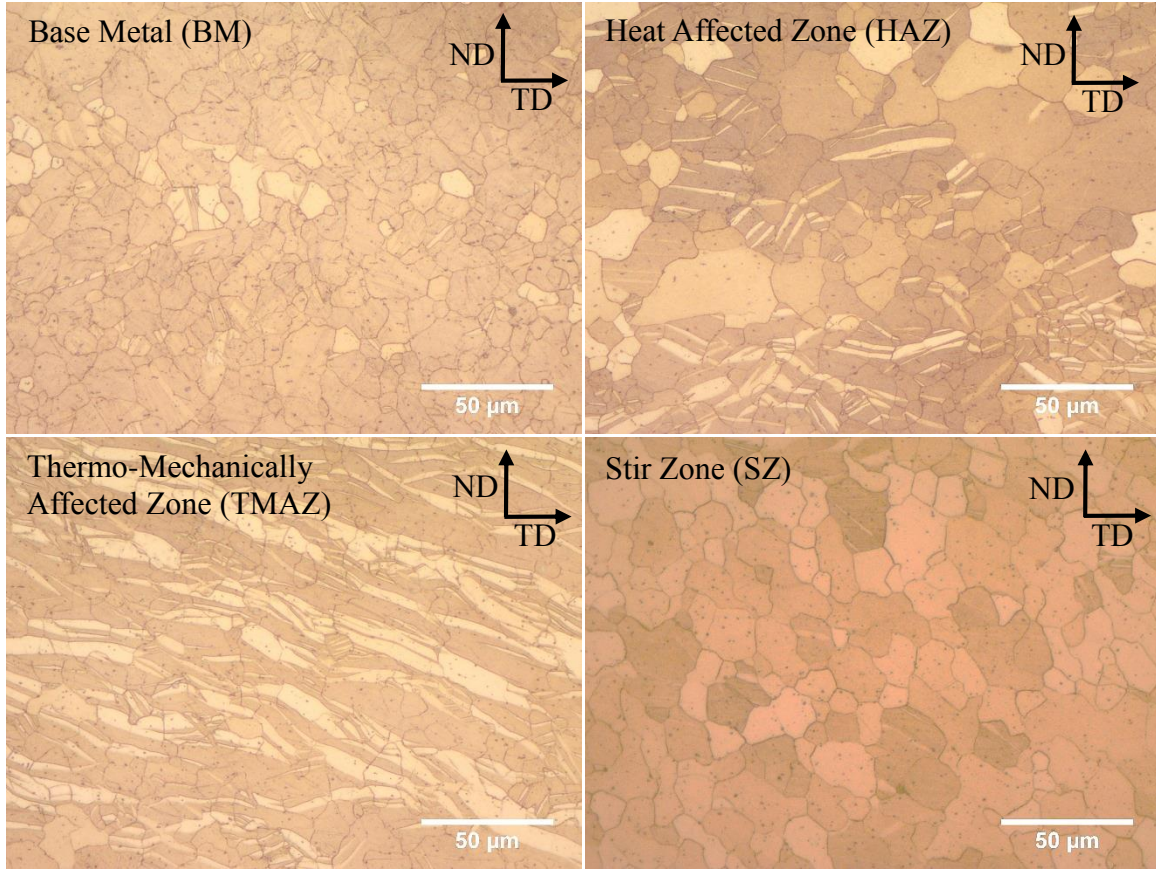
Figure III.19. The microstructure of the zones observed in the welded joint using parameters of 1200 rpm and 150 mm/min.

EBSD scans from three weld zones, SZ, TMAZ advancing side (AS) and TMAZ retreating side (RS) are shown in Figure III.20. The grain size, as well as the grains orientation on a larger number of grains, can be extracted from this figure. The EBSD-observed microstructures are in coherence with the optical microscope observation; a homogeneous distribution of the grains in the SZ and elongated grains with a larger number of twins in the TMAZ. The EBSD software revealed a grain size of 18.8 μm for the SZ, 7.8 μm for the TMAZ (AS) and 8 μm for the TMAZ (RS). The difference in the grain size between the OM micrographs and EBSD micrographs is likely due to the different grain size calculation methods used. From the EBSD scans the grain orientations of the three different weld zones was represented through pole figures in the (0002) and (1010) planes, as shown in Figure III.21. The as-received material has a typically rolled texture with the c axis of the grains perpendicular to the TD-RD plane (see (Rodriguez et al., 2013) and (Young et al., 2015)). Figure III.21 (a) shows the texture of the TMAZ and HAZ on the advancing side. The (0002) pole figure reveals a

texture strengthening with one basal peak that appears shifted from the left end of the ND axis. However, the (1010) pole figure shows a random orientation of the six prismatic planes. Figure III.21 (b) shows the texture of the nugget zone (stir zone). Two basal peaks appear along the ND axis shifted from the ends in the (0002) pole figure. The strengthening of the texture is most probably due to the rotation of the c axis around the transverse direction (TD). The (1010) pole figure shows some intensity peaks along the TD resulting from the lattice rotation. Finally, Figure III.21 (c) shows the texture of TMAZ and HAZ on the retreating side. The figure shows a high strengthening of the basal texture with the initial c axis being rotated about 10° degrees counter clockwise around WD.

SZ   TMAZ (AS)   TMAZ (RS)
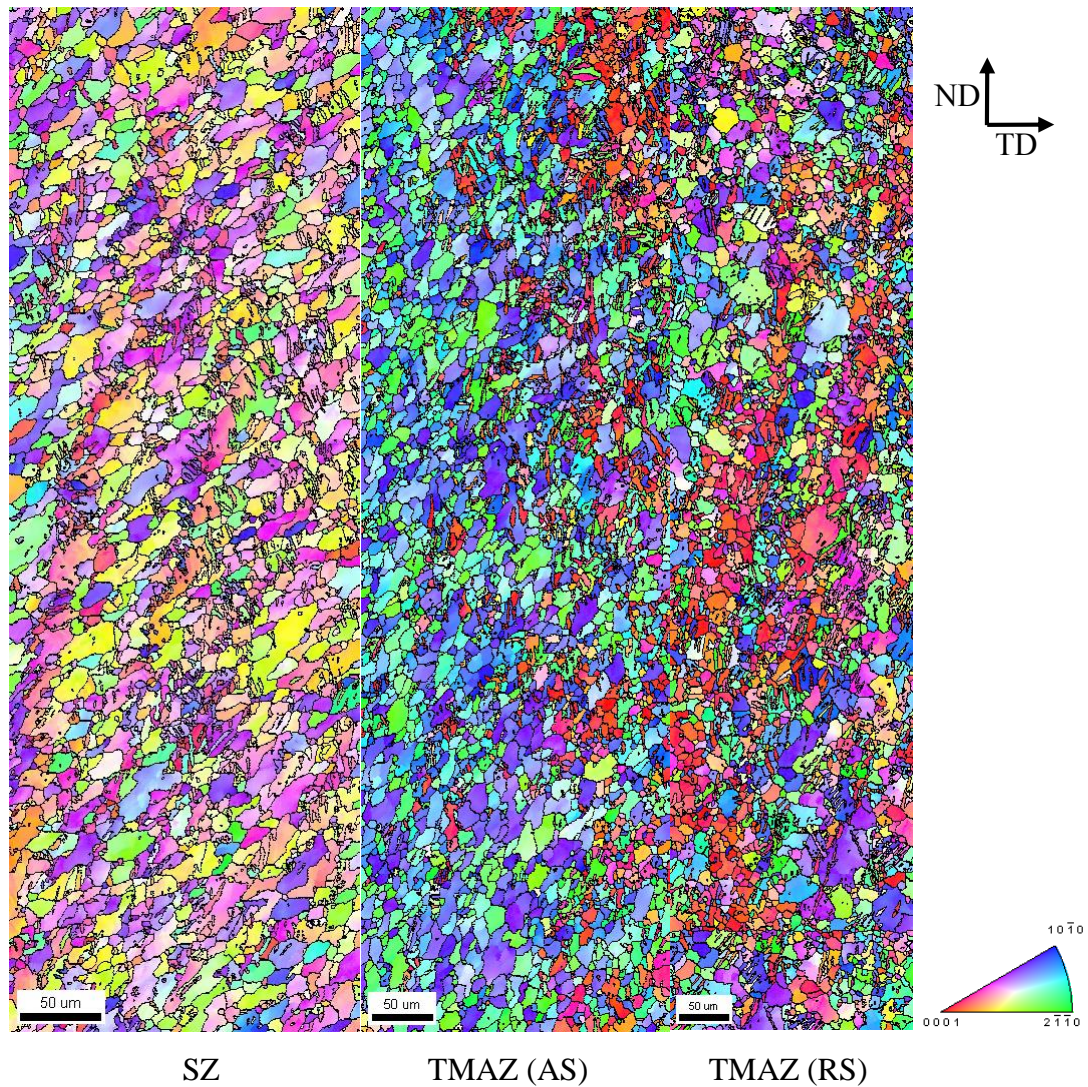
Figure III.20. EBSD scans of the three different weld zones, SZ, TMAZ in the advancing side (AS) and TMAZ in the retreating side (RS).
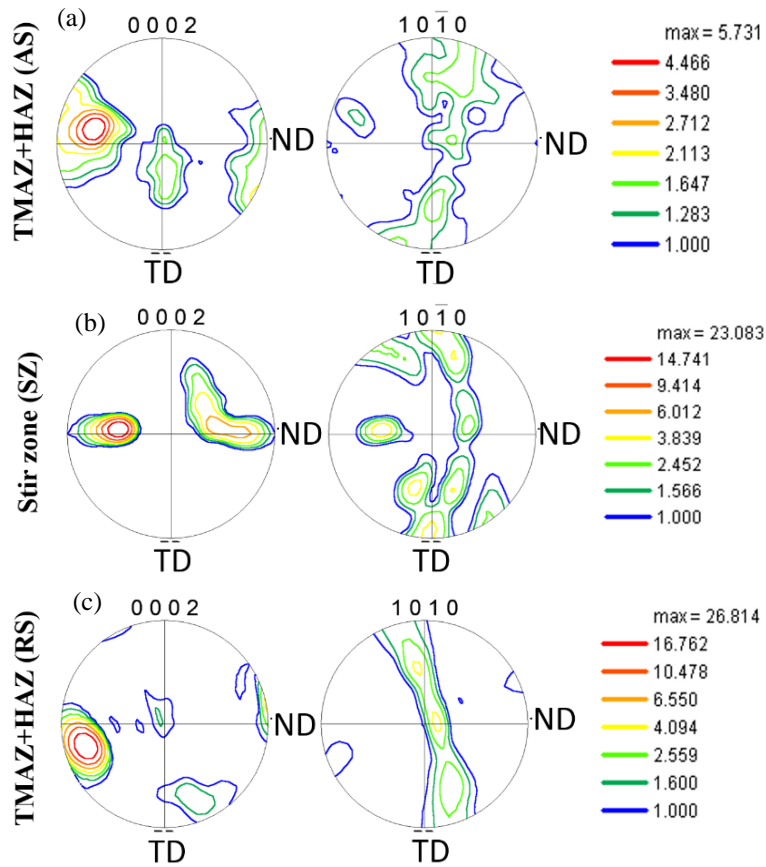
Figure III.21. Pole figures representing the texture for different samples, (a): TMAZ+HAZ on the advancing side; (b): Stir zone (SZ) and (c): TMAZ+HAZ on the retreating side (RS).

As a general observation, the SZ encountered severe deformation and the microstructural, and textural analysis showed a recrystallized microstructure with the strengthening of the basal texture. The microstructural and textural analysis of the TMAZ (AS) pointed to a low level of deformation as a slight modification of the microstructure and texture compared to the base metal was observed. A higher level of deformation appears to have taken place in the TMAZ (RS) as compared to the TMAZ (AS) (but a lower level of deformation has occurred as compared with the SZ with the strengthening of the basal texture).

III.2.3 Micro-Hardness Testing

In order to identify the zones in the weld where the fracture is more likely to occur, Vickers microhardness tests were performed along the TD on the TD-ND plane of the TRC friction stir welded sheets. The results are shown plotted in figure 5. A 100 g force was used with a dwell time of 15 s. The distance between two indentation points was 0.25 mm. The analysis was performed on three lines across the thickness of the sheet and parallel to TD as shown in Figure III.22, the distance between each line is 0.5 mm. The measured microhardness values were found to vary between a low of 55 and high of 85 HV. This variation is perhaps due to the evolution of the grain size along the TD in the joint as pointed out in Section 3. The center of the joint exhibited the least microhardness values compared to the other zones, which can be explained by the fact that the largest average grain size was obtained in the stir zone. Similar observations were reported by (Lee et al., 2003a) and Woo and (Woo and Choo, 2011) who reported that in addition to grain size evolution the dissolution of the precipitates due to frictional heating is one of the main causes of the decrease in the hardness and yield strength values.
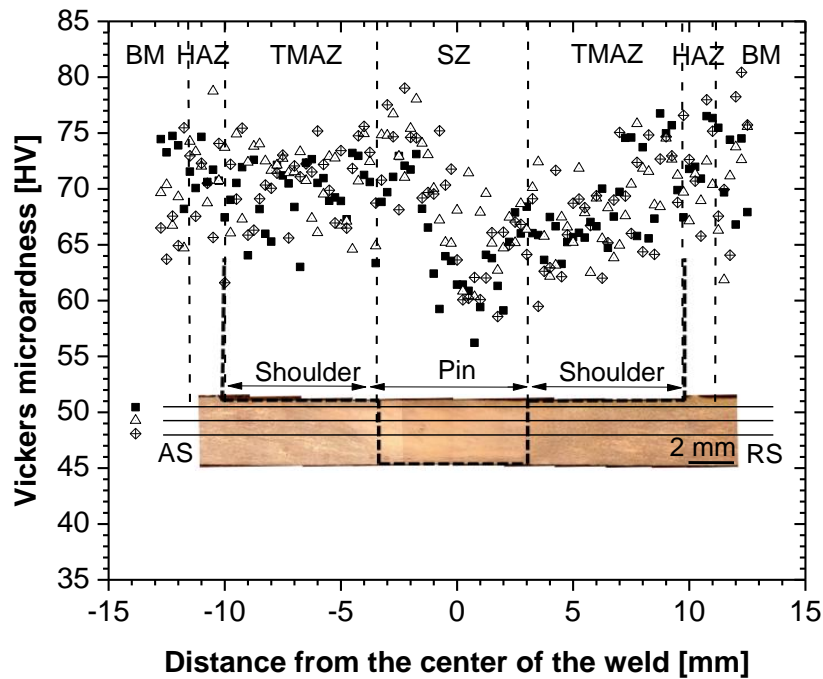
Figure III.22. Microhardness of the cross section of the weld.

The Vickers microhardness tests show a continuity in the microhardness values in the interface between the SZ and the TMAZ (RS) however a peak of microhardness was measured at the interface between the SZ and the TMAZ (AS). The discontinuity of the microhardness values between the SZ and the TMAZ (AS) can be related to an abrupt change in the microstructure, more precisely the grain size and also an abrupt change in the texture (as reported previously in the texture part). Therefore, we assume that a higher level of incoherency at the interface between the SZ and the TMAZ (AS) will induce higher accumulation of dislocation during loading that leads to the initiation of cracks. Figure III.23 presents a color mapping of the cross section of the weld obtained previously, it shows that discontinuity discussed in the previous figure, and how the microhardness is higher on the advancing side compared to the retreating side, with a drop in the center (blue color).
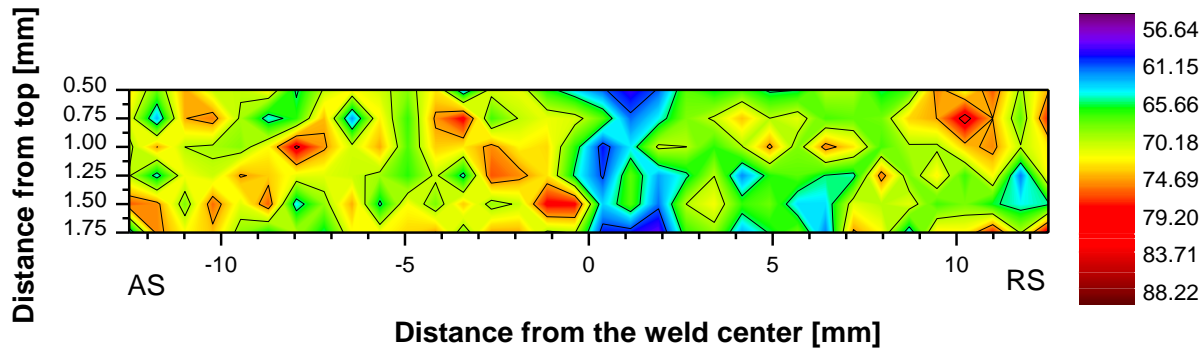
Figure III.23. Color mapping of the microhardness of the cross-section of the weld.

To highlight the relation between grain size and microhardness values, Figure III.24 plots the reciprocal of the square root of the average grain size ($d^{-1/2}$) as a function of the micro-hardness obtained along TD of the weld cross-section. Average hardness values are taken from the stir zone, the thermo-mechanically affected zone, the heat-affected zone, and the base metal were plotted in function of the average grain size of those different zones. It can be highlighted that the Vickers hardness values are strongly dependent on the grain size. A linear relation was

found and it is referred to as the Hall-Petch relationship. Similar trend was reported by (Afrin et al., 2008) who reported that the grain boundaries act as sinks of dislocation hence smaller grain size results in higher hardness.
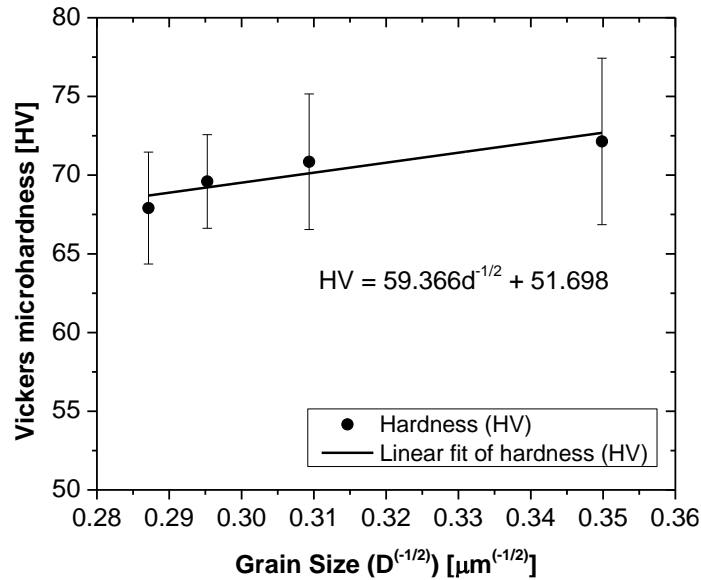
Figure III.24. Relationship between the grain size and micro-hardness.

III.2.4 Uniaxial Tensile Testing and fracture initiation

The quality of the weld can be verified first by characterizing the mechanical properties under tensile testing at different temperatures to account for potential ranges of service conditions. The tested samples were used to reveal the possible mechanisms that lead to fracture. Two types of tensile samples were machined from the joined AZ31B sheets: with their axis parallel (referred to as *FSW parallel direction* samples) and perpendicular to the welding direction (referred to as *FSW perpendicular* samples). The geometry of the tensile test samples is according to the ASTM E8 standards (ASTM-E8/E8M) and presented in Figure III.25. And the tensile tests have been established with respect to the ASTM E21 standards (ASTM-E21-09). The tensile test samples were ground to eliminate any wrinkles left on the surface by the FSW process or by the subsequent machining. The joint strength was measured for both types of samples. It is worth pointing out that the FSW tool pin diameter was equal to 6.4 mm, and the

sample gauge width is 6 mm. Therefore, the *FSW parallel direction* samples represent the stir zone behavior under uniaxial loading. Uniaxial tensile tests were performed at 25°C, 100°C, 200°C and 300°C under constant strain rate of $10^{-3}s^{-1}$ using an MTS Insight electromechanical testing machine with a 30 kN load cell equipped with an LBO-series Thermocraft LabTemp laboratory oven (Environmental chamber).
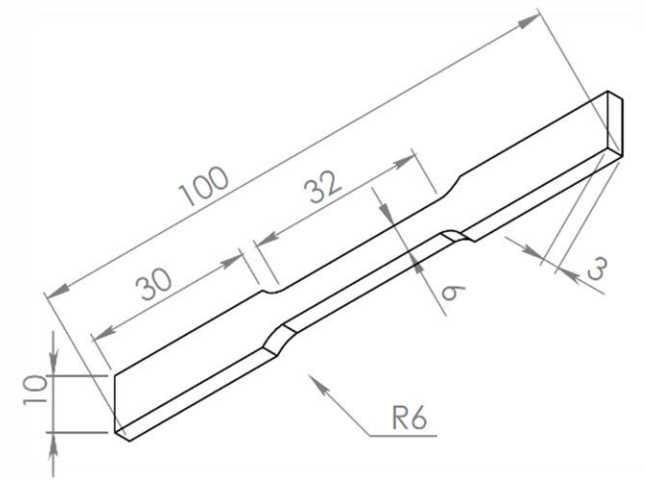
Figure III.25. Uniaxial tensile testing geometry (ASTM E8/E08M) (dimensions are in mm).

Figure III.26 presents the uniaxial true stress-strain curves of the base metal[1], the *FSW perpendicular direction* and *FSW parallel direction* samples at different temperatures. Overall, it was observed that the base material samples exhibit higher yield stress and ultimate tensile strength than the FSW perpendicular and parallel samples. As expected, it was observed that the FSW perpendicular samples exhibit higher ultimate tensile strength than the FSW parallel samples. Those last two observations can be explained by the grain size difference in the studied zones; we pointed out in section 3 that the stir zone has the largest average grain size. The grain boundaries act as dislocation barriers during deformation, as the stir zone has fewer grain boundaries. Therefore, we would expect that the stir zone would exhibit the lowest yield stress and ultimate tensile strength. These results were in agreement with the microstructure and microhardness data presented in section III.2.3. It was also observed that only work hardening

---

[1] The stress was calculated $\sigma = F/A$ with F being the measured load and A the current cross-sectional area. A was calculated by assuming that the material deforms at a constant volume although this assumption doesn't hold true after necking.

was present in these stress-strain curves. Figure III.26 shows that the FSW perpendicular samples encountered the lowest strain to fracture. The fracture in those samples occurred between the stir zone and the thermo-mechanically affected zone on the advancing side. The interfacial region between the SZ and the TMAZ (AS) is characterized by a higher degree of incoherency as an abrupt change of the texture is reported in section III.2.2.
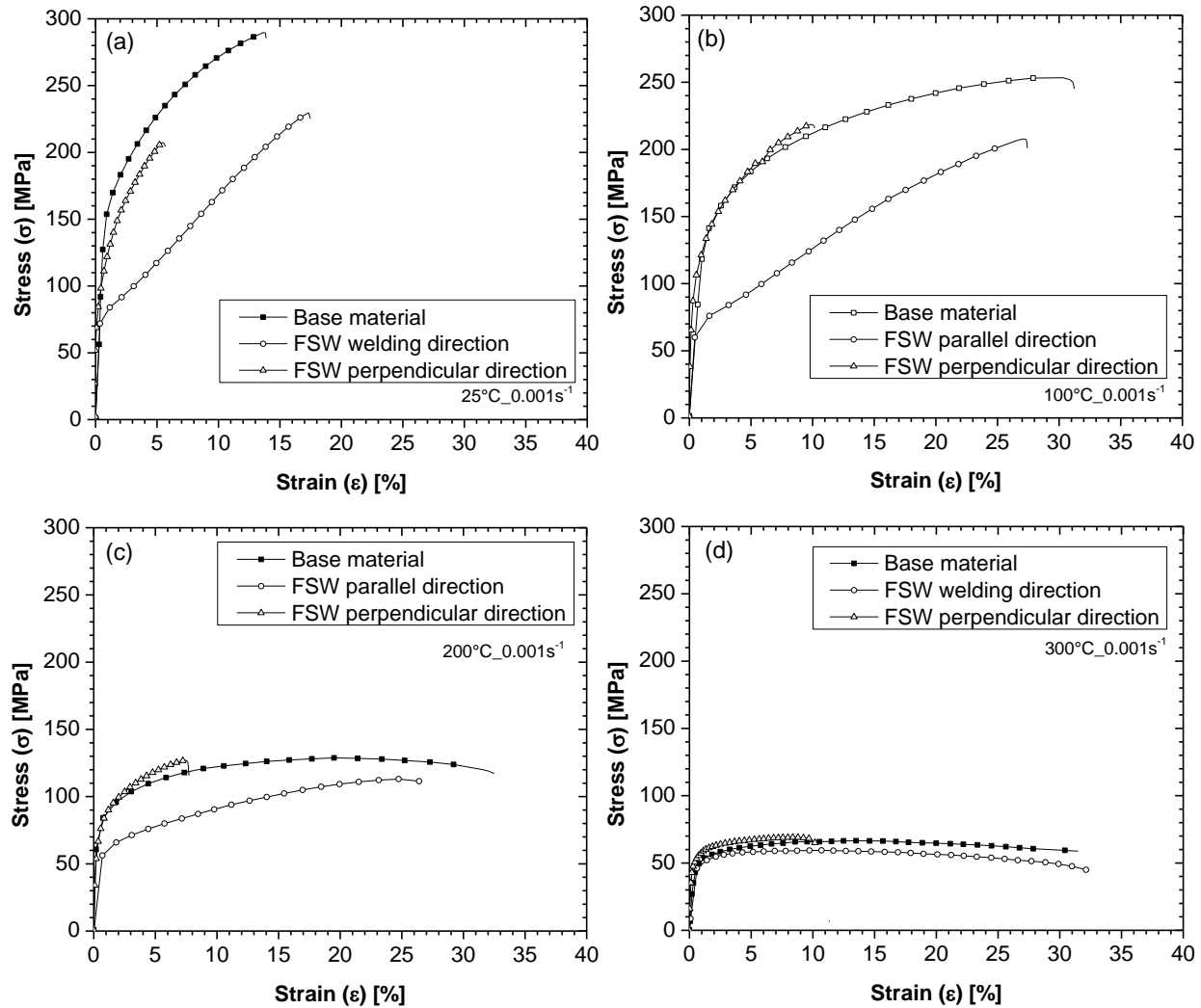
Figure III.26. True stress-true strain curves of uniaxial tensile tests of AZ31B base material, FS welded tested in the parallel direction, and perpendicular direction under strain rate of $10^{-3}s^{-1}$ (a): 25°C, (b): 100°C, (c): 200°C and (d): 300°C.

With increasing temperature we observed, for all samples, a decrease in the yield stress and ultimate tensile strength and an increase of the strain to fracture. It can be also reported that the work hardening decreased with increase in temperature. Work softening was not observed at RT for all samples but at 100 °C the base metal showed some softening, however, the welded samples didn't show any softening as they fractured after reaching the ultimate tensile strength. At 200 °C, it was observed that the base material shows work hardening and work softening during deformation and the welded material experienced work hardening and slight work softening before fracture. At 300°C, the work to softening was predominant in the deformation process before the fracture for the base material, and both welded specimens.

The evolution of the mechanical properties and more precisely the yield stress, ultimate tensile strength, the strain to fracture for the different samples and the Ramberg-Osgood hardening and plastic flow resistance coefficients (base metal samples, FSW parallel samples, and FSW perpendicular samples) tested at four different temperatures at are summarized in Figure III.27. Figure III.27 (a) shows that the yield stress gradually decreased with increasing temperature for the three tested samples; from 159 MPa to 56 MPa for the base metal, from 90 MPa to 49 MPa for the FSW perpendicular samples and finally from 77 MPa to 43 MPa for the FSW parallel samples. As was pointed out previously, the yield stress of the FSW perpendicular samples is higher than the yield stress of the FSW parallel direction. The ultimate tensile strength comparison of both base material and FSW samples in Figure III.27 (b) showed a significant decrease with increasing temperature; from 289 MPa to 66 MPa for the base metal, from 207 MPa to 69 MPa for the FSW perpendicular samples and finally from 229 MPa to 59 MPa for the FSW parallel samples. The strain to fracture, Figure III.27 (c), showed a significant increase in its values from 25°C to 300°C, 160% for the base metal, 83% for the FSW perpendicular samples and finally 100% for the FSW parallel samples. The FSW parallel samples showed higher ductility than the base material at room temperature and 300°C and slightly inferior values at 100°C and 200°C. The FSW perpendicular samples showed the lowest strain to fracture with a fracture occurring between the TMAZ (AS) and the SZ.
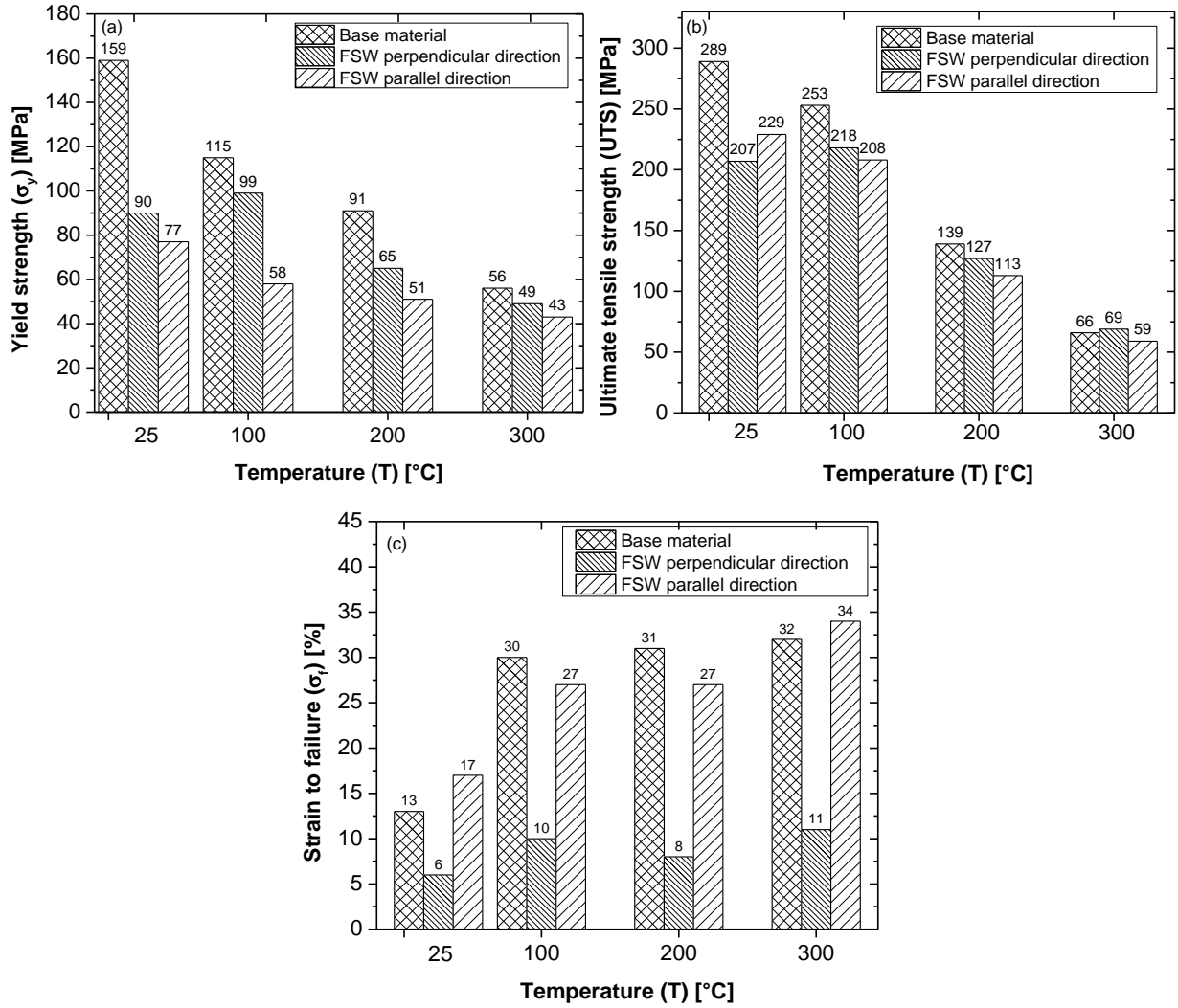
Figure III.27. (a) Ultimate tensile strength, (b) Yield strength, (c) Strain to failure of the base material and FSW specimens in the perpendicular and parallel directions, at different temperatures and constant strain rate of $10^{-3}s^{-1}$.

The variations in the mechanical properties during the plastic regime were studied using the Ramberg-Osgood macroscopic model:

$$\sigma = \sigma_y + K\varepsilon_p^{\,n} \qquad\qquad \text{III.2}$$

where σ is the stress, σ_y is the yield stress, ε^p is the plastic strain, K is the plastic flow resistance coefficient and n is the strain hardening exponent. The K and n referred to as the Ramberg-Osgood coefficients were obtained by linear regression, by writing Eq. III.2 in logarithmic formulation.

Figure III.28 (a) shows an overall decrease in strain hardening with increasing temperature. The FSW parallel samples exhibited the highest strain hardening at RT and 100°C. However, the base metal showed the highest strain hardening at higher temperatures. Figure III.28 (b) shows the effect of temperature on the plastic flow resistance coefficient. As a general trend, it is observed that the values of the coefficient K increase with increasing temperature and the highest values were found for the FSW perpendicular samples, while the lowest values were found for the base material. A gradual change in the coefficient K was noticed; from 652 MPa to 69 MPa for the base metal, from 1096 MPa to 96 MPa for the FSW perpendicular samples, and finally from 780 MPa to 68 MPa for the FSW parallel samples. It is worth noticing that the samples taken from relatively homogeneous materials (base metal and FSW parallel samples) exhibit similar values of coefficient K. However, much higher values are obtained for coefficient K with the FSW perpendicular samples, which may indicate the presence of high density of dislocation accumulation that translates by a higher hardening. Again, this observation is in coherence with our findings in sections 3 and 4, more precisely; the presence of incoherent interfaces between the SZ and the TMAZ (AS) which will act as sink for dislocations.
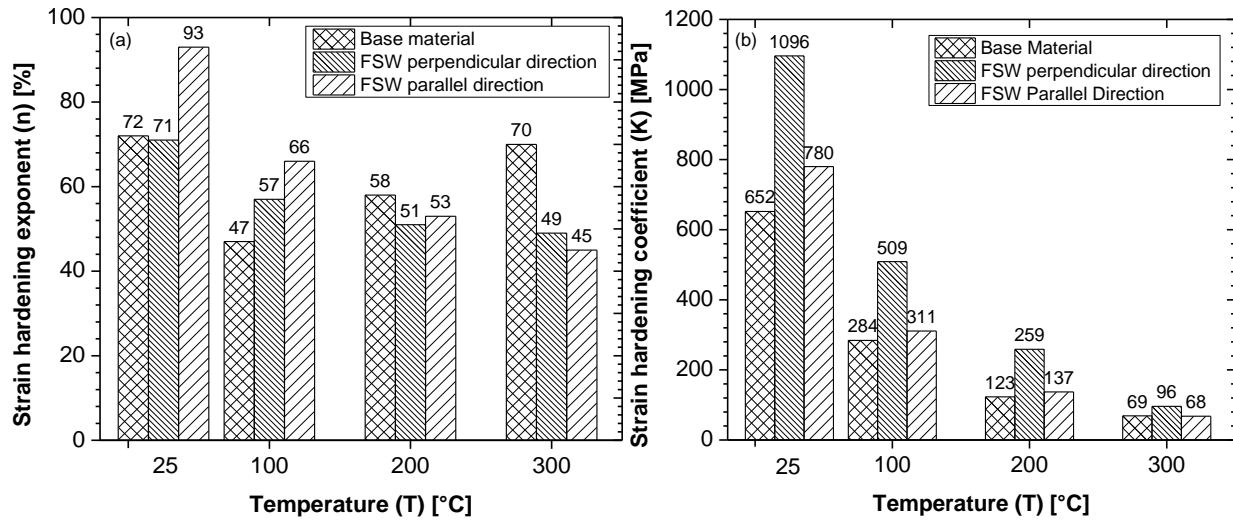
Figure III.28 (a) Strain hardening exponent and (b) strain hardening coefficient in function of temperature

Figure III.29 (a) shows pictures of the FSW perpendicular samples after fracturing under tensile test at temperatures of 25°C, 100°C, 200°C and 300°C. It is clearly shown that the fracture occurred between the SZ and the TMAZ on the advancing side with a slanted crack forming approximately at an angle of 45° with the major axis of the sample (Figure III.29 (b)). Figure III.18 also shows that the interface region between the SZ and the TMAZ (AS) forms approximately an angle of 45° with the transverse direction. Therefore, the crack was supposed to have propagated along this SZ and the TMAZ (AS) interface. This is in line with results reported by Afrin et al. (Afrin et al., 2008) and Yang et al. (Yang et al., 2010) who investigated the behavior of FS welded AZ31B. It can be concluded that the zone where cracks are the most probable to initiate in the friction stir welded AZ31 sheets is the interface line between SZ and the TMAZ (AS). Therefore, the FSW process parameters should be optimized to improve the microstructural gradient between the SZ and the TMAZ (AS) interface.
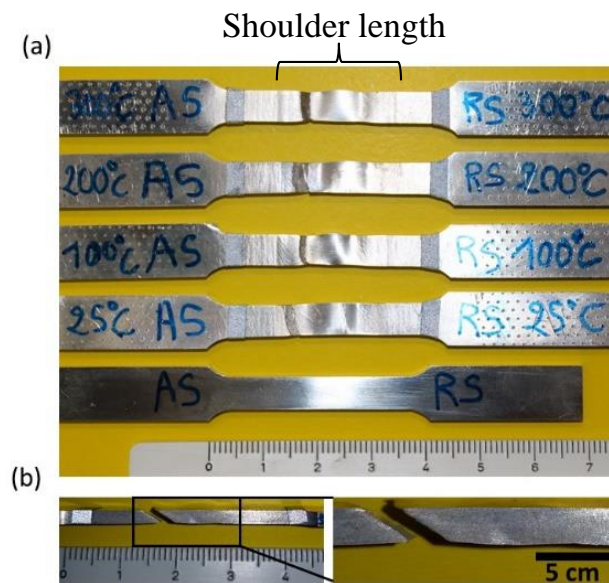
Figure III.29. (a) Fractured samples at different temperatures. (b) fractured sample showing the angle of the crack propagation.

III.2.5 Fractography analysis and damage mechanism in the stir zone

To investigate the damage mechanisms in the stir zone, the fracture surface of the FSW parallel samples were observed with SEM. Figure III.30 presents an SEM micrographs of the fracture surface of FSW parallel samples tested at room temperature. Figure III.30 (a) shows the

fracture surface with low magnification; a typical ductile fracture surface is observed; a crack propagation zone above the red curved line and a brittle fracture surface below the line. Three different area of this heterogeneous morphology is observed with higher magnification. Figure III.30 (b) shows the microstructure of the upper left region where the microscopic dimples direction is toward to left side. Figure III.30 (c) displays the microstructure of the cross-section upper right side, it can be seen that the microscopic dimples are toward the right side. Finally, Figure III.30 (d) shows the microstructure of the lower region where almost no dimples are observed. From those observations, it can be concluded that the crack initiated at the surface in the middle of the upper area of the sample and propagated in a shape of an arc of circles (as shown by the red curved line) until the samples couldn't withstand the load leading to a brittle fracture.
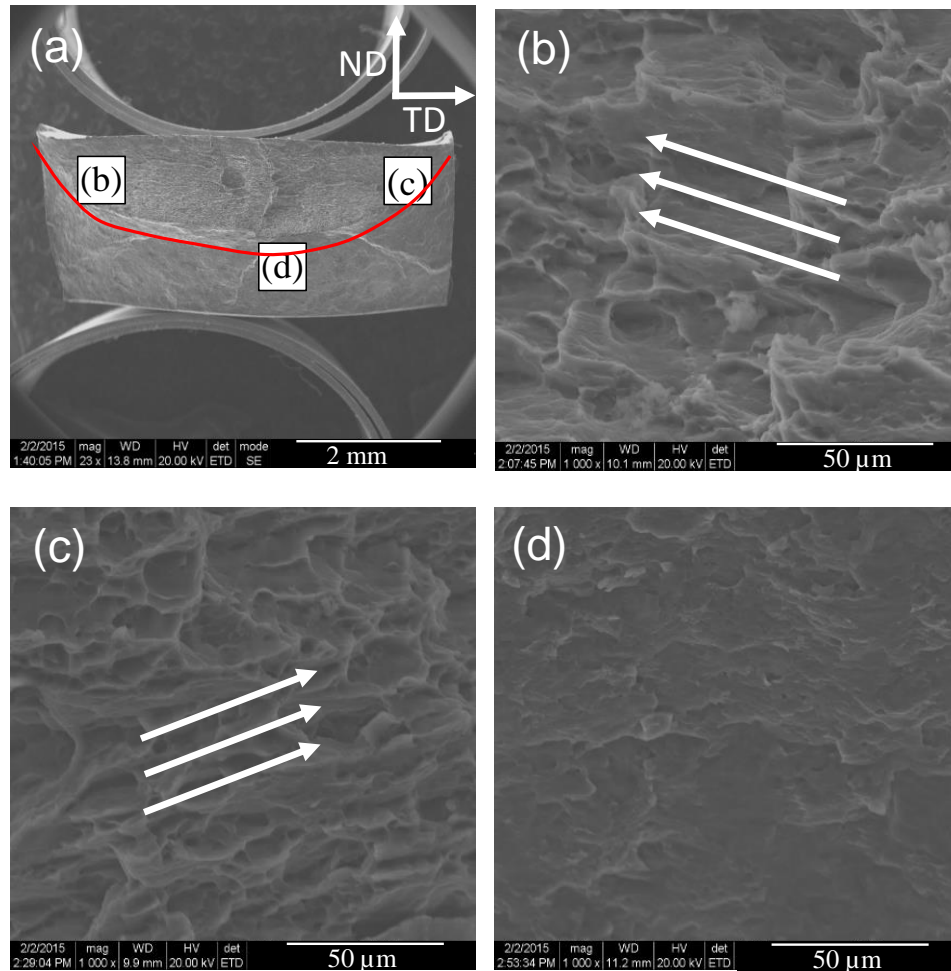
Figure III.30. Scanning Electron Microscope fractography of specimen deformed in the welding direction. (a) low magnification. (b), (c) and (d): magnified regions.

Furthermore, in order to study the crack initiation mechanisms in the stir zone, specimens from different planes were cut from the FSW parallel samples that were tested at various temperature. The specimens were polished then observed under an optical microscope. Figure III.31 presents an optical microscope mapping of the WD-TD plane of the failed sample previously deformed at room temperature. A low number of microcracks, mostly concentrated near the fracture surface, was observed explaining the lower ductility of the samples at RT. Figure III.31 (c) shows bands of recrystallized grains parallel to each other in a zone free of cracks.
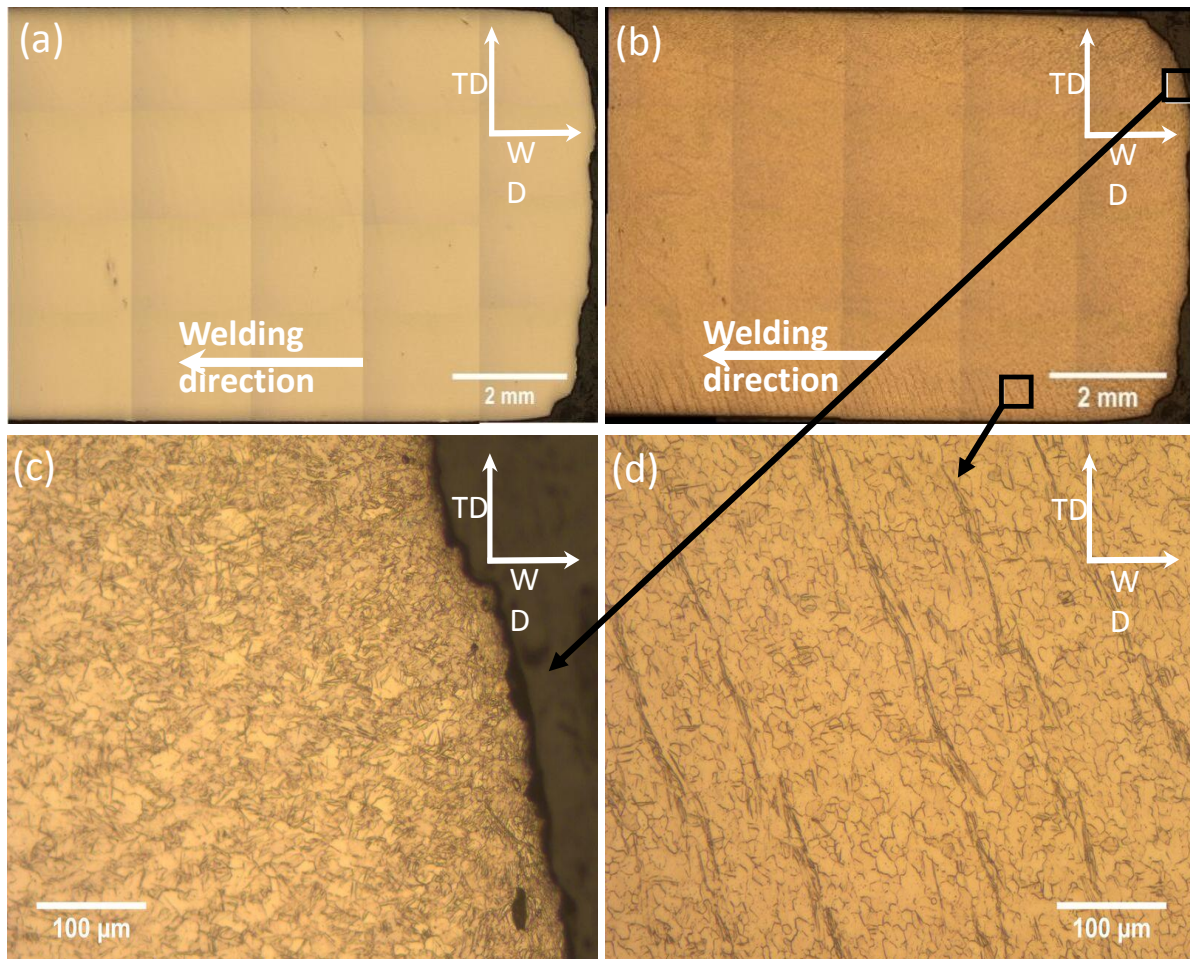
Figure III.31. Microstructure of fractured tensile test sample after tensile testing at 25°C.

Moreover, the WD-TD plane of a failed sample deformed at 200°C was observed with an optical microscope; the micrographs are shown in Figure III.32. The FSW parallel samples deformed at 200°C exhibited work softening hence we assume that observation of microcracks is easier than at RT. As showed in Figure III.32 the micrographs contained many cracks compared to RT condition. The cracks propagated in a zigzag shape, however overall the cracks seems to propagate perpendicularly to the loading direction.

(Kondori and Benzerga, 2014) studied the damage mechanisms in AZ31 at RT and reported that the majority of cracks initiate at the second phase particles and deformation twin. From Figure III.32 and Figure III.32 (d), we assume that that the majority of cracks initiated in the second phase particles as no cracks initiating at the deformation twins were observed.
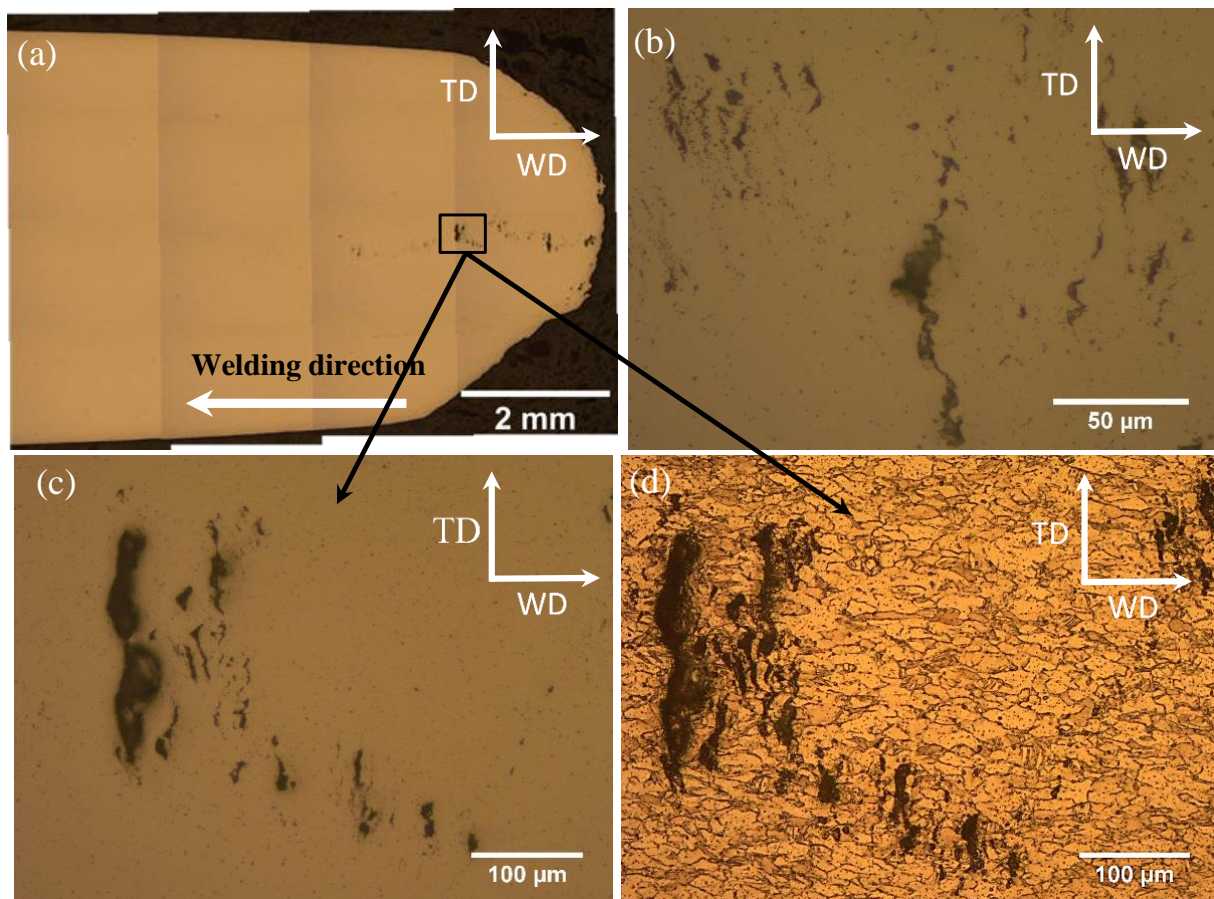
Figure III.32. The microstructure of fractured tensile test sample after tensile testing at 200°C.

III.2.6 Conclusions

In order to study the mechanical, microstructural and textural properties of FSW joints, 3 mm thick AZ31B sheets were welded using optimum FSW welding conditions, found for the particular tool geometry used to be at spindle speed and tool feed rate of 1200 rpm and 150 mm/min, respectively.

As general observation of the microstructure and the texture: (a) the SZ exhibited a recrystallized microstructure characterized by minor grain growth and strengthening of the basal texture due to a rotation of the crystal c-axis around the WD; (b) the TMAZ on the AS presented a slight modification of the microstructure and texture compared to the base metal; (c) the TMAZ on the RS showed higher level of deformation compared to its counterpart but lower than the SZ, some recrystallization and some strengthening of the basal texture was also observed.

Vickers microhardness values measured were maximum at the interface between the SZ and the TMAZ on the AS and were attributed to an abrupt change in the grain size and the micro-texture. Consequently, it was assumed that cracks would initiate at this interface between due to a higher level of incoherency, which may lead to an accumulation of dislocations.

Uniaxial tensile testing conducted at a strain rate of $10^{-3}s^{-1}$ and different temperatures (25°C, 100°C, 200°C, and 300°C) revealed a temperature dependent mechanical response. Specimens machined with their major axis parallel and perpendicular were tested, and the results were compared to the mechanical behavior of the base metal. FSW perpendicular direction samples exhibited higher strength levels. The highest tensile elongation was exhibited by the FSW parallel samples. However, the lowest strain to fracture was achieved by the FSW perpendicular samples that presented a fracture occurring between the TMAZ (AS) and the SZ.

Failure mechanisms in the stir zone were investigated, and a larger number of cracks were observed in the FSW (parallel samples) tested in tension at 200°C compared to samples tested at RT. It was observed that the majority of cracks had initiated in the second-phase intermetallic particles.

Chapter IV. Mechanical and Microstructural Properties of Dissimilar Al-to-Mg FSW welds

Heterogeneous Al-Mg joints using FSW welding process have been analyzed in chapter four, the FSW joints obtained using different tool rotation and advance speeds have been studied at elevated temperature as well as at room temperature. And to better understand the behavior of the welded joints and compare it to the base material, uniaxial tensile testing have been conducted at 25°C and 200°C, and their mechanical properties and fracture surfaces have been analyzed.

Summary

Introduction

Utilization of lightweight metals such as magnesium (Mg), aluminum (Al) and titanium (Ti) to form weight saving structural components in aerospace and automotive vehicles can significantly benefit in improving fuel efficiency and reducing harmful emissions (Mathaudhu and Nyberg, 2010; Pollock, 2010). The ability to produce components from different lightweight metal alloys and to integrate them together is an important technical challenge. One principal aim is to improve reliable inhomogeneous metal joining methods to enable the production and integration of mechanical components made from lightweight substitute metal alloys.

Magnesium and aluminum are two of the lightest structural metals and joining these two metals present several challenges. For this, several conventional welding techniques such as gas tungsten arc welding (GTAW) (Ben-Artzy et al., 2002; Liu et al., 2007b), electron beam welding (EBW) (Ben-Artzy et al., 2002; Chi et al., 2007), laser beam welding (LBW) (Bannour et al., 2013), have been used to weld Al alloys to Mg alloys. These conventional welding techniques result in coarse-grained and intermetallic (both large and continuous) regions in the weld zone followed by a prominent heat affected zone (HAZ) and the base material (BM) (Liu et al., 2014). Some of the other welding techniques such as brazing based on Zn-based filler materials (Liu et al., 2007a; Wang et al., 2012), diffusion bonding (Liu et al., 2009b; Zhao and Zhang, 2008), cold metal transfer MIG welding (Shang et al., 2012; Wang et al., 2008) and conventional MIG and TIG welding (Liu et al., 2013; Liu et al., 2012; Xue et al., 2011) have been used. In all of these welding techniques used to weld Al alloy to Mg alloy, solidification of the metal occurs resulting in the formation of intermetallic compounds. The resulting formation of various types of intermetallic compounds (IMC) in the weld zone undermines the weld integrity. Also, controllability of the distribution, size, and type of the brittle IMCs are difficult, and their presence has a detrimental effect on the weld strength.

To obtain defect free joining of dissimilar metals Al and Mg, studies have utilized solid state welding techniques such as ultrasonic welding (Panteli et al., 2012; Robson et al., 2012), resistance spot welding (Hayat, 2011), linear friction welding (Bhamji et al., 2012), and friction stir welding (FSW) (Cabibbo et al., 2012; Cao et al., 2013; Firouzdor and Kou, 2010a; Hunt et al., 2007; Malarvizhi and Balasubramanian, 2012; Mofid et al., 2012a; Morishige et al., 2008; Sato et al., 2004; Zettler et al., 2006; Zettler et al., 2005). The advantage of the solid welding

technique is that it offers controllability over heat generation and response times. To capitalize this benefit, a solid state metal joining technique, namely FSW that utilizes frictional heat, metal mixing and severe plastic deformation caused by a rotating shouldered tool with a pin and the metal to be welded, has been widely used (Mishra et al., 2014). The tool rotation results in stirring and plastic deformation of the metals at high temperature, which results in a joint with good weld integrity. The FSW process takes place below the melting temperature of the alloy, so several defects due to the solidification of the metals are avoided (Mishra and Ma, 2005).

Studies in existing literature have utilized FSW to weld dissimilar alloys of magnesium and aluminum alloys and have studied the weld microstructure and mechanical properties such as microhardness and tensile properties. Most of the studies on the existing literature have concentrated on optimizing process parameters based on the weld microstructure. Only a few studies are available on the mechanical properties of the weld. Also temperature effects on the tensile properties of dissimilar Al/Mg joints have not been investigated in the existing literature. Considering that the welded joints used in the automotive, aerospace and oil and gas industries will be subjected to temperature changes during their service life, understanding the properties of the joints at elevated temperature is important.

In this chapter, a characterization of the FS welded joints at high temperature as well as at room temperature is attempted, to better understand the behavior of the welded joints, compared with the base material. In this regard, the study has focused on the effect of process parameters on the weld zone microstructure and its subsequent impact on room temperature (25°C) and high temperature (200°C) mechanical and fracture properties.

IV.1 Experimental procedure

In the present work, the FSW operation was carried out using a Gantry FSW Machine (FSW-LM-08, Beijing FSW Tech. Co. Ltd.). The tool used utilized to join Al/Mg had a tool shoulder diameter of 10 mm with a threaded pin of length 2.96 mm. The maximum and minimum diameter of the threaded pin are 3.6 mm and 2.9 mm, respectively. All the FSW runs were performed with a tool tilt angle of 3°. The Al and Mg plates to be FS welded were $250 \times 50 \times 3$ mm^3 in dimensions and were cut from the base material. The plate edges were deburred to prevent any prior inhomogeneities. The base materials used are Al6061-T6 aluminum and AZ31B magnesium; obtained from commercial suppliers and their nominal chemical

composition are presented in Table IV.1. Prior to the microstructural examination on the base material and welded joint specimens the mounted specimens were grounded and polished up to 1200 grit followed by 1 µm diamond slurry and 0.04 µm colloidal silica. To observe the microstructural features, the Mg and the Al parts of the weld were etched using standard acetic-picral solution (4.2 g picric acid, 10 ml acetic acid, 70 ml ethanol and 10 ml distilled water) and Weck's reagent (4% $KMnO_4$ and 1% NaOH diluted in distilled water), respectively (Dorbane et al., 2015b).

Alloy	Wt. %	Al	Mn	Mg	Si	Cu	Cr	Fe	Zn	Ti	Ca	Ni	YS (MPa)	UTS (MPa)
Al6061-T6	Min	Bal	-	0.8	0.4	0.15	0.04	-	-	-	-	-	275	350
	Max	Bal	0.15	1.2	0.8	0.4	0.35	0.7	0.25	0.15	-	-		
AZ31B	Min	2.5	0.2	Bal	-	-	-	-	0.6	-	-	-	150	300
	Max	3.5	1	Bal	0.1	0.05	-	0.005	1.4	-	0.04	0.005		

Table IV.1. The nominal composition along with mechanical properties of Al and Mg alloys.

An optical (light) microscope (Zeiss AxioVert 40 MAT fitted with ERc5s camera) and a scanning electron microscope (SEM) were used to observe microstructure, intermetallics and different zones formed after the weld. The welded specimens were evaluated for Vickers micro-hardness using parameters of 100 gf and dwell time of 15 s. The microhardness measurements were performed at 2 mm from the top of the weld in the thickness plane (normal direction-transverse direction (ND-TD) plane, perpendicular to the welding direction). The hardness values were also measured at three different distances from the top of the weld to study the variation of the hardness of the welded joint. ASTM E8/E8M-15 tensile test specimen geometry was used for the tensile experiments. Uniaxial tensile tests were performed at room temperature and 200±3°C under constant strain rate of $10^{-3}s^{-1}$, using a computer controlled MTS insight tensile testing machine equipped with a 30 kN load cell and equipped with an LBO-series Thermocraft LabTemp laboratory oven (environmental chamber). For the high-temperature tensile testing, specimens were kept inside the environmental chamber for 5 minutes to homogenize the temperature, prior to starting the tensile experiment. SEM observations of the

thickness plane of the welded Al and Mg plates and the fractured tensile tested specimens were performed.

IV.2 Results and Discussion

IV.2.1 Macro and microstructure

IV.2.1.1 Base material

The investigated materials are; an Al 6061-T6 rolled sheets to a thickness of 3 mm and supplied by McMaster Inc. and an AZ31B twin rolled cast rolled to a thickness of 3 mm and supplied by POSCO. Figure IV.1 (a) and (b) represents the microstructure of the base materials (BM) (Al6061-T6 and AZ31B) used in the present study. Both microstructures are observed in the ND-TD plane. The grains of the Al6061-T6 have the shape of elongated ellipses, and the iron-rich phases and the magnesium silicide particles scattered throughout the microstructure are clearly observed (Dorbane et al., 2015b). The microstructure of the magnesium base metal reveals mainly equiaxed grained and some twins can be observed which are most probably due to the rolling conditions. Grain size analysis was performed on the BMs – Al and Mg showed an average grain size of 20.52±11.95 μm and 11.46±4.59 μm, respectively. The obtained microstructure of the BMs is helpful for comparison with the different observed weld zones.
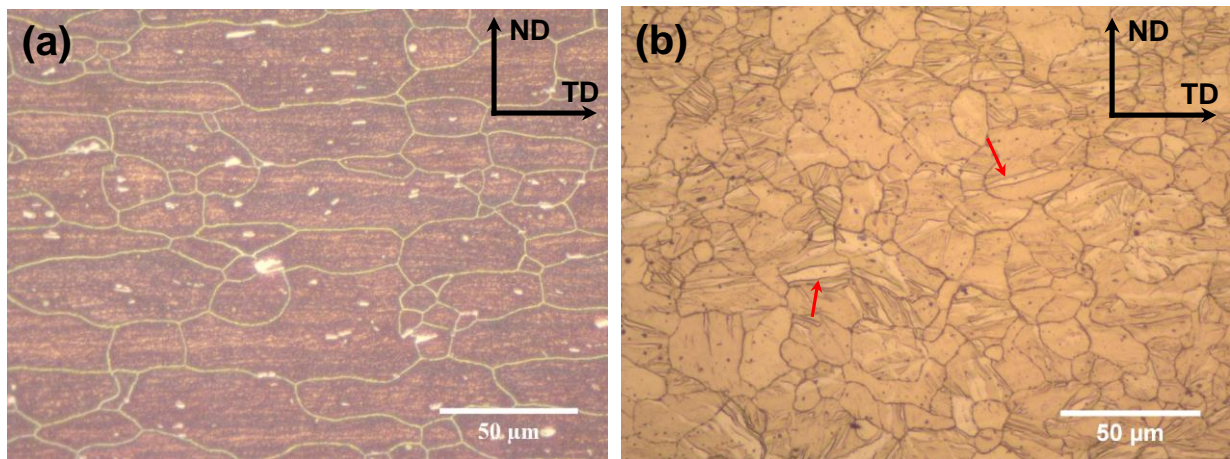
Figure IV.1. Microstructure of the base materials (a) Al 6061-T6 and (b) AZ31B.

IV.2.1.2 FSW joint – macrostructure

Figure IV.2 (a) and (b) represent the images of two welded specimens. Figure IV.2 (a) shows the dissimilar weld of Al and Mg carried out using tool rotational speed of 1600 rpm and translation speed of 250 mm/min with placing Mg on the advancing side (AS). While Figure IV.2 (b) presents, the visual aspect of FS welded plates employing 1400 rpm and 500 mm/min weld parameters with Al on the AS. From Figure IV.2, it could be observed that irrespective of the different welding parameters used for the two cases, the placement of Al has a significant effect on the weld integrity. Placing Al plates on the AS of the joint resulted in a defect-free weld as could be observed in Figure IV.2 (b). This observation was further validated by examining the weld zone under an optical microscope for the different welding parameters, with Al or Mg plates placed in AS. The obtained weld cross-sections optical microscope images (in ND-TD plane) were utilized to differentiate the two welded materials Al (6061-T6), and Mg (AZ31B) and to observe the weld defects.
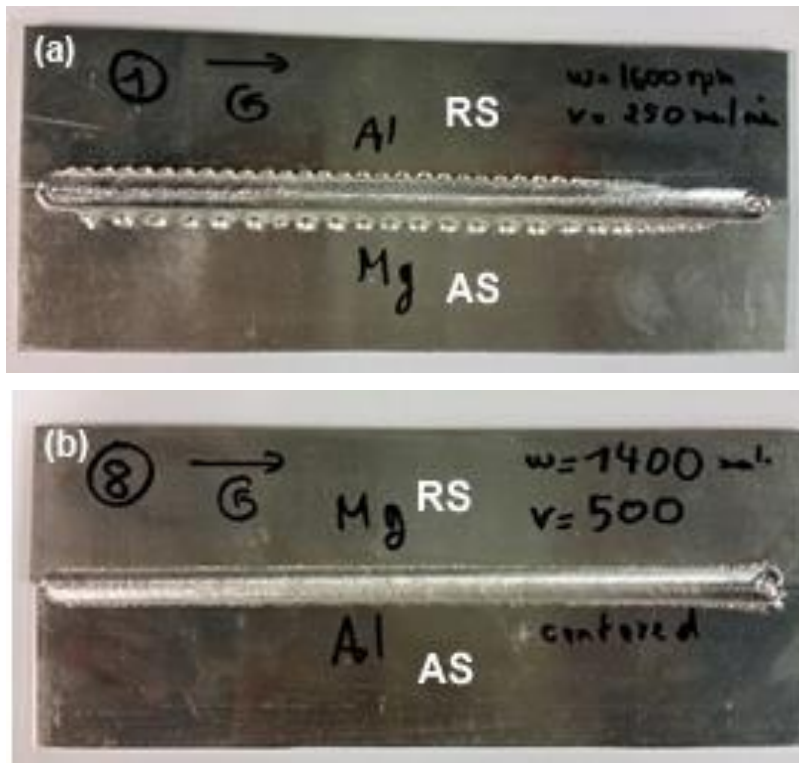
Figure IV.2. Al-Mg FS welded specimens (a) 1600 rpm, 250 mm/min, Mg on the AS and (b): 1400 rpm, 500 mm/min, Al on the AS (Mansoor et al., 2015a).

Figure IV.3 presents optical microscope images of the heterogeneous FS welded Al-Mg joints, obtained with different Al plate configurations and welding parameters. As a general observation; good welds are obtained by placing aluminum on the AS, confirming the observations in Figure IV.2. Placing aluminum on the Retreating Side (RS) resulted in defects such as voids and surface galling in the weld as can be seen in Figure IV.3 (a). Similar results with the placement of Al in the welding plate configuration, has been observed in literature studies and in the pilot work to this study, on dissimilar FSW of Al alloys to Mg alloys (Cabibbo et al., 2012; Cao et al., 2013; Firouzdor and Kou, 2010a; Hunt et al., 2007; Malarvizhi and Balasubramanian, 2012; Mansoor et al., 2015a; Mofid et al., 2012a; Morishige et al., 2008; Sato et al., 2004; Zettler et al., 2006; Zettler et al., 2005). The weld microstructure was observed by varying the tool rotation speed from 1200 rpm to 1600 rpm with the translation speed being kept at a constant speed of 500 mm/min. The microstructure corresponding to the welds using tool rotation speed of 1600, 1400 and 1200 rpm are shown in Figure IV.3 (b), (c) and (d), respectively. From these images it is observed that the welds with aluminum on the AS had fewer defects (Figure IV.3 (b, c)), in comparison to aluminum on the RS (Figure IV.3 (a)). Comparing Figure IV.3 (b), (c) and (d), some defects such as wormhole and voids are observed on the Mg side with the most evident defects detected in the 1200 rpm rotation speed specimen, in comparison to the other two rotation speeds. While analyzing the microstructures, the plate welded with aluminum placed in the AS with a rotation speed of 1400 rpm and translation speed of 500 mm/min presented the best observable weld quality.
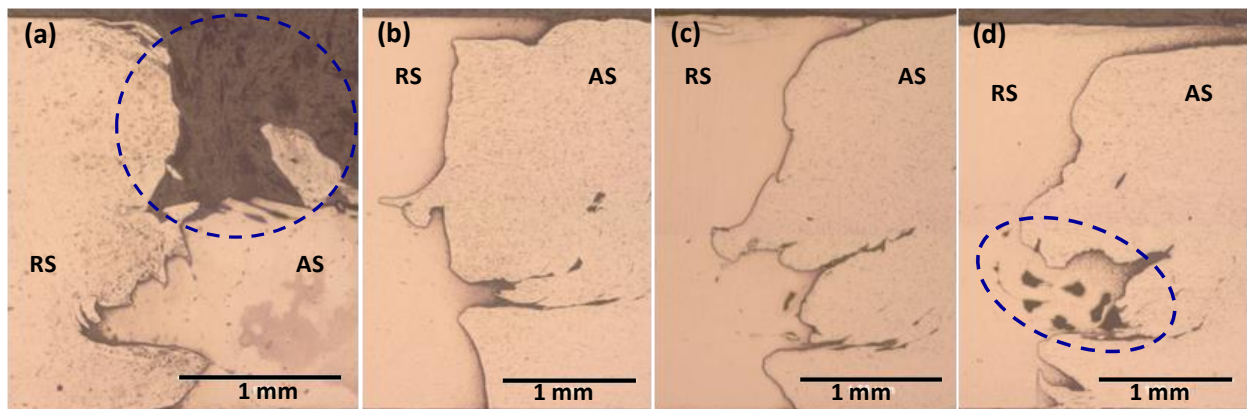
Figure IV.3. Optical microscope observation of the cross section of the welded joint obtained using parameters (a) 1600 rpm rotational and 250 mm/min translational speeds (Al on the RS).

(b-d) Fixed translational speed of 500 mm/min with variable rotational speeds of 1600, 1400, 1200 rpm, respectively with aluminum on the AS (Mansoor et al., 2015a).

IV.2.1.3 FSW joint – microstructure

The complete structure of the dissimilar Al-Mg friction stir welded joint cross-section (ND-TD plane) obtained with 1400 rpm and 500 mm/min weld parameters is shown in Figure IV.4. This figure displays the extent of the different zones constituting the cross-sectional microstructure namely base material (BM), heat affected zone (HAZ), thermo-mechanically affected zone (TMAZ) and stir zone (SZ) on both the magnesium and aluminum sides of the weld. A detailed microstructure analysis was carried out to study the grain size, grain boundaries, and intermetallic zone. The different zones of the weld cross-section (Figure IV.4) in the magnesium side and the aluminum side are represented in Figure IV.5 and Figure IV.6, respectively. Distinguishable microstructure can be observed in the four zones of each side of the joint.
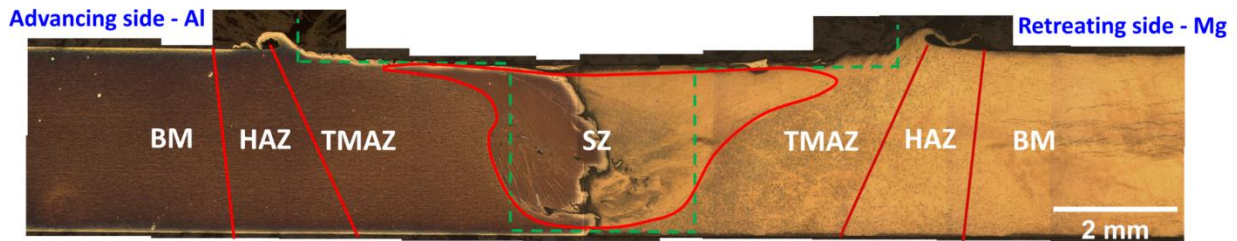
Figure IV.4. Cross section of Al/Mg weld prepared utilizing 1400 rpm and 500 mm/min weld parameters, showing the various zones of the weld.

The stir zone presents a considerable grain refinement when compared with the base material. On the magnesium side of the weld, the grain size in the SZ was 2.43±0.87 μm, in comparison to 11.46±4.59 μm in the base material. On the aluminum side, the grain size reduced from 20.52±11.95 μm in the base material to 0.94±0.24 μm in the SZ. The grain refinement obtained in the dissimilar FSW of Al-Mg alloys is corroborated with the results previously reported in existing literature on dissimilar FSW of Al-Mg alloys (Cabibbo et al., 2012; Cao et

al., 2013; Firouzdor and Kou, 2010a; Hunt et al., 2007; Malarvizhi and Balasubramanian, 2012; Mofid et al., 2012a; Morishige et al., 2008; Sato et al., 2004; Zettler et al., 2006; Zettler et al., 2005). The grain refinement can be correlated to the severe deformation encountered by the aluminum and magnesium in the SZ and also with the heat input that was not enough to induce grain growth. The prediction of grain size resulting from friction stir processing was investigated in function of the strain rate, the process induced temperature and the materials properties (Kumar et al., 2011; Morisada et al., 2015). However using these models to predict the grain size with dissimilar FSW can be challenging. In the magnesium side, the TMAZ shows a larger number of twins compared to the BM with an average grain size equal to 8.44±4.10 μm. The HAZ shows larger grains with an average size equal to 14.75±5.60 μm and fewer twins are perceptible. In the aluminum side, the TMAZ is characterized with more elongated and bigger grains compared to the BM, with an average grain size of 21.16±10.70 μm. Much bigger grains are observable in the HAZ, with a mean grain size equal to 26.15±8.78 μm.
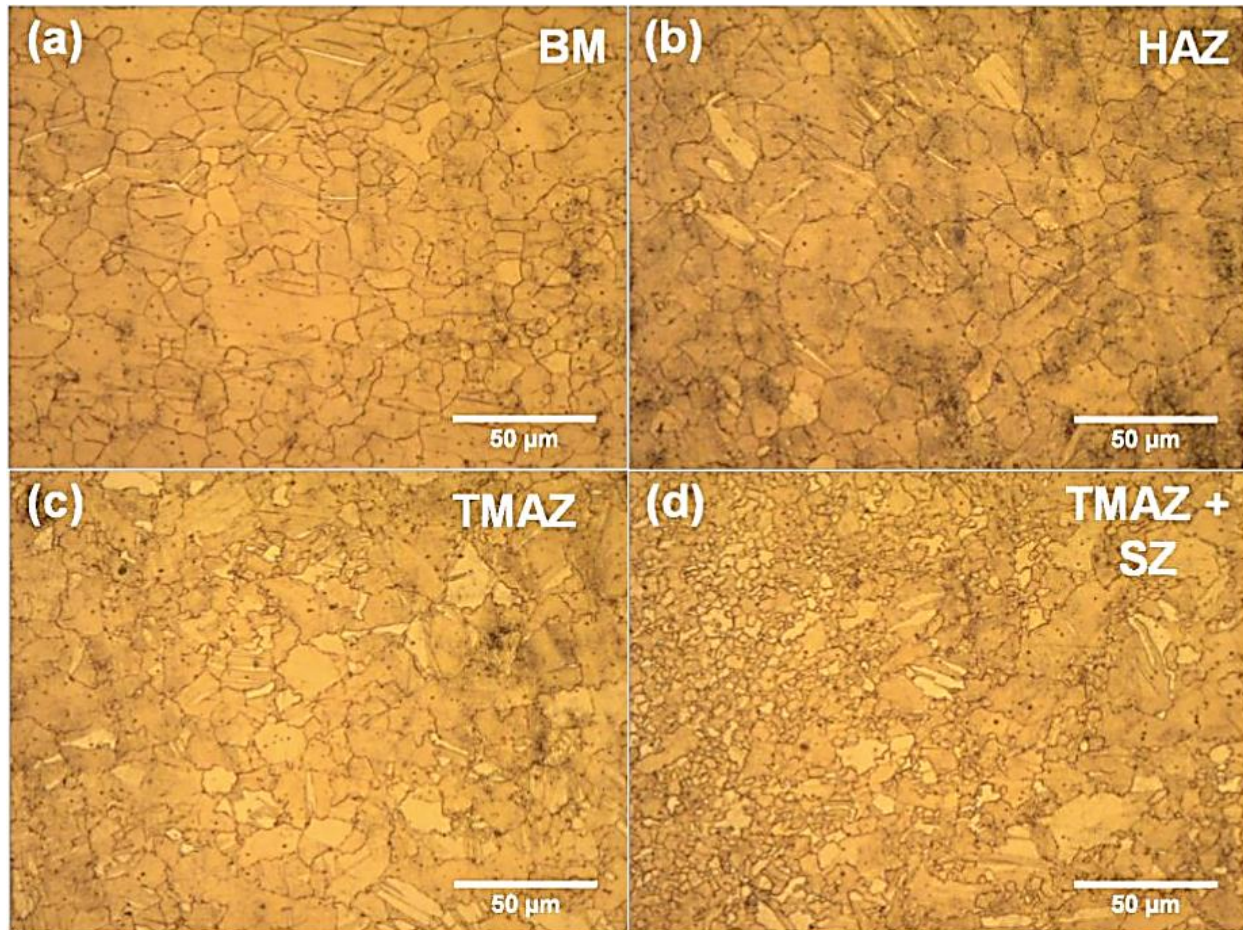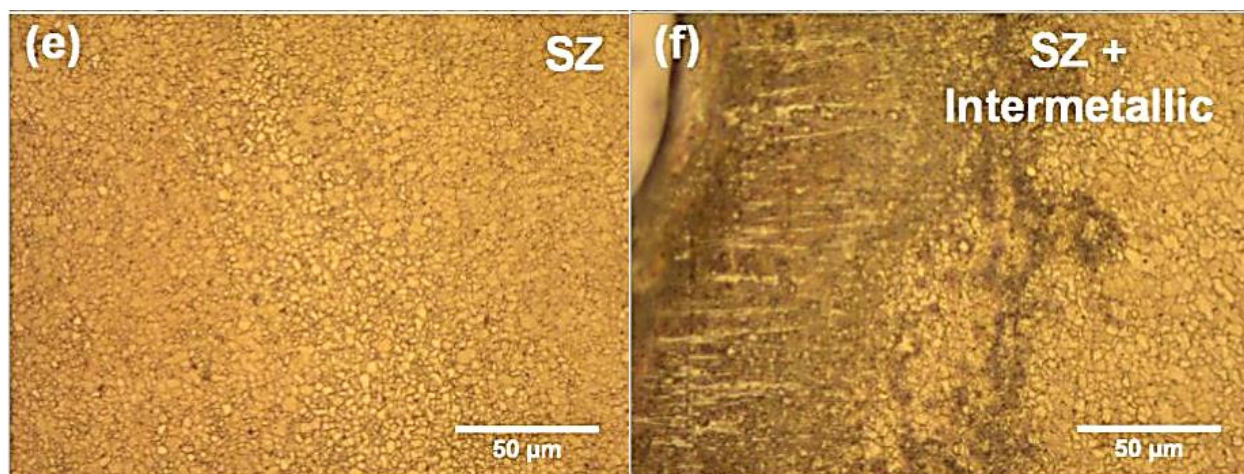
Figure IV.5. Microstructure of the different zones on the magnesium side of the FS welded dissimilar Al-Mg joint prepared using 1400 rpm and 500 mm/min (Mansoor et al., 2015a).
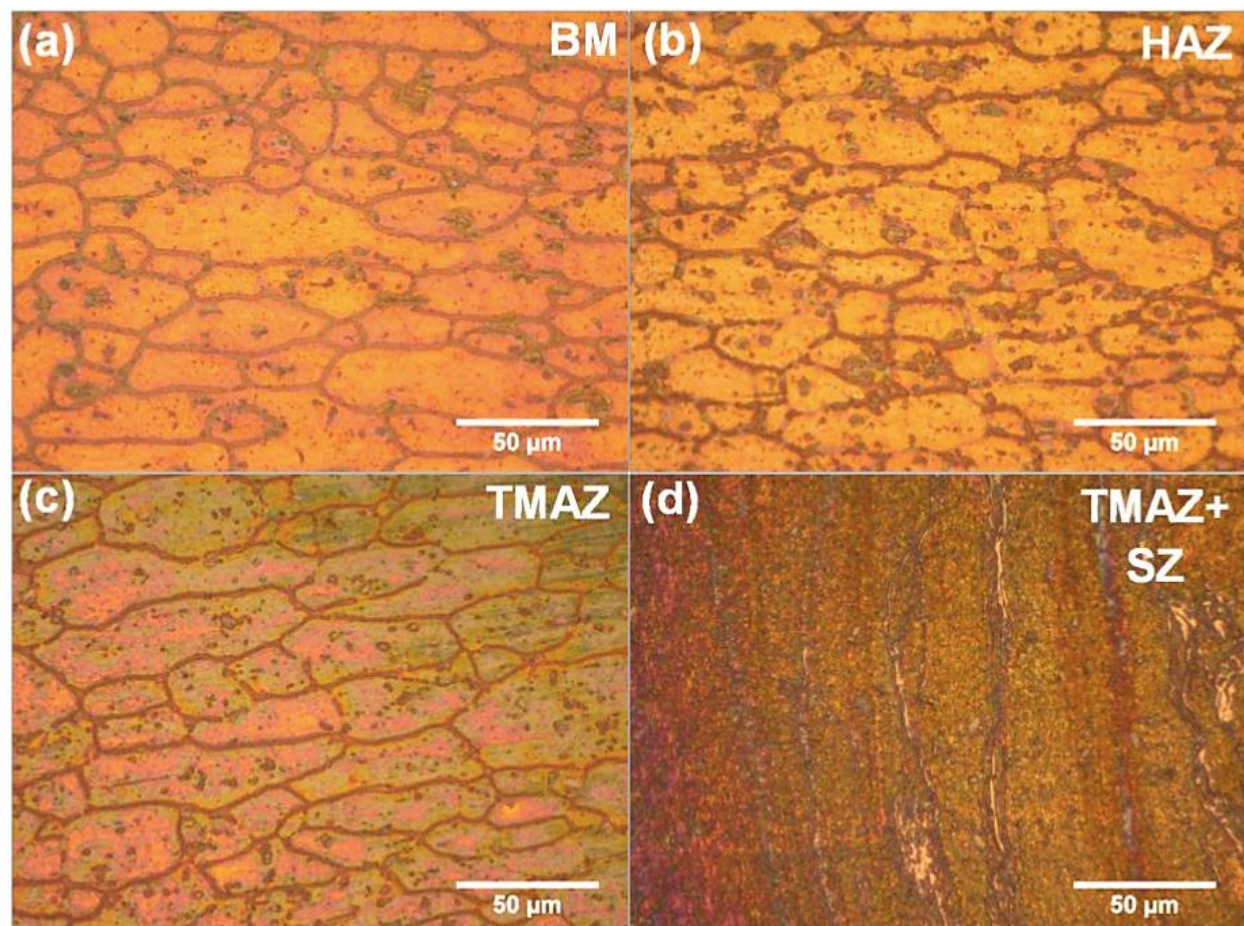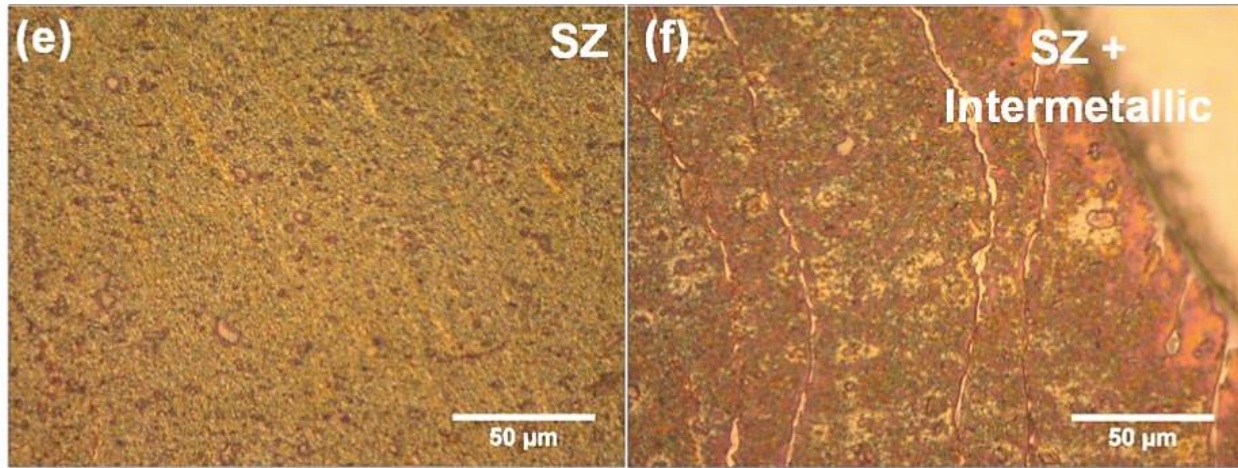
Figure IV.6. Microstructure of the different zones on the aluminum side of the FS welded dissimilar Al-Mg joint prepared using 1400 rpm and 500 mm/min.

IV.2.1.4 Scanning electron microscopy observations

Figure IV.7 shows SEM micrographs observation of the SZ of Al/Mg dissimilar welded sheet joined using 1400 rpm and 500 mm/min weld parameters placing aluminum on the AS. Figure IV.7 (a) and (b) reveal an equiaxed microstructure of the SZ in Mg and Al sides, respectively. The microstructure of the SZ seems to be the consequence of a complete recrystallization that resulted in a very fine grains structure. It can be assumed that the observed microstructure resulted from a severe deformation with not enough heat input to induce a sizeable grain growth. Figure IV.7 (c) shows the interface between Mg and Al separated by a thin layer of IMC. Friction stir welding of aluminum and magnesium results in the formation of brittle IMCs such as Mg_2Al_3 and $Mg_{17}Al_{12}$. The formation of IMC was reported to occur in localized fusion zones, which is strongly dependent on the heat input resulting from the weld parameters. Therefore, the IMCs are most likely to form in weld zone that encountered that highest temperature, more precisely at the interface between aluminum and magnesium and in some localized areas of the SZ. A higher percent of IMCs has been reported in the SZ compared to the BMs (Firouzdor and Kou, 2010b; Fu et al., 2015; Liang et al., 2013; Malarvizhi and Balasubramanian, 2012; Masoudian et al., 2014b; Mohammadi et al., 2015; Morishige et al., 2008; Zettler et al., 2006). Figure IV.7 (d) shows broken precipitates present in the Al part of the stirred zone, probably induced by the severe deformation encountered by the material during FSW (Dorbane et al., 2015b). The SEM images present a defect-free interface between the FS

welded Al6061-T6 and AZ31B alloys. The microstructure and the weld integrity analysis demonstrated that 1400 rpm rotational speed and 500 mm/min translational speed can be used as the optimum welding parameters in the present study. The optimum parameters observed in the study are based on the tool geometry used. The analysis of the microstructure revealed a defect free weld with the presence of brittle IMCs in the SZ. Observable IMC layer at the interface between magnesium and aluminum suggested that the interface reached a high temperature close to melting during the FSW process. Also, the presence of IMCs at the interface suggests that the most probable zone of crack initiation during mechanical loading will be the interface between the magnesium and aluminum.
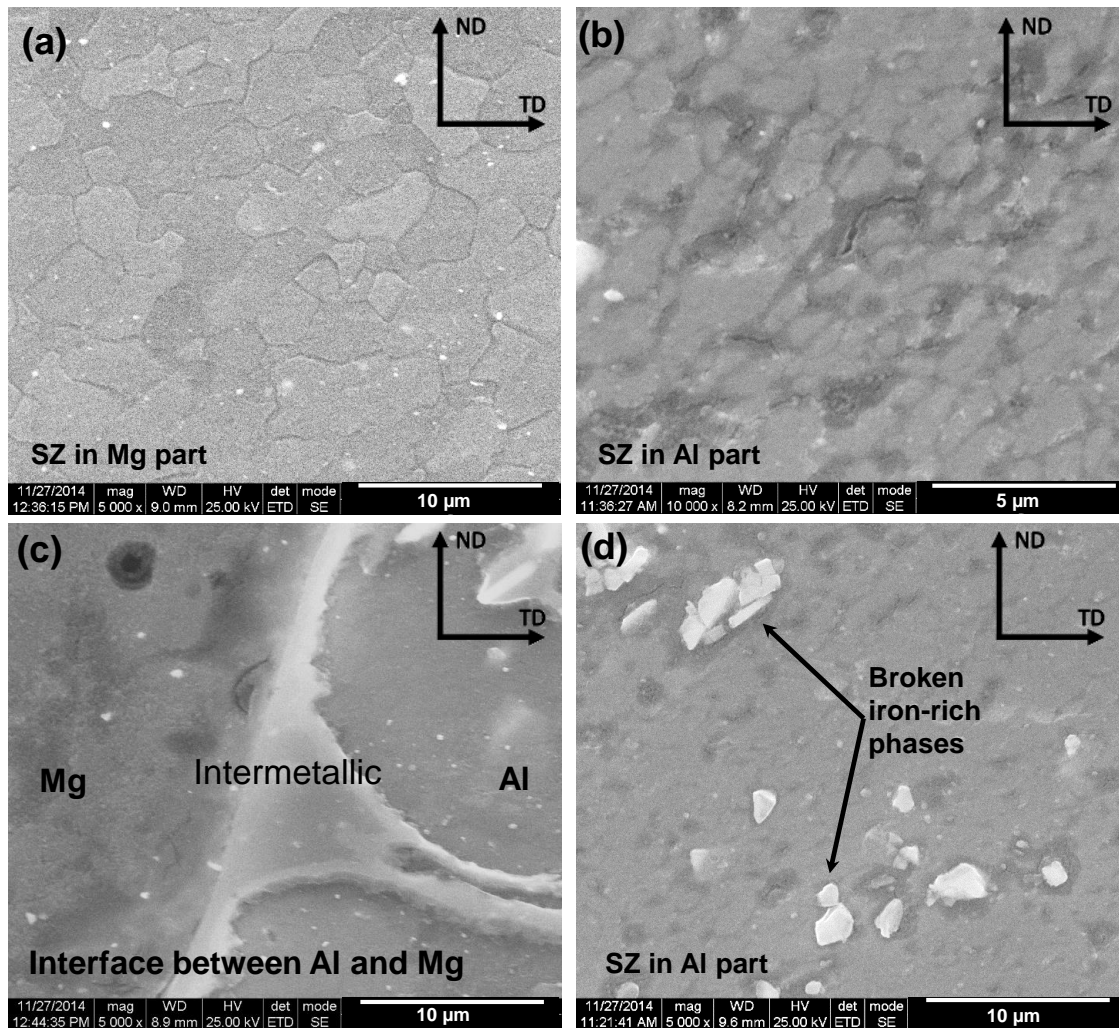
Figure IV.7. SEM analysis of the SZ in the joint prepared using 1400 rpm and 500 mm/min. (a) magnesium stir zone, (b) aluminum stir zone, (c) Intermetallic in the Al/Mg interface and (d) aluminum stir zone showing broken precipitates.

IV.2.2 Micro-hardness testing

The magnesium crystalline structure is a hexagonal-closed pack (HCP), the crystal unit cell of aluminum is face-centered cubic (FCC), $Mg_{17}Al_{12}$ has a body-centered cubic (BCC) crystal structure and finally, the Mg_2Al_3 intermetallic phase has a Fd-3m structure (Samson, 1965). The different crystalline structures composing the SZ induce a high level of incoherency at the interfaces between the various constituents. In order to detect the difference in the mechanical and microstructural properties of the different zones of the weld and for the purpose of identifying the zones of the welds where the fracture is most probable to occur micro-hardness testing were conducted.

The weld parameters analyzed with the microhardness were 1600 rpm, 250 mm/min, (Mg on AS); 1600 rpm, 500 mm/min, (Al on AS); 1400 rpm, 500 mm/min, (Al on AS); 1200 rpm, 500 mm/min, (Al on AS) and the results are shown in Figure IV.8. The hardness on the magnesium side (BM) of the weld was found to be between $55 - 65HV$ and on the aluminum side (BM) was between $120 - 135HV$. The measurements were conducted at the centerline of the weld between -10 to 10 mm on either side of the weld center in which -5 to 5 mm on either side of the weld center corresponds to the tool shoulder diameter. A transition in the hardness values can be observed between the Mg to the Al side. The region corresponding to the tool pin diameter (-1.5 to 1.5 mm on either side of the weld center) shows peaks in the hardness values that can be related to the finer grain structure exhibited by the SZ in addition to the presence of the intermetallic phases. Zhang et al. reported that the microhardness value of the intermetallic phases is much greater than the magnesium BM (Zhang et al., 2010a). Grain boundaries resist the occurrence of deformation hence large grain boundary will result in higher yield stress. A much smaller average grain size was obtained in the SZ compared to the BM as reported in the previous section. As a result, the SZ consists of larger grain boundaries compared to the BM and the other weld zones. Therefore, higher hardness values can be expected. Furthermore, we can observe that the change in hardness values from the BM to the SZ is steeper on the Al side compared to the Mg side. This hardness rate difference can be explained by the grain size reduction between the BM and the SZ in the Al and the Mg sides. In fact, the grain size of SZ in the Al side reduced to reach 5% of the grain size of the BM, however, the grain size of the SZ in the Mg side reached 21% of the grain size of the BM.
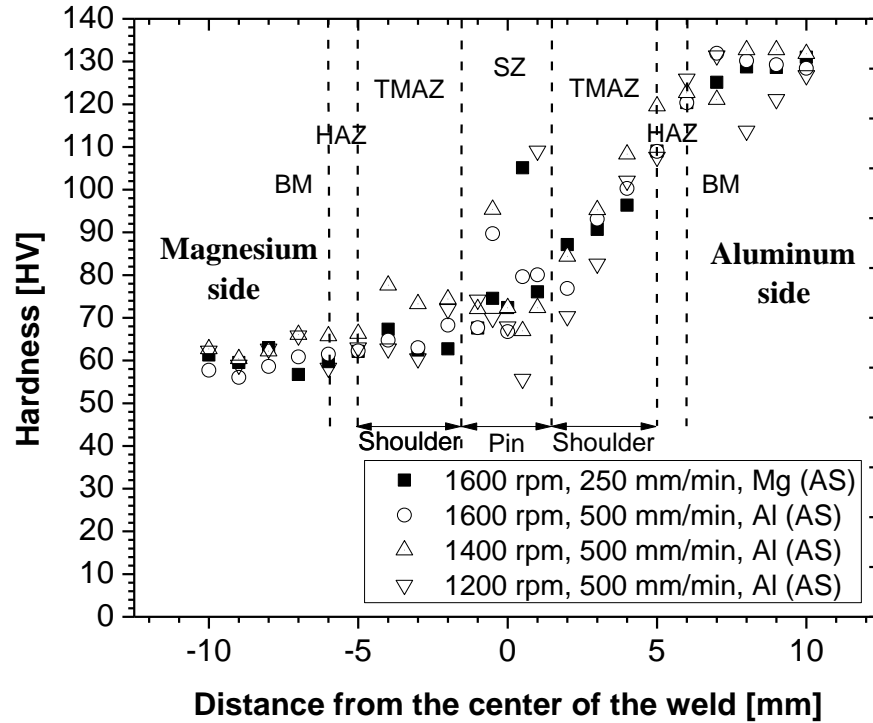
Figure IV.8. Microhardness values obtained at 2 mm from the top of weld for the various parameters studied.

The hardness values at three different distances from the top of the weld are shown in Figure IV.9 for the 1400 rpm, 500 mm/min (Al on AS) weld parameters. The hardness values are consistent for the three distances, suggesting good weld integrity. Similar to the previous observation a peak of hardness is measured in the SZ, and it appears corresponding to the micro-hardness of the interface between the Al and Mg sides. The 2.5 mm micro-hardness curve shows highest values in Al side compared to the two other micro-hardness curves, which can be associated with a higher percentage of the intermetallic compounds. Figure 4 shows that the region of the SZ matching with the 2.5 mm micro-hardness line in the Al side has a slightly different color compared to the other region of the SZ in the Al side. Furthermore, (Ammouri et al., 2015; Chen et al., 2013) reported through simulation that a peak of heat flux, strain rate, and flow stress was obtained around the pin tip, and more precisely on the advancing side. The formation of IMCs is related to the heat generation during the FSW process (Firouzdor and Kou, 2010b; Fu et al., 2015; Liang et al., 2013; Mohammadi et al., 2015; Morishige et al., 2008).

Therefore, we can assume that this change in color is affected by the change in the composition of this part; hence, we assume a higher percentage of IMCs.
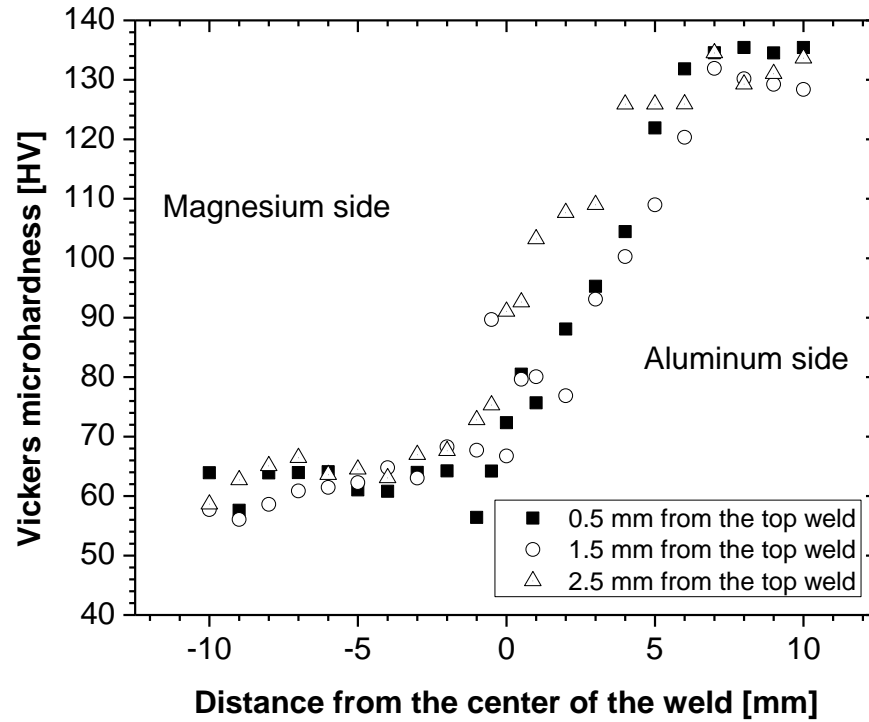
Figure IV.9. Micro-hardness obtained on weld prepared using 1400 rpm and 500 mm/min at three different distances from the top of the weld.

A color mapping of the previous microhardness graph is presented in Figure IV.10. It can be observed from that figure how the microhardness differs between the base materials, and in the center of the weld where the stir zone was created, we can better observe the FSW zones in this graph, the red color clearly refers to the aluminum base material, and the dark violet color to the magnesium base material, and in the between are the other FSW zones, the light blue color refers to the stir zone, the yellow and blue colors refers to the TMAZ in the aluminum and magnesium side respectively, these results can be correlated with the microstructure of the cross section obtained previously.
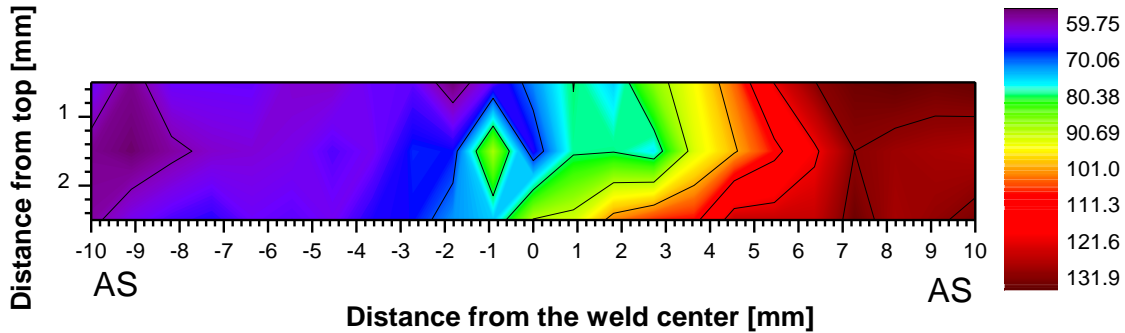
Figure IV.10. Color mapping of a Vickers microhardness of a cross-section Al-Mg welded using 1400 rpm and 250 mm/min.

Although aluminum and magnesium have different hardness, continuity in the evolution of the hardness was measured by scanning with the micro-indenter the weld region between the two BMs. However, a peak in the hardness values was found at the interface between the aluminum and the magnesium. The peak in the hardness values between the aluminum and the magnesium can be related to an abrupt change in the microstructure, more precisely the grain size and also to the presence of the IMCs (as reported previously in section 3.1). As the interface between the aluminum and the magnesium is formed by the IMCs, we assume that a higher level of incoherency will induce higher accumulation of dislocations during deformation. Therefore, the process of crack initiation will be further accelerated when the weld is subjected to tensile loading conditions owing to his higher density of dislocations.

IV.2.3 Uniaxial tensile testing

In the purpose of studying the joint efficiency of different weld parameters, to account for potential ranges of operation conditions and finally to study the failure mechanisms; the mechanical response of tensile tests conducted at room temperature and 200°C at a strain rate of 10^{-3} s^{-1} are presented in Figure IV.11.

IV.2.3.1 Room temperature

The engineering stress-strain tensile response of dissimilar FSW of Al (on AS) and Mg using constant tool rotation speed of 1600 rpm, and tool displacement speeds of 250, 500 and 750 mm/min are presented in Figure IV.11 (a). From this figure, it could be observed that decreasing the displacement speed resulted in higher strain to failure but lower strength. This observation can be explained by the fact that reducing the tool displacement speed leads to an increase in the heat input, which consequently increase the average grain size resulting in higher strain to failure and lower strength. The stress-strain response of the joint obtained using 750 mm/min as displacement speed presented the lowest strain to failure, which can be the consequence of the less heat input that results in smaller grain size (Albakri et al., 2013; Ammouri et al., 2015; Commin et al., 2009; Young et al., 2015).

The mechanical response of joints obtained by fixing the tool translational speed at 500 mm/min, and varying the tool rotational speeds between 1200 rpm to 1600 rpm (with Al on AS) are plotted in Figure IV.11 (b). From this figure, it can be observed that the joint obtained with 1600 rpm tool rotation speed presented the lowest strain to failure and strength compared to the other welding parameters. It was also observed that the joints obtained using 1400 rpm tool rotation speed showed the highest strain to failure. Those observations can be explained by the fact that using 500 mm/min and 1400 rpm as weld parameters produced the optimum heat generation and strain rate which resulted in defect-free joint and higher mechanical properties. The optimum weld parameters found through the current study are associated with the choice of the tool geometry, as heat generation, and the strain rate during welding is strongly dependent on the tool geometry.
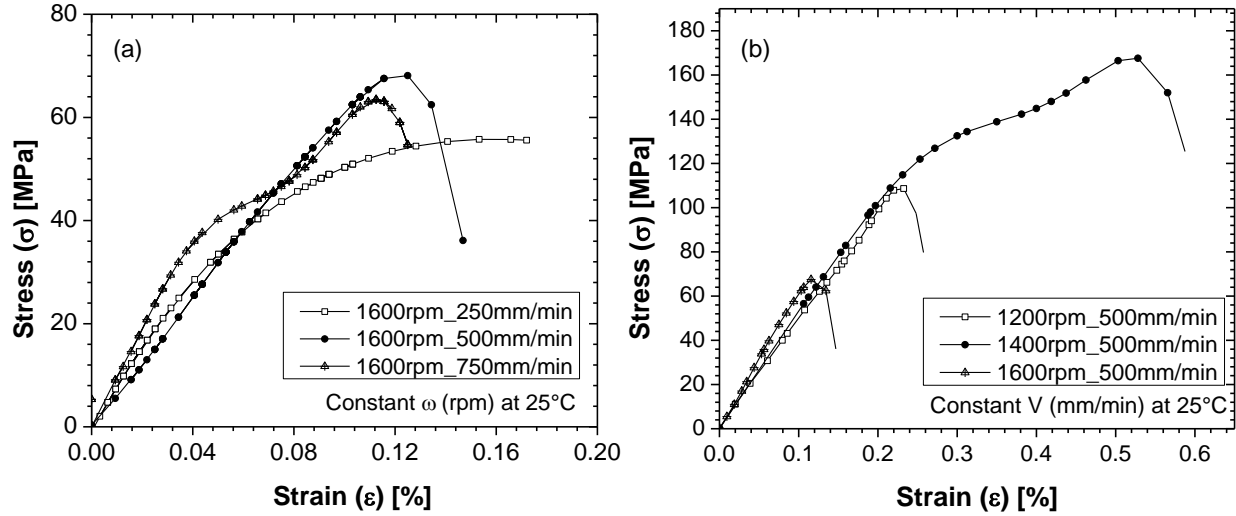
Figure IV.11. Engineering stress – strain curves of uniaxial tensile tested welds at room temperature and 10^{-3} s^{-1} with (a): constant tool rotation speed, (b): constant tool displacement speed.

The stress-strain response of the studied dissimilar Al/Mg welds exhibited a brittle behavior. In the purpose of analyzing the mechanical properties of the welds, the modulus of the dissimilar welds was calculated in the initial elastic region and compared to the Young's modulus of the AZ31B magnesium alloy (BM). Figure IV.12 (a) presents the modulus of magnesium (BM) compared to dissimilar welded Al/Mg joints obtained using constant tool rotational speed of (1600 rpm). The modulus of the BM (Mg) was observed to be 38.09 GPa. The welded specimens yielded to higher modulus with values equal approximately to 1.6 – 2.5 times the BM's modulus for varying tool displacement speeds. It can also be reported from Figure IV.12 (b) that the modulus was increased by 1.2 – 1.6 times the BM's modulus for joints obtained at constant tool displacement speed of 500 mm/min and by increasing the tool rotational speed. The increase in the modulus values can be explained by the formation of intermetallics that contributes to increasing the resistance to deformation (Masoudian et al., 2014b; Mohammadi et al., 2015).
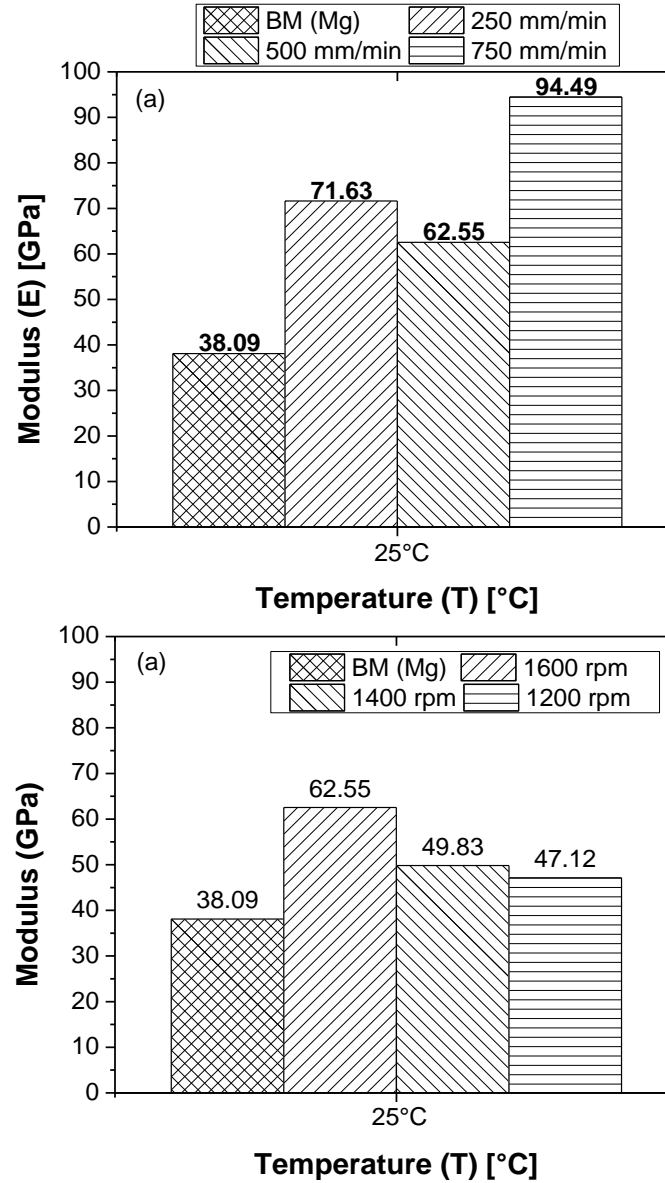
Figure IV.12. Modulus calculated at different tool rotation speed and tool displacement speed, (a): at constant tool rotation speed (1600 rpm) and (b): at constant tool displacement speed (500 mm/min)

To analyze and compare the mechanical properties of the studied welds, the joint efficiency of the welds was evaluated by normalizing the ultimate tensile strength (UTS) of the dissimilar Al/Mg joint by the UTS of the BM (Mg). At constant tool rotation speed, the FS welded joints exhibited a weak joint efficiency of approximately between 18% and 27% (see Figure IV.13 (a)) showing that the maximum joint efficiency was obtained at 500 mm/min tool

displacement speed. Figure IV.13 (b) presents the ultimate tensile strength of joints obtained at constant tool displacement speed and tool rotation speeds of 1200 rpm, 1400 rpm, and 1600 rpm. The joint efficiency was ranging between 27% and 55% with the higher value obtained at 1400 rpm rotation speed.
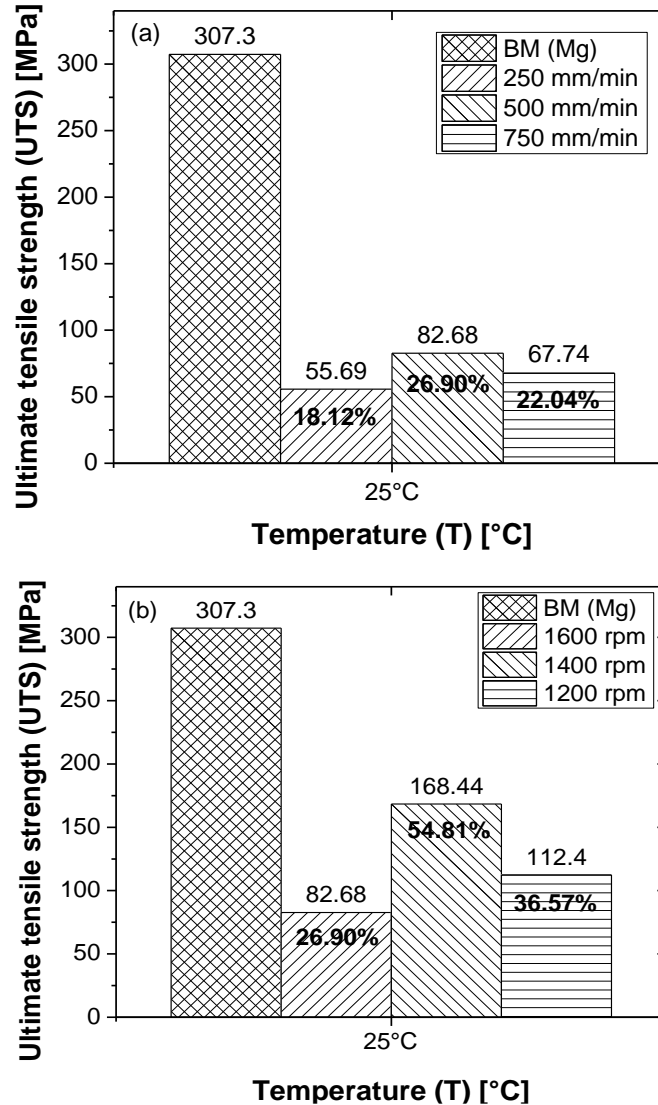
Figure IV.13. Ultimate tensile strength (UTS) calculated at different tool rotation speed and tool displacement rate (a) and (b) at room temperature

IV.2.3.2 High temperature

The engineering stress-strain response of uniaxial tensile tests conducted at 200°C of dissimilar butt welded Al/Mg joints with Al in the AS obtained using constant rotational speed (1600 rpm), is presented in Figure IV.14 (a). It can be noticed that using tool displacement speed of 750 mm/min resulted in higher strain to failure compared to the specimen obtained using 250 mm/min or 500 mm/min. The tool displacement speed of 750 mm/min is observed to present the optimum mechanical properties at elevated temperatures compared to the two other weld conditions. Figure IV.14 (b) presents the tensile stress-strain curves at 200°C of Al/Mg joints obtained using constant tool displacement speed (500 mm/min) and varying tool rotational speed. It is observed that using 1400 rpm tool rotation speed resulted in the highest tensile strength and strain to failure.
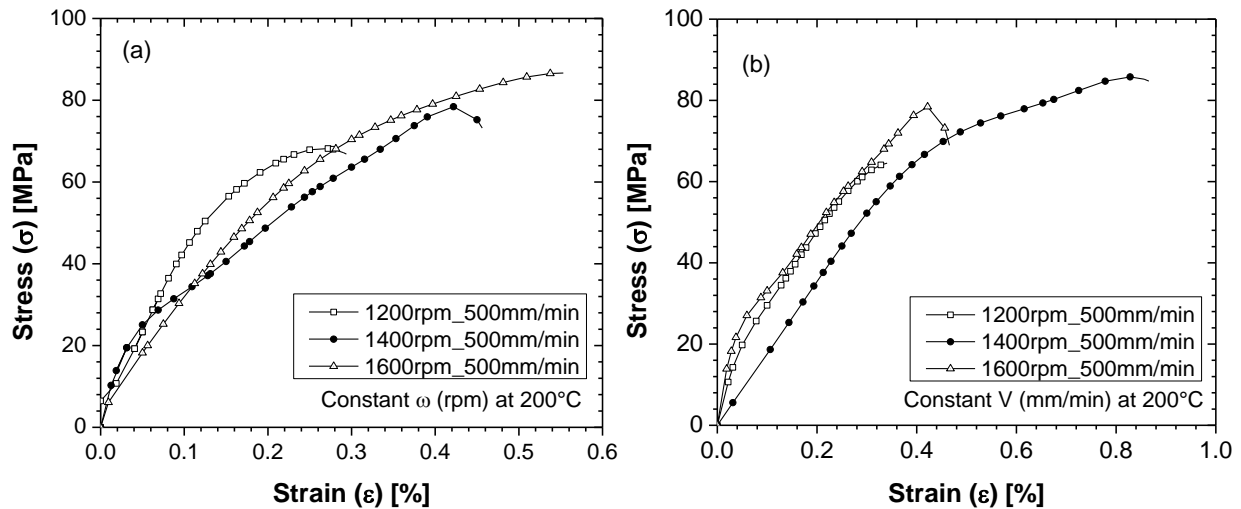
Figure IV.14. Engineering stress – strain curves of uniaxial tensile tested welds at room temperature and 10^{-3} s^{-1} at 200°C with (c): and constant tool rotation speed, (d): at constant tool displacement speed.

The joint efficiency of the welds at 200°C was calculated, and the results were presented in Figure IV.15. Under constant tool rotational speed of 1600 rpm (Figure IV.15 (a)), an improvement of the joint efficiency at 200°C is evident compared to room temperature and the values were found to be between 66 and 79%. The joint efficiency is observed to increase with

increasing tool displacement speed to reach its maximum value at 750 mm/min. In the case of constant displacement speed (500 mm/min) the joint efficiency reached a maximum value of approximately 77% using 1400 rpm tool rotation speed, as shown in Figure IV.15 (b).
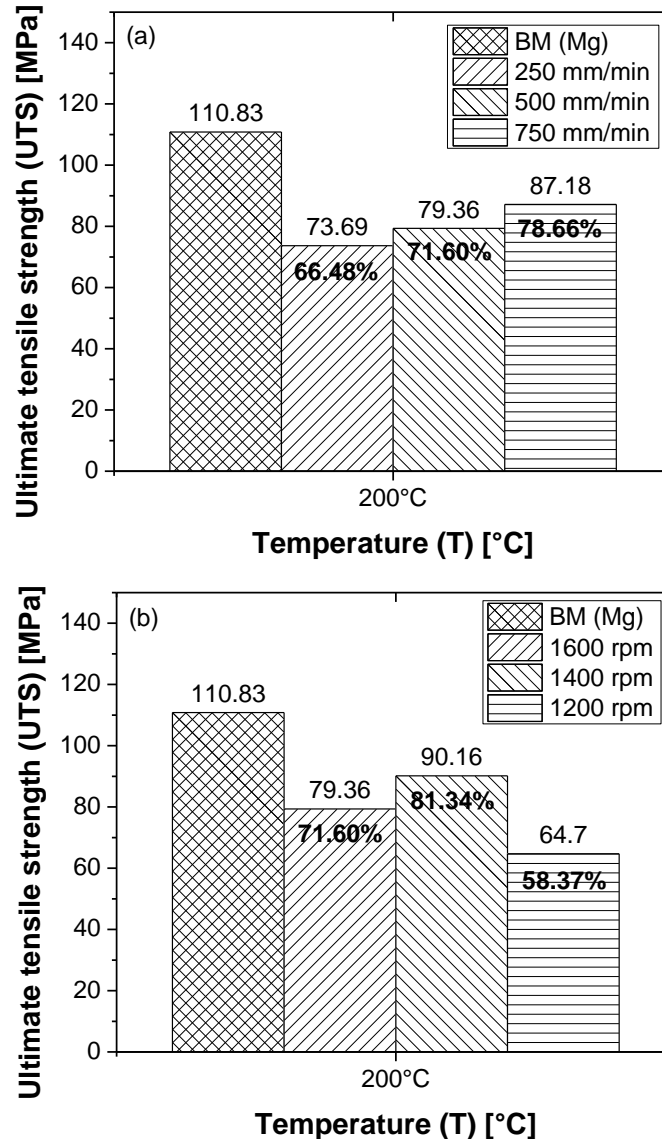
Figure IV.15. Ultimate tensile strength (UTS) calculated at different tool rotation speed and tool displacement rate (a) and (b) at room temperature, (c) and (d) at 200°C, respectively

IV.2.4 Fractography

In order to visually investigate the Al-to-Mg FS welded joint specimen failure, a tensile test specimen was ground up to 1200 grit SiC polishing paper. Images were obtained after tensile testing to observe the failure characteristics of the welded joint. Figure IV.16 presents a

specimen failed under tensile test with the joint being prepared using 1400 rpm tool rotational speed and 500 mm/min tool displacement speed with Al on the AS. Figure IV.16 (a) and (b) are observations of the failed specimen in the ND-TD plane. It can be observed from that the failure occurred along the line of the joint, between aluminum and magnesium. Moreover, the fracture seems to have initiated in the IMCs forming the interface between aluminum and magnesium. Furthermore, the cracks seem to have occurred along the interface between the aluminum and the IMCs, as we can observe aluminum fractions in the magnesium part of the weld. These results are in correlation with the observations in Figure IV.8, precisely, the peak in the microhardness values in the SZ and the variation of the percentage of IMCs on the aluminum side. Dorbane et al. reported that at a temperature lower or equal to 200°C the main crack initiation mechanism in Al 6061 T6 is particles fracture which also presented with lower ductility compared to AZ31B Mg (Dorbane et al., 2015b).
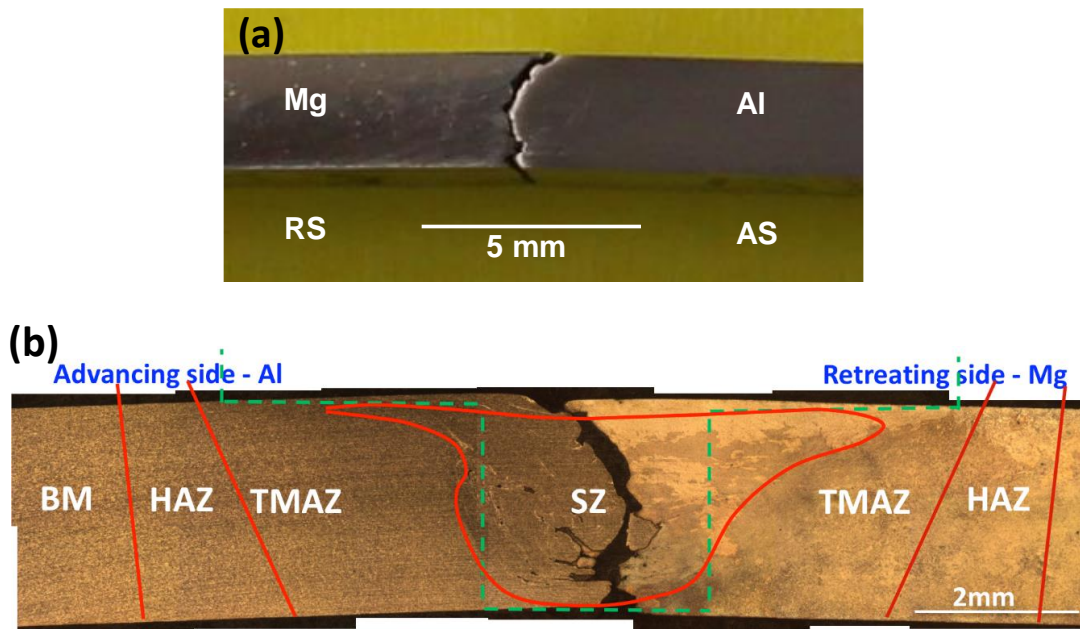
Figure IV.16. Dissimilar FS welded specimen using 1400 rpm and 500 mm/min fractured after tensile loading, (a) macroscopic observation (b) etched specimen observed with an optical microscope.

Moreover, the IMCs have a brittle behavior; with the dislocation accumulation at the interface with aluminum or magnesium, the IMCs will develop cracks. In the purpose of bringing further insight on the crack initiation mechanism, the fractured surface on the magnesium side of

a specimen tensile tested at room temperature, prepared using 1400 rpm and 500 mm/min weld parameters is shown in Figure IV.17. Figure IV.17 (a) presents chevron patterns on the fractured surface, which is characteristic of a brittle fracture. Figure IV.17 (b) presents a magnified region of the upper zone of the fracture surface showing ridges and broken IMCs. From the previous observation, we can suppose that the cracks are initiating either in the IMCs forming the interface between the aluminum and the magnesium parts, or by debonding at the interface between the IMCs and the aluminum part.
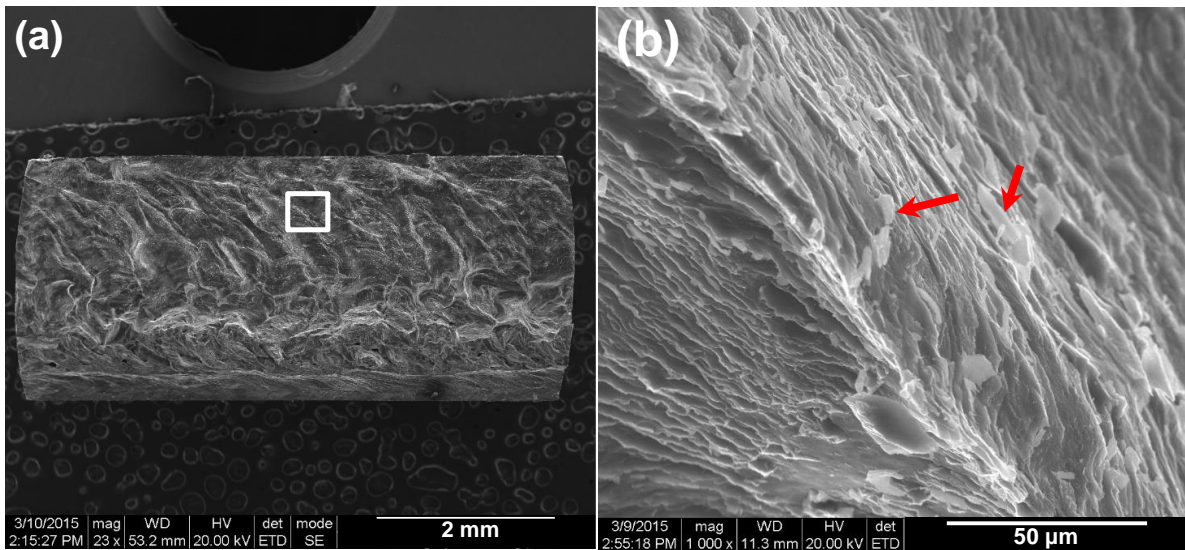
Figure IV.17. SEM fractography of an FS welded sample using 1400 rpm and 500 mm/min at room temperature.

IV.3 Conclusions

The following conclusions can be made based on the present study on friction stir welding on dissimilar metals – aluminum and magnesium:

- AZ31B magnesium alloy was successfully FS welded with 6061-T6 aluminum alloy with different parameters and material configurations.
- The examination of the FS welded joints cross section area, having aluminum on advancing side of the FSW resulted in better welds with fewer defects in the stir zone.

- Both Mg-rich and Al-rich sides of the stir zone revealed grain refinement, with the SZ grain sizes reducing to 2.43±0.87 μm and 0.94±0.24 μm on the Mg and Al sides, respectively.

- A thin layer of intermetallic compounds (IMC) were observed in the stir zone at the interface between the welded sheets, which affected the weld properties.

- The microhardness showed a lower hardness values (55 – 65HV) in the magnesium base material and higher values (120 – 135HV) in aluminum base material, with a transition in the stir zone and some peaks due to the IMCs in the SZ.

- Uniaxial tensile testing was performed at different temperatures, the strength of the joint was influenced by both FSW parameters and tensile testing temperature. Room temperature joint efficiency of the welds prepared in the current study were between 18 – 55% while at elevated temperature the joint efficiency were between 58 – 79% for the different parameters.

- Brittle fracture was observed on the specimens tested under tensile loading, with the fracture surface showing chevron pattern. The specimens have fractured along the welded joint with the fracture initiating in the IMCs between the Al and Mg.

General conclusion

This work has the objective to first optimize the welding quality and second to characterize the mechanical, texture and microstructural properties of similar and dissimilar friction stir welded materials.

For that purpose the microstructural and mechanical characterization of the base materials 6061-T6 aluminum and AZ31B magnesium alloys was achieved. The mechanical behavior and the microstructural evolution of Al 6061-T6 and AZ31B were studied under uniaxial loading condition performed at different temperatures (25, 100, 200, and 300 °C) and strain rates (10^{-4}, 10^{-3}, 10^{-2}, 10^{-1} s^{-1}). For the Al 6061-T6: (i) The Yield stress and the ultimate tensile strength were observed to increase with increasing strain rate and decreasing temperature. The maximum strain to failure was found to increase with increasing temperature and decreasing strain rate for tests performed at room temperature and 100°C. By contrast, the maximum strain to failure was found to decrease with increasing temperature and decreasing strain rate for tests performed at 200°C and 300°C. (ii) The analysis of fracture surfaces of the tested specimen has confirmed the ductile behavior nature of the studied materials as coalesced micro-voids and microscopic dimples were observed. Insightful analysis has been conducted with the aim to track the damage mechanisms of the Al 6061 T6 by observing the microstructure of samples subjected to interrupted tests. It was noted that the intermetallic phase particles are the privileged sites of crack initiation. For AZ31B: (iii) At room temperature, AZ31B magnesium alloy is not influenced by the strain rate, but at higher temperature it shows a strong dependence of the mechanical behavior of material with the strain rate, with lowering the strain rate values, the strain to failure increases and the UTS decreases simultaneously. (iv) Slip and Twinning is probably the main deformation mechanism at 25°C, in addition dynamic recrystallization is observed to occur at 200°C, and at 300°C.

In order to study the mechanical and microstructural and textural properties of FSW joints, 3mm thick Al 6061 T6 and AZ31B sheets were welded using an optimized FSW welding condition, found for the particular tool geometry used. Defect-free friction stir welding joints was successfully achieved for Al 6061-T6: (v) The FSW joints exhibited approximately the same behavior as the base material regarding the decrease in the elongation at high temperature. (vi) The hardness values showed a W-shape profile. Pointing out to the presence of two competing mechanisms: first grain refinement that leads to the increase in the hardness values and second

precipitates dissolution that leads to decrease of the hardness values. The hardness results showed that the region under the tool exhibited lower hardness compared to the other zones. Which yields to the following conclusion: the precipitates dissolution mechanism is the predominant mechanism. Defect-free friction stir welding joints was successfully achieved for AZ31B at spindle speed and tool feed rate of 1200 rpm and 150 mm/min, respectively: (vii) As general observation of the microstructure and the texture: (a) the SZ exhibited a recrystallized microstructure characterized by minor grain growth and strengthening of the basal texture due to a rotation of the crystal c-axis around the WD; (b) the TMAZ on the AS presented a slight modification of the microstructure and texture compared to the base metal; (c) the TMAZ on the RS showed higher level of deformation compared to its counterpart but lower than the SZ, some recrystallization and some strengthening of the basal texture was also observed. (viii) Vickers micro-hardness values measured were maximum at the interface between the SZ and the TMAZ on the AS and were attributed to an abrupt change in the grain size and the micro-texture. Consequently, it was assumed that cracks would initiate at this interface between due to a higher level of incoherency, which may lead to an accumulation of dislocations. (ix) Failure mechanisms in the stir zone were investigated, and a larger number of cracks were observed in the FSW (parallel samples) tested in tension at 200°C compared to samples tested at RT. It was observed that the majority of cracks had initiated in the second-phase intermetallic particles.

Furthermore, we studied the mechanical, microstructural and fracture properties of heterogeneous FSW welds obtained by developing the tool rotation and translation speeds. The dissimilar welds microstructure and mechanical properties were evaluated and correlated with the FSW parameters to obtain the optimum weld conditions. (x) The results showed that placing aluminum on the advancing side of the weld resulted in better quality welds. (xi) A discontinuity in the microhardness values, attributed to the intermetallic compounds (IMC) present, was observed at the weld interface between Mg and Al sheets. (xii) The specimen showed brittle behavior under tensile testing, and the specimen fracture occurred along the weld joint. The specimen fracture seems to have initiated in the brittle Mg_2Al_3 and $Mg_{17}Al_{12}$ IMCs formed between the welded sheets.

Work prospect

This Ph.D. dissertation focused on the mechanical and microstructural characterization of the friction stir welding of aluminum and magnesium alloys, many results were obtained and interesting discussions were made in this work.

As a work prospect for this thesis, we propose the following:

1. Studying the kinetics of intermetallic formation and optimizing their volume fraction distribution in the welded joints on the overall behavior.
2. Studying the sustainability of welded joints under fatigue loading in function of the weld parameters.
3. Modeling of the friction stir welding process inspired by models implemented for non-Newtonian fluids, to predict strain rates, temperatures and generated textures.

References

Afrin, N., Chen, D.L., Cao, X., Jahazi, M., 2008. Microstructure and tensile properties of friction stir welded AZ31B magnesium alloy. Materials Science and Engineering: A 472, 179-186.

Agarwal, H., Gokhale, A.M., Graham, S., Horstemeyer, M.F., 2003. Void growth in 6061-aluminum alloy under triaxial stress state. Materials Science and Engineering: A 341, 35-42.

Albakri, A.N., Mansoor, B., Nassar, H., Khraisheh, M.K., 2013. Thermo-mechanical and metallurgical aspects in friction stir processing of AZ31 Mg alloy—A numerical and experimental investigation. Journal of Materials Processing Technology 213, 279-290.

Alvarez, P., Janeiro, G., da Silva, A.A.M., Aldanondo, E., Echeverría, A., 2010. Material flow and mixing patterns during dissimilar FSW. Science and Technology of Welding and Joining 15, 648-653.

Ambriz, R.R., Barrera, G., García, R., López, V.H., 2009. A comparative study of the mechanical properties of 6061-T6 GMA welds obtained by the indirect electric arc (IEA) and the modified indirect electric arc (MIEA). Materials & Design 30, 2446-2453.

Ambriz, R.R., Barrera, G., García, R., López, V.H., 2010. The microstructure and mechanical strength of Al-6061-T6 GMA welds obtained with the modified indirect electric arc joint. Materials & Design 31, 2978-2986.

Ammouri, A., Achdjian, H., Dorbane, A., Ayoub, G., Kridli, G., Hmade, R., 2014. Characterization of optimized friction stir welded twin roll cast AZ31B sheets, International Mechanical Engineering Congress and Exposition, Montreal, Canada

Ammouri, A.H., Kridli, G., Ayoub, G., Hamade, R.F., 2015. Relating grain size to the Zener–Hollomon parameter for twin-roll-cast AZ31B alloy refined by friction stir processing. Journal of Materials Processing Technology 222, 301-306.

Aonuma, M., Nakata, K., 2012. Dissimilar metal joining of ZK60 magnesium alloy and titanium by friction stir welding. Materials Science and Engineering: B 177, 543-548.

Arbegast, W.J., 2008. A flow-partitioned deformation zone model for defect formation during friction stir welding. Scripta Materialia 58, 372-376.

ASM, 1992. ASM Handbook. ASM International.

ASTM-E3-11, Standard Guide for Preparation of Metallographic Specimens, ASTM International, West Conshohocken, PA, 2011, www.astm.org.

ASTM-E8/E8M, Standard Test Methods for Tension Testing of Metallic Materials, ASTM International, West Conshohocken, PA, 2015, www.astm.org.

ASTM-E21-09, Standard Test Methods for Elevated Temperature Tension Tests of Metallic Materials, ASTM International, West Conshohocken, PA, 2009, www.astm.org.

Atharifar, H., Lin, D., Kovacevic, R., 2008. Numerical and Experimental Investigations on the Loads Carried by the Tool During Friction Stir Welding. Journal of Materials Engineering and Performance 18, 339-350.

Badarinarayan, H., Shi, Y., Li, X., Okamoto, K., 2009. Effect of tool geometry on hook formation and static strength of friction stir spot welded aluminum 5754-O sheets. International Journal of Machine Tools and Manufacture 49, 814-823.

Bahrami, A., Miroux, A., Sietsma, J., 2013. Modeling of Strain Hardening in the Aluminum Alloy AA6061. Metallurgical and Materials Transactions A 44, 2409-2417.

Bakavos, D., Prangnell, P.B., 2009. Effect of reduced or zero pin length and anvil insulation on friction stir spot welding thin gauge 6111 automotive sheet. Science and Technology of Welding and Joining 14, 443-456.

Balluffi, R.W., 1970. On measurements of self-diffusion rates along dislocations in F.C.C. Metals. physica status solidi (b) 42, 11-34.

Bannour, S., Abderrazak, K., Mattei, S., Masse, J.E., Autric, M., Mhiri, H., 2013. The influence of position in overlap joints of Mg and Al alloys on microstructure and hardness of laser welds. Journal of Laser Applications 25, 032001.

Ben-Artzy, A., Munitz, A., Kohn, G., Bronfin, B., Shtechman, A., 2002. Joining of light hybrid constructions made of magnesium and aluminum alloys, TMS Annual Meeting, pp. 295-302.

Benavides, S., Li, Y., Murr, L.E., Brown, D., McClure, J.C., 1999. Low-temperature friction-stir welding of 2024 aluminum. Scripta Materialia 41, 809-815.

Bethge, H., Heydenreich, J., 1987. Electron microscopy in solid state physics. Elsevier.

Bhamji, I., Preuss, M., Moat, R., Threadgill, P., Addison, A., 2012. Linear friction welding of aluminium to magnesium. Science and Technology of Welding and Joining 17, 368-374.

Blaz, L., Evangelista, E., 1996. Strain rate sensitivity of hot deformed Al and AlMgSi alloy. Materials Science and Engineering: A 207, 195-201.

Bozzi, S., Etter, A.L., Baudin, T., Robineau, A., Goussain, J.C., 2008. Mechanical Behaviour and Microstructure of Aluminum-Steel Sheets Joined by FSSW. Texture, Stress, and Microstructure 2008, 1-8.

Brandes, E.A., Brook, G.B., 1992. Smithells Metals Reference Book (Seventh Edition). Butterworth-Heinemann, Oxford.

Buffa, G., Hua, J., Shivpuri, R., Fratini, L., 2006. Design of the friction stir welding tool using the continuum based FEM model. Materials Science and Engineering: A 419, 381-388.

Cabibbo, M., Ciccarelli, D., Di Salvia, A., Quercetti, G., Spigarelli, S., 2012. Microstructural aspects of a fiction stir welded joint of magnesium AZ31 and aluminium 6060 alloys. Metallurgia Italiana, 13-18.

Cao, X., Garnier, C., Wanjara, P., 2013. Tensile strength of friction stir spot welded dissimilar AA5754-to-AZ31B alloys, 9th International Conference on Trends in Welding Research, June 4, 2012 - June 8, 2012. ASM International, Chicago, IL, United states, pp. 572-579.

Cao, X., Jahazi, M., 2009. Effect of welding speed on the quality of friction stir welded butt joints of a magnesium alloy. Materials & Design 30, 2033-2042.

Cao, X., Jahazi, M., 2011. Effect of tool rotational speed and probe length on lap joint quality of a friction stir welded magnesium alloy. Materials & Design 32, 1-11.

Cary, H.B., Modern Welding Technology, Prentice-Hall, New Jersey, 2002.

Chang, S.-Y., Lee, K.-S., Choi, S.-H., Hyuk Shin, D., 2003. Effect of ECAP on microstructure and mechanical properties of a commercial 6061 Al alloy produced by powder metallurgy. Journal of Alloys and Compounds 354, 216-220.

Chao, Y.J., Liu, S., Chien, C.H., 2008. Friction stir welding of al 6061-T6 thick plates: Part I - experimental analyses of thermal and mechanical phenomena. Journal of the Chinese Institute of Engineers 31, 757-767.

Chen, G.-q., Shi, Q.-y., Li, Y.-j., Sun, Y.-j., Dai, Q.-l., Jia, J.-y., Zhu, Y.-c., Wu, J.-j., 2013. Computational fluid dynamics studies on heat generation during friction stir welding of aluminum alloy. Computational Materials Science 79, 540-546.

Chen, T.P., Lin, W.B., 2010. Optimal FSW process parameters for interface and welded zone toughness of dissimilar aluminium–steel joint. Science and Technology of Welding and Joining 15, 279-285.

Chen Z., 2010. Superplasticity of coarse grained aluminum alloys. University of Groningen.

Chi, C.-T., Chao, C.-G., Liu, T.-F., Lee, C.-H., 2007. Aluminum element effect for electron beam welding of similar and dissimilar magnesium–aluminum–zinc alloys. Scripta Materialia 56, 733-736.

Choi, C.-H., Lee, D., 1997. Evolution of recrystallization texture from aluminum sheet cold rolled under unlubricated condition. Metallurgical and Materials Transactions A 28, 2217-2222.

Chowdhury, S.M., Chen, D.L., Bhole, S.D., Cao, X., 2010. Tensile properties of a friction stir welded magnesium alloy: Effect of pin tool thread orientation and weld pitch. Materials Science and Engineering: A 527, 6064-6075.

Coelho, R.S., Kostka, A., Sheikhi, S., dos Santos, J., Pyzalla, A.R., 2008. Microstructure and Mechanical Properties of an AA6181-T4 Aluminium Alloy to HC340LA High Strength Steel Friction Stir Overlap Weld. Advanced Engineering Materials 10, 961-972.

Colegrove, P.A., Shercliff, H.R., 2003. Experimental and numerical analysis of aluminium alloy 7075-T7351 friction stir welds. Science and Technology of Welding and Joining 8, 360-368.

Colegrove, P.A., Shercliff, H.R., 2004a. Development of Trivex friction stir welding tool Part 1 – two-dimensional flow modelling and experimental validation. Science and Technology of Welding and Joining 9, 345-351.

Colegrove, P.A., Shercliff, H.R., 2004b. Development of Trivex friction stir welding tool Part 2 – three-dimensional flow modelling. Science and Technology of Welding and Joining 9, 352-361.

Collier, M., Steel, R., Nelson, T.W., Sorensen, C., Packer, S., 2003. Grade development of polycrystalline cubic boron nitride for friction stir processing of ferrous alloys, Materials Science Forum. Trans Tech Publ, pp. 3011-3016.

Colligan, K., 1999. Material flow behavior during friction welding of aluminum. Welding Journal 75, 229s-237s.

Commin, L., Dumont, M., Masse, J.E., Barrallier, L., 2009. Friction stir welding of AZ31 magnesium alloy rolled sheets: Influence of processing parameters. Acta Materialia 57, 326-334.

Commin, L., Dumont, M., Rotinat, R., Pierron, F., Masse, J.-E., Barrallier, L., 2012. Influence of the microstructural changes and induced residual stresses on tensile properties of wrought magnesium alloy friction stir welds. Materials Science and Engineering: A 551, 288-292.

Cui, G.R., Ma, Z.Y., Li, S.X., 2008. Periodical plastic flow pattern in friction stir processed Al–Mg alloy. Scripta Materialia 58, 1082-1085.

Davis, J.R., 2004. Tensile testing, second edition. ASM International, Materials Park, Ohio.

Dawes, C.J., Thomas, W.M., 1996. Friction stir process welds aluminum alloys. Welding. Journal Vol. 75, pp. 41-45.

De Pablos, A., Osendi, M.I., Miranzo, P., 2002. Effect of Microstructure on the Thermal Conductivity of Hot-Pressed Silicon Nitride Materials. Journal of the American Ceramic Society 85, 200-206.

Dieter, G.E., 1986. Mechanical Metallurgy. DI Metric Edition.

Donath, T., Beckmann, F., Zettler, R., dos Santos, J., Lohwasser, D., Lippman, T., Clemens, H., Schreyer, A., 2004. Investigation of Material Flow in Friction Stir Welding using Computed Microtomography. AIP Conference Proceedings 705, 1312-1315.

Dorbane, A., Ayoub, G., Mansoor, B., Hamade, R., Kridli, G., Imad, A., 2015a. Mechanical Response and Evolution of Damage of Al6061-T6 Under Different Strain Rates and Temperatures, TMS Middle East - Mediterranean Materials Congress on Energy and Infrastructure Systems (MEMA 2015). John Wiley & Sons, Inc., pp. 259-265.

Dorbane, A., Ayoub, G., Mansoor, B., Hamade, R., Kridli, G., Imad, A., 2015b. Observations of the mechanical response and evolution of damage of AA 6061-T6 under different strain rates and temperatures. Materials Science and Engineering: A 624, 239-249.

Dorbane, A., Ayoub, G., Mansoor, B., Hamade, R.F., Kridli, G., Shabadi, R., Imad, A., 2016. Microstructural observations and tensile fracture behavior of FSW twin roll cast AZ31 Mg sheets. Materials Science and Engineering: A 649, 190-200.

Duffy, L., 1996. Magnesium Alloys. Magnesium Alloys Magnesium Alloys Materials World, Vol 4. No.3,pp. 127-30, 1996.

Dutta, I., Allen, S.M., 1991. A calorimetric study of precipitation in commercial aluminium alloy 6061. Journal of Materials Science Letters 10, 323-326.

Dwight, J., 2002. Aluminium Design and Construction. CRC Press.

Edwards, G.A., Stiller, K., Dunlop, G.L., 1994. APFMI investigation of fine-scale precipitation in aluminum alloy 6061. Applied Surface Science 76/77, 219–255.

Etter, A.L., Baudin, T., Fredj, N., Penelle, R., 2007. Recrystallization mechanisms in 5251 H14 and 5251 O aluminum friction stir welds. Materials Science and Engineering: A 445-446, 94-99.

Fahimpour, V., Sadrnezhaad, S.K., Karimzadeh, F., 2013. Microstructure and Mechanical Property Change During FSW and GTAW of Al6061 Alloy. Metallurgical and Materials Transactions A 44, 2187-2195.

Firouzdor, V., Kou, S., 2009. Al-to-Mg friction stir welding: effect of positions of Al and Mg with respect to the welding tool. Welding Journal, 213-223.

Firouzdor, V., Kou, S., 2010a. Al-to-mg friction stir welding: effect of material position, travel speed, and rotation speed. Metallurgical and Materials Transactions A (Physical Metallurgy and Materials Science) 41, 2914-2935.

Firouzdor, V., Kou, S., 2010b. Formation of Liquid and Intermetallics in Al-to-Mg Friction Stir Welding. Metallurgical and Materials Transactions A 41, 3238-3251.

Friedrich, H., Schumann, S., 2001. Research for a "new age of magnesium" in the automotive industry. Journal of Materials Processing Technology 117, 276-281.

Frost, H.J., Ashby, M.F., 1982. Deformation-mechanism maps : the plasticity and creep of metals and ceramics. Pergamon Press, Oxford [Oxfordshire]; New York.

Fu, B., Qin, G., Li, F., Meng, X., Zhang, J., Wu, C., 2015. Friction stir welding process of dissimilar metals of 6061-T6 aluminum alloy to AZ31B magnesium alloy. Journal of Materials Processing Technology 218, 38-47.

Fu, M.W., Tham, Y.W., Hng, H.H., Lim, K.B., 2009. The grain refinement of Al-6061 via ECAE processing: Deformation behavior, microstructure and property. Materials Science and Engineering: A 526, 84-92.

Fujii, H., Cui, L., Maeda, M., Nogi, K., 2006. Effect of tool shape on mechanical properties and microstructure of friction stir welded aluminum alloys. Materials Science and Engineering: A 419, 25-31.

Gan, W., Li, Z.T., Khurana, S., 2007. Tool materials selection for friction stir welding of L80 steel. Science and Technology of Welding and Joining 12, 610-613.

Genevois, C., Deschamps, A., Denquin, A., Doisneaucottignies, B., 2005. Quantitative investigation of precipitation and mechanical behaviour for AA2024 friction stir welds. Acta Materialia 53, 2447-2458.

Ghahremaninezhad, A., Ravi-Chandar, K., 2012. Ductile failure behavior of polycrystalline Al 6061-T6. International Journal of Fracture 174, 177-202.

Guerra, M., Schmidt, C., McClure, J.C., Murr, L.E., Nunes, A.C., 2002. Flow patterns during friction stir welding. Materials Characterization 49, 95-101.

Hassan, K.A.A., Norman, A.F., Price, D.A., Prangnell, P.B., 2003a. Stability of nugget zone grain structures in high strength Al-alloy friction stir welds during solution treatment. Acta Materialia 51, 1923-1936.

Hassan, K.A.A., Prangnell, P.B., Norman, A.F., Price, D.A., Williams, S.W., 2003b. Effect of welding parameters on nugget zone microstructure and properties in high strength aluminium alloy friction stir welds. Science and Technology of Welding and Joining 8, 257-268.

Hatch, J.E., Association, A., Metals, A.S.f., 1984. Aluminum: Properties and Physical Metallurgy. American Society for Metals.

Hayat, F., 2011. The effects of the welding current on heat input, nugget geometry, and the mechanical and fractural properties of resistance spot welding on Mg/Al dissimilar materials. Materials & Design 32, 2476-2484.

Heinz, B., Skrotzki, B., 2002. Characterization of a friction-stir-welded aluminum alloy 6013. Metallurgical and Materials Transactions B 33, 489-498.

Hirano, S., Okamoto, K., Doi, M., Kamura, O., Inagaki, M., Aono, Y., 2004. Microstructure of the interface in magnesium alloy to aluminium alloy dissimilar joints produced by friction stir welding. Welding International 18, 702-708.

Hovanski, Y., Santella, M.L., Grant, G.J., 2007. Friction stir spot welding of hot-stamped boron steel. Scripta Materialia 57, 873-876.

Hull, D., Bacon, D.J., 2011. Introduction to Dislocations. Fifth Edition.

Hunt, F., Yang, Q., Badarinarayan, H., Okamoto, K., Platt, D., 2007. Friction stir welding of dissimilar magnesium alloys for automotive applications, 2007 World Congress, April 16, 2007 - April 19, 2007. SAE International, Detroit, MI, United states.

Hwang, Y.M., Fan, P.L., Lin, C.H., 2010. Experimental study on Friction Stir Welding of copper metals. Journal of Materials Processing Technology 210, 1667-1672.

Jasthi, B.K., Arbegast, W.J., Howard, S.M., 2008. Thermal Expansion Coefficient and Mechanical Properties of Friction Stir Welded Invar (Fe-36%Ni). Journal of Materials Engineering and Performance 18, 925-934.

Jata, K.V., Sankaran, K.K., Ruschau, J.J., 2000. Friction-stir welding effects on microstructure and fatigue of aluminum alloy 7050-T7451. Metallurgical and Materials Transactions A 31, 2181-2192.

Jata, K.V., Semiatin, S.L., 2000. Continuous dynamic recrystallization during friction stir welding of high strength aluminum alloys. Scripta Materialia 43, 743-749.

Jiang, J.Z., Lindelov, H., Gerward, L., Ståhl, K., Recio, J.M., Mori-Sanchez, P., Carlson, S., Mezouar, M., Dooryhee, E., Fitch, A., Frost, D.J., 2002. Compressibility and thermal expansion of cubic silicon nitride. Physical Review B 65, 161202.

Jiang, L., Jonas, J.J., Luo, A.A., Sachdev, A.K., Godet, S., 2006. Twinning-induced softening in polycrystalline AM30 Mg alloy at moderate temperatures. Scripta Materialia 54, 771-775.

Kang, S.H., Bang, W.H., Cho, J.H., Han, H.N., Oh, K.H., Lee, C.G., Kim, S.J., 2005. Microtexture Analysis of Friction Stir Welded Al 6061-T651 Plates. Materials Science Forum 495-497, 901-906.

Kashihara, K., Inagaki, H., 2009. Effect of Precipitation on Development of Recrystallization Texture in a 6061 Aluminum Alloy. Materials Transactions 50, 528–536.

Kheireddine, A.H., Ammouri, A.H., Kridli, G.T., Hamade, R.F., 2013. Experimentally validated thermo-mechanically coupled FE simulations of Al/Mg friction stir welded joints International Mechanical Engineering Congress and Exposition, San Diego, California, USA

Khodaverdizadeh, H., Mahmoudi, A., Heidarzadeh, A., Nazari, E., 2012. Effect of friction stir welding (FSW) parameters on strain hardening behavior of pure copper joints. Materials & Design 35, 330-334.

Khodir, S.A., Morisada, Y., Ueji, R., Fujii, H., 2012. Microstructures and mechanical properties evolution during friction stir welding of SK4 high carbon steel alloy. Materials Science and Engineering: A 558, 572-578.

Kim, J.K., Kim, H.K., Park, J.W., Kim, W.J., 2005. Large enhancement in mechanical properties of the 6061 Al alloys after a single pressing by ECAP. Scripta Materialia 53, 1207-1211.

Kimapong, K., Watanabe, T., 2005. Lap Joint of A5083 Aluminum Alloy and SS400 Steel by Friction Stir Welding. MATERIALS TRANSACTIONS 46, 835-841.

Kondori, B., Benzerga, A.A., 2014. Effect of Stress Triaxiality on the Flow and Fracture of Mg Alloy AZ31. Metallurgical and Materials Transactions A 45, 3292-3307.

Kostka, A., Coelho, R.S., dos Santos, J., Pyzalla, A.R., 2009. Microstructure of friction stir welding of aluminium alloy to magnesium alloy. Scripta Materialia 60, 953-956.

Kuijpers, N.C.W., Vermolen, F.J., Vuik, C., Koenis, P.T.G., Nilsen, K.E., Zwaag, S.v.d., 2005. The dependence of the β-AlFeSi to α-Al(FeMn)Si transformation kinetics in Al–Mg–Si alloys on the alloying elements. Materials Science and Engineering: A 394, 9-19.

Kumar, A., Raju, L.S., 2012. Influence of Tool Pin Profiles on Friction Stir Welding of Copper. Materials and Manufacturing Processes 27, 1414-1418.

Kumar, K., Kailas, S.V., Srivatsan, T.S., 2008. Influence of Tool Geometry in Friction Stir Welding. Materials and Manufacturing Processes 23, 188-194.

Kumar, N., Mishra, R.S., Huskamp, C.S., Sankaran, K.K., 2011. The effect of friction stir processing on the microstructure and mechanical properties of equal channel angular pressed 5052Al alloy sheet. Journal of Materials Science 46, 5527-5533.

Kwon, Y.-J., Shim, S.-B., Park, D.-H., 2009. Friction stir welding of 5052 aluminum alloy plates. Transactions of Nonferrous Metals Society of China 19, Supplement 1, s23-s27.

Kwon, Y.J., Shigematsu, I., Saito, N., 2008. Dissimilar friction stir welding between magnesium and aluminum alloys. Materials Letters 62, 3827-3829.

Lassance, D., Fabregue, D., Delannay, F., Pardoen, T., 2007. Micromechanics of room and high temperature fracture in 6xxx Al alloys. Progress in Materials Science 52, 62-129.

Leal, R.M., Leitão, C., Loureiro, A., Rodrigues, D.M., Vilaça, P., 2008. Material flow in heterogeneous friction stir welding of thin aluminium sheets: Effect of shoulder geometry. Materials Science and Engineering: A 498, 384-391.

Lee, K.-J., Kwon, E.-P., 2014. Microstructure of stir zone in dissimilar friction stir welds of AA6061-T6 and AZ31 alloy sheets. Transactions of Nonferrous Metals Society of China 24, 2374-2379.

Lee, W.-B., Jung, S.-B., 2004. The joint properties of copper by friction stir welding. Materials Letters 58, 1041-1046.

Lee, W.-S., Shyu, J.-C., Chiou, S.-T., 1999. Effect of strain rate on impact response and dislocation substructure of 6061-T6 aluminum alloy. Scripta Materialia 42, 51-56.

Lee, W., Chung, K.-H., Kim, D., Kim, J., Kim, C., Okamoto, K., Wagoner, R.H., Chung, K., 2009. Experimental and numerical study on formability of friction stir welded TWB sheets based on hemispherical dome stretch tests. International Journal of Plasticity 25, 1626-1654.

Lee, W.B., Yeon, Y.M., Jung, S.B., 2003a. Joint properties of friction stir welded AZ31B– H24 magnesium alloy. Materials Science and Technology 19, 785-790.

Lee, Y., Kwon, Y., Lee, J., Park, C., Kim, S., 2003b. Effects of strain and strain rate on tensile behavior of hot-forged Al 6061-T6. Materials Science and Engineering: A 362, 187-191.

Li, D., Yang, X., Cui, L., He, F., Shen, H., 2014. Effect of welding parameters on microstructure and mechanical properties of AA6061-T6 butt welded joints by stationary shoulder friction stir welding. Materials & Design 64, 251-260.

Li, W.Y., Li, J.F., Zhang, Z.H., Gao, D.L., Chao, Y.J., 2013. Metal Flow during Friction Stir Welding of 7075-T651 Aluminum Alloy. Experimental Mechanics 53, 1573-1582.

Li, Y., Murr, L.E., McClure, J.C., 1999. Flow visualization and residual microstructures associated with the friction-stir welding of 2024 aluminum to 6061 aluminum. Materials Science and Engineering: A 271, 213-223.

Li, Y., Trillo, E.A., Murr, L.E., 2000. Friction-stir welding of aluminum alloy 2024 to silver. Journal of Materials Science Letters 19, 1047-1051.

Liang, Z., Chen, K., Wang, X., Yao, J., Yang, Q., Zhang, L., Shan, A., 2013. Effect of Tool Offset and Tool Rotational Speed on Enhancing Mechanical Property of Al/Mg Dissimilar FSW Joints. Metallurgical and Materials Transactions A 44, 3721-3731.

Lim, S., Kim, S., Lee, C.-G., Kim, S., 2004. Tensile behavior of friction-stri-welded Al 6061-T651. Metallurgical and Materials Transactions A 35, 2829-2835.

Liu, C., Chen, D.L., Bhole, S., Cao, X., Jahazi, M., 2009a. Polishing-assisted galvanic corrosion in the dissimilar friction stir welded joint of AZ31 magnesium alloy to 2024 aluminum alloy. Materials Characterization 60, 370-376.

Liu, F., Ren, D., Liu, L., 2013. Effect of Al foils interlayer on microstructures and mechanical properties of Mg–Al butt joints welded by gas tungsten arc welding filling with Zn filler metal. Materials & Design 46, 419-425.

Liu, F., Zhang, Z., Liu, L., 2012. Microstructure evolution of Al/Mg butt joints welded by gas tungsten arc with Zn filler metal. Materials Characterization 69, 84-89.

Liu, G., Murr, L.E., Niou, C.S., McClure, J.C., Vega, F.R., 1997. Microstructural aspects of the friction-stir welding of 6061-T6 aluminum. Scripta Materialia 37, 355-361.

Liu, H.J., Shen, J.J., Zhou, L., Zhao, Y.Q., Liu, C., Kuang, L.Y., 2011. Microstructural characterisation and mechanical properties of friction stir welded joints of aluminium alloy to copper. Science and Technology of Welding and Joining 16, 92-98.

Liu, L., Ren, D., Liu, F., 2014. A Review of Dissimilar Welding Techniques for Magnesium Alloys to Aluminum Alloys. Materials 7, 3735-3757.

Liu, L., Tan, J., Liu, X., 2007a. Reactive brazing of Al alloy to Mg alloy using zinc-based brazing alloy. Materials Letters 61, 2373-2377.

Liu, L.M., Zhao, L.M., Xu, R.Z., 2009b. Effect of interlayer composition on the microstructure and strength of diffusion bonded Mg/Al joint. Materials & Design 30, 4548-4551.

Liu, P., Li, Y., Geng, H., Wang, J., 2007b. Microstructure characteristics in TIG welded joint of Mg/Al dissimilar materials. Materials Letters 61, 1288-1291.

Liu, P., Shi, Q., Wang, W., Wang, X., Zhang, Z., 2008. Microstructure and XRD analysis of FSW joints for copper T2/aluminium 5A06 dissimilar materials. Materials Letters 62, 4106-4108.

Liyanage, T., Kilbourne, J., Gerlich, A.P., North, T.H., 2009. Joint formation in dissimilar Al alloy/steel and Mg alloy/steel friction stir spot welds. Science and Technology of Welding and Joining 14, 500-508.

Lorrain, O., Favier, V., Zahrouni, H., Lawrjaniec, D., 2010. Understanding the material flow path of friction stir welding process using unthreaded tools. Journal of Materials Processing Technology 210, 603-609.

Ma, Z.Y., Mishra, R.S., Mahoney, M.W., 2002. Superplastic deformation behaviour of friction stir processed 7075Al alloy. Acta Materialia 50, 4419-4430.

Mahoney, M.W., Rhodes, C.G., Flintoff, J.G., Bingel, W.H., Spurling, R.A., 1998. Properties of friction-stir-welded 7075 T651 aluminum. Metallurgical and Materials Transactions A 29, 1955-1964.

Maisonnette, D., Suery, M., Nelias, D., Chaudet, P., Epicier, T., 2011. Effects of heat treatments on the microstructure and mechanical properties of a 6061 aluminium alloy. Materials Science and Engineering: A 528, 2718-2724.

Malarvizhi, S., Balasubramanian, V., 2012. Influences of tool shoulder diameter to plate thickness ratio (D/T) on stir zone formation and tensile properties of friction stir welded dissimilar joints of AA6061 aluminum–AZ31B magnesium alloys. Materials & Design 40, 453-460.

Manes, A., Peroni, L., Scapin, M., Giglio, M., 2011. Analysis of strain rate behavior of an Al 6061 T6 alloy. Procedia Engineering 10, 3477-3482.

Mansoor, B., Dorbane, A., Ayoub, G., Imad, A., 2015a. Friction stir welding of AZ31B magnesium alloy with 6061-T6 aluminum alloy: Influence of processing parameters on microstructure and mechanical properties, in: Mishra, R.S., Mahoney, M.W., Sato, Y., Hovanski, Y. (Eds.), Friction Stir Welding and Processing VIII - The Minerals, Metals and Materials Society. Wiley, Somerset, NJ, pp. 259-266.

Mansoor, B., Dorbane, A., Ayoub, G., Imad, A., 2015b. Friction stir welding of AZ31B magnesium alloy with 6061-T6 aluminum alloy: Influence of processing parameters on microstructure and mechanical properties, TMS Annual Meeting, pp. 259-266.

Mansoor, B., Ghosh, A.K., 2012. Microstructure and tensile behavior of a friction stir processed magnesium alloy. Acta Materialia 60, 5079-5088.

Masoudian, A., Tahaei, A., Shakiba, A., Sharifianjazi, F., Mohandesi, J.A., 2014a. Microstructure and mechanical properties of friction stir weld of dissimilar AZ31-O magnesium alloy to 6061-T6 aluminum alloy. Transactions of Nonferrous Metals Society of China 24, 1317-1322.

Masoudian, A., Tahaei, A., Shakiba, A., Sharifianjazi, F., Mohandesi, J.A., 2014b. Microstructure and mechanical properties of friction stir weld of dissimilar AZ31-O

magnesium alloy to 6061-T6 aluminum alloy. Trans. Nonferrous Met. Soc. China 24, 1317-1322.

Mathaudhu, S.N., Nyberg, E.A., 2010. MAGNESIUM ALLOYS IN U.S. MILITARY APPLICATIONS: PAST, CURRENT AND FUTURE SOLUTIONS, in: Agnew, S.R., R., N.N., A., N.E., H., S.W. (Eds.), Magnesium Technology 2010, pp. 27-32.

Matsushita, M., Kitani, Y., Ikeda, R., Ono, M., Fujii, H., Chung, Y.D., 2011. Development of friction stir welding of high strength steel sheet. Science and Technology of Welding and Joining 16, 181-187.

McLean, A.A., Powell, G.L.F., Brown, I.H., Linton, V.M., 2003. Friction stir welding of magnesium alloy AZ31B to aluminium alloy 5083. Science and Technology of Welding and Joining 8, 462-464.

Meran, C., Kovan, V., Alptekin, A., 2007. Friction stir welding of AISI 304 austenitic stainless steel. Materialwissenschaft und Werkstofftechnik 38, 829-835.

Merzoug, M., Mazari, M., Berrahal, L., Imad, A., 2010. Parametric studies of the process of friction spot stir welding of aluminium 6060-T5 alloys. Materials & Design 31, 3023-3028.

Meyers, M.A., Chawla, K.K., 2009. Mechanical behavior of materials, second edition.

Midling, O.T., 1994. Proceedings of the Fourth International Conference on Aluminum Alloys, , in: Sanders, T.H., Strake, E.A. (Eds.), Georgia Institute of Technology, School of Materials Science and Engineering, Atlanta, GA, USA,, pp. 451-458.

Mishra, R.S., De, P.S., Kumar, N., 2014. Friction stir welding and processing. Springer International Publishing.

Mishra, R.S., Ma, Z.Y., 2005. Friction stir welding and processing. Materials Science and Engineering: R: Reports 50, 1-78.

Mishra, R.S., Mahoney, M.W., 2001. Friction Stir Processing: A New Grain Refinement Technique to Achieve High Strain Rate Superplasticity in Commercial Alloys. Materials Science Forum 357-359, 507-514.

Mishra, R.S., Mahoney, M.W., 2007. Friction stir welding and processing. ASM International, Materials Park, Ohio.

Mofid, M.A., Abdollah-Zadeh, A., Ghaini, F.M., Gur, C.H., 2012a. Submerged friction-stir welding (SFSW) underwater and under liquid nitrogen: An improved method to join Al alloys to Mg alloys. Metallurgical and Materials Transactions A: Physical Metallurgy and Materials Science 43, 5106-5114.

Mofid, M.A., Abdollah-zadeh, A., Malek Ghaini, F., 2012b. The effect of water cooling during dissimilar friction stir welding of Al alloy to Mg alloy. Materials & Design 36, 161-167.

Mohammadi, J., Behnamian, Y., Mostafaei, A., Izadi, H., Saeid, T., Kokabi, A.H., Gerlich, A.P., 2015. Friction stir welding joint of dissimilar materials between AZ31B magnesium and 6061 aluminum alloys: Microstructure studies and mechanical characterizations. Materials Characterization 101, 189-207.

Morisada, Y., Imaizumi, T., Fujii, H., 2015. Determination of strain rate in Friction Stir Welding by three-dimensional visualization of material flow using X-ray radiography. Scripta Materialia 106, 57-60.

Morishige, T., Kawaguchi, A., Tsujikawa, M., Hino, M., Hirata, T., Higashi, K., 2008. Dissimilar Welding of Al and Mg Alloys by FSW. Materials Transactions 49, 1129-1131.

Nageswara rao, P., Jayaganthan, R., 2012. Effects of warm rolling and ageing after cryogenic rolling on mechanical properties and microstructure of Al 6061 alloy. Materials & Design 39, 226-233.

Neto, D., Neto, P., 2013. Numerical modeling of friction stir welding process: a literature review. Int J Adv Manuf Technol 65, 115-126.

Nowotnik, G.M., Sieniawski, J., Wierzbiñska, M., 2007. Intermetallic phase particles in 6082 aluminium alloy. Archives of Materials Science and Engineering 28, 69-76.

Ofem, U.U., Colegrove, P.A., Addison, A., Russell, M.J., 2010. Energy and force analysis of linear friction welds in medium carbon steel. Science and Technology of Welding and Joining 15, 479-485.

Okamura, H., Aota, K., 2004. Joining of dissimilar materials with friction stir welding. Welding International 18, 852-860.

Ouyang, J., Kovacevic, R., 2002. Material flow and microstructure in the friction stir butt welds of the same and dissimilar aluminum alloys. Journal of Materials Engineering and Performance 11, 51-63.

Ouyang, J., Yarrapareddy, E., Kovacevic, R., 2006. Microstructural evolution in the friction stir welded 6061 aluminum alloy (T6-temper condition) to copper. Journal of Materials Processing Technology 172, 110-122.

Ozturk, F., Sisman, A., Toros, S., Kilic, S., Picu, R.C., 2010. Influence of aging treatment on mechanical properties of 6061 aluminum alloy. Materials & Design 31, 972-975.

Padmanaban, G., Balasubramanian, V., 2009. Selection of FSW tool pin profile, shoulder diameter and material for joining AZ31B magnesium alloy – An experimental approach. Materials & Design 30, 2647-2656.

Pan, W., Li, D., Tartakovsky, A.M., Ahzi, S., Khraisheh, M., Khaleel, M., 2013. A new smoothed particle hydrodynamics non-Newtonian model for friction stir welding: Process modeling and simulation of microstructure evolution in a magnesium alloy. International Journal of Plasticity 48, 189-204.

Panteli, A., Robson, J.D., Brough, I., Prangnell, P.B., 2012. The effect of high strain rate deformation on intermetallic reaction during ultrasonic welding aluminium to magnesium. Materials Science and Engineering: A 556, 31-42.

Park, S.H.C., Sato, Y.S., Kokawa, H., Okamoto, K., Hirano, S., Inagaki, M., 2003. Rapid formation of the sigma phase in 304 stainless steel during friction stir welding. Scripta Materialia 49, 1175-1180.

Peel, M., Steuwer, A., Preuss, M., Withers, P.J., 2003. Microstructure, mechanical properties and residual stresses as a function of welding speed in aluminium AA5083 friction stir welds. Acta Materialia 51, 4791-4801.

Pollock, T.M., 2010. Weight Loss with Magnesium Alloys. Science 328, 986-987.

polmear, L., 2006. Light Alloys: From Traditional Alloys to Nanocrystals.

Pourahmad, P., Abbasi, M., Mehrabi, H.A., 2013. Bimetal friction stir welding of aluminum to magnesium. Journal of Advanced Materials and Processing 1, 27-38.

Prado, R.A., Murr, L.E., Shindo, D.J., Soto, K.F., 2001. Tool wear in the friction-stir welding of aluminum alloy 6061+20% Al2O3: a preliminary study. Scripta Materialia 45, 7580.

Prado, R.A., Murr, L.E., Soto, K.F., McClure, J.C., 2003. Self-optimization in tool wear for friction-stir welding of Al 6061+20% Al2O3 MMC. Materials Science and Engineering: A 349, 156-165.

Rai, R., De, A., Bhadeshia, H.K.D.H., DebRoy, T., 2011. Review: friction stir welding tools. Science and Technology of Welding and Joining 16, 325-342.

Ramulu, P.J., Narayanan, R.G., Kailas, S.V., Reddy, J., 2012. Internal defect and process parameter analysis during friction stir welding of Al 6061 sheets. Int J Adv Manuf Technol 65, 1515-1528.

Rao, P.N., Singh, D., Jayaganthan, R., 2014. Mechanical properties and microstructural evolution of Al 6061 alloy processed by multidirectional forging at liquid nitrogen temperature. Materials & Design 56, 97-104.

Ravi, C., Wolverton, C., 2004. First-principles study of crystal structure and stability of Al–Mg–Si–(Cu) precipitates. Acta Materialia 52, 4213-4227.

Ren, S.R., Ma, Z.Y., Chen, L.Q., 2007. Effect of welding parameters on tensile properties and fracture behavior of friction stir welded Al–Mg–Si alloy. Scripta Materialia 56, 69-72.

Rhodes, C.G., Mahoney, M.W., Bingel, W.H., Spurling, R.A., Bampton, C.C., 1997. Effects of friction stir welding on microstructure of 7075 aluminum. Scripta Materialia 36, 69-75.

Robson, J., Panteli, A., Prangnell, P.B., 2012. Modelling intermetallic phase formation in dissimilar metal ultrasonic welding of aluminium and magnesium alloys. Science and Technology of Welding and Joining 17, 447-453.

Rodriguez, A.K., Kridli, G., Ayoub, G., Zbib, H., 2013. Effects of the Strain Rate and Temperature on the Microstructural Evolution of Twin-Rolled Cast Wrought AZ31B Alloys Sheets. Journal of Materials Engineering and Performance 22, 3115-3125.

Rodriguez, N.A., Almanza, E., Alvarez, C.J., Murr, L.E., 2005. Study of friction stir welded A319 and A413 aluminum casting alloys. Journal of Materials Science 40, 4307-4312.

Sakthivel, T., Mukhopadhyay, J., 2007. Microstructure and mechanical properties of friction stir welded copper. Journal of Materials Science 42, 8126-8129.

Samson, S., 1965. The crsytal structure of the phase β Mg2Al3. Acta Crystallographica 19, 401-413.

Sanders, R., Jr., 2001. Technology innovation in aluminum products. JOM 53, 21-25.

Santos, T.G., Miranda, R.M., Vilaça, P., Teixeira, J.P., dos Santos, J., 2011. Microstructural mapping of friction stir welded AA 7075-T6 and AlMgSc alloys using electrical conductivity. Science and Technology of Welding and Joining 16, 630-635.

Sato, Y.S., Kokawa, H., Enomoto, M., Jogan, S., Hashimoto, T., 1999. Precipitation sequence in friction stir weld of 6063 aluminum during aging. Metallurgical and Materials Transactions A 30, 3125-3130.

Sato, Y.S., Park, S.H.C., Michiuchi, M., Kokawa, H., 2004. Constitutional liquation during dissimilar friction stir welding of Al and Mg alloys. Scripta Materialia 50, 1233-1236.

Savolainen, K., Saukkonen, T., Hänninen, H., 2012. Banding in copper friction stir weld. Science and Technology of Welding and Joining 17, 111-115.

Schmidt, H.N.B., Dickerson, T.L., Hattel, J.H., 2006. Material flow in butt friction stir welds in AA2024-T3. Acta Materialia 54, 1199-1209.

Scialpi, A., De Filippis, L.A.C., Cavaliere, P., 2007. Influence of shoulder geometry on microstructure and mechanical properties of friction stir welded 6082 aluminium alloy. Materials & Design 28, 1124-1129.

Shackelford, J.F., Alexander, W., 2001. CRC Materials Science and Engineering Handbook, Third Edition. Boca Raton: CRC Press LLC.

Shang, J., Wang, K., Zhou, Q., Zhang, D., Huang, J., Li, G., 2012. Microstructure characteristics and mechanical properties of cold metal transfer welding Mg/Al dissimilar metals. Materials & Design 34, 559-565.

Shankar, M.R., Chandrasekar, S., King, A.H., Compton, W.D., 2005. Microstructure and stability of nanocrystalline aluminum 6061 created by large strain machining. Acta Materialia 53, 4781-4793.

Shi, M.F., Meuleman, D.J., 1995. On certain aspects of strain rate sensitivity of sheet metals. Journal of Materials Engineering and Performance 4, 321-333.

Shindo, D.J., Rivera, a.R., Murr, L.E., 2002. Shape optimization for tool wear in the friction-stir welding of cast AI359-20 % SiC MMC. Journal of materials science 7, 4999-5005.

Somasekharan, A., Murr, L., 2004a. Microstructures in friction-stir welded dissimilar magnesium alloys and magnesium alloys to 6061-T6 aluminum alloy. Materials Characterization 52, 49-64.

Somasekharan, A., Murr, L., 2004b. Microstructures in friction-stir welded dissimilar magnesium alloys and magnesium alloys to 6061-T6 aluminum alloy. Mater. Charact. 52, 49-64.

Sorensen, C.D., Stahl, A.L., 2007. Experimental Measurements of Load Distributions on Friction Stir Weld Pin Tools. Metallurgical and Materials Transactions B 38, 451-459.

Springer, H., Kostka, A., dos Santos, J.F., Raabe, D., 2011. Influence of intermetallic phases and Kirkendall-porosity on the mechanical properties of joints between steel and aluminium alloys. Materials Science and Engineering: A 528, 4630-4642.

Su, J.-Q., Nelson, T.W., Sterling, C.J., 2005. Microstructure evolution during FSW/FSP of high strength aluminum alloys. Materials Science and Engineering: A 405, 277-286.

Su, J.Q., Nelson, T.W., Mishra, R., Mahoney, M., 2003. Microstructural investigation of friction stir welded 7050-T651 aluminium. Acta Materialia 51, 713-729.

Sun, N., Yin, Y.H., Gerlich, A.P., North, T.H., 2009. Tool design and stir zone grain size in AZ31 friction stir spot welds. Science and Technology of Welding and Joining 14, 747-752.

Sutton, M.A., Reynolds, A.P., Yang, B., Taylor, R., 2003. Mode I fracture and microstructure for 2024-T3 friction stir welds. Materials Science and Engineering: A 354, 6-16.

T. Akinlabi, E., A. Akinlabi, S., 2012. Effect of Heat Input on the Properties of Dissimilar Friction Stir Welds of Aluminium and Copper. American Journal of Materials Science 2, 147-152.

Tan, E., Kibar, A.A., Gür, C.H., 2011. Mechanical and microstructural characterization of 6061 aluminum alloy strips severely deformed by Dissimilar Channel Angular Pressing. Materials Characterization 62, 391-397.

Tanaka, T., Morishige, T., Hirata, T., 2009. Comprehensive analysis of joint strength for dissimilar friction stir welds of mild steel to aluminum alloys. Scripta Materialia 61, 756-759.

Tang, W., Guo, X., McClure, J.C., Murr, L.E., Nunes, A., 1998. Heat Input and Temperature Distribution in Friction Stir Welding. Journal of Materials Processing & Manufacturing Science 7, 163-172.

Tang, X., Li, D., Prakash, V., Lewandowski, J.J., 2011. Effects of microstructure on high strain rate deformation and flow behaviour of Al–Mg–Si alloy (AA 6061) under uniaxial compression and combined compression and shear loading. Materials Science and Technology 27, 13-20.

Tao, Y., Zhang, Z., Ni, D.R., Wang, D., Xiao, B.L., Ma, Z.Y., 2014. Influence of welding parameter on mechanical properties and fracture behavior of friction stir welded Al–Mg–Sc joints. Materials Science and Engineering: A 612, 236-245.

Tharumarajah, A., Koltun, P., 2007. Is there an environmental advantage of using magnesium components for light-weighting cars? Journal of Cleaner Production 15, 1007-1013.

Thomas, W.M., Nicholas, E.D., Needham, J.C., Murch, M.G., Temple-Smith, P., C.J., D., 1991. Friction -stir butt welding. GB Patent No. 9125978.8, International Patent No. PCT/GB92/02203.

Thomson, R.D., Hancock, J.W., 1984. Ductile failure by void nucleation, growth and coalescence. International Journal of Fracture 26, 99-112.

Tiwari, S.K., Shukla, D.K., Chandra, R., 2013. Friction Stir Welding of Aluminum Alloys: A Review. International Journal of Mechanical, Aerospace, Industrial, Mechatronic and Manufacturing Engineering Vol. 7, 2403 - 2408.

Tucker, M.T., Horstemeyer, M.F., Whittington, W.R., Solanki, K.N., Gullett, P.M., 2010. The effect of varying strain rates and stress states on the plasticity, damage, and fracture of aluminum alloys. Mechanics of Materials 42, 895-907.

Vargas, J.A., Torres, J.E., Pacheco, J.A., Hernandez, R.J., 2013. Analysis of heat input effect on the mechanical properties of Al-6061-T6 alloy weld joints. Materials & Design 52, 556-564.

Venukumar, S., Yalagi, S., Muthukumaran, S., 2013. Comparison of microstructure and mechanical properties of conventional and refilled friction stir spot welds in AA 6061-T6 using filler plate. Transactions of Nonferrous Metals Society of China 23, 2833-2842.

Vukčević, M., Savičević, S., Janjić, M., Šibalić, N., 2011. Measurement in friction stir welding process, Proceedings of 15th TMT Conference, Prague, Czech Republic, pp. 12-18.

Wadeson, D.A., Zhou, X., Thompson, G.E., Skeldon, P., Oosterkamp, L.D., Scamans, G., 2006. Corrosion behaviour of friction stir welded AA7108 T79 aluminium alloy. Corrosion Science 48, 887-897.

Wan, L., Huang, Y., Guo, W., Lv, S., Feng, J., 2014. Mechanical Properties and Microstructure of 6082-T6 Aluminum Alloy Joints by Self-support Friction Stir Welding. Journal of Materials Science & Technology 30, 1243-1250.

Wang, J., Feng, J.C., Wang, Y.X., 2008. Microstructure of Al–Mg dissimilar weld made by cold metal transfer MIG welding. Materials Science and Technology 24, 827-831.

Wang, Z., Wang, H., Liu, L., 2012. Study on low temperature brazing of magnesium alloy to aluminum alloy using Sn–xZn solders. Materials & Design 39, 14-19.

Watanabe, T., Takayama, H., Yanagisawa, A., 2006. Joining of aluminum alloy to steel by friction stir welding. Journal of Materials Processing Technology 178, 342-349.

Woo, W., Choo, H., 2011. Softening behaviour of friction stir welded Al 6061-T6 and Mg AZ31B alloys. Science and Technology of Welding and Joining 16, 267-272.

Xu, W.F., Liu, J.H., Chen, D.L., 2011. Material flow and core/multi-shell structures in a friction stir welded aluminum alloy with embedded copper markers. Journal of Alloys and Compounds 509, 8449-8454.

Xue, P., Xiao, B.L., Zhang, Q., Ma, Z.Y., 2011. Achieving friction stir welded pure copper joints with nearly equal strength to the parent metal via additional rapid cooling. Scripta Materialia 64, 1051-1054.

Xunhong, W., Kuaishe, W., 2006. Microstructure and properties of friction stir butt-welded AZ31 magnesium alloy. Materials Science and Engineering: A 431, 114-117.

Yadava, M.K., Mishra, R.S., Chen, Y.L., Carlson, B., Grant, G.J., 2010. Study of friction stir joining of thin aluminium sheets in lap joint configuration. Science and Technology of Welding and Joining 15, 70-75.

Yan, J., Xu, Z., Li, Z., Li, L., Yang, S., 2005. Microstructure characteristics and performance of dissimilar welds between magnesium alloy and aluminum formed by friction stirring. Scripta Materialia 53, 585-589.

Yan, Y., Zhang, D.-t., Qiu, C., Zhang, W., 2010. Dissimilar friction stir welding between 5052 aluminum alloy and AZ31 magnesium alloy. Transactions of Nonferrous Metals Society of China 20, Supplement 2, s619-s623.

Yang, J., Wang, D., Xiao, B.L., Ni, D.R., Ma, Z.Y., 2012. Effects of Rotation Rates on Microstructure, Mechanical Properties, and Fracture Behavior of Friction Stir-Welded (FSW) AZ31 Magnesium Alloy. Metallurgical and Materials Transactions A 44, 517-530.

Yang, J., Xiao, B.L., Wang, D., Ma, Z.Y., 2010. Effects of heat input on tensile properties and fracture behavior of friction stir welded Mg–3Al–1Zn alloy. Materials Science and Engineering: A 527, 708-714.

Yin, Y.H., Sun, N., North, T.H., Hu, S.S., 2010. Influence of tool design on mechanical properties of AZ31 friction stir spot welds. Science and Technology of Welding and Joining 15, 81-86.

Young, J.P., Askari, H., Hovanski, Y., Heiden, M.J., Field, D.P., 2015. Thermal microstructural stability of AZ31 magnesium after severe plastic deformation. Materials Characterization 101, 9-19.

Zettler, R., da Silva, A.A.M., Rodrigues, S., Blanco, A., dos Santos, J.F., 2006. Dissimilar Al to Mg Alloy Friction Stir Welds. Advanced Engineering Materials 8, 415-421.

Zettler, R., Dos Santos, J.F., Blanco, A., Da Silva, A., 2005. A study on dissimilar friction stir welds between Al and Mg alloys, 7th International Conference on Trends in Welding Research, May 16, 2005 - May 20, 2005. ASM International, Pine Mountain, GA, United states, pp. 413-419.

Zhang, H.J., Liu, H.J., Yu, L., 2011. Microstructural evolution and its effect on mechanical performance of joint in underwater friction stir welded 2219-T6 aluminium alloy. Science and Technology of Welding and Joining 16, 459-464.

Zhang, M.X., Huang, H., Spencer, K., Shi, Y.N., 2010a. Nanomechanics of Mg–Al intermetallic compounds. Surface and Coatings Technology 204, 2118-2122.

Zhang, Y., Sato, Y.S., Kokawa, H., Park, S.H.C., Hirano, S., 2010b. Grain structure and microtexture in friction stir welded commercial purity titanium. Science and Technology of Welding and Joining 15, 500-505.

Zhang, Y.N., Cao, X., Larose, S., Wanjara, P., 2012. Review of tools for friction stir welding and processing. Canadian Metallurgical Quarterly 51, 250-261.

Zhao, L.M., Zhang, Z.D., 2008. Effect of Zn alloy interlayer on interface microstructure and strength of diffusion-bonded Mg–Al joints. Scripta Materialia 58, 283-286.

Zhu, D., Mobasher, B., Rajan, S., Peralta, P., 2011. Characterization of Dynamic Tensile Testing Using Aluminum Alloy 6061-T6 at Intermediate Strain Rates. Journal of Engineering Mechanics 137, 669-679.

Zwieg, T., 2004. A Universal Method for the Mechanical Preparation of Aluminium Alloy Specimens with High Edge Retention and their Subsequent Colour Etchin. Praktische Metallographie 38, 3-6.